IMPACT OF SUBSURFACE HETEROGENEITIES ON THE CO_2 STORAGE POTENTIAL OF AQUIFERS

NFR KLIMATEK PROGRAM

FINAL REPORT

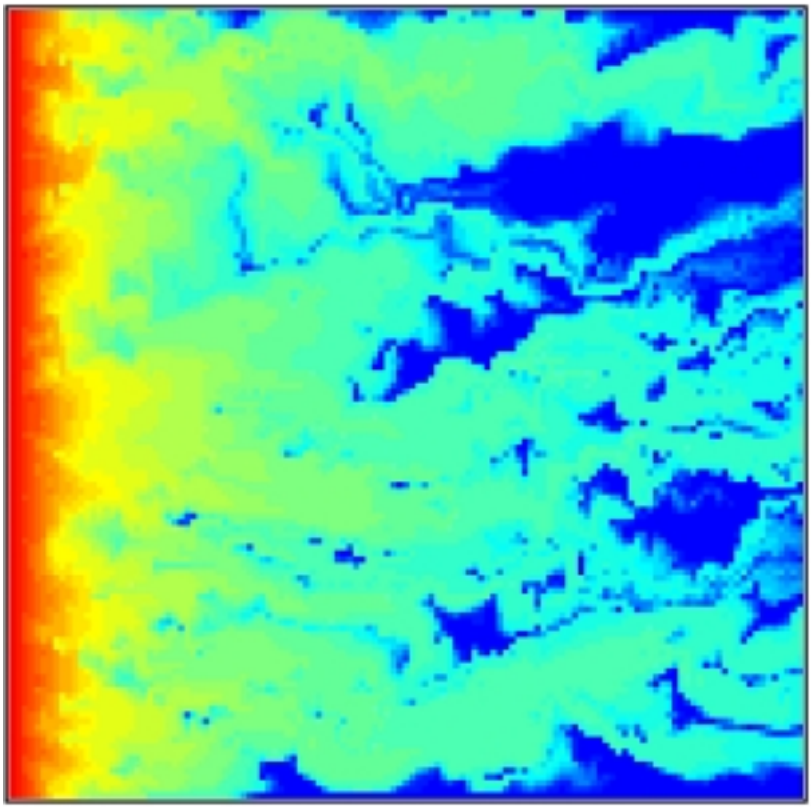

Noelle E. Odling - Eric Bonnet

Nansen Environmental and Remote Sensing Centre (NERSC)

Bergen - Norway

December 2000

PART A. INTRODUCTION 11

A-1. KLIMATEK PROJECT AND CO_2 DISPOSAL 11

A-2. APPROACH USED 12

1- DEFINITION OF HETEROGENEOUS SYSTEM 12
2- THE HETEROGENEITY IN UTSIRA FORMATION 13

A-3. OBJECTIVES 13

PART B. GEOLOGY 15

B-1. THE UTSIRA FORMATION AND THE UTSIRA SAND 15

1- REGIONAL GEOLOGY 15
2- DETAILED GEOLOGY OF THE UTSIRA FORMATION AND THE NORDLAND SHALES AT SLEIPNER 16
3- PETROGRAPHY 17
4- DEPOSITIONAL ENVIRONMENT 17

B-2. TURBIDITES 18

1- DEFINITION AND GENERALITY 18
1-1 CLASSIC TURBIDITES 18
1-2 MASSIVE SANDSTONES 19
1-3 PEBBLY SANDSTONES 19
1-4 CLAST SUPPORTED CONGLOMERATES 19
1-5 MATRIX SUPPORTED BEDS 20
2- RELATION OF FACIES TO FAN MORPHOLOGY 20
3- STRATIGRAPHIC EVOLUTION OF FANS 20
4- THE UTSIRA FORMATION. 20

B-3. LENGTH AND SPATIAL DISTRIBUTION OF TURBIDITE BEDS 21

1- THICKNESS AND LENGTH DISTRIBUTION 21
2- SPATIAL ORGANISATION 22

B-4. PERMEABILITY AND POROSITY OF SANDS AND CLAY 23

1- PERMEABILITY AND POROSITY OF SANDS 24
2- PERMEABILITY AND POROSITY OF CLAY 26

PART C. MODELS 28

C-1. MODELLING SEDIMENTARY ARCHITECTURES 28

1- THE COUPLED MARKOV CHAIN MODEL 28
1-1 GENERATING A 2D FIELD USING THE COUPLED MARKOV CHAIN METHOD 29
1-2 GENERATING TRANSITION PROBABILITY MATRICES 31
2- FRACTAL PATTERN 31

C-2. GENERATING PERMEABILITY AND POROSITY FIELDS FOR INPUT TO FLOW MODELS 34

1- SIMPLE GEOMETRY 34
1-1 SINGLE LAYERS 34
1-2 MULTIPLE PARALLEL LAYERS 36
1-3 CROSS-CUTTING LAYERS 38
2- TURBIDITES SEQUENCES 39
2-1 CROSS BEDDING 41
2-2 FLUID ESCAPE STRUCTURE 42
2-3 COMPLEX CROSS-CUT PATTERNS 43

C-3. TWO-PHASE FLOW IN HETEROGENEOUS SEDIMENTS 45

1- GENERALITY 45
2- PERMEABILITY RATIO 46
3- RELATIVE PERMEABILITY, FRACTIONAL FLOW AND FLUID FRONT 47
3-1 RELATIVE PERMEABILITY 47
3-2 FRACTIONAL FLOW FUNCTION 48
4- PSEUDO FUNCTIONS FOR ROCK VOLUMES 49

C-4. A TWO PHASE FLOW MODEL FOR HETEROGENEOUS SEDIMENTS 50

1- THE MODEL 50
2- MODEL INPUT 50
2-1 PERMEABILITY AND POROSITY FIELD 50
2-2 VISCOSITY OF WATER AND SUPERCRITICAL CO_2 51
2-3 RELATIVE PERMEABILITY CURVES FOR WATER-LIQUID CO_2 51
2-4 MODEL BOUNDARY CONDITION 51
3- MODEL OUTPUT AND STUDY PARAMETERS 51

PART D. NUMERICAL MODEL RESULTS 54

D-1. SIMULATED SIMPLE LAYER PATTERNS AND FRACTURE SYSTEMS: SATURATION EVOLUTION AND PSEUDO CURVES 55

1- SIMPLE LAYERS GEOMETRIES 55
1-1 TYPE OF HETEROGENEITY 55

1-2 FLOW ORIENTATION AND MATRIX HETEROGENEITY 57
2- CONSTANT LENGTH FRACTURES 60
2-1 MULTIPLE PARALLEL FRACTURES 60
2-2 DIAGONAL AND ORTHOGONAL FRACTURES 61
3- VARIABLE LENGTH FRACTURES 67
3-1 MULTIPLE PARALLEL FRACTURES 67

D-2. COMPLEX TURBIDITES GEOMETRY 70

1- BULK ROCK PERMEABILITY 70
2- SATURATION FIELD EVOLUTION 71
3- SATURATION EVOLUTION PLOTS 81
4- PSEUDO-CURVES AND SENSIBILITY ANALYSIS 83

D-3. FRACTAL FRACTURE PATTERNS: FLOW BARRIERS AND CONDUITS 90

1- PERMEABILITY CONTRAST DEPENDENCE 90
1-1 SATURATION FIELD 92
1-2 PSEUDO RELATIVE AND FRACTIONAL FLOW CURVES 94
1-3 PRESENCE OF AN ESCAPE STRUCTURE 95
2- DENSITY DEPENDENCE 102
2-1 PRESENTATION 102
2-2 SATURATION EVOLUTION - BARRIER CASE 104
2-3 SATURATION EVOLUTION - PREFERENTIAL PATH CASE 108
2-4 PSEUDO RELATIVE AND FRACTIONAL FLOW CURVES 112
3- VARIABLE FRACTAL DIMENSION 117
3-1 INTRODUCTION AND GEOMETRICAL CHARACTERISTICS 117
3-2 SATURATION FIELD 120
3-3 DENSITY DEPENDENCE 121

PART E. DISCUSSION AND CONCLUSION 125

PART F. BIBLIOGRAPHY 129

INDEX OF TABLES AND FIGURES 133

PART A. INTRODUCTION

A-1. Klimatek project and CO_2 disposal

Injection of CO_2 from the Sleipner West platform into the Utsira Formation has been on-going at a rate of around 1 million tonnes per year since October 1996. Petroleum produced from the Sleipner field which lies deeper within the stratigraphic column, contains a high level of CO_2. The CO_2 content is reduced from 9% to 2.5% in order to meeting regulations and the extracted CO_2 is injected via a shallowly dipping well into a salt water aquifer in a sandy section of the Utsira Formation at a depth of 987m below sea level (Figure 1). This represents the first attempt on an industrial scale to dispose of CO_2 to a sub-sea aquifer and represents a unique chance to increase the knowledge on this method of CO_2 disposal and its impact on the environment.

In 1997 research activities through a number of projects were initiated to investigate and monitor the behaviour and migration of the injected CO_2 and its interaction with the aquifer sediments and fluids. These activities are co-ordinated by Statoil in Trondheim (Norway) and involve a large number of partners in the industrial and research sectors including the energy companies Statoil, BP Exploration, Mobil Norway, Norsk Hydro and Vattenfjall AB, and the research institutes BGS (UK), BRGM (France), IFP (France), GEUS (Denmark), IKU (Norway), NERSC (Norway), TNO (Netherlands) and IEA-GHG. Funding comes from the energy companies, EU Thermie program, and national research councils.

Activities started with an initiation project, SACS Zero Phase, in which a thorough data search and preliminary studies were carried out. This was followed by the SACS project (Saline Water CO_2 Storage) from (01.11.1998 to 31.10,1999) and by SACSII which started 01.03.2000 and is of 2 years duration, both funded through the energy companies and the EU Thermie. The SACS projects have associated with them a number of nationally funded projects including two through the Klimatek program of NFR in Norway. These include the Klimatek project reported here entitled '*Impact of Subsurface heterogeneity on the CO_2 storage potential of aquifers*' which is of 12 man months duration over the two year period 01.01.1999-31.12.2000.

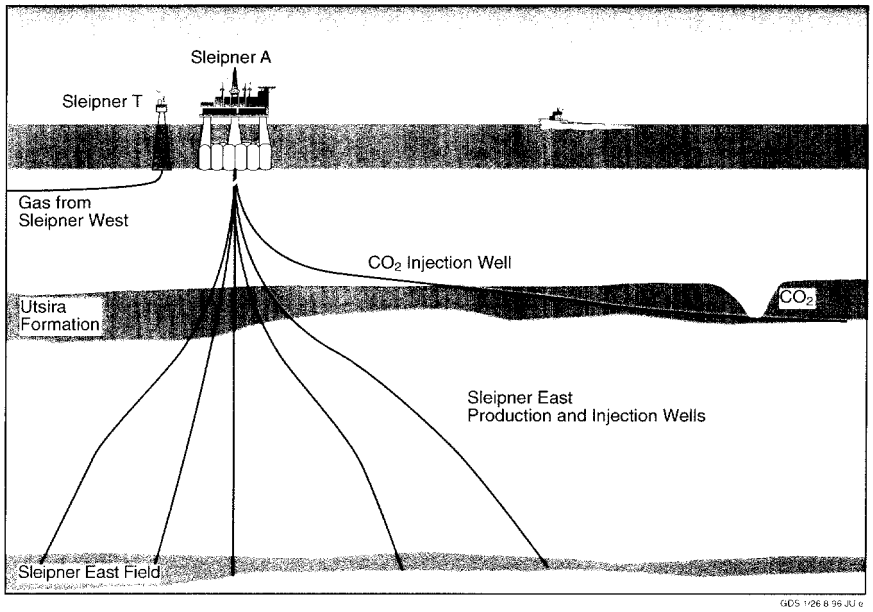

Figure 1: Cross-section showing the Sleipner field and Sleipner A platform. CO_2 removed from produced oil is re-injected into a salt water aquifer in the Utsira Formation.

A-2. Approach used

The project comprises a study, through numerical modelling, of the influence of rock heterogeneity in aquifers on the behaviour of injected supercritical CO_2.

1- Definition of heterogeneous system

A heterogeneous system (or similarly a disordered material) is a system whose local properties vary spatially. Therefore the degree of heterogeneity (or the amount of disorder) can be defined as the way the distribution of the local properties inside the system deviates from its average (Figure 2), and one measure of the heterogeneity consist in the standard deviation of the distribution. Following this definition, a homogeneous system will have a null standard deviation.

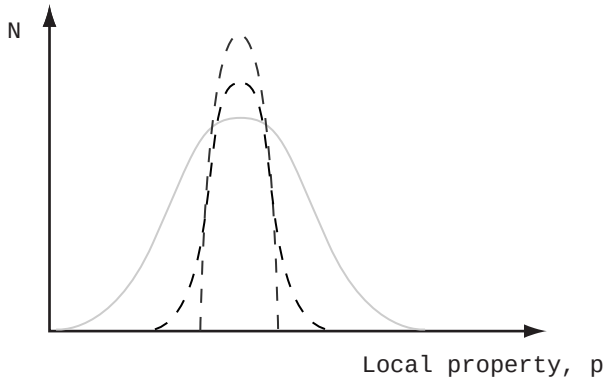

Figure 2: for a given system, distribution of a local property *p*. Two different distributions having the same mean value are shown. The thick grey line displays a broader spectrum than the dashed dark one, which indicates a more heterogeneous system.

Two main types of heterogeneity can be distinguished: static disorder and dynamic disorder. The first one corresponds to a disorder introduced at the beginning and which is definitively fix. This inherent disorder is for example the distribution of pore size for a porous media. The second type of disorder is dynamic *i.e.* the nature of the heterogeneity is evolving with time. For example a growing fault is a dynamic heterogeneity since during deformation it is continuously increasing in size. In the following section, we will only consider the case of static disorder, which may takes various forms. Here we will consider essentially two types of heterogeneities:

- **The heterogeneity in composition**. It is associated to the presence of elements presenting different physical or chemical properties compare to the embedding volume. For example, in our case, this will corresponds to the presence of a shale layer or a fracture with a different permeability k_I and different porosity Φ_I.

- **The geometrical heterogeneity**. It describes the way heterogeneities of composition are organised in space. These heterogeneities can be clustered or strongly correlated or, on contrary distributed in a random way in the considered system. Two parameters can describe this type of heterogeneity; *(i)* the size distribution of object and *(ii)* the spatial organisation of heterogeneity.

2- The heterogeneity in Utsira formation

Little is presently known about the Utsira Formation. There is very little material from cores and most presently available information comes from seismic sections and one bore hole log. One of the main questions from the point of view of fluid flow is what sort of heterogeneities exists in the Utsira. Recent studies by *Gregersen et al.* [1997] suggest that the lower parts of the Utsira Formation are composed of basinal stacked low stand deposits with transgressive high stand deposits in more land-ward parts. The bore hole log, presently being studied by IKU, shows indications of shale layers. A reasonable interpretation of the sedimentary setting thus seems to be turbidite sequences composed of sands with intermittent shale layers. The shale layers will act as permeability barriers and their abundance and spatial distribution will affect the migration of CO_2 through the Utsira Formation. Other possible sources of heterogeneity in the Utsira Formation include faults which may be present in the lower parts of the Formation where mounds (possibly mud volcanoes) are present. Such faults may act as flow conduits or flow barriers. In addition, the nature of sedimentary layering such as internal laminations and cross-bedding within the sand bodies may influence fluid flow.

Therefore, form a general point of view and using the definition used above, both tupe of heterogeneities are present (composition and geometry). Hence, hereafter we will consider their influence on flow and migration of CO_2.

A-3. Objectives

Heterogeneity types present in the Utsira Formation are identified. Flow of CO_2 in the aquifer is simulated with a two- phase flow model which can reproduce the complex saturation distributions and fluid fronts resulting from the large viscosity contrast between supercritical CO_2 and water. The model is then used to test the sensitivity of injected CO_2 behaviour to rock heterogeneities, and to determine bulk rock permeabilities and pseudo functions (relative permeabilities for CO_2 and water) for large rock volumes, parameters that can be used as input to a large scale flow simulator. The objectives of the project are:

1. To model the time dependent evolution of the distribution and dissolution of supercritical CO_2 injected into heterogeneous aquifers

2. To assess the potential impact of rock heterogeneity types expected in the Utsira Formation on the behaviour of injected supercritical CO_2

3. To determine the sensitivity of injected CO_2 behaviour to different types of rock and sediment heterogeneity

4. To determine effective bulk permeabilities and pseudo functions (relative permeabilities) for volumes of rock and sediment with sizes comparable to grid blocks used in large scale flow simulations

5. To use scaled up permeability and pseudo functions as input to a large scale flow model of CO_2 injection, with the aim of assessing the importance of accounting for the effects of rock and sediment heterogeneity on the behaviour of injected supercritical CO_2.

This report constitutes the report on the work done during the first and second half of the project and concentrates on the impact of heterogeneities of a sedimentary nature (acting as preferential path or as barriers) on the migration of injected CO_2 in the supercritical phase, contributing to objectives 1 to 4.

PART B. GEOLOGY

B-1. The Utsira formation and the Utsira sand

1- Regional geology

The Cenozoic stratigraphy of the North Sea has been described by several authors [*Degan and Scull* 1977; *Isaksen and Tonstad*, 1989; *Jordt et al.*, 1995; *Gregersen et al.*, 1997, 1998; *Eidvin et al.*, 1999] and more recently in detail in a number of reports produced in connection with the SACS project [*Lothe and Zweigel*, 1999; *Torp*, 1999]. The Utsira Formation forms the basal part of the Cenozoic dominantly argillaceous Nordland Group [*Gregersen et al.*, 1997] which was deposited in the Mid-Miocene and lies largely in the Norwegian sector of the Southern Viking Graben between the Jaren High and the Tampen Spur, see Figure 3. It forms an elongated sub-crop trending N-S about 430 km long and around 85 km wide. It contains two main depo-centres, north and south of 60° N and reaches a maximum thickness of 550m. The Utsira Formation can be traced laterally into the Hutton sands in the British sector. It contains thick sand bodies in its central portions which grad into more shale rich sediments at the margins. The Utsira Formation is over-lain by the shale rich members of the Nordland Group of Pliocene age which down-lap on the top of the Utsira Formation. This sequence is dominated by prograding sequences with sediment transport from the Norwegian shelf to the W and NW.

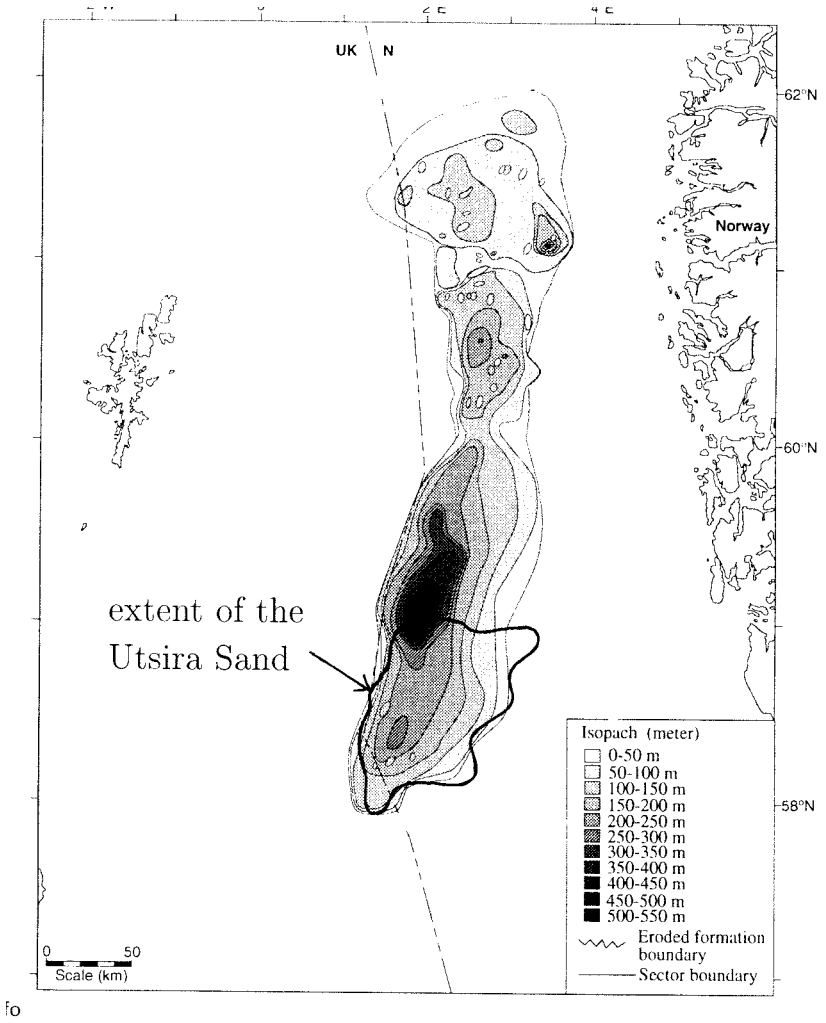

Figure 3: The extent of the Utsira Formation and the Utsira Sand in the Northern North Sea (modified from *Gregersen* [1997].

2- Detailed geology of the Utsira formation and the Nordland shales at Sleipner

In the Sleipner area, more detailed interpretation of seismic data has revealed that the sands into which CO_2 is being injected form a restricted sand body within the Utsira formation which has been termed the 'Utsira Sand'. The Utsira Sand sub-crops over an area of 12 by 9 km in the Sleipner area [*Lothe and Zweigel*, 1999; *Torp*, 1999] at the location where the Utsira Formation is at its thickest, see Figure 3. This unit has a maximum depth of around 300m and grades into more shale rich sediments on all sides. At the location of the injection well the Utsira Sand has a thickness of 200m.

Detailed analysis of seismic data, well logs and some core have revealed information about the Utsira Sand and the Nordland shale in the vicinity of the Sleipner area [*Lothe and Zweigel*, 1999; *Torp*, 1999]. The top and base of the Utsira Formation form strong seismic reflectors and abrupt changes in electrical logs reflect sharp transitions from sand rich to clay rich sediments. Toplap regionally to the west onto the base reflector of the Utsira Sand suggest it represents an erosional boundary (the Miocene unconformity). The top of the Utsira Formation forms the base of prograding units of the Nordland shales which onlap from east and west towards the depo-centre of the Utsira Sand. In the Sleipner area, the base Utsira forms an elongate depression trending NW-SW steepening to the SW. The Utsira Sand is thickest north of the injection site and thins westwards from the injection well showing that this area lies on the western flank of the Utsira Sand unit.

The overlying Pliocene Nordland shales show rather uniform thickness in the vicinity of the injection well. Here there is a sand wedge of around 16m thickness separated from the Utsira Sand by 5m of shale but does not appear to be connect to the Utsira Sand anywhere. Log cuttings indicate that, apart from this sand wedge, these sediments represent a continuous clay sequence. In the area of the injection site the Pliocene sediment package is around 230 m thick. Seismically, the Utsira Formation shows internally parallel continuous to discontinuous layering. Internal features of gamma and resistivity logs are though to reflect thinning upwards sequences but signs of coarsening upward cycles are also seen. Locally high gamma and resistivity values within the Utsira Sand are thought to reflect clay layers around 1m thick or less. Four of these clay layers could be traced locally from well to well but correlations over distances of over 2 km are not possible. In the injection well (in which resolution is highest due to the deviated nature of this well) some 14 of these shale layers were detected. Limited resolution of the electrical logs means this number is a minimum and additional thinner shale and clay layer may be present.

The base of the Utsira Sand shows mounds over-lain by onlapping or downlapping layering. These mounds show generally elongated forms, 1-2 km across and are interpreted as mud volcanoes formed by mud diapirism sourced by the underlying Hordaland shales. The bulk of mud diapirism seems to have taken place after the deposition of the Utsira sands and to have formed mud sheets within the lower parts of the Utsira Sand. The top of the Utsira Sand is often depressed over these mounds thought to be caused by the greater compaction of the clay forming these mounds. They seem also to associated with disturbed areas on seismic section interpreted as gas chimneys formed by the upward migration of natural gas [*Heggland*, 1997]. This is corroborated by mud-log reports of shallow gas in the Utsira Formation and overlying shales. Mud volcanoes development may have been triggered and / or formed preferential routes for the migration of natural gas. In the overlying shales, high seismic amplitudes (reflecting shallow gas occurrence) show a weak NW-SE alignment which may reflect a structural pattern such as small scale faults or joints which may have controlled gas migration.

3- Petrography

The only core material available is from well 15 / 9-A23 (sampled at 905.4-910.8 TVD from the Utsira Sand) which has been analysed by IKU (Norway), GEUS (Denmark) and BGS (UK) [*Lothe and Zweigel*, 1999; *Torp*, 1999]. This is composed of grey, very fine grained, moderate to well-sorted sand. The sediment is rather homogeneous without internal structures and contains shell and rock fragments. Grains are angular to sub-angular with a few rounded grains. Modal analysis gives porosities in the range 27-31%. The sand has a high content of quartz (77-85%) and is little cemented (minor amounts of chlorite cement). Cuttings from several wells in the Sleipner area show that the Utsira Sand varies from very fine to medium coarse sand which is largely poorly cemented. Occasionally fragments of greenish grey claystone are seen but clay is under-represented in cuttings as most clays are washed out but the high content of pyrite indicates the presence of shales. Cuttings from the Nordland shale overlying the Utsira Sand consists of quartz (23-36%) plagioclase (8-15%), and clay minerals (40-60%). The clay minerals consist of mica / illite (18-30%), mixed layer clays (5-15%) and kaolinite (7-16%).

4- Depositional environment

Gregersen et al. [1997] interpret the Utsira Formation as representing basinal stacked lowstand fan deposits basinward and transgressive highstand deposits landward. Other earlier interpretations include shallow marine tidal sand ridges [*Buller et al.*, 1982; *Rundberg*, 1989, *Isaksen and Tonstad*, 1989] thick stacked barrier island sands inter-layered with lagoonal clays. The Pliocene shales are believed to represent lowstand sequences in the basal parts over-lain by thicker transgressive highstand sequences [*Gregersen et al.*, 1997]. Information on water depth of deposition is rather contradictory. Minimum water depth from depth reconstructions and decompaction algorithms give a minimum water depth for the Utsira sands of 100m and 250m for the top of the lower Pliocene shale unit [*Lothe and Zweigel*, 1999]. This, however, contrasts with estimates of 30-100m from *Eivind et al.* [1999] based

on palaeo-environmental data. More recent estimates of water depth made from microfossils in a sample from well 15/9-A23 [*Wilkinson* I.P. 1999] suggest middle to outer shelf water depths at the time of deposition (100-200m). These recent estimates on water depths, although spanning a range from 30 to 300m, favours a deeper water marine fan system over a shallow marine tidal environment.

Such marine fan deposits are typically composed of turbidite sequences. The lack of bedding plane structures in the core suggests a chaotic deposition process and the high quartz content indicates mature sediments with possibly long transport distances or reworking, both of which are consistent with sediments laid down by turbidity currents. The Utsira Sand appears to grade laterally into shales over about 70 km. This is consistent with 'lobe' structures (see below) found in many ancient and modern marine fan systems whose sediments are dominated by turbidites.

B-2. Turbidites

1- Definition and generality

The `most likely environment of the Utsira Formation is thought to be marine fans composed of turbidites and related sediments. Marine fans form major sedimentary structures in marine basins and are frequently found off-shore from large rivers and their deltas and can form large prisms of sediment up to 1 km thick extending laterally several 100's of kilometres, see Figure 4. They are built up by a number of sedimentary processes which include rock falls, sediment slides, debris flow and turbidity currents [*Stow*, 1992]. Sediment slides comprise the bodily movement of sediments on a fluidised basal shear plane. Debris flows consist of slurry like sediment-water mixtures with laminar flow that move on a fluidised basal shear zone. Turbidity currents are density currents of relatively dilute sediment-water mixtures where the sediment is maintained in suspension by turbulent flow. These currents are capable of transporting sediment over very long distances (1000's km) down very low slopes (less than 1 degree) without significant erosion or deposition and are a major supplier of sediments to the deeper parts of ocean basins. They may form either channelized flows around 1 km wide and 10's km long or laterally unconfined slope flows. These sedimentary processes build up large fan structures with distinctive sedimentary structures, see Figure 4.

A good summary of turbidite morphology is given by *Walker* [1978]. The typical rock types found in sub-marine fans are *(1)* classic turbidites, *(2)* massive sandstones, *(3)* pebbly sandstones, *(4)* clast supported conglomerates and *(5)* matrix supported sediments. The first four are deposited by currents where turbulence was important in supporting the sediment. In the fifth class, fluid turbulence is much less important.

1-1 Classic turbidites

The distinctive features of classic turbidites are very parallel bedding with regular alterations of sandstone and shale normally without channeling or major lateral changes in bed thickness for 100s to 1000s m. They are characterized by a number of distinctive features including erosional marks associated with the sharp base of the sandstone beds (sole marks), a suite of internal structures in the sandstone beds (graded bedding, horizontal lamination and ripple cross-lamination) and a pelitic layer on top of each sandstone. *Bouma* [1962] divided classic turbidite beds into divisions A to E. Division A consists of massive sandstones, B of medium to fine grained sandstones with horizontal laminations, C of sandstones with ripple cross laminations and convolution, D of horizontal laminations of silt and clay, and E, a layer of structure-less silt or clay. Each division of the Bouma sequence represents progressively waning currents upward through the bed. Turbidity currents also wane in their journey across the basin floor. Near their source, turbidites tend to begin with A, with B further from the source and C in the most distal parts. Turbidites in the area of initial deposition (proximal turbidites) also tend to be thicker bedded (20-30 cm), coarser grained (medium sand or

coarser), have a higher sand / shale ratio. Finer, thinner bedded turbidites beginning with B or C divisions can indicate distal parts of the system or areas on channel levees.

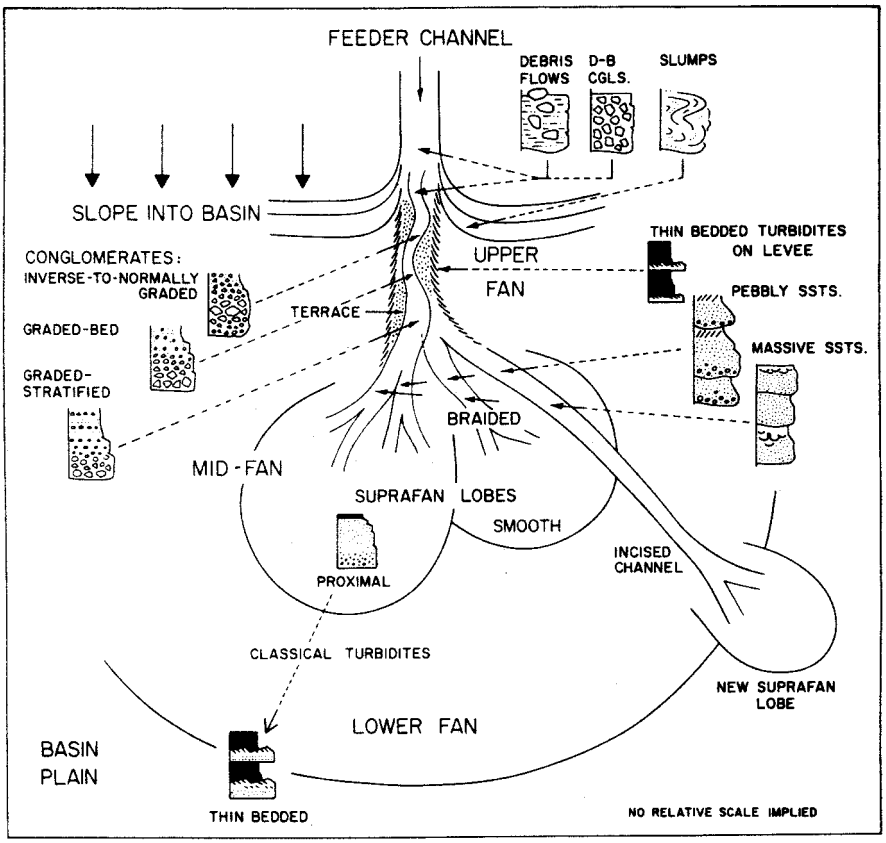

Figure 4: Sketch of submarine fan morphology and sediment types (after *Walker* [1978]).

1-2 Massive sandstones

Classic turbidites can grade laterally into massive sandstones composed of A division beds alone. Beds are typically 0.5 to 5m thick and may be composite. Internally beds are often ungraded and the major internal sedimentary structures are vertical interganular fluid escape tubes and dish structures (thin, sub-horizontal flat to concave upwards argillaceous laminations) which formed during fluid escape.

1-3 Pebbly sandstones

Beds range from 0.5 to over 5m thick and are characterized by sharp bases and an absence of shaley layers. Internal sedimentary features are stratification and cross-stratification. Stratification consists of alternating pebble-rich and pebble-poor layers with gradational bases and tops. Average layer thickness is 5-10 cm. Cross-stratification consisted of sets most commonly around 5 cm high with trough or planar cross-bedding. Pebbly sandstone are commonly lenticular and show scoured bases. Many formations are 10's to 1000's m thick built up of many graded beds.

1-4 Clast supported conglomerates

Individual beds range from 1m to over 50m thick, have sharp commonly channelized bases and tend to be laterally impersistent. Shale layers are very uncommon. Beds may show normal or inverse graded bedding or massive bedding. Imbrication of pebbles is common.

1-5 Matrix supported beds

This sediment type is typical of debris flows. Beds tend to be irregular and lack scour marks. Internally beds are chaotic and resemble tillites. The clast-support mechanism is matrix strength and large clasts can float in the upper parts of the flow often projecting up from the top of the bed.

It is well established that classic turbidites form a complete gradation between thin-bedded (CDE) to proximal (ABCDE) types. Gradation also occurs between classic turbidites and massive sandstones where the loss of bedding regularity is due to increased amounts of scouring and channelization. Pebbly sandstones and clast supported conglomerates probably represent a different depositional mechanism and are thus a distinct lithology from classic turbidites.

2- Relation of facies to fan morphology

In the upper fan there is a single channel that may have a meandering channel within it, flanked by flat terraces with levee deposits. The middle fan is built up by the deposition of supra-fan lobes which shift position with time. The inner parts of the lobes are composed of shallow braided channels with no levees, while the outer parts are smooth and grades into the lower fan region. The basinal plain and lower fan regions are smooth low-gradient areas with hemipelagic deposition and occasional turbidity currents. Sediments are thin and parallel bedded classic turbidites, which become thicker towards the middle fan. Proximal turbidites with monotonous inter-layered sandstones and shales can form on the outer parts of supra-fan lobes. In the supra-fan lobes, deposition within braided channels gives rise to massive sandstones characterised largely by lenticular bedding and shallow channels. Small turbidity currents in the channels may deposit classic turbidites within them. In the upper fan, conglomerates deposited in the channels and perhaps on the terraces are the dominating lithology. Feeder channels can be 10's to 100's m deeps and 100's m to kilometres wide while channel levees are composed of fine grained thin sandstones and mudstones (thin-bedded turbidites). Channels can be plugged with coarse material, such as debris flows and conglomerates, or by very fine materials such as clays and mudstones.

3- Stratigraphic evolution of fans

In a pro-grading fan sequence, the changing sedimentation environment will lead to a sequence of lithologies from different parts of the fan. Progradation of the lower fan leads to classic turbidites with sandstones beds that become coarser and thicker up-section. Above this are the middle fan sediments where classic turbidites give way to massive or pebbly sandstones. Bed thickness, grain size and sand/shale ratio all increase upwards. Shifting of sediment channels and deposition lead to fining upward sequences in individual lobes ending with the deposition of fine grained mudstones over the abandoned fan. Fining and thinning upwards sequences can be developed in the supra-fan channels, as channels are abandoned with time. Thus, the overall stratigraphy developed during a period of progradation consists of one major coarsening upward sequence with smaller coarsening upward sequences in the lower part and fining upward sequences in the upper part.

4- The Utsira formation.

Seismic studies by *Gregersen* [1997, 1998] have identified a number of large scale lens like bodies and a channel feature leading to the interpretation of the Utsira Formation as a sub-marine fan structure. In the area of the Sleipner platform, available information appears to suggest that the Utsira Sand is dominated by sands. Bore hole logs, however, show that there are also a number of shale layers which can be followed on seismic over distances of 2 km. Samples from the only core available are of a fine, well-sorted sand without visible internal sedimentary structures. This may represent massive sandstones of a channel fill, for instance. If the Utsira Formation is sand dominated, as available information suggests, then the most appropriate interpretation of the Formation may be as middle fan

deposits composed largely of channel fill sands. The laterally continuous shale layers which can be traced on seismic may then represent hemipelagic layers deposited when supra-fan lobes and their channels were abandoned as sites of deposition. As sub-marine fan deposits, the sediments are likely to be heterogeneous and contain a number of possible sedimentary structures on a variety of scales that could have an impact on fluid flow and the migration of injected CO_2. On a large scale these include the laterally continuous shale layers are likely to form barriers to upward migration. On the scales of 10s m, heterogeneities include the inter-layering of sands and clays / shales of classic turbidite sequences, and the mixtures of massive sandstones and turbidite sequences expected in channel fills. On a small scale (10's cm to 1 m), internal structures such as ripple cross-bedding and dish-structures could impact on fluid pathways.

B-3. Length and Spatial distribution of Turbidite beds

1- Thickness and length distribution

A number of studies based on the analysis of boreholes or outcrops, have shown that the distribution of the thickness *T* of turbidites beds was following a power-law [*Stølum*, 1991, *Hiscott et al.*, 1992; *Rothman et al.*, 1994; *Pirmez et al.*, 1997]. This law takes the form

$$n(T) = \beta T^{-a_1} \qquad \text{(Eq. 1)}$$

where *n(T)* is the density distribution and refers to the number of bed whose thickness *T* belongs to the interval [*T*, *T*+*dT*], β is a density constant, and a_1 is the exponent. In general the cumulative distribution *C(T)* is preferentially used and corresponds to the number of beds whose measured thickness is greater than *T* (Figure 5). However, because of strong finite size effects associated with this distribution, it is better to use the density distribution *n(T)*. Exponent *c* of the cumulative distribution is related to the exponent a_1 of the density distribution by the relation $c=a_1-1$ (see *Bonnet et al.*, [accepted] for a full discussion about density and cumulative distribution).

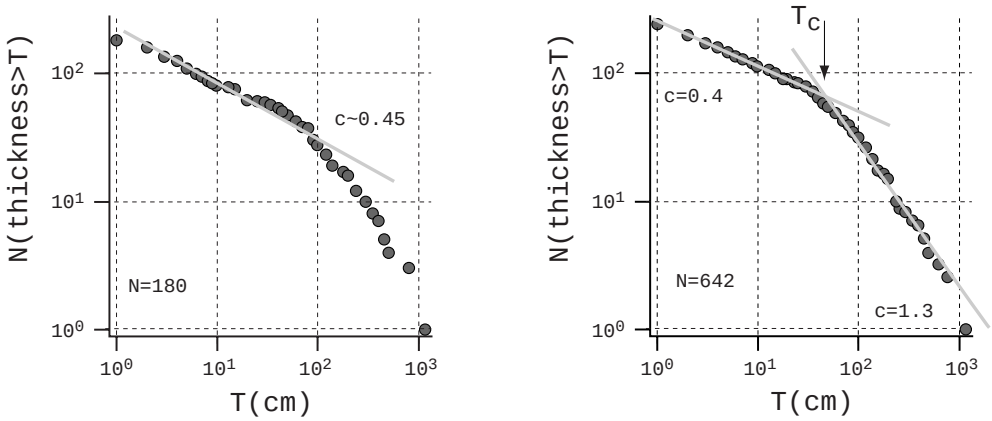

Figure 5: cumulative distribution of the measured thickness of turbidite beds from the Amazon fan. Distribution follows a power law characterised either by one or two exponents (After *Pirmez et al.*, [1997]).

In some particular cases, two exponents are necessary to describe the size distribution. For example, for bed thickness smaller than a characteristic size T_c, we observe a_1=1.4 (*i.e* c=0.4) and for bed thickness greater a_1=2.3 (Figure 5 - right). However, in general exponent a_1 of the bed thickness distribution vary between 2.1 and 2.4 [*Hiscott et al.*, 1992; *Rothman et al.*, 1994].

The length of turbidite beds *l* can be related to the maximum thickness T_{max} of the depocentre through the relation

$$l = \lambda\, T_{max}^{\xi} \qquad \text{(Eq. 2)}$$

where the exponent ξ fixes the scaling of the length of the bed and its thickness, and where λ is a constant. The value of ξ varies and is found to lie in the range 0.7 to 1.1 for bed thickness greater than 10 cm [*Pilkey et al.*, 1980; *Malinverno*, 1997]. Therefore from eq. (1) and eq. (2) it follows that the length distribution of turbidite beds *n(l)* evolves also as a power law of the form

$$n(l) = \alpha l^{-a} \qquad \text{(Eq. 3)}$$

where $a = a_1 / \xi$. Assuming that a_1 varies between 1.7 and 2.5, and that ξ lie in the interval 0.7 to 1.1, the exponent *a* describing the length distribution of turbidite beds should fluctuates between 1.5 and 3.5.

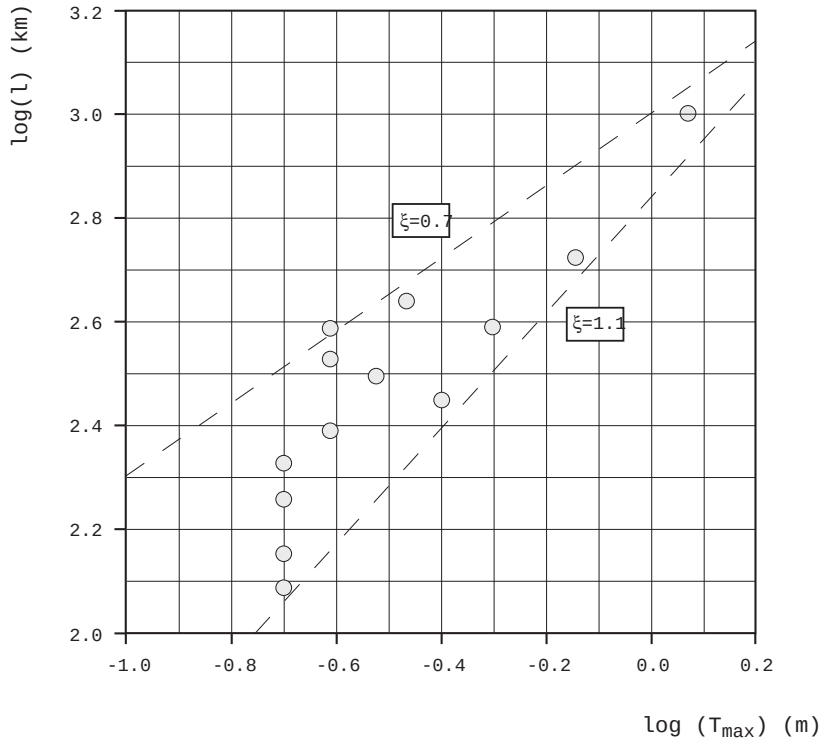

Figure 6: bed length versus bed thickness from the Hatteras abyssal plain data (from *Pilkey et al.*, [1980]). The lines represents the slope for the relationship between *l* and T_{max} as in eq. (2). In that case, the exponent ξ lie in the range 0.7, 1.1 (Modified after *Malinverno* [1997]).

2- Spatial Organisation

Fractal dimension

To quantify the spatial distribution of bed depocentres in two dimensions, we reduce each individual bed to its barycentre. The way these barycentre are organised spatially can be describe using the correlation dimension which is determined using the distances between each pair of points in the set of N number of points. The correlation integral C(*r*) is defined as

$$C(r) = \lim_{N\to\infty} \frac{1}{N^2} [\text{number of pairs } i, j \text{ whose distance } |y_i - y_j| < r] \qquad \text{(Eq. 4)}$$

and C(*r*) follow a power law of the form

$C(r) \sim \delta r^D$ (Eq. 5)

Where δ is a constant and where D is the correlation dimension. The dimension *D* is estimated by plotting log(*C(r)*) with respect to log*(r)* (see *Bonnet et al.* [accepted] for a discussion on the determination of fractal dimension).

The correlation dimension takes a value between 0 and 2. If all turbidites beds are located in the same place, then *D*=0 (Figure 7). When they are disposed along a line, in the horizontal plane, C(*r*) should be linearly proportional to *r* and *D*=1. Finally, the dimension corresponding to randomly distributed bed is 2. In general, the dimension *D* is non-integer and is called the fractal dimension.

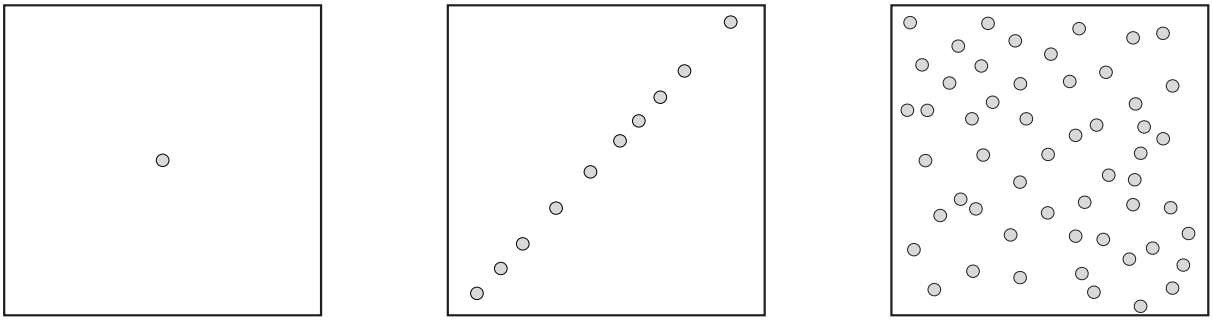

Figure 7: bed depocentres barycentre in map view and the corresponding correlation dimension D.

Density definition

The density of elements present in a system can be estimated using several methods. In the case of a fractal organisation, the density can be defined as

$d = M_t / L^D$

Where M_t is the mass (the length of all fault or turbidites beds present in the system in our case), *L* is the system size and *D* is the fractal dimension, or as

$d = N_t / L^D$

Where N_t is the total number of elements presents in the system of size L and D the fractal dimension[1].

The two densities defined above are dependent on the size of the considered system. Hence, to get free from this scale dependency, and since we are dealing with a model constituted by a finite number of grid elements (see section C4), we have defined the density as the percentage *P* of grid element that correspond to a heterogeneity. This definition has been used in the next section to characterise the various studies geometry.

B-4. Permeability and porosity of sands and clay

The heterogeneities that may be present in the Utsira Formation and the Nordland Shales which over lie it, result in heterogeneous permeability and porosity fields which will exert an important control

[1] Note that for D=2, *i.e.* a random spatial distribution, we obtained the classical definition of the density: the number of elements divided by the area.

on the transport and dispersion of injected CO_2. Of major importance to the modelling of CO_2 injection is therefore the range of permeabilities and porosities that can be expected in the Utsira Sand and overlying shales. From limited core and cuttings the Utsira Sand appears to be either completely or very poorly consolidated. The permeability of the sediments will therefore be close to their at a maximum since there is little compaction or cementing material in the pore space. Measurements of permeability from core material conducted by GEUS give values of 800 to 1450 mD at 39% porosity and by one measurement by IKU gives a permeability of 3D at a porosity of 35% [*Torp*, 1999]. The high permeability values emphasis the poor consolidation and lack of compaction in the Utsira Sand. To help assign relevant permeabilities and porosities to models for the heterogeneities that could be present in the Utsira Sands, an overview of permeability and porosity in sands and shales and their major controlling factors is presented.

1- Permeability and porosity of sands

The permeability and porosity of unconsolidated sands depends on grain size, sorting and degree of compaction and consolidation and cementation [*Fetter*, 1988]. Generally, for a give consolidation state, permeability increases as grain size increases but decreases as sorting becomes poorer (*i.e.* as the spread in grain sizes increases). Experiment by *Pfannkuch*, [1963] made on sand and glass-ball show how permeability fluctuates with the average grain size (*Table 1*). Also, the shape of the grains act on the permeability measure and for a similar mean size, glass ball which are perfect sphere shows a greater permeability than the Pyla sand.

Holland Sand	<d>= 0.710 mm	Φ = 0.370	k = 250 darcys
Pyla Sand	<d>= 0.355 mm	Φ = 0.340	k = 40 darcys
Glass Ball	<d>= 2.100 mm	Φ = 0.388	k = 1200 darcys
Glass Ball	<d>= 0.447 mm	Φ = 0.388	k = 118 darcys

Table 1: measured permeability k and porosity Φ achieved for different granular medium (<d> corresponds to the mean grain size).

Porosity is controlled by the size and frequency of pores but permeability is controlled chiefly by the pore throat size. This leads to a complex relationship between porosity and permeability that is not easy to predict. For a sand composed of a constant grain size, permeability increases as the grain size increases (porosity however stays constant) because the pores and pore throats increase in size. However, when a wide range of grain sizes are present, small grains tend to fill the spaces between larger grain so that both porosity and permeability decrease. Thus small amounts of clay or cement can clog pore throats and markedly reduce permeability without significantly reducing porosity.

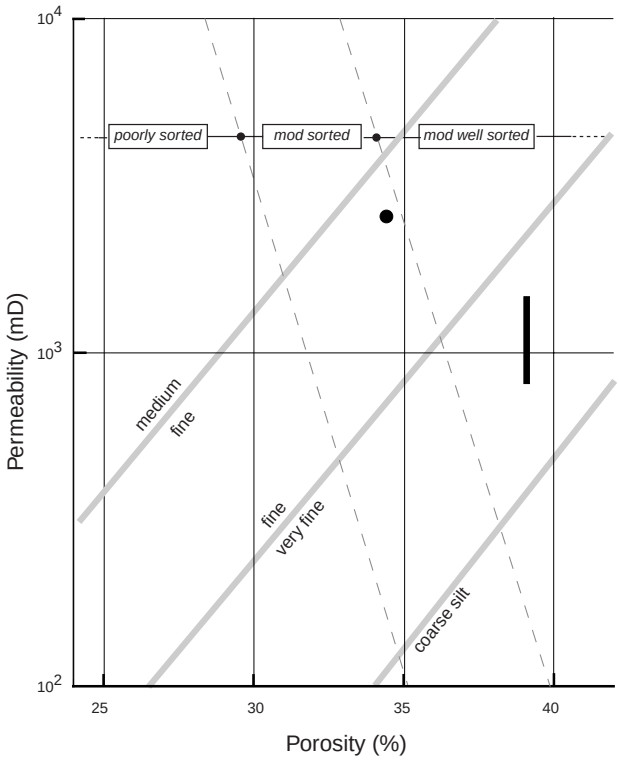

Figure 8: Porosity versus permeability for slightly to unconsolidated sands (modified from *Gidman et al.* [1993]). The bar and open circle are estimates of porosity and permeability for the Utsira Sand.

The permeability of sands can range over 5 orders of magnitude depending on grain size, sorting and compaction. Clean, unconsolidated, coarse to medium grain sized, well sorted sands have been reported to give permeabilities in the range 10 to 150 D [Weber et al 1972]. Sands that are slightly to unconsolidated and buried a few hundreds of meters show permeabilities in the range 10mD to 1D [*Gidman et al.*, 1993, *Hurst* 1991, 1993; *Marrow et al.*, 1969]. Sandstones tend to show somewhat lower permeabilities in the mD rang, e.g. 1-20mD for turbidite sandstones in the Pyrenees [*Schuppers* 1993]. In order to estimate the likely range of permeability and porosity in the Utsira permeability and porosity of slightly consolidated to unconsolidated sands were used as a guide. These values lie in the range of 10mD-3D for permeability and 25-40% porosity. The few measurements of permeability (800mD-3D) and porosity (35-39%) from the Utsira sand lie within this range. *Gidman et al.*, [1993] investigated the permeability and porosity of deep marine, poorly consolidated sandstones in the Inglewood Field, in the Los Angeles Basin. These consist of interbedded sandstones and mudstone (bed thickness 3 cm to 5 m) of Miocene age from a turbidite setting which may be broadly equivalent to the Utsira Sand. The lithologies ranges from massive mudstone, through interbedded mudstones and sandstones to massive sandstones. The sandstones represent a wide range of grain size and sorting. Measurements of porosity, and permeability were made on 719 core plugs giving an average porosity of 32% and a geometric mean permeability of 461mD. The data collected were also used to map out the relationship between porosity, permeability, grain size and sorting, illustrated in Figure 8. Here plots of porosity versus permeability are contoured for grain size and sorting. The contours are complex but show a tendency to form 'zones' of grain size and sorting which can act as a guide to the permeability and porosity if grain size and sorting are known (e.g. from bore hole cuttings). Plotting the permeability and porosity measurements from the core samples from the Utsira Sand indicates fine, moderately to well sorted sand which is in generally good agreement with the sample descriptions.

2- Permeability and porosity of clay

Permeability and porosity of clays and shales represent among the largest uncertainties in quantifying flow [*Neuzil*, 1994]. Generally permeability of clays and shales tends to be over-estimated due to the difficulty of measuring such low values close to the detection limits of instrumentation. Permeability and porosity of clays and shales are sensitive to the type of clay minerals and depth of burial. The permeability of pure clay ranges over 5 orders of magnitude. ranging from 0.1 mD (Kaolinite), to 5 10^{-4} (illite) and 10^{-6} (smectite) [*Mersi and Olsen*, 1971] at a porosity of 50%. Porosities reduce from 80-90% to 5-10% and permeabilities reduce by up to 10 orders of magnitude for burials of up to 5 km. Generally, there is a log-linear relationship between permeability and porosity, see Figure 9 (modified from *Neuzil* [1994]). There are a number of empirical and theoretical algorithms relating porosity, permeability, mineralogy and depth of burial for clays and shales (e.g. the Kozeny-Carmen relation, equation from *England et al.* [1978]). However, due to the range of pore throat sizes in clays and shales permeability can easily vary by 3 orders of magnitude for the same porosity [*Neuzil* 1994].

The porosity and permeability of clay-silt mixtures reaches a minimum where the clay fills the pore spaces between the silt grains which are in contact with each other, generally around clay constants of 20-40% [*Dewhurst and Aplin* 1998, *Rueil and Cathles* 1999]. However, it is likely that shales and clays remain permeable even at low flows with minimum permeabilities around 10^{-6}mD, and never become complete flow barriers [*Neuzil* 1994]. Due to the plately nature of clay minerals, permeabilities of up to 3 orders of magnitude are also possible [*Neuzil* 1994].

The above relationships between clay mineralogy, clay content and depth of burial and be used to estimate a porosity and permeability range likely for shales in the Utsira Sand and overlying Nordland shales. Data from cuttings [*Lothe and Zweigel*, 1999] show that the average of six samples from the Nordland shales show clay contents of 52% (range 40-60%), with average clay mineral content of kaolinite (11%), mica / illite (25%), mixed layer clays (9%), chlorite (5%) and smectite (2%). The clay mineral composition is dominated by illite and kaolinite which show higher permeabilities (0.1-5 10^{-4}mD) at medium porosities (50%). A clay content of 40 to 60% is probably above to clay content needed to simply fill the pore space between the silt grains. Thus porosity and permeability will be dominated by the clay mineralogy. The pressure in the Utsira Sand is around 20MPa (at 1000m depth) which compares with three of the fields grey cross hatched in Figure 9 identified by *Neuzil* [1994]. This gives a range of porosities of 10-40% and permeabilities of 0.001 to 10^{-7}mD. The equation of *England* [1987] relating permeability and porosity:

$$k = 4.053\phi^8 mD \qquad \text{Eq. 6}$$

gives a similar range of permeabilities of 10^{-10} to 0.003 mD for porosities of 10-40%. Thus much depends on the level of compaction of the clays in the Utsira Sand and Nordland shale for which there is presently no information. Additional information on the general trends of porosity with depth for the North Sea [*Sclater and Christie*, 1980] may help to narrow this range.

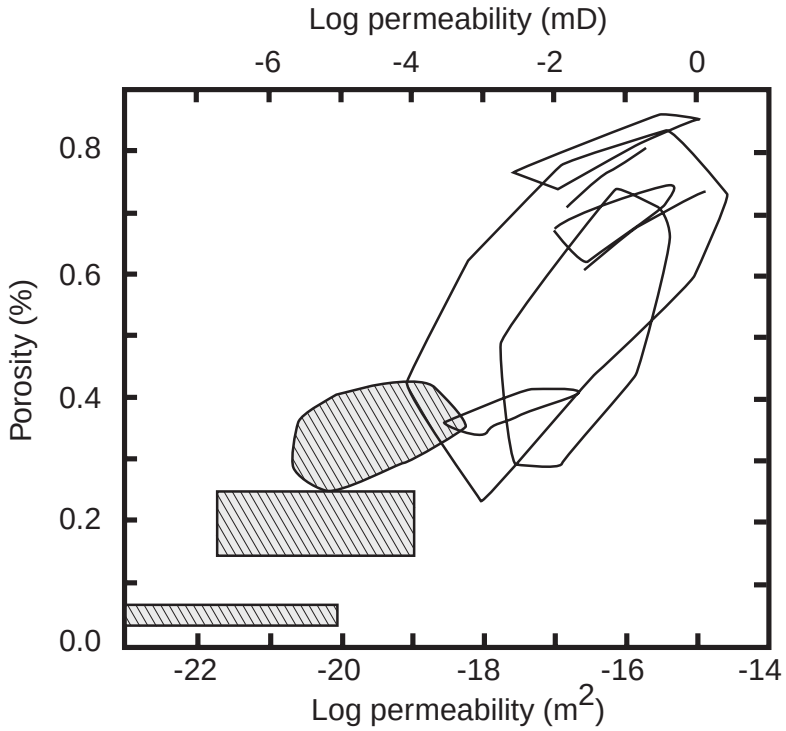

Figure 9: Permeability versus porosity for shales (modified from *Neuzil* [1994]). The grey cross-hatched fields are those that have pressure conditions most closely resembling that of the Utsira Formation.

These trends (Figure 10) suggest porosities of around 40% for sandstones at 1000m depth which is in good agreement with the measured porosities from the core samples (39%). The shale trend (Figure 10) suggests porosities of around 30%. In the formula from *England et al.* [1978] this gives a permeability of 3 10^{-4} mD and on the plot of *Neuzil* [1994] suggests a range of possible permeabilities from 10^{-2} to 10^{-6} mD.

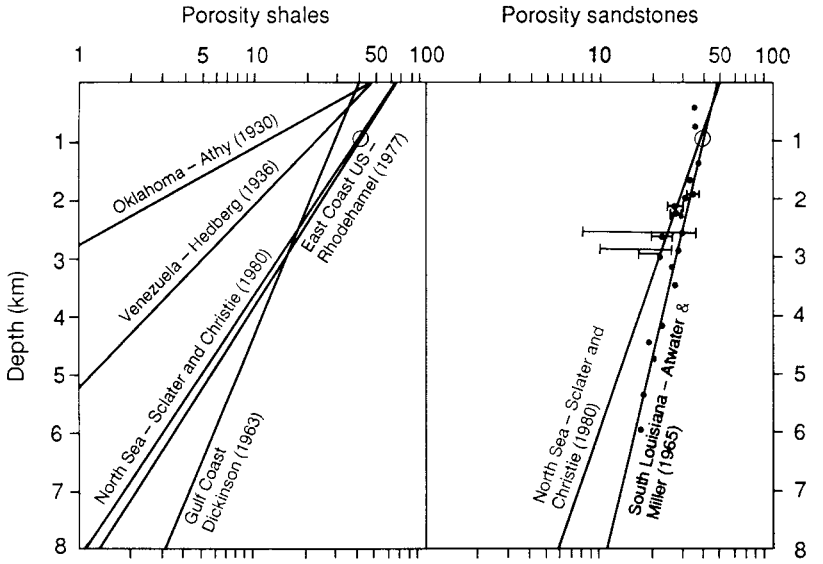

Figure 10: Trends for porosity versus depth for sands and shales (after Sclater and Christie *[1980]*). The open circles represent the depth of the Utsira Formation at the injection point.

PART C. MODELS

C-1. Modelling sedimentary architectures

Observations of rocks and sediments show that their physical properties (such as hydraulic or mechanical properties) show significant variability. Geological formations are composed of a number of distinct features such as layers of differing lithology, sedimentary structures, and tectonic structures such as fractures (joints, faults) and folds. As a result, field measurements of physical and chemical properties such as porosity and permeability show a large degree of variability. In addition, hard data on rock properties through measurements from bore holes or geophysical surveys are generally sparse and the measurement themselves often uncertain. As a result, the level of information is rarely sufficient to allow a deterministic approach to estimating flow and transport properties. It is therefore more realistic to adopt a stochastic approach where the precise geometry of any location cannot be faithfully reproduced but where realizations that posses similar spatial properties are created. In addition, properties of geological formations rarely vary in a smooth fashion but variations tend to be discrete in nature such as beds of differing lithology and occurrence of fractures.

A variety of techniques have been developed to describe geological heterogeneity. These include the kriging, spectral, perturbation, multi-variate, turning bands and nearest neighbour methods. Most of these methods require hard data in the form of measurements of properties to be simulated such as porosity and permeability. Generally, there is very sparse hard data available, but data of a soft nature may be much more readily available such as geological maps and bore hole logs which are easier and often less expensive to collect. One of the approach adopted here is to simulating hydraulic parameter fields such as porosity and permeability using the coupled Markov Chain method [*Elfeki, et al.,* 1997] which can take full advantage of 'soft' data. Other advantages are that it is simple to implement, conditional simulation is easy, and it is not computationally intensive. The second approach consists in the generation of permeability and porosity field using a fractal generator. This will create fields with geometrical properties identical to natural patterns and permits to capture the average behaviour of such sedimentary patterns.

1- The coupled Markov chain model

In terms of a spatial field, a Markov chain is a probabilistic model where the state at any point is dependent only on its immediate surroundings and is independent of states further away. This model

does not use variograms or autocovariance functions as most other models do, but uses conditional probabilities. Conditional probabilities have the advantage that they can be interpreted in terms of geology more easily than variograms or autocovarience functions. The state at any point is given by a 'transition probability' which specifies the probability of the state type given the states in its immediately vicinity. Transition probabilities are defined as a relative frequency of transitions from a certain state to another state in a system that is composed of a number of states. These probabilities can be arranged in matrix form:

$$\begin{bmatrix} p_{11} \cdot p_{12} \cdots\cdots\cdots\cdots p_{1n} \\ p_{21} \cdot p_{22} \cdots\cdots\cdots\cdots p_{2n} \\ . \\ . \\ p_{n1} \cdot p_{n2} \cdots\cdots\cdots\cdots p_{nn} \end{bmatrix}$$

where P_{kl} is the probability of transition from state S_k to state S_l and n is the number of states in the system. Here the elements must be positive and the elements of each row must sum to 1. A coupled Markov chain describes the joint behaviour of pairs of independent systems. The coupled transition probability matrix is given by:

$$P_{(ij,lk)} = P_{il} \, . \, P_{jk}$$

In the case of a 2D field, these two matrices are the horizontal and the vertical transition probability matrices which define the probabilities of a change of state in the horizontal and vertical directions.

1-1 Generating a 2D field using the coupled Markov chain method

The method is illustrated below for the simple case of parallel horizontal layers. In the horizontal direction, the state is constant (no change), thus the probability that the initial state gives rise to itself is 1.0 and to any other state is zero. The horizontal transition probability matrix, for a system of 4 states, is thus:

$$\begin{bmatrix} 1.0 & 0.0 & 0.0 & 0.0 \\ 0.0 & 1.0 & 0.0 & 0.0 \\ 0.0 & 0.0 & 1.0 & 0.0 \\ 0.0 & 0.0 & 0.0 & 1.0 \end{bmatrix}$$

In the vertical direction transitions between a state and any other are equally likely and the vertical transition probability matrix is:

$$\begin{bmatrix} 0.25 & 0.25 & 0.25 & 0.25 \\ 0.25 & 0.25 & 0.25 & 0.25 \\ 0.25 & 0.25 & 0.25 & 0.25 \\ 0.25 & 0.25 & 0.25 & 0.25 \end{bmatrix}$$

A 2D field of regular cells satisfying these two transition probability matrices is generated in the following manner:

1. Generate the top row using the horizontal transition probability matrix. The first cell is assigned (randomly or deterministically) a state, *j*, and the probabilities of the state of the next cell are given by *jth* row of the horizontal transition matrix. The next state is chosen randomly, conditioned by these probabilities. Since in this case the probabilities are zero except in the case of state *j*, the row is composed of cells of the same state in all cases.

2. Generate the left hand column using the vertical transition matrix in the same manner as the top row. The vertical transition probability matrix has elements of equal value and therefore there is an equal chance of any state, including the previous one, occurring.

3. Generate the rest of the grid of cells starting at the left hand edge of row 2 and working down to the right hand cell of the bottom row. In these cells, the state of each cell depends on the states of the cell to its left and the cell above. Now the probabilities are determined by multiplying the appropriate rows of the horizontal and vertical transition probability matrices together. These products must be normalized by the sum of the products to ensure that the probabilities sum to 1. In this example, only one of the products is non-zero and so rows of same state cells are generated, determined by the first column of cells, see Figure 11(a).

In addition to horizontal layering, sloping bedding can be simulated by altering the algorithm above so that the state of a cell depends on the states of the cell to the left (horizontal transition probability matrix) and the cell to the left or right of the cell above (vertical transition probability matrix). This produces beds with slopes to the right or left. The angle of the slope depends on the cell shape and in the case of square cell produces slopes of 45^o. Complex nested models can also be created by superimposing models that sloping bedding on simulations of horizontal layering. In Figure 11, a variety of fields and their horizontal and vertical transition probability matrices are shown.

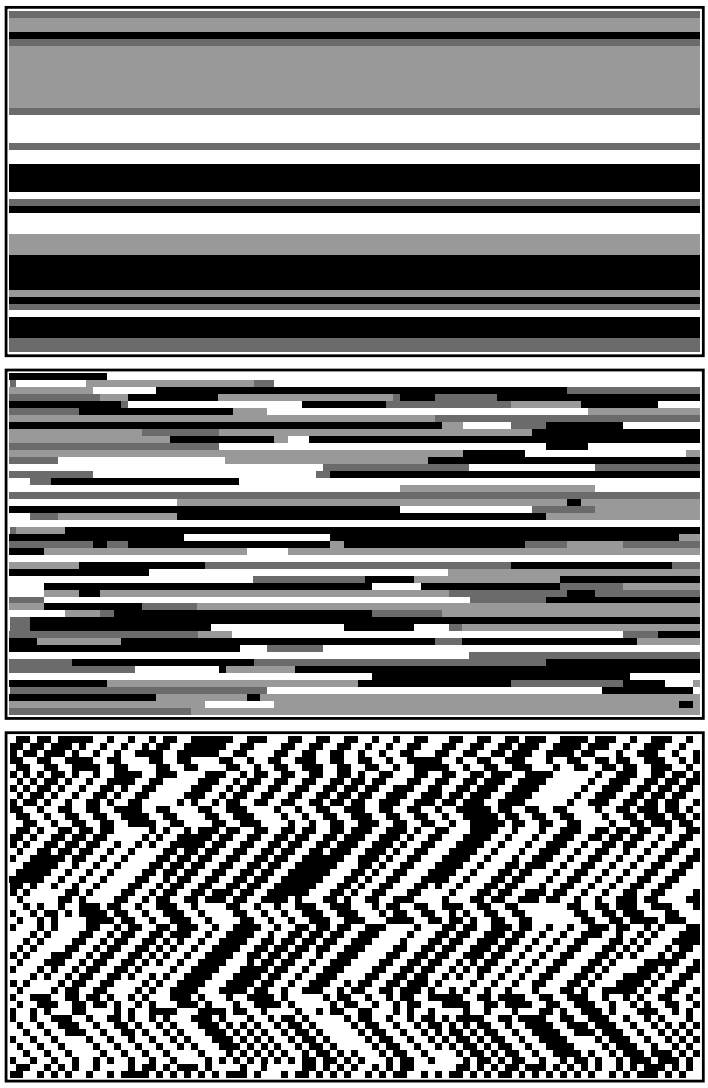

Figure 11: Examples of fields generated using the coupled Markov chain model. Top – horizontal continuous layers, middle – horizontal discontinuous layers, bottom – cross-bedding.

1-2 Generating transition probability matrices

Horizontal and vertical transition probability matrices can be generated from geological maps or sections (e.g. seismic) or well logs by the following procedure:

1. Divide the section through the map or the borehole log into equal sized cells, of the size required for the final model. These cells should be small enough to capture the level of detail required in the section. Assign to each division a 'state'. This could be based on, for instance, lithology, grain size, sedimentary structure type, fracture frequency, or physical properties such as permeability and porosity.

2. From the sequence of states, count the number of transitions from each state to the next for all possible combinations of states. Enter these values into a matrix and normalise each row by the sum of transitions so that the elements sum to 1. This is the transition probability matrix.

Horizontal and vertical transition probability matrices generated in this way can then be used to create any number of stochastic realisations of the sedimentary architecture that share the same spatial properties. Such realisations can form input for flow models and be used to conduct analysis of the sensitivity of the bulk rock properties (permeability, dispersion) on spatial distribution and permeability contrasts.

2- Fractal pattern

Natural pattern can be described using the fractal dimension, that depicts the spatial organisation, and the size distribution exponent of the layer properties (length, thickness, aperture distribution…) (see section B-3). Hence another approach consists *a priori* in assigning to the sedimentary architecture we want to study, a fractal dimension and a size distribution exponent. Using these two parameters (respectively *D* and *a*) permits to group together various geometry and to better constrain how they influence the saturation evolution.

As seen previously, the size distribution can corresponds to length, thickness, aperture… To a first attempt we have chosen to consider only the length distribution, which is the factor controlling the connectivity of the structures and the flow. This length exponent generally lies in the range 1.5 to 3.5 (see section B3). Similarly, the fractal dimension has also been found to vary between 1.5 and 2 [*Stølum*, 1991].

To generate this type of patterns, we have used two different procedures. The first one has been used to generate power law length distribution and is described in *Bour and Davy* [1997]. The second one generates a fractal distribution of fracture or turbidites beds centroids, which is analogous to the generation of heterogeneous Sierpinski carpets [*Gouyet*, 1992]. Note that the orientation effect has not been taken into account. The patterns are constituted of conjugate layers with two different orientation.

- Power-law length distribution:

Bour and Davy [1997] have developed the procedure we used here to obtain a length distribution *n(l)*. The complete development can also be found on the web site *www.mathworld.wolfram.com*. To generate a power law distribution *n(l)*, we have to consider a uniform distribution *n(l')*. First let us defined the probability density function *n(l)* as

$$n(l)=\alpha l^{-a}$$

for l lying in the interval $[l_o, l_1]$. Then normalisation gives the cumulative distribution, which takes the form

$$C(l) = \int_{l_o}^{l_1} n(l)dl \qquad \textit{i.e.} \qquad C(l) = \frac{\left[\alpha l^{-a+1}\right]_{l_o}^{l_1}}{-a+1} = 1,$$

The constant term α can be deduced and is equal to

$$\alpha = (-a+1) \Big/ (l_1^{-a+1} - l_o^{-a+1}) \qquad \text{Eq. 7}$$

We assume now that *l'* is a uniformly distributed random variable on [0, 1]. As seen above, the cumulative distribution *C(l)* is defined as

$$C(l) = \int_{l_o}^{l} n(l')dl' = \alpha \int_{l_o}^{l} l'^{-a}\, dl'$$

i.e.

$$C(l) = \alpha(l^{-a+1} - l_o^{-a+1}) \Big/ (-a+1)$$

By equating *C(l)* to *l'*, the variable *l* is given by

$$l = \left[\frac{-a+1}{\alpha} l' + l_o^{-a+1}\right]^{1/-a+1} \qquad \text{Eq. 8}$$

and is distributed as *n(l)* (*e.g.* the power law defined eq. 3). Substituting the α term defined in (eq. 7) into (eq.8) gives

$$l = \left[\left(l_1^{-a+1} - l_o^{-a+1}\right) l' + l_o^{-a+1}\right]^{1/-a+1}$$

and $l \sim l'^{1/a-1}$

a=1.5 *a*=2.5 *a*=3.5

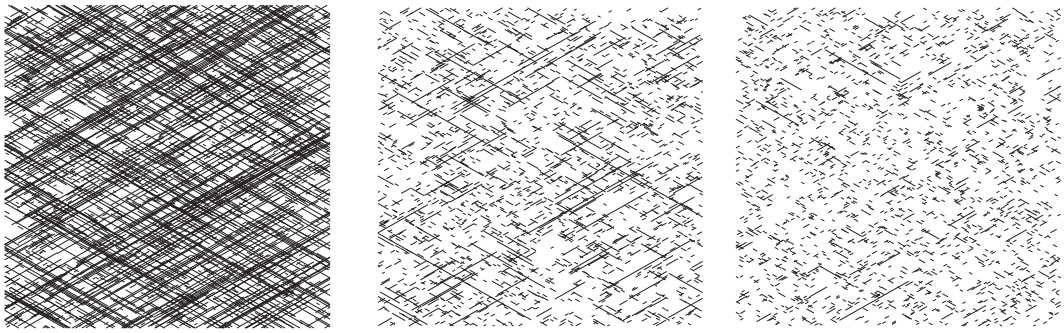

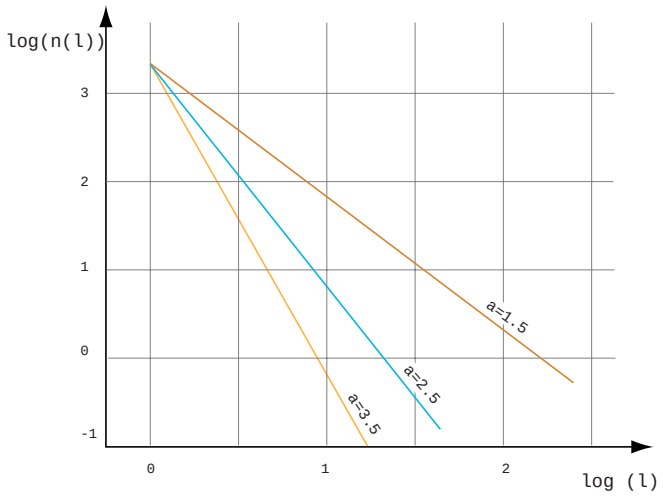

Figure 12: *(Top)* example of three different pattern showing the same fractal dimension (*D*=2) and three different length exponent (*a*=1.5-left, *a*=2.5-medium, and *a*=3.5-rigth). *(Bottom)* the corresponding length distribution *n(l)*.

Figure 12 presents three possible length distribution realisations for a fractal dimension of 2. The number of fractures in each considered case is the same. When decreasing the value of the exponent, more and more long faults are generated, that span the considered system.

- Fractal distribution of centroids:

The fractal pattern has been created following the Sierpinski carpet method. It gives a statistically fractal distribution of fractures centroids (Figure 13). On this spatial information, we have superposed the length information described above.

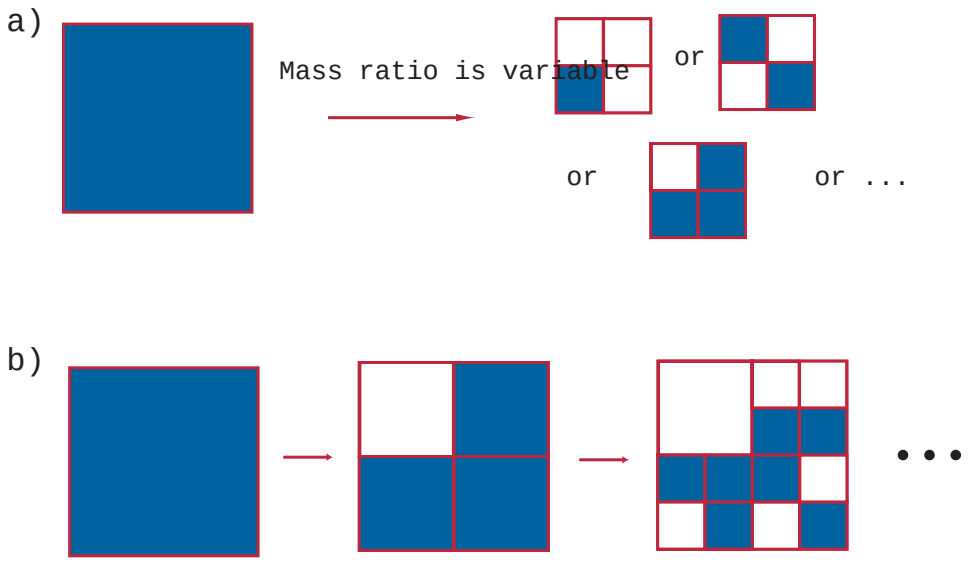

Figure 13: principle of a heterogeneous statistical fractal (from *Bour* [1997]). (a) A dark square indicates that fault centroids are present inside and a white square indicates its absence. Passage from one scale to another depends on the mass ratio that allows several configurations. (b) Example of three successive steps using this type of generator to create a fractal pattern.

We first fix the fractal dimension *D* then we start with a square Sq(0) and of length L(0) containing all centroids. We divide this square into several congruent squares Sq(1) of size L(1) which depends on

the fixed fractal dimension. Occupation of these squares by centroids depends also on *D* and is controlled by the defined mass ratio (variable in our case - see Figure 13). We iterate this procedure to obtain a decreasing sequence of squares Sq(2), Sq(3)… inside which centroids are or are not present until the fixed lower limit.

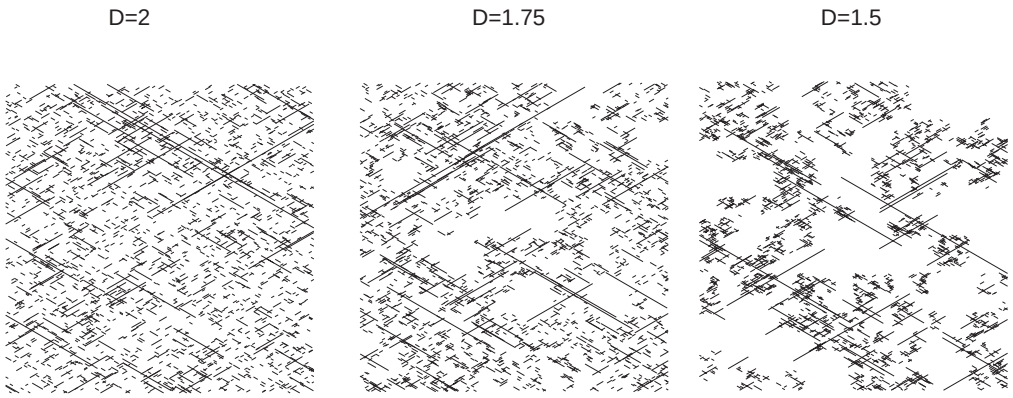

Figure 14: example of three different pattern showing the same length exponent (*a*=2.7) and three different fractal dimension (*D*=2.0-left, *D*=1.75-medium, and *D*=1.50-rigth).

Figure 14 shows three different patterns produced using this generator. These patterns have been used to generate permeability and porosity field as input for the two phase flow model.

C-2. Generating permeability and porosity fields for input to flow models

The information available from seismic, core and well logs suggests that one of the more likely origins for the Utsira Formation is a series of sub-marine fans composed of turbidites and related sediments. The Utsira Sand is probably composed dominantly of sands with some shales and passes into more shale rich sequences on all sides, above and below [*Lothe and Zweigel* 1999]. A possible interpretation of this unit is that it represents a sub-marine fan lobe (see Figure 4) built up by turbidity currents which formed a braided pattern over the surface of the lobe. If the Utsira Formation represents a submarine-fan, the sedimentary structures that might be found within the Utsira Sand and more widely throughout the Utsira Formation are typically turbidite sequences of graded sand beds and inter-bedded shales on the scale of 10s metres, and cross-bedding and fluid escape structures such as dish structures and fluid escape pipes, on the scale of 10s cm to 1m. Examples of each of these structures were generated and used to create permeability and porosity fields which form input to a two-phase flow model (section C-4). The different sedimentary structures simulated are described below.

1- Simple geometry

To first visualise how the geometrical heterogeneities act on the front geometry and on the saturation evolution, we have considered some simple geometrical cases. These cases are regroup in the following three different types: single layer, multiple parallel layers, and orthogonal layers.

1-1 Single layers

The first simulation patterns consist of *(i)* one single layer spanning the entire system, *(ii)* three '*en echelon*' layers of constant length and *(iii)* three parallel layers of constant length. These layers are

disposed in the centre of the system and are parallel to the inflow boundary (Figure 15 and Table 2). To test the sensitivity of the results and more particularly the sensitivity of the relative permeability curves on the orientation of the layers, we have performed simulations with the same pattern oriented perpendicularly to the flow.

Name	Area (m^2)	Mass (m)	Density (m/m^2) (d= Mass/Area)	N_{layers}	Density (m^{-2}) (d=N_{layers}/Area)	Proportion P of elements	N_{int}	l_{max} (m)
SG1	1	1	1	1	1	0.39%	0	1
SG2	1	1.25	1.25	3	3	0.49%	0	0.416
SG3	1	1.25	1.25	3	3	0.48%	0	0.416

Table 2: parameters of the three considered simple networks[2].

The case of a homogeneous and heterogeneous matrix has been considered (Table 3). We assume that the local matrix permeability follows a lognormal law and we assigned for the standard deviation a null value in the homogeneous case and a value of 0.10 in the other case. This means that 90% of the permeability distribution will lie within a range of 0.6 of an order of magnitude.

The geometry for which only one layer is present has been also used assuming that the layer behaves as a preferential path, through which fluids go preferentially, and as a barrier. In that latest case, the matrix is supposed to be homogeneous and all local matrix elements have the same permeability. Table 3 synthesised the different patterns and parameters used for this simulation.

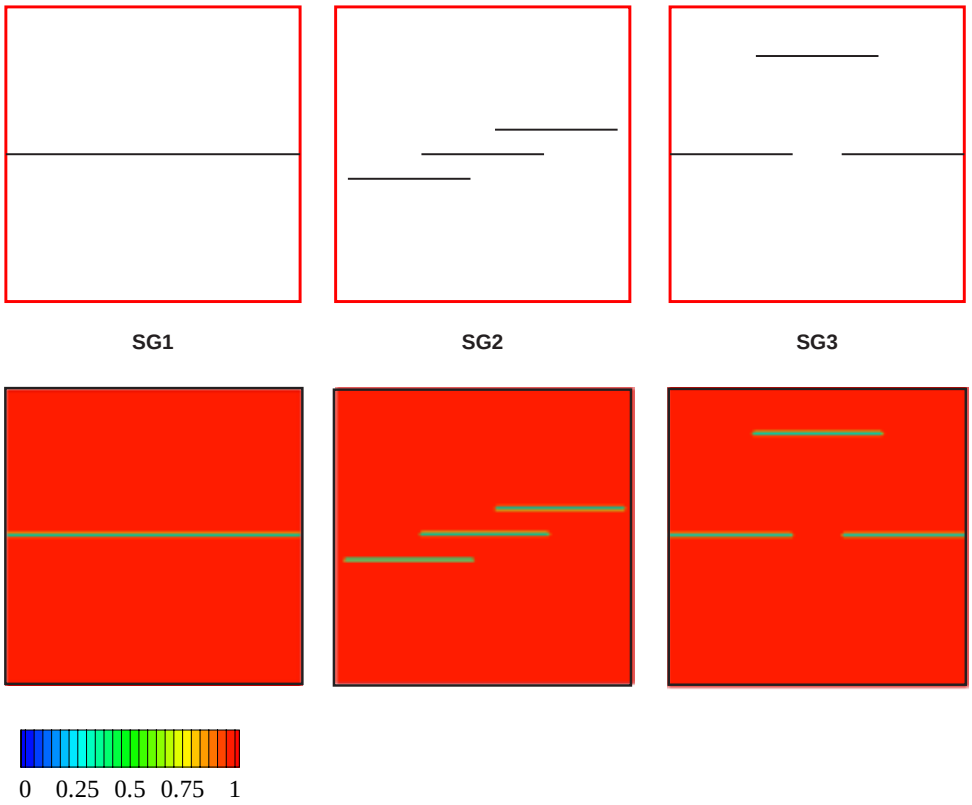

Figure 15: simulated simple geometry of layer used as input to the two-phase flow model in the case of a homogeneous matrix. Permeability is normalised so that in all cases the maximum permeability is 1.

[2] In this table and the following one, the Mass corresponds to the length of all layers, N_{layers} is the number of layers present, N_{int} is the number of intersections, and l_{max} is the length of the longest layer.

	Orientation flow/layers	η_{water} (Pa.s)	η_{CO2} (Pa.s)	Flow rates ($m.s^{-1}$)	Φ_l	Φ_m	<Km> (darcy)	σ	R_k
SG1 - Sim1	Parallel	1	10	0.225	0.05	0.5	0.005	0.0	16.90
SG1 - Sim2	Parallel	1	10	0.225	0.10	0.3	1	0.0	$2.1\ 10^{-4}$
SG1 - Sim3	Perpendicular	1	10	0.225	0.10	0.3	1	0.0	$2.1\ 10^{-4}$
SG1 - Sim4	Perpendicular	1	10	0.225	0.10	0.3	1	0.15	$2.1\ 10^{-4}$
SG2 - Sim1	Parallel	1	10	0.225	0.10	0.3	1	0.0	$2.1\ 10^{-4}$
SG2 - Sim2	Perpendicular	1	10	0.225	0.10	0.3	1	0.0	$2.1\ 10^{-4}$
SG2 - Sim3	Perpendicular	1	10	0.225	0.10	0.3	1	0.15	$2.1\ 10^{-4}$
SG3 - Sim1	Parallel	1	10	0.225	0.10	0.3	1	0.0	$2.1\ 10^{-4}$
SG3 - Sim2	Perpendicular	1	10	0.225	0.10	0.3	1	0.0	$2.1\ 10^{-4}$
SG3 - Sim3	Perpendicular	1	10	0.225	0.10	0.3	1	0.15	$2.1\ 10^{-4}$

Table 3: parameters assigned in the simulation using patterns SG1, SG2 and SG3 [3]. Note that Simulation 1 for the pattern SG1 corresponds to the case where the layer acts as a preferential path. All others simulations considers layers as a flow barrier.

1-2 Multiple parallel layers

Several patterns of parallel layers are considered including constant and variable length.

- Constant length

Layers have a length of 2m, and are placed randomly throughout the model area of 10m by 10m (Figure 16a). The fractures are oriented parallel to the direction of the flow and are more permeable than the matrix. Therefore, they will act as preferential path through which CO_2 will flow. Two different density have been considered (Figure 16a) and variation in the aperture has been considered.

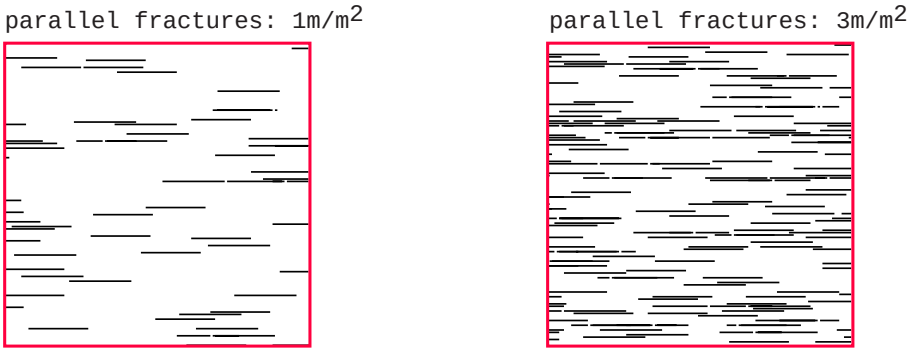

Figure 16a : simulated multiple parallel layers of constant length used as input to the two-phase flow model.

[3] η_{water} is the water viscosity, η_{CO2} the carbon dioxide viscosity, Φ_l and Φ_m are respectively the layers and matrix porosity, <Km> is the mean matrix permeability, σ is the standard deviation of the lognormal law describing the matrix local permeability distribution, and R_k is the permeability ratio between the layer and the matrix.

- Variable length

Layers have been disposed randomly in space (the fractal dimension *D* is equal to 2) inside a square area of 1m², and presents a random length distribution (Table 4). The effect of pattern orientation on the geometry of the flow has been investigated (parallel and perpendicular to the input flow). Also we have realised simulations for homogeneous and heterogeneous matrix permeability and porosity field. Two different patterns have been considered to test the density dependence.

Table 5 synthesised the different parameters used and simulations performed with these different types of geometry.

Name	Area (m^2)	Mass (m)	Density (m/m^2) (d= Mass/Area)	N_{layers}	Density (m^{-2}) (d=N_{layers}/Area)	Proportion of elements	N_{int}	l_{max} (m)
SG4	1	10.23	10.23	30	30	4.0%	0	0.992
SG5	1	17.75	17.75	45	45	6.94%	0	0.998

Table 4: geometrical characteristics of the multiple parallel layers patterns, with variable length.

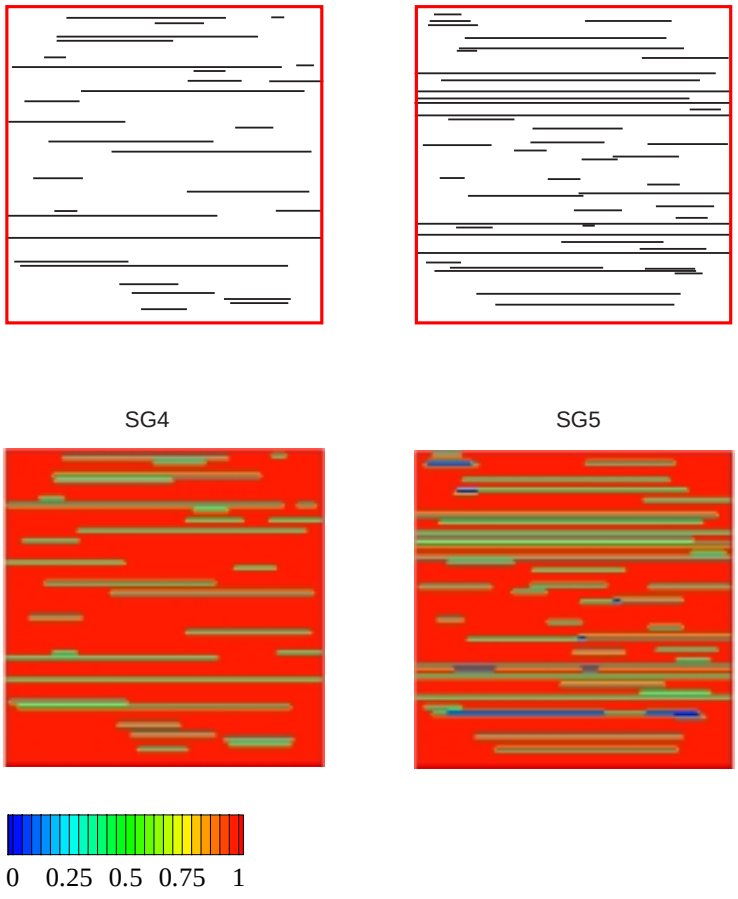

Figure 16b : simulated multiple parallel layers of variable length used as input to the two-phase flow model (top) and normalised permeability field (bottom).

	Orientation flow/layers	η_{water} (Pa.s)	η_{CO2} (Pa.s)	Flow rates ($m.s^{-1}$)	Φ_l	Φ_m	<Km> (darcy)	σ	R_k
SG4 - Sim1	Parallel	1	10	0.225	0.10	0.3	1	0.0	$2.1\ 10^{-4}$
SG4 - Sim2	Perpendicular	1	10	0.225	0.10	0.3	1	0.0	$2.1\ 10^{-4}$
SG4 - Sim3	Perpendicular	1	10	0.225	0.10	0.3	1	0.15	$2.1\ 10^{-4}$
SG5 - Sim1	Parallel	1	10	0.225	0.10	0.3	1	0.0	$2.1\ 10^{-4}$
SG5 - Sim2	Perpendicular	1	10	0.225	0.10	0.3	1	0.0	$2.1\ 10^{-4}$
SG5 - Sim3	Perpendicular	1	10	0.225	0.10	0.3	1	0.15	$2.1\ 10^{-4}$

Table 5 : parameters used and simulations realised in the case of multiple parallel layers with variable length.

1-3 Cross-cutting layers

- Orthogonal layers

A fracture pattern with two-orientation set was generated. One set is parallel and the other perpendicular to the flow direction (**Figure 17a**). Patterns with densities ranging from 1 to 5 m/m^2, in $1m/m^2$ interval; and with aperture of 10, 15, 20, 50, 75 and 100 µm were run.

- Diagonal layers

As previously and in order to test the orientation effect, several patterns have been created that consist of two set of constant length fractures oriented at 45° to the flow direction (**Figure 17b**). Numerical experiment were conducted to estimates the effect of fracture density and aperture.

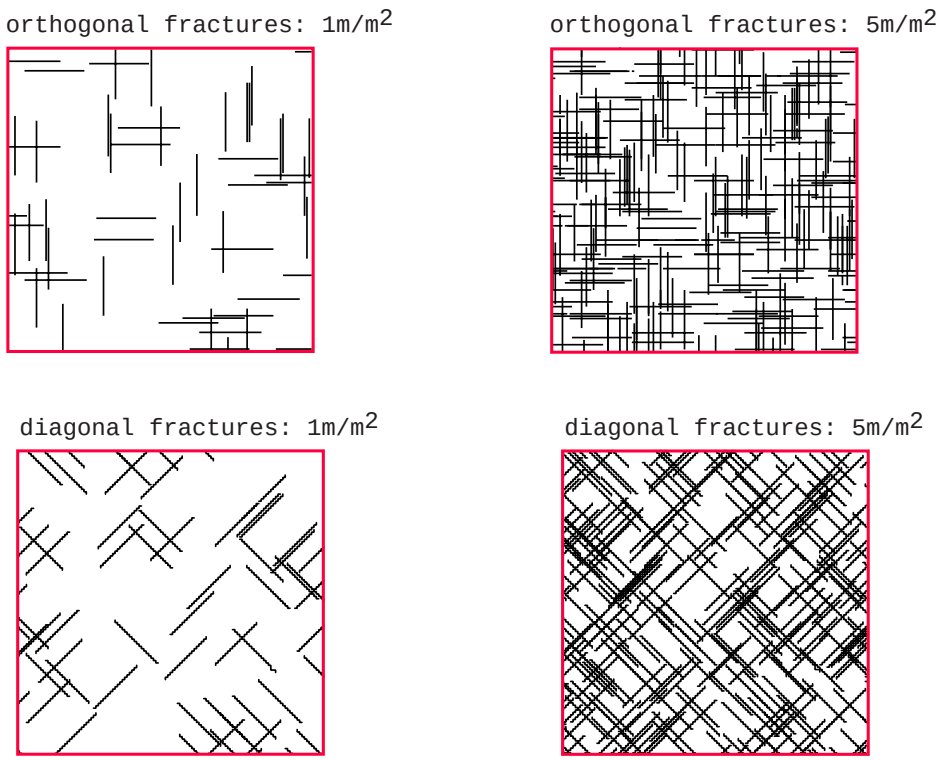

Figure 17: Orthogonal (top) and diagonal (bottom) pattern generated and used as input in the two-phase flow model.

2- Turbidites sequences

Good examples of turbidite sequences are preserved and exposed on land in a number of locations [*Pickering et al.* 1995]. One example that has been extensively studied is found in the Pyrennian Mountains near the village of Ainsa in northern Spain [*Pickering et al* 1995; *Schuppers* 1993]. Here the architecture of a sequence of late to mid Eocene age turbidite-filled (sandstones and mudstones) channels is exposed in a cliff section some 600m long and 20-40m high. The sequence shows signs of multi-phase filling and is composed of two major thinning upward sequences separated by a mudstone that spans the channel. The sediments consist of normally graded sandstone beds, sandy conglomerates, intercalations of very fine-grained, thin bedded (2-6 cm) sandstones and mudstones, and mudstones [*Schuppers* 1993]. Overall the sediments are dominated by sands but have many mudstones from 10 cm to 2 m thick inter-bedded with sands. The channel is most sand-rich near the centre where sections of sandstones with no shales up to 15 m and frequently over 2-3 m occur. The majority of mudstones layers are under 1m thick and very few are over 2 m thick. These features are consistent with the available information from the Utsira Sand, i.e. that sections of 9 m of uninterrupted sand occur (core) and that 14 shale claystone horizons thicker than around 1m occur in some in 200m of the sediments, giving a mean spacing of 14m [*Lothe and Zweigel*, 1999, *Torp* 1999]. This section thus provides, as far as the present state of knowledge allows, a reasonable analogue for the Utsira Sand.

Detail vertical logs with a total length of 111m of the lithologies and their grain sizes from the Ainsa section [*Clark* 1995] were used to generate a vertical transition probability matrix for the Ainsa sequence. For this, cells of 30 cm size were used which adequately represents most of the mudstone layers. The mudstone layers extend laterally from 600m down to around 5m and show a log-normal length distribution which is very similar to that estimated from the Frigg Field in the North Sea [*Schuppers* 1993]. This indicates that the majority of shales are short, around the mode of about 50m or less.

Lithology	<Km> (D)	σ	Φ
shale / clay	0.00005	0.1	0.3
very fine sand	0.01	0.1	0.32
fine sand	0.4	0.1	0.37
medium sand	0.2	0.1	0.27
coarse sand	0.2	0.1	0.27

Table 6- lithology classes for the Ainsa turbidite sequence and associated permeability and porosity.

In order to test the effect of shale or mudstone length on the fluid flow behaviour, three models with varying horizontal persistence of the layering were generated, see Figure 18 for examples. The generated area represents a 38 by 38 region and the minimum shale length in the simulations varies from over 40m, to around 20m and around 5m in length. Permeabilities and porosities were assigned to lithologies using the information on grain size [*Clark* 1995] and the relation between grain size, sorting and permeability and porosity presented in Figure 8 (adapted from *Gidman et al.* [1993]). For all lithologies, it was assumed that permeability is log-normally distributed about a mean with a spatially randomly distribution. From the literature, permeability variations of half an order of magnitude within single sedimentary beds are common [*Morrow et al* 1969, *Hurst* 1991, *Hurst* 1993, *Schuppers* 1993]. To mimic this behaviour, a standard deviation of log permeability of 0.1 was used. This means that 90% of the permeability distribution will lie within a range of 0.6 of an order of magnitude. The parameters for the different lithologies are listed in Table 6.

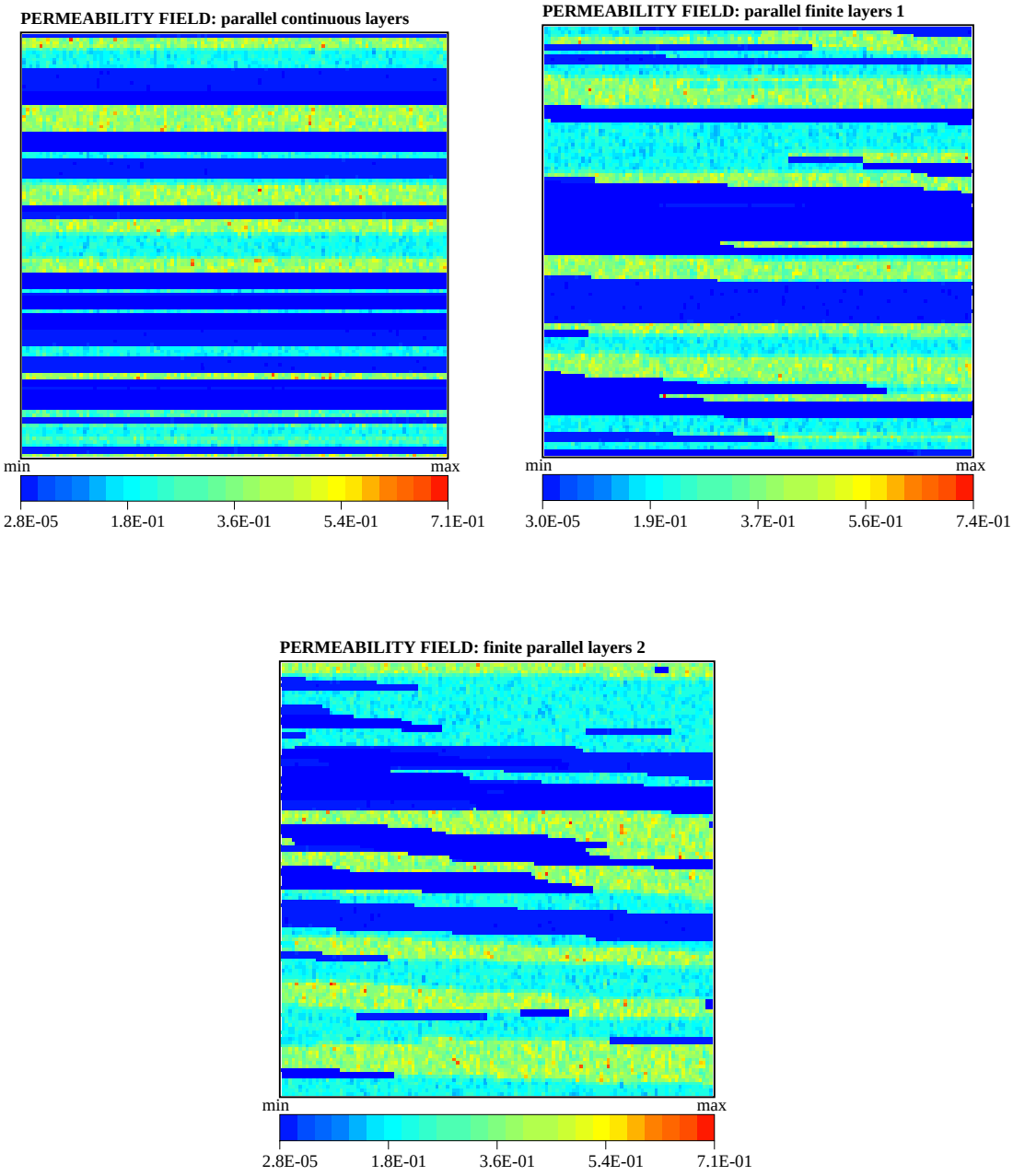

Figure 18: Permeability fields for examples of turbidite sequences representing an area of 38 by 38m. Top left – parallel continuous layers, top right – discontinuous layers (shales around 40m), bottom - discontinuous layers (shales around 5m).

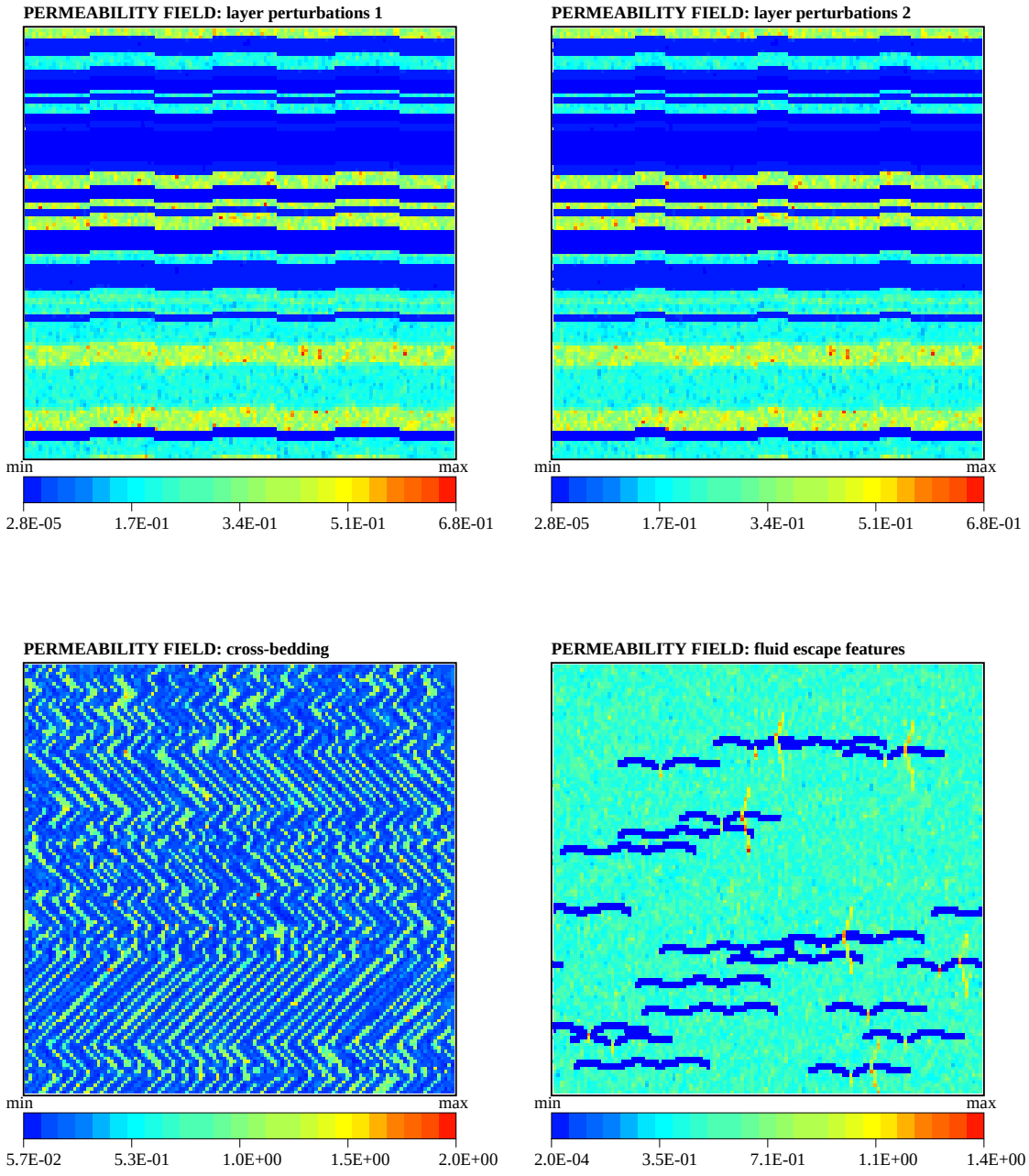

Figure 18 (cont.): Permeability fields for:, top left – parallel continuous layers with wave like perturbations 1, top right – parallel continuous layers with wave like perturbations 2 (38 by 38m), bottom left – cross-bedding (0.5 by 0.5m) and bottom right – massive sands with fluid escape structures (0.6 by 0.6m).

Another possible deviation from horizontal parallel layering could be caused by minor folding. Such folding may occur due to differential compaction around mud volcanoes at the base of the Utsira Formation [*Lothe and Zweigel* 1999] or around faults. To test the effect of small perturbation in the geometry of the layering, two sinusoidal waves of small amplitude (1 cell and 3 cells) were imposed on the layering, see Figure 18.

2-1 Cross bedding

Cross-bedding on a variety of scales is a common feature of sandstones of all environments. In turbidites, ripple cross laminations are common in division C (sandstone) of the classic turbidite

Bouma sequence that might be expected on supra-fan lobes and basin parts of the fan, and in coarse grain and pebbly sandstones expected in the middle (supra-fan lobes) to upper fan areas . The sets are commonly 5 to 10 cm thick with trough or planar cross bedding. Each cross beds consists of graded unit with coarser material at the base and finer material at the top. This can generate permeability differences by commonly a factor of three and up to 1 order of magnitude [*Weber et al* 1972, *Pickup et al* 1996].

In order to simulate successive cross laminated beds using the coupled Markov chain model, a simulation was first made of horizontal beds of varying thickness and then each bed was superimposed by a sloping cross lamination pattern using two states. These two states were given permeabilities representative of fine sand and medium grained sand (**Fig.4-original**), see Table 7. A contrast of 1 order of magnitude was chosen to represent the maximum possible effect on fluid flow. An example of a simulated permeability field is shown in Figure 18.

Lithology	<Km>(D)	σ	Φ
fine sand	0.1	0.1	0.3
medium sand	1.0	0.1	0.35

Table 7: lithologies and parameters for cross-bedding simulations

2-2 Fluid escape structure

Massive sandstones found within marine fan sequences often contain fluid escape features. These sandstones are generally deposited rapidly from a sediment loaded turbidity current within which sediment is kept in suspension by turbulent flow. On deposition, the sediment grains settle under gravity and large quantities of fluid must escape to allow the sediment to stabilize. The process of water expulsion gives rise to fluid escape structures. These include dish structures, thin horizontal layers (less than 1 mm thick) of fine grain sediment with spoon-shaped geometries, and fluid escape pipes, vertical pipe-like structures of clean sand. The dish structures represent potential flow barriers while the fluid escape pipes have enhanced permeability because the fine sediment has been washed out. Dish structures and fluid escape pipes often occur together and fluid escape pipes sometimes occur where two upturned edges of dish structures meet forming a channel for fluid flow. Dish structures are commonly 10 cm long and can occurs in strings. Fluid escape pipes are commonly 10 cm long and around 1 cm wide.

Lithology	<Km> (D)	σ	Φ
Dish structure	0.0002	0.0	0.30
Fluid escape pipe	1.00	0.1	0.37
Massive sands	0.5	0.1	0.32

Table 8: lithologies and parameters for massive sandstone with fluid escape structures.

A simulation of massive sandstones with dish structures and fluid escape pipes was generated using a 'template' method. Three templates were constructed for *(a)* **dish structures alone**, *(b)* **dish structures with fluid escape pipes** and *(c)* **fluid escape pipes alone**. These three templates were then placed randomly in a homogeneous field representing massive sandstones. The cells representing massive sandstone, dish structure and fluid escape pipe were assigned permeabilities and porosities listed in Table 8. An example of the permeability field for these simulations, representing an area of 63 by 63 cm, is shown in Figure 18.

The above simulations of sedimentary architecture on a variety of scales (turbidites sequences, cross bedding and fluid escape structures) were used to generate a total of seven permeability and porosity field types. Ten realizations of each field type were generated and these fields were used as input to

the two phase flow model described in the next section to test the sensitivity of the flow properties to variations in sedimentary architecture.

2-3 Complex cross-cut patterns

Turbidites bed thickness, length and spatial organisation have been found to follow scaling law [*Malinverno*, 1997]. We have used a fractal generator presented section (C-1.2-) to generate the patterns shown below. Three different geometry have been considered here that takes into account the power law length distribution and the fractal spatial organisation (see Figure 12 and Figure 14). From these patterns, permeability and porosities fields have been created.

(a)- Length dependence

Patterns presented here contain the same number of fractures but different length exponent. An increase of this exponent corresponds to the presence of much more small layers (see Figure 12 for the pattern and Figure 19 for the permeability field). The area is 1 m, 30 m and 1000 m.

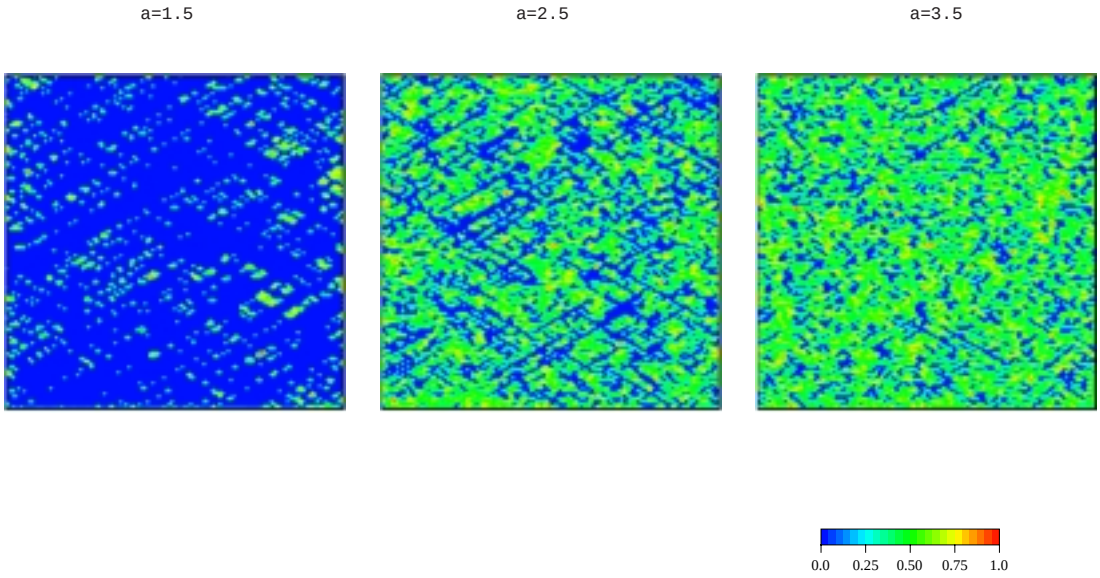

Figure 19: permeability field generated for a fractal pattern with the same dimension (D=2) and for different length distribution exponent (*a*=1.5,2.5 and 3.5). The number of faults and the size is the same for the three different patterns. The density (mass/area) is respectively equal to *(a)* 208.0 m/m², *(b)* 50.1 m/m² and *(c)* 32.3 m/m²

The parameters used for the simulation are listed in Table 9. These patterns have been used to test the effect of permeability contrast on the geometry of the front and on the saturation evolution. The contrast has been defined as the ratio between the fracture (layer) permeability K_l and the matrix permeability K_m. On Figure 19, it corresponds to 10^{-3}.

	L (m)	N_{layers}	*d* (m/m²)	*P* (%)	Φ_l	Φ_m	Aperture (μm)	<Km> (darcy)	σ
a=1.5	1	2000	208.0	64.8	0.1	0.6	0.1	1.0	0.10
a=2.5	1	1997	50.1	19.7	0.1	0.3	0.05	0.2	0.15
a=3.5	1	1997	32.3	13.4	0.1	0.3	0.05	0.2	0.15

Table 9: parameters of the three different patterns shown on Figure 19.

The effect of density and system size has also been considered. Indeed, although the number of fractures is the same for each pattern (N=2000), the density can be identical (density = number / area) or can be different (density = mass / area) according to its definition. As statutes in section B-3.2-, we have chosen the proportion *P* of element that belongs to the pattern to get free from the length scale introduced in the density definition (the area in the first case, the mass and the area in the second).

(b)- Spatial dependence

Figure 20 illustrates the permeability field derived from the pattern shown on Figure 14. The length distribution exponent is the same (*a*=2.7) and the fractal dimension D differs. Three cases are considered D=2, 1.75 and 1.5.The patterns used here contain nearly the same number of fractures (see table). The area is 1 m² and the effect of permeability contrast and density has been studied.

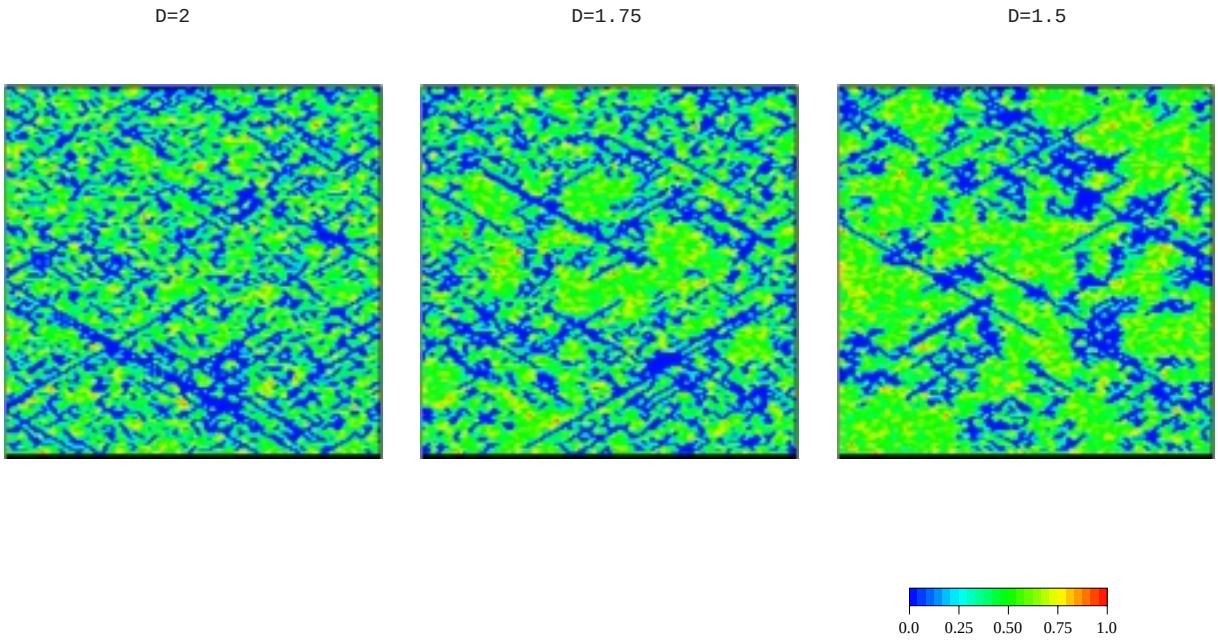

Figure 20: permeability field generated for a fractal pattern with the same length distribution exponent (*a*=2.5) and for different fractal dimension (D=2, 1.75 and 1.5). The number of faults and the size is the same for the three different patterns. The density (mass/area) is respectively equal to *(a)* 46.2 m/m², *(b)* 46.6 m/m² and *(c)* 44.5 m/m². *P* is respectively equal to 18.4%, 17.3% and 14.8%.

	L (m)	N_{layers}	*d* (m/m²)	*P* (%)	Φ_f	Φ_m	Aperture (μm)	<Km> (darcy)	σ
D=1.5	1	1939	44.5	14.8	0.1	0.3	0.05	0.2	0.15
D=1.75	1	2000	46.6	17.3	0.1	0.3	0.05	0.2	0.15
D=2	1	1988	46.2	18.4	0.1	0.3	0.05	0.2	0.15

Table 10: parameters of the three different patterns shown on Figure 20.

C-3. Two-phase flow in heterogeneous sediments

1- generality

The presence of heterogeneities in permeable sediments results in highly heterogeneous permeability fields which have a large impact on the relative flow of two immiscible fluids. This results in 'viscous fingering' [*Feder* 1989] which generates complex fluid fronts and highly variable fluid saturation fields. Such phenomena make prediction of the migration rates and dispersion of injected fluid behaviour difficult. This phenomenon has been intensively studied for the case of oil and water where such effects make efficient recovery from petroleum reservoirs difficult and complex [*Barker and Thibeau* 1997; *Kyte and Berry* 1975; *Langlo* 1992; *Pickup et al* 1994]. In the case of injected supercritical CO_2, the fluids have different densities (CO_2 is slightly less dense than water), but also different viscosities with about an order of magnitude difference between CO_2 and water. Supercritical CO_2 is soluble in water but the dissolution takes place very slowly so that on a time scale of hours to months advection effects dominate and supercritical CO_2 and water can be treated as two immiscible fluids. The extreme viscosity ratio (of the order 1:10)[4] results is a more smeared out fluid front and more extreme fingering effects due to sediment heterogeneities than is normally the case for water and oil.

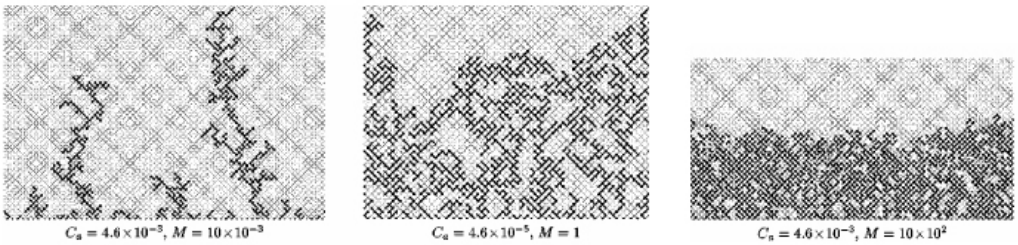

Figure 21: different front geometry observed depending on the capillary number *Ca* and on the viscosity ratio V_R. Left: viscous fingering, medium: capillary fingering, and right stable displacement (from [*Aker et al.* 1998]).

If the geometry of the front depends on the viscosity ratio, it is also dependent on another dimensionless number, the capillary number *Ca* [*Aker et al.*, 1998]. This number describes the competition existing between capillary and viscous forces. Depending on its value and also on the viscosity ratio, three different regimes corresponding have been individualised which corresponds to three different geometry; *(i)* Viscous fingering, *(ii)* stable displacement, and *(iii)* capillary fingering (Figure 21).

This model illustrates how the interaction between two fluids can lead to three different patterns. In the model we use here, we were not able to define a capillary number since, because of the algorithm used, capillary forces were neglected. However we are dealing with strongly heterogeneous system. Hence, apart the viscosity ratio, the main controlling factor will be the permeability ratio between the matrix and the heterogeneities. Therefore, we will in a first approach, consider its influence on the geometry of the front.

[4] The viscosity ratio is defined in our case as the ratio between the invading fluid viscosity (CO_2) and the defending fluid viscosity (water), and will be called hereafter V_R.

2- Permeability ratio

Simulations have been realised to test the influence of the permeability contrast on the geometry of the front. When heterogeneities act as a preferential path the migration of injected fluid will be enhanced and inversely when it acts as barriers. However, the way the front is modified when the permeability contrast varies remains an open question. Indeed is there sharp transition between well defined geometry or on contrary, shall we observe a continuous evolution of the geometry of the front?

A study made on joints acting as preferential path shows that two main different behaviour exist [*Taylor et al.* 1999]. These two regimes are function of the permeability contrast existing between the matrix and the joint, and are separated by a transitional zone (Figure 22). In the first case, the permeability contrast should be smaller than three orders of magnitudes, and the flow system is dominated by indirect connections controlled by the matrix permeability. In that case, geometry of the flow is distributed through all the space. In the second regime, joint permeability exceeds the matrix permeability by more than 6.5 orders of magnitude. The flow is dominated by the direct connections between fractures leading to a highly localised flow pattern (Figure 22).

Between these two *'extreme behaviour*', a transitional zone exist where the permeability contrast strongly influence the geometry (a small modification of half an order of magnitude in the permeability contrast can change the geometry of the flow from distributed to localised).

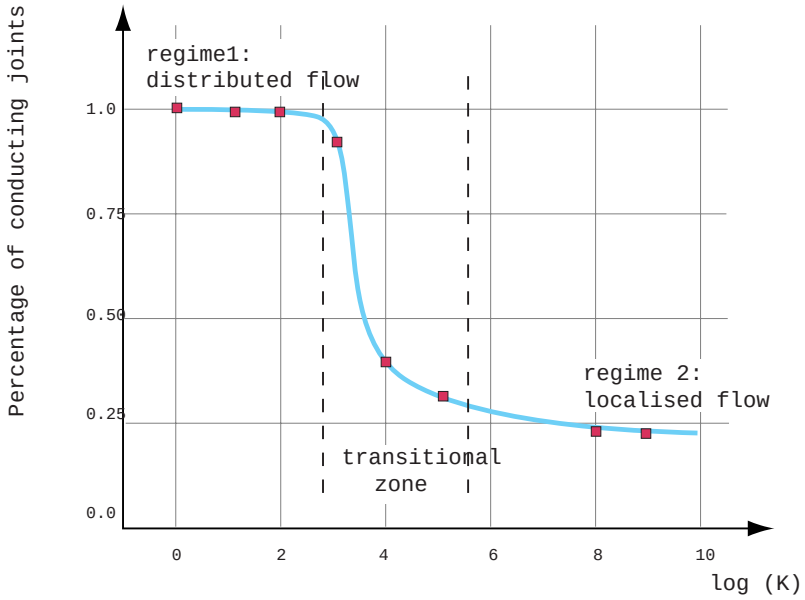

Figure 22: evolution of the geometry of the flow index with respect to the permeability contrast.

This study have shown that the geometry of the fluid flow within a joint set is influenced by the geometric arrangement of joints and the hydraulic properties of both joints and the matrix.

Here, we will focus on the case where joints act as barriers meaning that their permeability is much smaller than the permeability of the matrix. The model used (see section C-4) allow a permeability contrast up to 4 orders of magnitude. We have defined the permeability ratio R_k as the ratio between the layers permeability K_l and the matrix permeability K_m. For a given geometry, we have cover a range lying from a null contrast (heterogeneity and matrix have the same permeability) to a contrast of 10^{-4} (Figure 23). Because of numerical constraints we were not able to simulate higher contrasts. However the way the geometry of the front evolves with R_k on that range will give us indications on the existence of any transition.

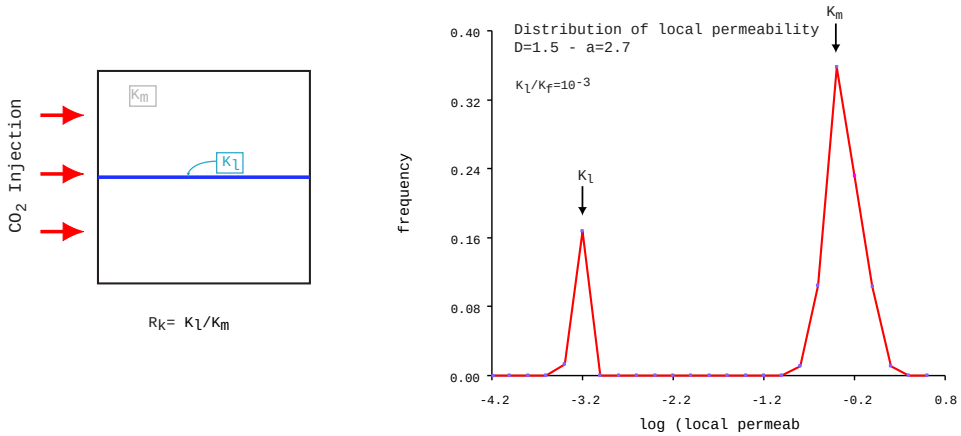

Figure 23: distribution of local permeability for a simulation performed with a fractal dimension D=1.5 and a length distribution exponent *a*=2.7 (see Figure 20). The parameters used leads to a difference of three orders of magnitude between the matrix and the layers.

The permeability of the layer has been express in Darcy and determined using the formula:

$K_l = (b^2/12) / 9.8697\ 10^{-13}$ Eq. 9

Where *b* is the hydraulic aperture of the fracture expressed in meters. Normalising this permeability by the matrix permeability gives the permeability contrast (or ratio) R_k. The sand permeability found in the Utsira formation approximates a few Darcy (see Figure 8). Hence assuming a permeability value of 1 Darcy require to fix a hydraulic aperture of $3.4\ 10^{-2}$ µm to get a permeability contrast of 10^{-4}. Note that the required value for the hydraulic aperture is small but since barriers inhibits the flow, the *b* value in eq. (9) should be very little.

3- Relative permeability, fractional flow and fluid front

3-1 Relative permeability

When the two immiscible phases occupy the rock pore space, the space through which each phase can flow depends on the saturation [*Pettersen* 1990]. Thus the relative permeability of each phase depends on the absolute permeability of the rock and the saturation (or concentration) of that phase. The simultaneous flow of the two fluid phases through a rock mass can be described by the two phase version of Darcy's law:

$$U_1 = \frac{K_{r1}}{12\mu_1}\Delta P_1 \qquad \text{(Eq. 10)}$$

and

$$U_2 = \frac{K_{r2}}{12\mu_2}\Delta P_2 \qquad \text{(Eq. 11)}$$

where K_{r1} and K_{r2} are the relative permeabilities, μ_1 and μ_2 are the viscosities and ΔP_1 and ΔP_2 are the pressure gradients in the fluid phases 1 and 2.

When two phases occupy the pore space, one fluid is wetting and the other non-wetting. In a rock with oil and water, water is normally the wetting phase. The wetting phase has the greater affinity for the rock surface and forms a thin film around the rock grains. Due to friction between the wetting fluid and the rock grains, this film of fluid will always remain and gives rise to an irreducible water saturation, IS_w. In addition, due to the complex geometry of the pore space, small pockets of the non-

wetting phase become trapped and form an irreducible fraction, IS_{nw}. Thus under flow the saturation of the two phases vary between these two values. There is no information available about the relative wetting properties of water and supercritical CO_2. However, since the pore space is water filled before CO_2 injection it is assumed that the rock is water wet.

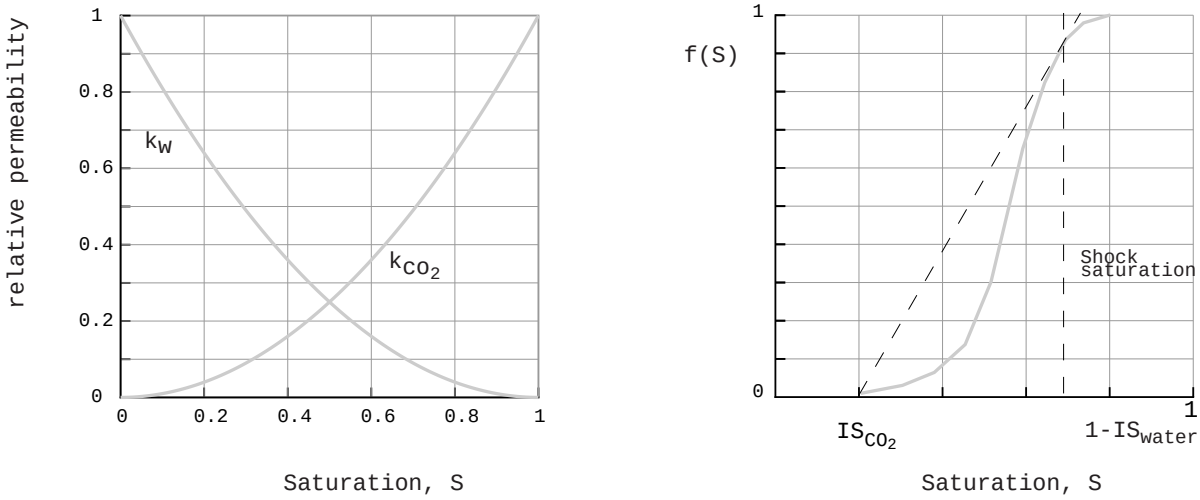

Figure 24: (a) Assumed simple rock relative permeability curves for water (k_w) and CO_2 (k_{CO2}). Here the CO_2 correspond to the invading or wetting phase and water is the non wetting phase. (b) Form of a fractional flow curve for a homogeneous permeable medium. From the fractional flow function, the shock saturation can be determined.

Fluids with intermediate values of saturation travel faster than fluids with low saturations. In the case of water injection, this means that intermediate water saturations try to 'overtake' the lower saturations resulting in the formation of a saturation discontinuity or a '*shock*' front. This phenomenon acts to maintain a sharp contact between the two fluids at which there are very abrupt changes in saturation. The shock saturation is independent of time. The relative permeabilities in equations 10 and 11 vary between 0 and 1 and depend on the saturation of the fluids in the rock. At irreducible water saturation, IS_w, water will not flow and K_w=0, while at residual saturation, IS_{nw}, the non-wetting phase will not flow and K_{nw}=0. Between these values, relative permeabilities can take on different values depending on the properties of the rock, but generally such that their sum is less than 1.

For rock matrix, relative permeability curves are generally determined from rock samples in the laboratory. For the case of water and oil they show the typical form shown in Figure 24a. However, there is at present no information on what rock relative permeability curves look like for supercritical CO_2 and water, so the simple curves illustrated in Figure 24a are used.

3-2 Fractional flow function

A measure of how much of the flow constitutes CO_2 is given by the fractional flow function [*Dake* 1978]

$$f(S) = \frac{q_{CO_2}}{q_t} = \zeta_{CO_2} / (\zeta_w + \zeta_{CO_2}) \qquad \text{(Eq. 12)}$$

where $\zeta_i = k_i / \mu_i$, corresponds to the mobility of the fluid *i*. Eq 12 gives

$$f(S) = \frac{1}{\left[1 + \frac{K_w}{K_{CO_2}} V_R\right]} \qquad \text{(Eq. 13)}$$

The fractional flow function, *f(S)*, in a homogeneous porous media increases from 0 at the minimum saturation, IS_w, to 1.0 at maximum saturation IS_{nw} (=1-IS_w), see Figure 24b.The fractional flow function has several useful properties from which information on the shock saturation and velocity can be easily determined. The velocity of fluid at saturation, S, within the porous medium is given by the first derivative (slope) of the fractional flow function, at S. It can be seen in Figure 24b that the fractional flow curve has an inflexion point so that its slope, and therefore velocity of the fluid, increases and then decreases with increasing S. This means that fluids with intermediate values of water saturation travel faster than fluids with low saturations. In the case of water injection, this means that intermediate water saturations try to 'overtake' the lower saturations resulting in the formation of a saturation discontinuity or a 'shock' front [*Pettersen*, 1990]. This phenomenon acts to maintain a sharp contact between the two fluids at which there are very abrupt changes in saturation. The shock saturation is independent of time. It can be determined from the fractional flow curve by finding the point at which a line through *f(s)*=0 at minimum saturation is tangential to the curve, see Figure 24b. The shock height (difference in saturation over which abrupt changes take place) is also constant with time. The shock saturation for water and oil is about 0.7. The shock velocity is proportional to the slope of the tangent in Figure 24b and depends on the total flow (and therefore on absolute permeability) and on porosity. In heterogeneous rocks, therefore, the front will travel at different velocities in different parts of the rock creating a complex front geometry.

4- Pseudo functions for rock volumes

Relative permeability curves from laboratory experiments on rock samples some cm in size are only valid for larger volumes as long as the rock remains homogeneous. Generally this is not the case, and heterogeneities such as sedimentary structure and fractures significantly modify the behaviour of two phase flow. Thus for describing two phase flow in the average simulator grid block which is of the order of 100's metres, 'pseudo' relative permeability curves must be determined.

A number of methods exist for determining pseudo curves for oil and water in petroleum reservoirs and a summary is given by *Barker and Thibeau* [1996]. Most widely used is the method by *Kyte and Berry* [1975]. Here fine grid simulations which can resolve the fine details of the heterogeneous permeability field are used to determine the time dependent average saturation of the block and flow rates of oil and water out of the block. These values are substituted into the two phase Darcy equations (equations 10and 11) to give the relative permeabilities of oil and water for each average saturation. Other methods (non-dynamic) include calculating weighted averages (e.g. by transmissibility) of fine grid relative permeabilities, and the total mobility method. No method is, however, always reliable and the applicability of the results is dependent on boundary conditions of the grid block *in situ*.

To date, there exists little information in the literature on pseudo functions for different kinds of geological heterogeneity. *Pickup et al.* [1994] have built a '*geopseudo atlas*', in which geological models of fine scale sedimentary structure can be built, or selected from templates, and bulk permeabilities and pseudo relative permeability curves determined. To date, however, there exists no information on pseudos for the flow of supercritical CO_2 and water in heterogeneous sediments. Some large scale simulators, such as Eclipse, contain routines for calculating pseudo curves. The reliability of the results are, however, dependent on the ability of the simulator to cope with high permeability contrasts. In addition, the capability of the simulator to simulate the details of the sediment architecture is often limited.

In this project, a two phase flow program (written at the Department of Applied Mathematics, University of Bergen, *Langlo* [1992]), specifically designed to handle large permeability contrasts and reproduce accurately the complexity of saturation front, has been used to determine pseudo functions for different sediment heterogeneities. The pseudo curves determined from these patterns can be used a first guide to pseudo functions for supercritical CO_2 and water in the heterogeneous sediments that might occur in the Utsira Formation.

C-4. A two phase flow model for heterogeneous sediments

Sediment heterogeneities can represent permeability differences of several orders of magnitude and therefore made high demands on the numerical methods used. The model must also be able to handle large discontinuities in the permeability field that result from the presence of e.g. shale layers adjacent to high permeability sands and to resolve sharp and geometrically complex fluid fronts. At the Institute of Applied Mathematics in Bergen University much expertise in the numerical modeling of two phase flow in heterogeneous porous media has been carried out through the group of Prof. *Magne Espedal*. The chosen model was developed by Peder Langlo and was originally designed to simulate two phase flow in heterogeneous porous media [*Langlo,* 1992].

1- The model

The pressure equation is solved by a finite element method, where multigrid is used as a solver. The velocity, u_x, is determined from the pressure by a central difference method:

$$u_x = KM(p(i+1, j) - p(i-1, j)) / 2dx \qquad \text{(Eq. 14)}$$

where *K* is the permeability, *M* is a mobility function which contains the relative permeabilities and *p(i,j)* is the pressure at the *ith* and *jth* node.

The saturation equation is solved by an operator splitting method where the hyperbolic part of the equation is solved by integrating backwards along the characteristics to determine a approximate solution on the new time level.

The remaining elliptic part of the saturation equation is solved by a finite element method, with a conjugate gradient solver on sub-domains in the vicinity of the saturation front. However it was found that the model, as it is today, could not handle Dirichlet boundary conditions at the outlet and thus the model was run without this part. This means that capillary forces are neglected. In an oil recovery situation this does not create great errors, because the saturation equation is dominated by the convective / hyperbolic part of the equation. However, there may be effects which the model in its present state will not capture. The main weakness of the model is the way that velocity is derived from the pressure by a central difference scheme, because it can not guarantee that the mass is conserved to a high degree of accuracy. There are other codes that handle the mass balance better, such as Eclipse, but these models tend to smooth the velocity field and do not capture the full effects of the heterogeneous permeability field.

2- Model input

Input to the model consists of permeability and porosity fields, local (core scale) relative permeability curves, fluid viscosities, flow rates at left and right boundaries, number of time steps and time step size.

2-1 Permeability and porosity field

Permeability and porosity fields were determined using the coupled Markov chain simulation model and the fractal methods described in the section C-1, generating field of 128 by 128 cells. From these, the permeability governing the flow of fluid from each cell to its neighbour above and to the right are calculated from the harmonic average of the two cell permeabilities. These vertical and horizontal permeability fields of 127 by 127 cells are used as input to the model.

2-2 Viscosity of water and supercritical CO_2

The reservoir conditions at a depth of 987m are a pore fluid pressure of 10MPa and temperature of 37°C [*Torp* 1999]. At atmospheric pressures, CO_2 becomes liquid at 37°C . In the system H_2O-CO_2, the invariant point where liquid and gaseous CO_2 phases and water coexist is at around 10°C and 4.5 MPa [*Wadsley* 1993]. For temperatures above 10-15°C, the possible combinations are liquid CO_2 and liquid H_2O at higher pressures (above 5-10 MPa) and gaseous CO_2 and liquid water at lower pressures. The reservoir conditions (37°C, 10MPa) lie close to the boundary of these two states but it is thought that CO_2 exists primarily as a liquid at these depths [*Torp* 1999]. The two-phase flow model is only valid for two immiscible liquids and thus can only simulate the behaviour of supercritical CO_2 and water. The viscosities of water and liquid CO_2 at the depth and temperature of the reservoir can be estimated from the available data given in Table 11. These values of the viscosity of liquid CO_2 compare with the viscosity of gaseous CO_2 of 0.014 mPa s. These data give a viscosity ratio for CO_2: water of around 15:1 for pure CO_2 and water in the temperature range 20-40°C. However, the formation waters in the Utsira Sand are saline with salinities probably similar to that at '*Oseberg*' 200 km to the north of 33g/l [*Torp* 1999]. This is slightly less saline than sea water (35g/l). In addition the CO_2 injected contains some 2-3% methane the effect of which on viscosity is unknown. For the purposes of simulation a conservative estimate of the viscosity ratio of 1 order of magnitude (10:1) was used. This viscosity ratio V_R is much higher than is commonly the case for oil and water (around 1:2 for water:oil).

T (°C)	Viscosity of water at 49 MPa, (mPa s)	T (°C)	Viscosity of supercritical CO_2 (MPa)
20	0.992	-50	0.227
30	0.796	0	0.089
50	0.339	30	0.053

Table 11: data on viscosity of water and liquid CO_2 [*James and Lord*, 1992].

2-3 Relative permeability curves for water-liquid CO_2

No data is presently available for rock relative permeability curves for liquid CO_2 and water. Thus for the simulations simple symmetrical, convex curves (Fig.9) were used for all lithologies. This implies some influence of capillary forces at the pore scale. However user defined relative permeability curves can be input to the model, so there is the possibility of modifying them when more information is available.

2-4 Model boundary condition

The top and bottom boundaries of the model are set to no flow and, at the first time step, constant flow rates are set along the left and right hand boundaries. Using the permeability field and the input flow rates the pressure field is determined and this pressure difference across the model maintain thorough the run. The pressure field internal to the model is recalculated at every time step. At the start of simulations, the supercritical CO_2 saturation is set to 1 at the left boundary and decreases linearly to the shock saturation in 0.2 times the model size. The model was run for 100 to 200 time steps for which the saturation, pressure and velocity fields were determined. The model was run on the Cray Origin 2000 at the University of Bergen (*ParaLab*). Runs of 200 time steps take about 10 to 15 minutes of run time.

3- Model output and study parameters

The model outputs the pressure, velocity and saturation fields at user specified time intervals. These consist of values are every node in the 127 by 127 grid. In order to save space, saturation fields are output at user specified time intervals, while the saturation at the outflow boundary are output at every time step. A series of graphic programs have been created to present the model results.

'*Snapshots*' of the saturation field at specific time intervals can be produced. A flow evolution plot is created which shows the changes in saturation along the outflow boundary with time. These saturation are summed to show the total saturation at the outflow boundary with time.

From the output of the flow model, the relative permeabilities for the whole region at each time step are calculated using the method by *Kyte and Berry* [1975]. The flows of water and oil (or CO_2) at the outflow boundary are determined from the column of cells at the right hand side of the model. The relative permeabilities of these cells are determined from their saturation and the input rock relative permeability curves. These relative permeabilities are used with the pressure difference across each cell and the intrinsic permeability to determine the flows of water and oil through these cells. Pseudo relative permeabilities for the whole model are then calculated from the sum of these flows using the following formula:

$$k_{ri} = \sum \frac{q(i)\mu}{\Delta P k_g} \qquad \text{(Eq. 15)}$$

where *i* is supercritical CO_2 and water. Finally, for each time step the average saturation of the whole model is calculated. The values of pseudo relative permeabilities are plotted against the average saturation for the whole model at each time step to give pseudo relative permeability curves for the modelled region.

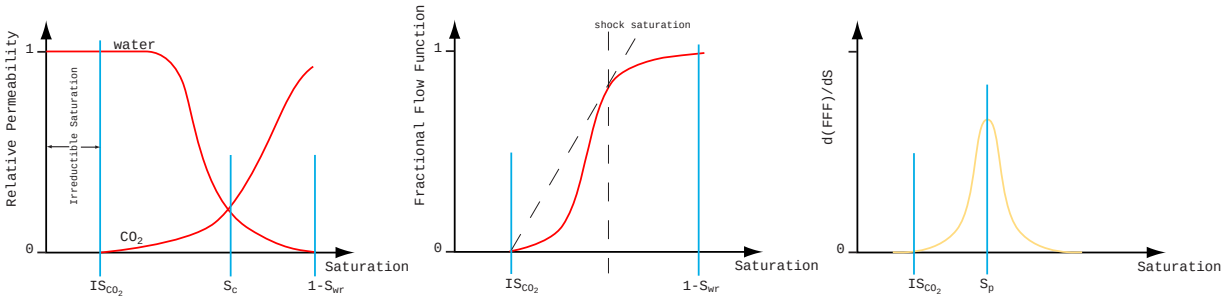

Figure 25: pseudo relative curves (left), fractional flow function (middle) and its derivative (right) with the definition of the quantities deducted from the different curves (see text).

We have follow the evolution of three parameters with respect to the *(i)* density of heterogeneity *(ii)* their geometry and *(iii)* the permeability ratio. These parameters are the irreducible CO2 saturation, the critical saturation and the peak saturation.

- Irreducible CO_2 saturation

For all simulations, we have determined the irreducible CO_2 saturation. This saturation corresponds to the moment when the CO_2 relative permeability or the fractional flow function of CO_2 (FFF) differs from zero (Figure 25). Since the derivative of the FFF curves with respect to the saturation is a measure of the front velocity, the irreducible CO2 saturation (IS_{CO2}) corresponds to the saturation required before the CO_2 starts to move.

- Critical saturation

The expression in eq.(10) and eq.(11) can also be express in terms of mobility. Indeed, the ratio k_i/μ_i represents the mobility ζ_i of the fluid where k_i is the relative permeability and μ_i the viscosity of the considered fluid. Note also that using eq. (10) and (11) indicates that the mobility evolved also as $U_i / \Delta P_i$. When $k_{water} > k_{CO2}$, in terms of mobility we have $\zeta_{water} > V_R.\zeta_{CO_2}$ and inversely when $k_{water} < k_{CO2}$.

Therefore, when both relative permeability are equal, the mobility of both fluids depends only on the viscosity ratio and

$$\zeta_{water} = V_R.\zeta_{CO_2} \qquad \text{Eq. 16}$$

Using pseudo-relative permeability curves allows the determination of the crossover saturation (S_c) between water and CO_2 for which $k_{water}=k_{CO2}$ and for which this equality holds (Figure 25). This corresponds to the moment where both mobility are similar. For saturation greater than S_c, the invading fluid will be more mobile than the defending one and will control the permeability of the system.

Also, the sum of both fluids relative permeability, $k_{water}+k_{CO2,}$ (which evolves in a similar way than the sum of fluid mobility) is not a constant and presents a minimum. This minimum is related to the moment when the invading phase becomes preponderant compare to the defending one and corresponds also to the crossover saturation S_c.

- Peak saturation and intensity

From the two phase version of Darcy's law, the fractional flow function has been derived. The function df/dS corresponds to the front velocity and present a peak, indicating the moment where fluids with intermediate values of CO_2 saturation travel faster than fluids with low saturation. The saturation associated to this peak, and also its amplitude (Figure 25) might depend on the degree of heterogeneity present in the system.

PART D. NUMERICAL MODEL RESULTS

The various cases of permeability-porosity fields generated to represent various kinds of sediment heterogeneity have been used as input to the two-phase flow model. These comprise

- Simple geometry corresponding to single, parallel, diagonal and orthogonal layers to first test the model.
- Three cases turbidite sequences with layering of varying continuity representing shale layers *(i)* continuous *(ii)* around 40 m and *(iii)* around 5 m. Each model represents an area of 38 by 38 m.
- Two cases of turbidite sequences with wave like perturbations. Each model represents an area of 38 by 38m.
- Cross-bedded sandstones. Each model represents an area of 0.5 by 0.5 m.
- Massive sandstones with fluid escape features (dish structures and fluid escape pipes). Each model represents an area of 0.6 by 0.6 m.
- Three different sedimentary patterns with *(i)* various fractal dimension and a fix length exponent and *(ii)* three different pattern presenting a fix fractal dimension and a various length exponent. The area varies between 1m by 1m to 10^3 by 10^3 m.
- Given a length exponent and a fractal dimension, six different patterns presenting the same permeability ratio but different density have been study. Three different geometry (various *a* and *D*) have been considered.

These models of sediment heterogeneity were used to conduct the following numerical experiments:

- Using a single-phase flow model, the bulk rock permeability for each model was determined.
- Series of snapshots were created to give a picture of the migration of injected CO_2.
- A sensitivity analysis was made for pseudo relative permeability curves and saturation variation with injected fluid volume using multiple realisations of the permeability and porosity fields.
- An analysis on the sensitivity of the front geometry and pseudo relative curves on the permeability ratio for a given pattern.
- A study on the influence of the density and geometry of heterogeneity on pseudo-relative curves and fractional flow functions has also been performed.

D-1. Simulated simple Layer Patterns and Fracture Systems: saturation evolution and pseudo curves

1- Simple layers geometries

The case of an individual layer spanning the entire system has first been investigated. Several configuration have been study:

- Layer acting as a preferential path and as a barrier.
- Flow parallel and perpendicular to the layer.
- Homogeneous and heterogeneous matrix.

1-1 Type of heterogeneity

(a)- Saturation field and time evolution

The fractures have successively been considered as a preferential path for the flow and as a barrier. The permeability of the matrix is respectively 0.005 and 1 darcy (see Table 3 - sectionC-2). The area is 1x1 m and the matrix is homogeneous.

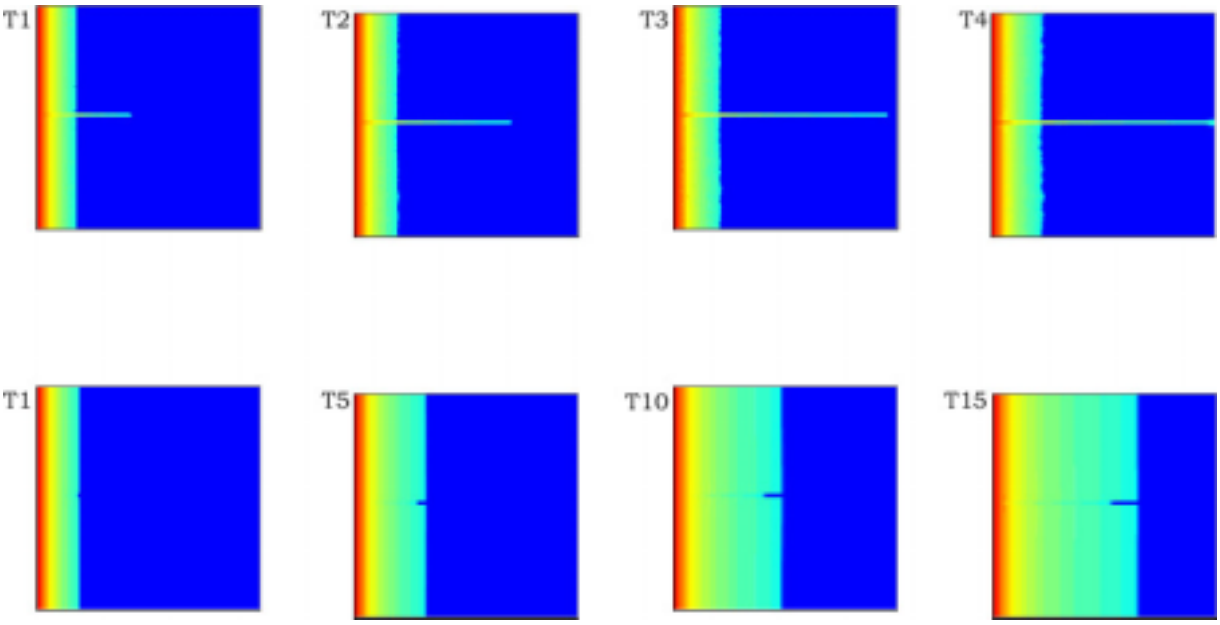

Figure 26: snapshot of the CO_2 saturation for 4 different time step. (Top) layer act as a preferential path for injected CO_2 and (bottom) as a barrier. Permeability ratios are respectively equal to 16.8 and 2.1 10^{-4}.

The time step for both experiments is similar. Simulations indicate that the connection between the left and right part of the models is much faster when the layer acts as a preferential path, between T3 and

T4 (Figure 26). Even when the permeability ratio is not very important[5], the flux remains localised into the fracture during the first steps and no diffusion between the layer and the matrix occurred.

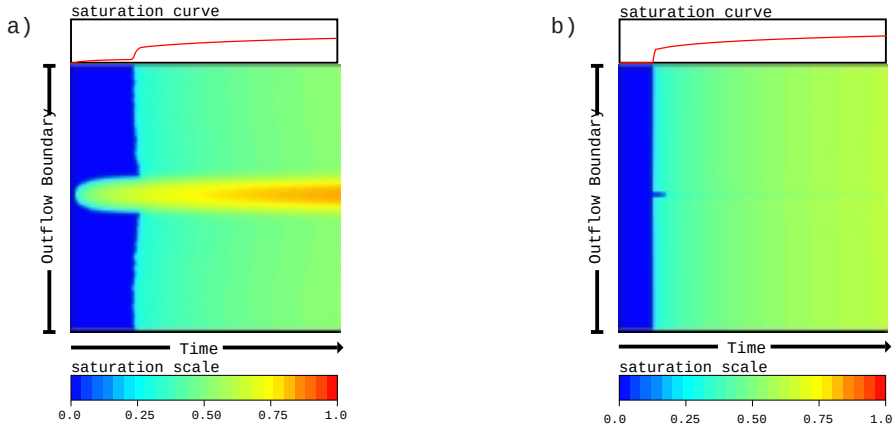

Figure 27: Saturation evolution plot showing the change in the saturation at the outflow boundary with time for the pattern SG1 (see section C-2). (a) layer act as a preferential path for injected CO_2 and (b) as a barrier.

Figure 27 gives indications on the saturation at the outflow boundary at each considered time step. If the presence of a preferential path modify the transport of CO2, the presence of a barrier does not affect dramatically the saturation evolution. Indeed, for this latest case (case b) the front remains nearly planar during all the simulation. On contrary, when R_k>1 (case a) we observe a depression in the central part where the layer is present and where exchange between the layer and the matrix takes place. Also saturation in CO_2 reach rapidly its maximum in the layer.

(b)- Pseudo relative curves

For each case, the pseudo relative and fractional flow curves have been determined (Figure 28). The fractional flow curve (FFF) shows the fraction of CO_2 arriving at the outflow boundary plotted against the average CO_2 saturation for the whole model region. If the behaviour of the FFF curves is similar and cannot be distinguish for saturation greater than 0.40, for smaller saturation it presents two different evolution (Figure 28a). In the case of layer acting as a barrier, the FFF is similar to that of the matrix alone and is null for S<0.40. On contrary, when layer act as a preferential path, the FFF differs nearly instantaneously from 0 and we observe a continuous increase. This implies that as soon as the injection of CO_2 has been initiated, the CO_2 starts to be mobile. This early mobility is associated to the saturation inside the heterogeneity as observed on Figure 26. For S~0.40, we observe an abrupt modification in the FFF value. This should be related to the matrix saturation as illustrated by the same observe jump in FFF value in the case of matrix alone.

When the layer act as a barrier, the FFF curve is similar to that of the matrix indicating that although the permeability contrast is ~10^{-4}, it is the matrix that control the saturation evolution *i.e.* the heterogeneity plays a minor role.

[5] in the case of preferential path, the permeability contrast is R_k=16.8

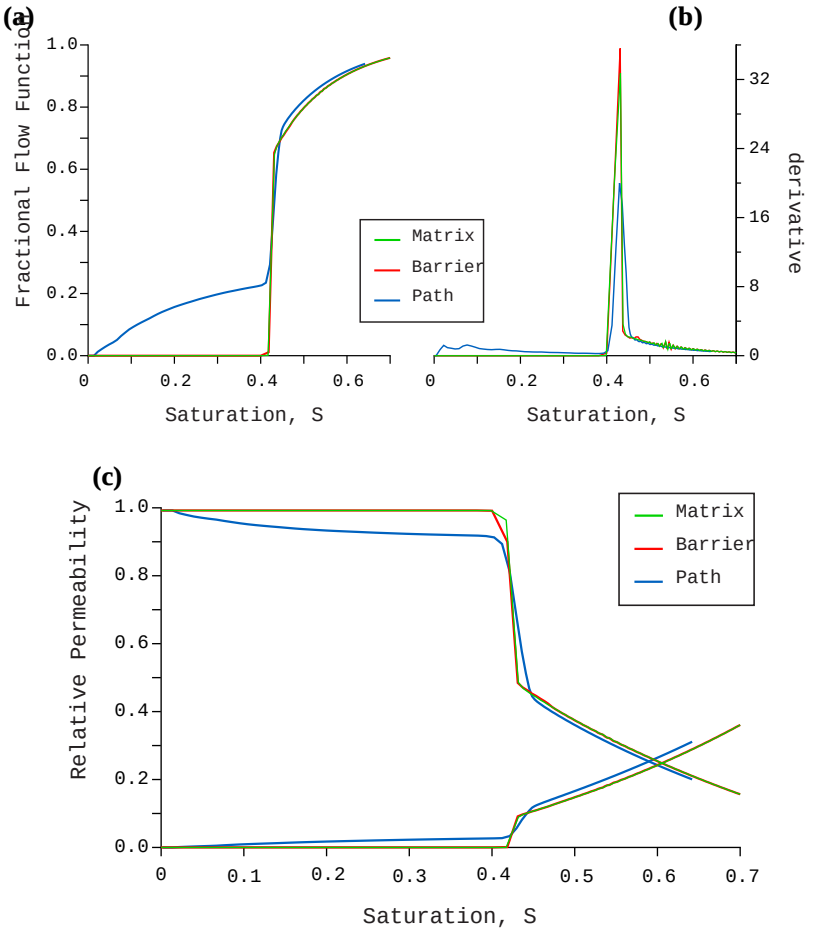

Figure 28: Comparison of the relative permeability curves, the fractional flow functions and its derivative, determined for the simulations shown above.

The derivative of the fractional flow curve (Figure 28b) corresponds to the velocity of the front with respect to the saturation and expresses the observed variation of the FFF curves. For both cases, an important and narrow peak takes place for saturation close to 0.45. The amplitude differs slightly and is larger in the case of the layer acting as a barrier. This suggests that the front velocity is more important in that case. Also, in the case of preferential path, we observe for low saturation (S<0.2) a small increase and decrease of $dFFF/dS$ associated to the saturation of the layer.

The general shape of the pseudo curves for path and barrier differs essentially in the very first step of the saturation history. As observe previously, the irreducible CO_2 saturation is smaller in the case of path, indicating that the injected fluid is already mobile. This mobility increases with the saturation leading to a modification in the slope of the pseudo-curves. The pseudo curves for the matrix and barrier cases are similar. The cross over saturation is the same in the case of matrix and barrier, and is slightly less important when layer behaves as a path.

1-2 Flow orientation and matrix heterogeneity

We have realised several simulations using simple geometry to determine how the orientation of the flow with respect to the layers influences the saturation evolution. Also we consider the case of a flow perpendicular to the sedimentary structures and a heterogeneous matrix (see Table 3- section C-2). Here we presents snapshots, time evolution and pseudo curves for the case of *'en echelon'* layers only; the other studied geometry giving similar results. This *en echelon* array is made of three discontinuous layers having the same length equals to 1/3 of the system size. Figure 29 shows four saturation field in

the case of *(i)* flow parallel and *(ii)* perpendicular to the layers for a homogeneous matrix permeability field and *(iii)* flow perpendicular to the layer with a heterogeneous matrix permeability field.

(a)- Saturation evolution

Whatever the orientation of the structures, the saturation front is roughly at the same position for the three cases. Small perturbations are locally observed that correspond to heterogeneity. However, this does not affect the global saturation. In the case of heterogeneous matrix the front is no more planar but presents small-scale fingering. When comparing the saturation field observed at T15 in the case of perpendicular flow, we observe that this small fingering hide the presence of heterogeneity.

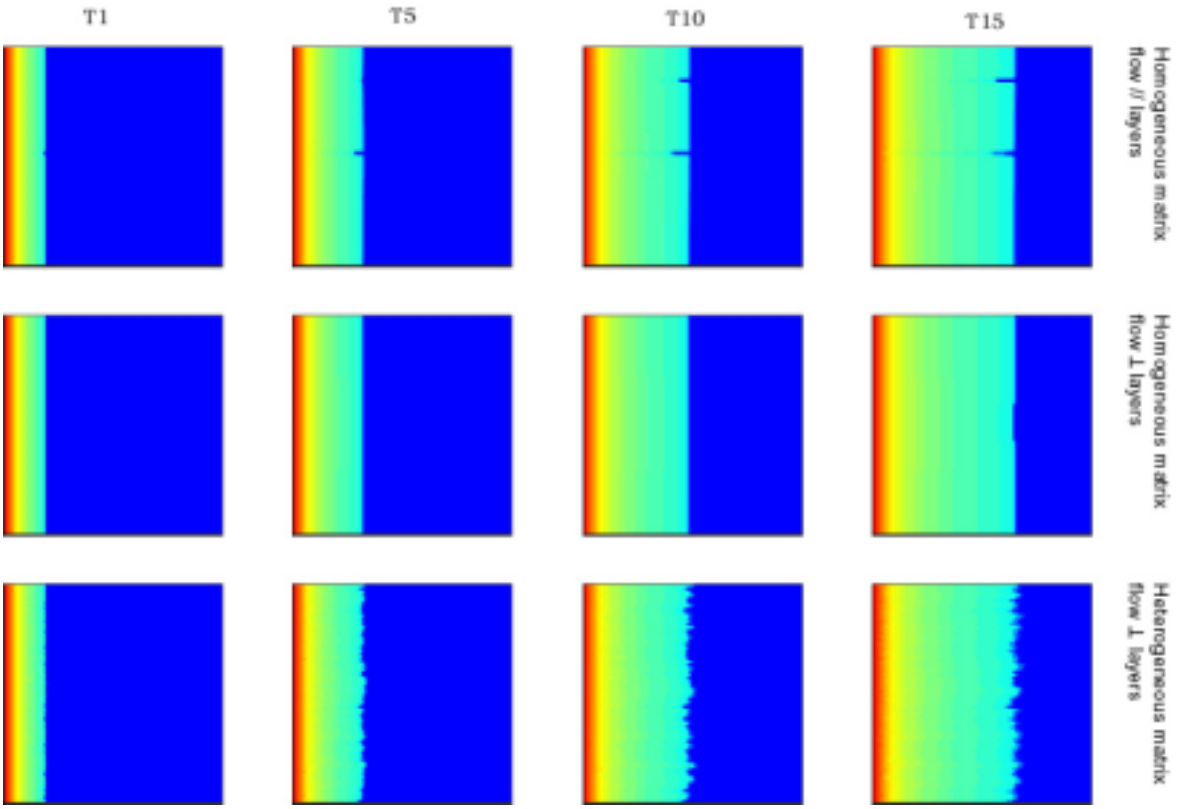

Figure 29: Four different saturation field observed at instant T1, T5, T10 and T15. (Top row) homogeneous matrix permeability field and flow parallel to layers. (Middle row) homogeneous matrix and flow perpendicular to the layers. (Bottom row) Heterogeneous matrix permeability field with flow perpendicular to the layers.

The saturation evolution represented Figure 30 displays the same general front geometry. No clear difference exists when flow is parallel or perpendicular. Assuming a heterogeneous permeability field for the matrix leads to the formation of small-scale perturbations. The saturation evolution curves are also similar in the three cases.

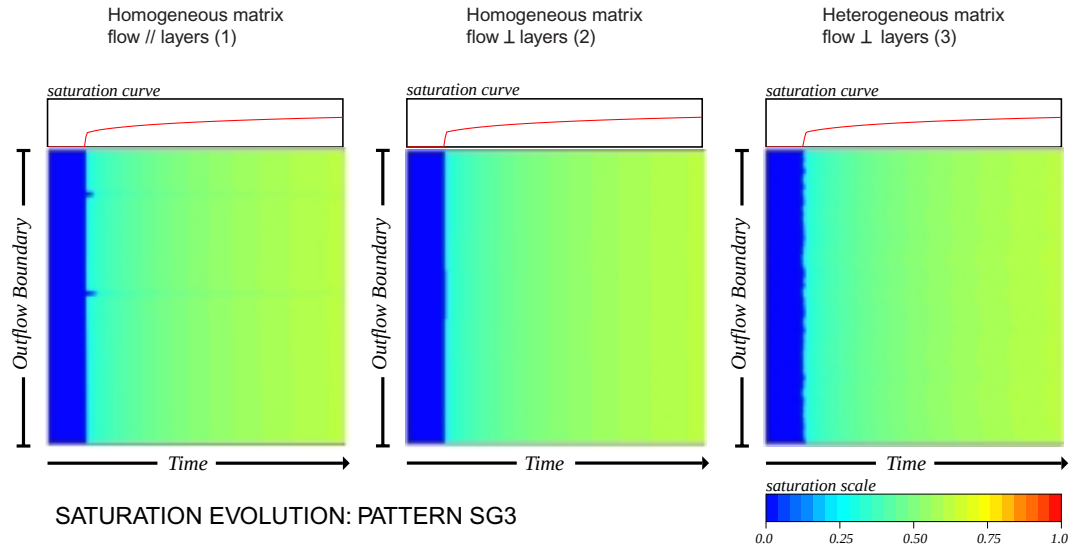

Figure 30: Time evolution of the saturation when the flow is parallel (left) and perpendicular (middle) to the layer with a homogeneous matrix (see Table 3- section C-2). On the right is the saturation evolution when the flow is perpendicular to the layers and the matrix heterogeneous.

(b)- Pseudo relative curves

The pseudo relative and fractional curves show no differences between the different study configuration. The three different curves, corresponding to the cases shown above, are superposed (Figure 31). Therefore, the orientation of the sedimentary structure with respect to the flow seems to be negligible when only a few layers acting as barriers are present.

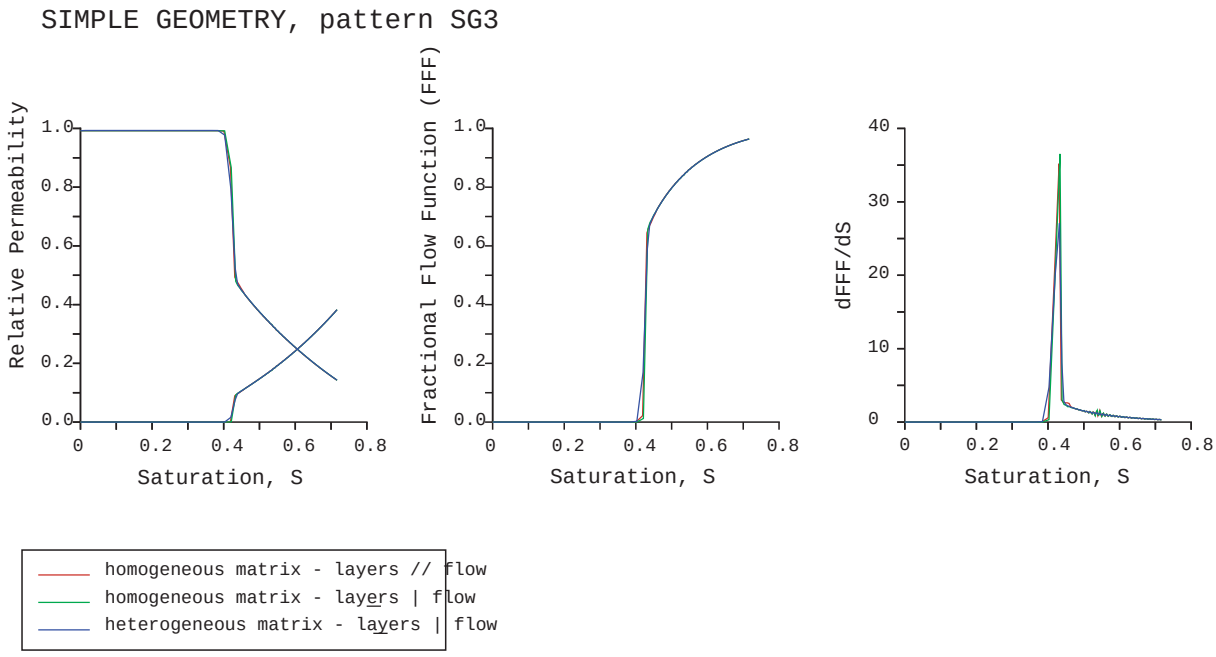

Figure 31: Relative permeability curves (left), fractional function (middle) and its derivative (right) calculated in the three different cases shown on Figure 30.

2- Constant length fractures

2-1 Multiple Parallel fractures

(a)- Variable density

Four simulations with fracture densities of 0.5, 1.0, 2.0 and 3.0 m / m2 (corresponding to 28, 59, 121 and 183 fractures in the 10x10 m region) with constant aperture at 50 μm were run and the results presented in Figure 32. The permeability contrast between fracture and matrix cells is around 2 orders of magnitude. The flow evolution plot (Figure 32) shows early arrivals at places where fractures meet the outflow boundary and also where fast routes via fractures favours early arrival. The fracture system is unconnected so no continuous paths exist across the modelled region through the fracture network. However, because the matrix is permeable, large pressure gradient are generated between fractures that are close to each over. In this way the fractures generate fast flow path across the region even though fractures are discontinuous. Comparing the flow evolution plots for densities of $1m/m^2$ and $3m/m^2$ (Figure 32) shows that the increase fracture density leads in an increase in the time interval over which the combination of oil and water arrive at the outflow boundary[6]. This is reflected in water saturations curves which show a shallower slope for the higher fracture densities.

The fractional flow curves are compared to that for matrix alone in Figure 32. These curves show the fraction of water arriving at the outflow boundary plotted against the average water saturation for the whole model region. The curve for a homogeneous matrix shows a very steep curve which reflect the arrival of the shock at the outflow boundary. The plot shows that the main effect of fractures is to lower the slope of the curve and shift them to the left reflecting the earlier initial arrival of water and the increased time interval over which both water and oil arrive at the outflow boundary. The pseudo curves (Figure 32) show similar characteristics with a shallowing of the slope relative to that of the matrix only and a progressive shifting of the curves towards lower saturations. However as density increases, slope begin to increase again, showing that the system is tending toward that of homogeneous matrix but with a lower shock saturation. The point where the curve for relative permeabilities of oil and water cross remains at a constant relative permeability value but moves toward lower saturations with increasing fracture density.

(b)- Variable aperture

The parallel fracture pattern with a fracture density of $1m/m^2$ (59 fractures) and a matrix permeability of 2*mD* was run for six different fracture apertures (10, 15, 20, 50, 75 and 100 microns). This represents permeability contrasts in the model up to three orders of magnitude (Table 12). Comparing the flow evolution plots for aperture of 10 and 100 microns (Figure 33) shows that at 10 μm the form of the shock front for a homogeneous matrix is still recognisable, modified by many small indentations as the spaces between fractures still contains oil. In the flow evolution plot of 100 μm apertures, this pattern is no longer discernible as arrival of water at the outflow boundary is spread over a longer time interval.

Apertures (μm)	10	15	20	50	75	100
Fracture/matrix permeability Ratio	$4.22\ 10^3$	$9.49\ 10^3$	$1.68\ 10^4$	$1.05\ 10^5$	$2.37\ 10^5$	$4.22\ 10^5$

Table 12: permeability ratio corresponding to the various apertures used in the multiple parallel fracture patterns.

[6] In that particulars case the invading fluid (water) has a lower viscosity than the defending fluid (oil). The viscosity ratio is 1/2.

The fractional flow curve for apertures of 10 μm (Figure 33) mimics that for a homogeneous matrix for part of its length but at lower water saturation, showing that the shock has maintained something of its original form in a homogeneous matrix but been translated to lower saturations. The curves for larger apertures show that this characteristic disappears and is replaced by shallower slopes. In addition, the intersection point between the relative permeability curve for oil and water migrate to the left with increasing aperture. It can be seen, however, that for aperture greater than 50 μm, increasing aperture does not produce major changes in the pseudo curves. At these large apertures, the permeable matrix becomes the limiting factor for flow and larger apertures do not produce significantly larger flow rates.

2-2 Diagonal and orthogonal fractures

The second fracture pattern simulation investigated consists of two sets of perpendicular constant length fractures oriented at 45° to the flow direction (diagonal fracture patterns) and parallel to it (orthogonal fracture patterns). The patterns are presented Figure 17 - section C-2. Numerical experiments were conducted to investigate the effect of fracture density and fracture aperture.

Figure 32: Simulations of two-phase flow in permeable regions with variable densities of parallel fractures. Above - flow evolution plots of fractured regions at densities of 1m/m² (left) and 3m/m² (right). Fracture aperture is 50 μm and the matrix permeability is 2 mD. Below left - fractional flow curves from fracture densities of 0.5 to 3 m/m². Below right - pseudo relative permeability curves for the fracture densities of 0.5 to 3 m/m².

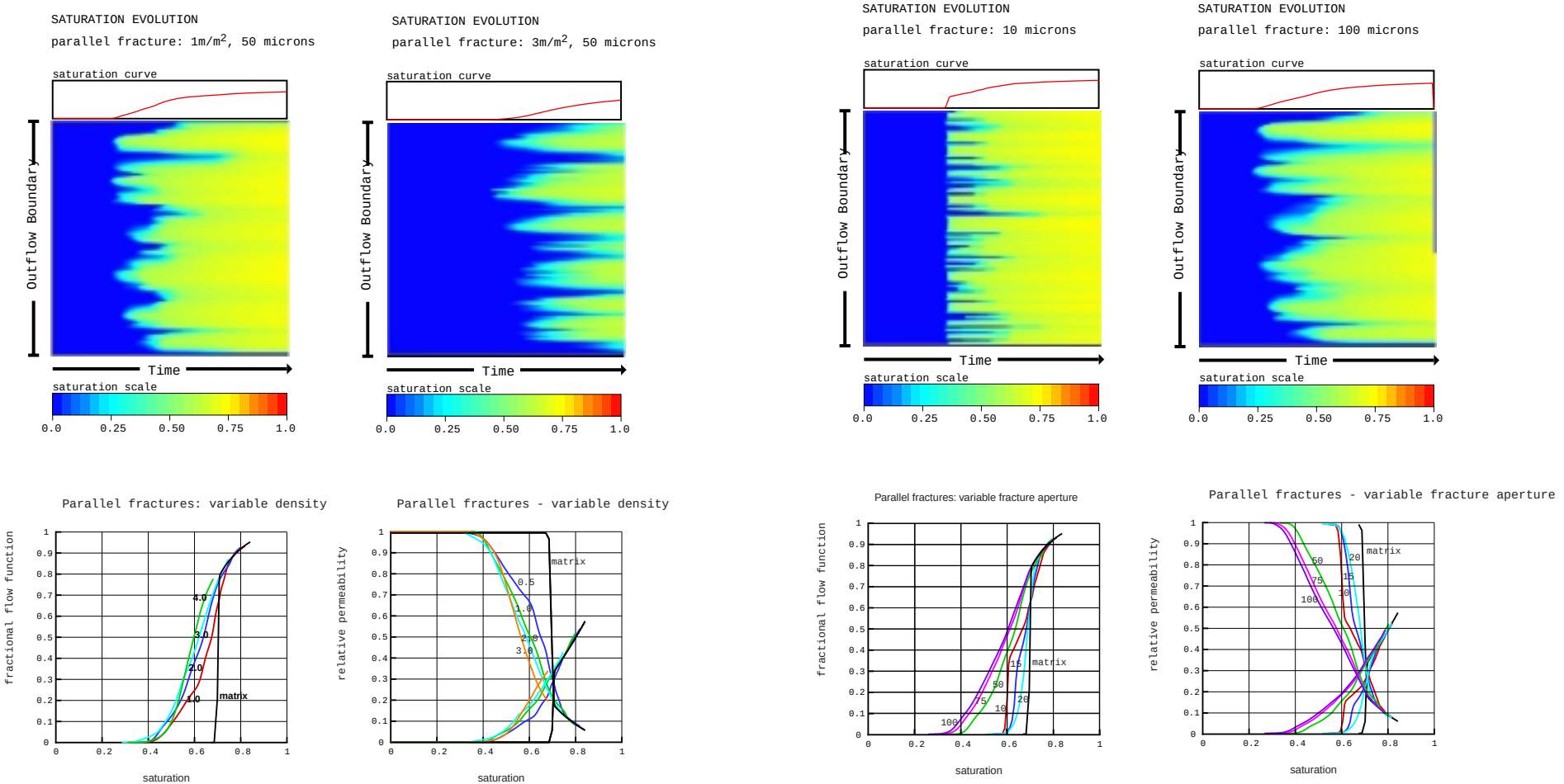

Figure 33: Simulations of two-phase flow in permeable regions with parallel fractures of variable aperture. Above - flow evolution plots of fractured regions at apertures of 10 μm (left) and 100 μm (right). Fracture density is 1m/m² and the matrix permeability is 2 mD. Below left - fractional flow curves from fracture apertures of 10 to 100 μm. Below right - pseudo relative permeability curves for fracture apertures of 10 to 100 μm.

(a)- Diagonal fracture patterns

- Variable density

Simulations with fracture densities from 1 to 5 m/m^2, in $1m/m^2$ intervals were run. Patterns were unconnected below and including a density of $3m/m^2$. The flow evolution plot (fig. B-1-8) show similar characteristics to that of parallel fracture pattern, but not as extreme, so that the slope of the water saturation curve with time is steeper, indicating less smearing of the oil/water front. The fractional flow curves show shallower slopes than the homogeneous matrix for all fracture densities. However the slope is shallowest for a density of $2m/m^2$ and steepens again for greater fracture densities. This indicates that the matrix and fracture system at densities greater than $2m/m^2$ is tending toward the behaviour of a homogeneous matrix but with a lower shock saturation. This behaviour is also reflected in the pseudo curves (Figure 34). As in the case of the parallel fracture patterns, the intersection of the pseudo curves for oil and water maintain their relative permeability value but migrates to lower saturations.

- Variable aperture

Simulation with apertures of 10, 15, 20, 50, 75 and 100 mm were run. The flow evolution plot shows that at 10 μm the picture is only slightly different from that of a homogeneous matrix while at 100 μm, the oil/water contact is smeared out with oil and water arriving at the outflow boundary simultaneously overlarge time intervals. The fractional flow and pseudo curves show a simple and consistent pattern of shallower slopes with increasing aperture. The curve for 10, 15, and 20 mm lie almost on top of each over showing that the effects occurring in the parallel fracture pattern at these aperture have been reduced by the presence of two sets of fracture orientations. As before, the intersection of the pseudo curves for oil and water maintain the relative permeability value but migrate with increasing density to lower saturations.

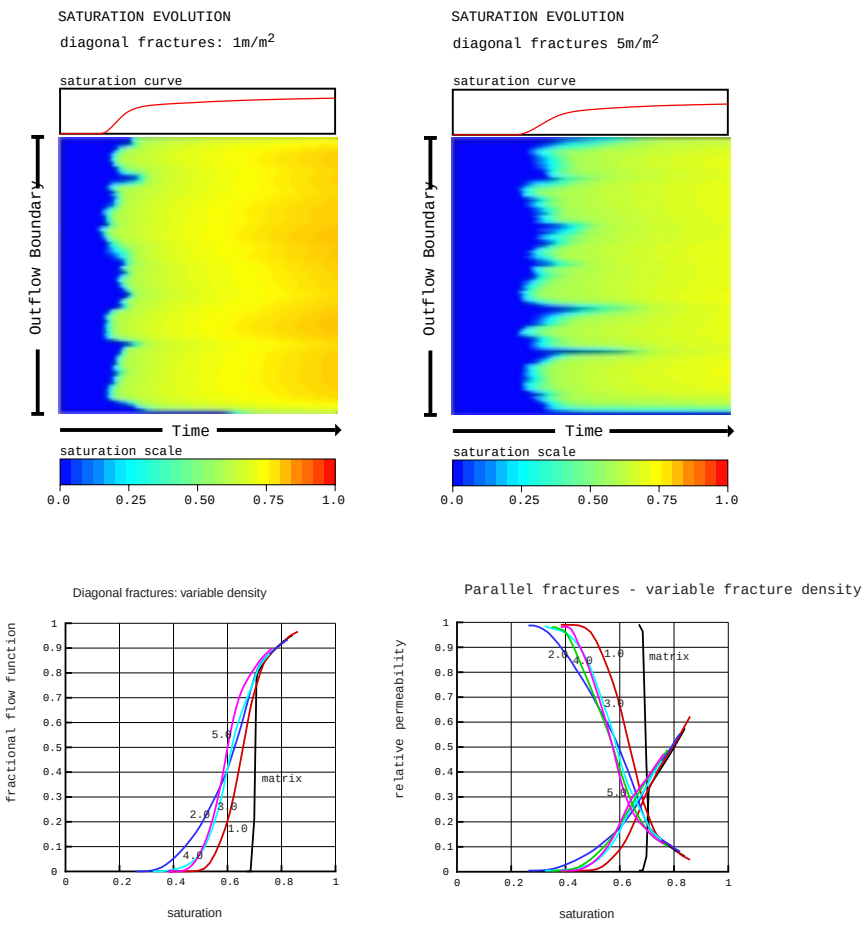

Figure 34: Simulations of two-phase flow in permeable regions with variable densities of diagonal fractures. Above - flow evolution plots of fractured regions at densities of 1m/m² (left) and 5m/m² (right). Fracture aperture is 50 μm and the matrix permeability is 2 mD. Below left - fractional flow curves from fracture densities of 1 to 5 m/m². Below right - pseudo relative permeability curves for the fracture densities of 1 to 5 m/m².

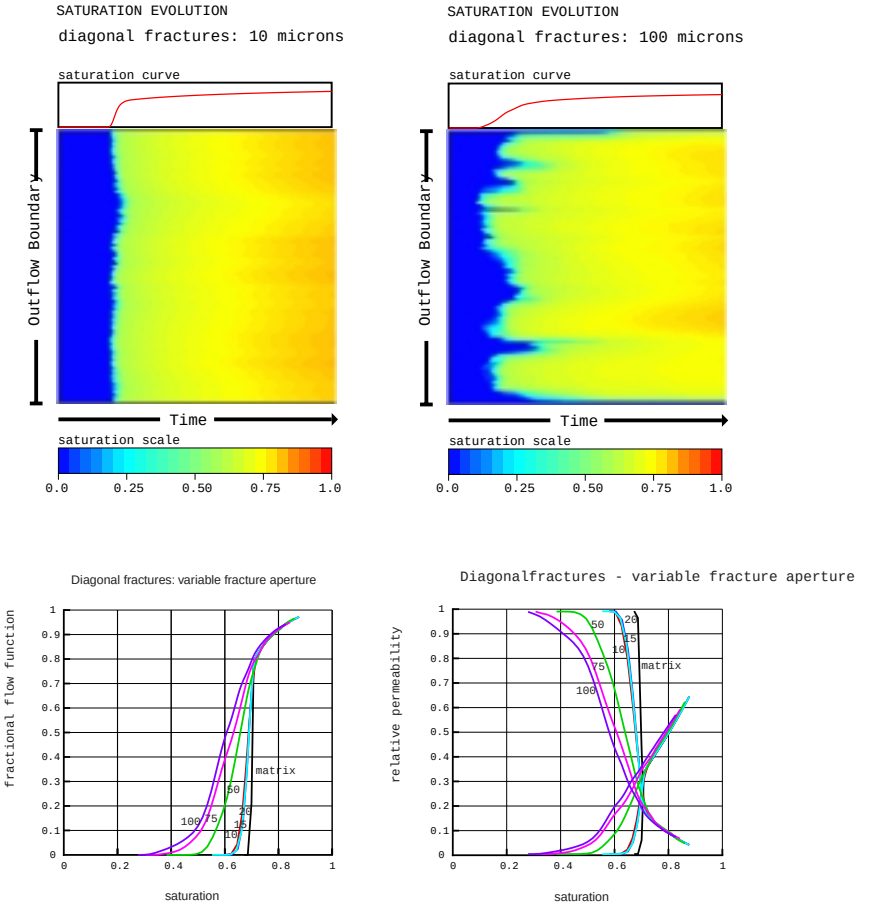

Figure 35: Simulations of two-phase flow in permeable regions with diagonal fractures of variable aperture. Above - flow evolution plots of fractured regions at apertures of 10 μm (left) and 100 μm (right). Fracture density is 1m/m² and the matrix permeability is 2 mD. Below left - fractional flow curves from fracture apertures of 10 to 100 μm. Below right - pseudo relative permeability curves for fracture apertures of 10 to 100 μm.

- Variable area

To test the effect of the area modelled, different areas containing the diagonal fracture pattern at 1m / m2 and an aperture of 50 mm were run. These models represents area of dimension 5, 10 and 50m which contain 19, 64 and 1329 fractures respectively. The results in Figure 36 show that with decreasing area, the fractional flow curves and the pseudo relative curves become shallower and more irregulars. For the smaller area, the fractures have lengths comparable to the model size. These transport water rapidly across the model leading to early breakthrough at the outflow boundary. The mixture of long fractures, parts of fractures in the modelled region and permeable matrix results in irregular slopes as these elements have contrasting effects on the flow of water. The largest area modelled (50m) has many more fractures all of which are short compared to the modelled area. Here the behaviour shown by the fractional flow and pseudo relative curves is closer to an homogeneous medium. As the modelled area size increases, the intersection between the pseudo curves for water and oil occurs at progressively lower saturations. This indicates that the behaviour of the system is approaching that of homogeneous medium but with shock saturation lower that the matrix only case.

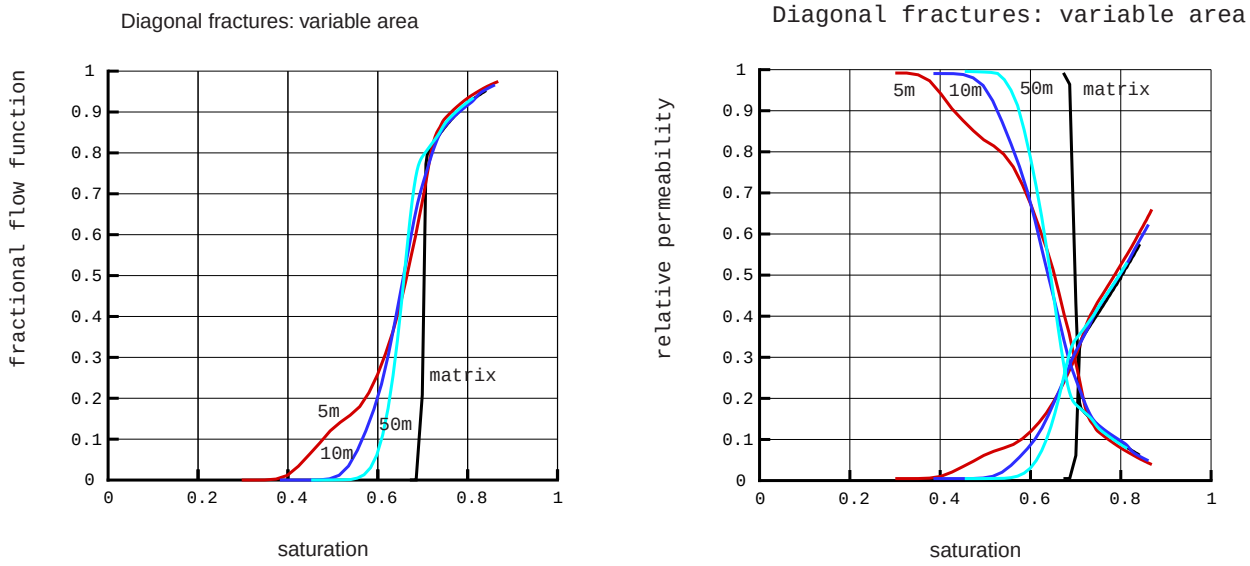

Figure 36: fractional flow and pseudo relative curves for three different area sizes, 5, 10 and 50 m.

(b)- Orthogonal fracture

To test the influence of fracture orientation, a second fracture pattern type with two orientation sets were generated, but this time with one set parallel and the other perpendicular to the flow direction (Figure 17). As in the case of diagonal fracture patterns, densities ranging from 1 to 5 m / m^2, in 1 m / m^2 intervals, and apertures of 10, 15, 20, 50, 75 and 100 µm were run.

The flow evolution plots, fractional flow function and pseudo curves show behaviour intermediate between the parallel and the diagonal fracture pattern (Figure 37 and Figure 38). In common with the parallel fracture pattern, pseudo curves for fracture apertures of 10, 15 and 20 mm migrate to the right slightly with increasing aperture, but are smoother that the equivalent curves for the parallel fracture pattern (**Fig, b11**). In common with the diagonal fracture pattern, increasing apertures beyond 50 µm produces only small changes in the pseudo curves. In common with the diagonal fracture pattern, increasing fracture density beyond 2m / m^2 produces a steepening of the pseudo curves (**figb1-10**), showing that their behaviour is tending that of a homogeneous medium but with a lower shock saturation.

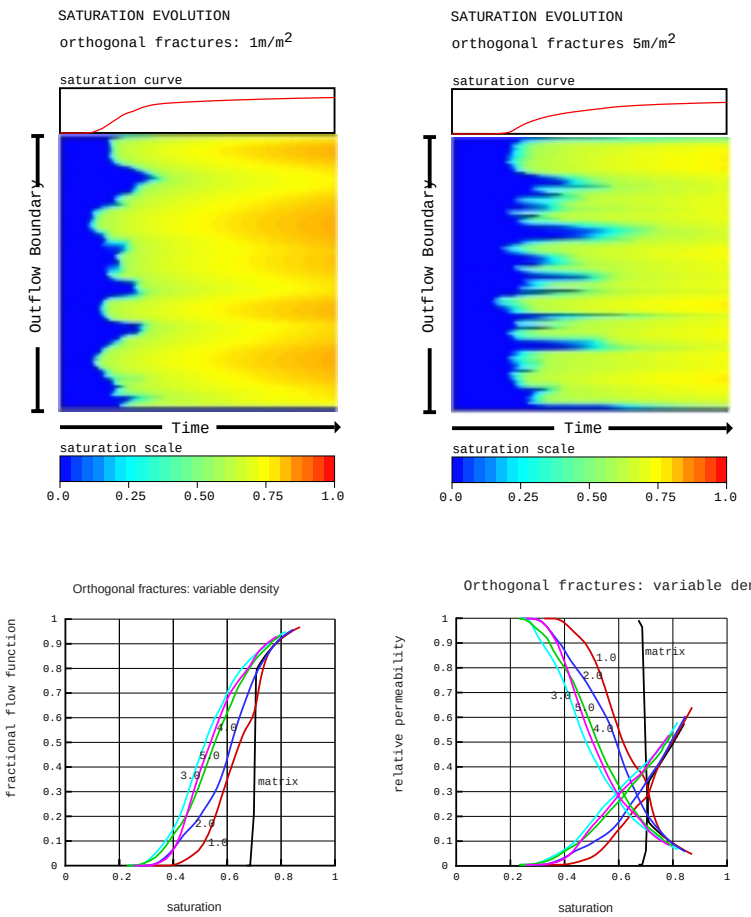

Figure 37: Simulations of two-phase flow in permeable regions with variable densities of orthogonal fractures. Above - flow evolution plots of fractured regions at densities of 1m/m² (left) and 5m/m² (right). Fracture aperture is 50 μm and the matrix permeability is 2 mD. Below left - fractional flow curves from fracture densities of 1 to 5 m/m². Below right - pseudo relative permeability curves for the fracture densities of 1 to 5 m/m².

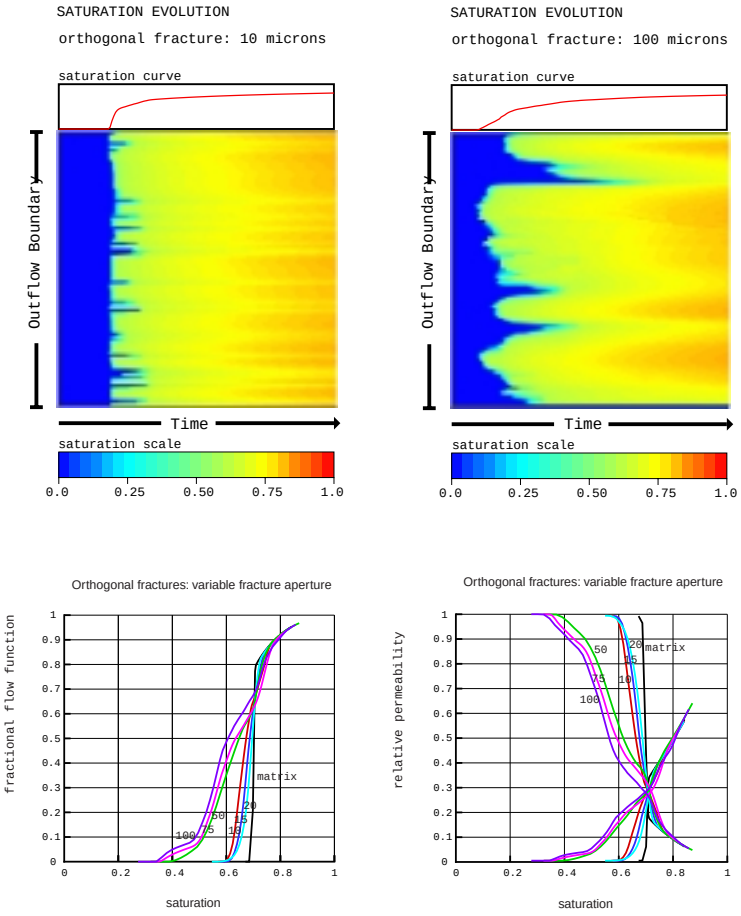

Figure 38: Simulations of two-phase flow in permeable regions with orthogonal fractures of variable aperture. Above - flow evolution plots of fractured regions at apertures of 10 μm (left) and 100 μm (right). Fracture density is 1 m/m² and the matrix permeability is 2 mD. Below left - fractional flow curves from fracture apertures of 10 to 100 μm. Below right - pseudo relative permeability curves for the fracture apertures of 10 to 100 μm.

3- Variable length fractures

3-1 Multiple parallel fractures

We have realised several simulations using parallel fractures with variable length. The patterns and permeability fields for a homogeneous matrix are shown Figure 16. Fractures are perpendicular to the flow direction and have length ranging between 5% to 100% of the system size. The fracture / matrix permeability ratio is equal to $2.1\ 10^{-4}$. The snapshots in Figure 39 shows the evolution of the saturation at four different time step.

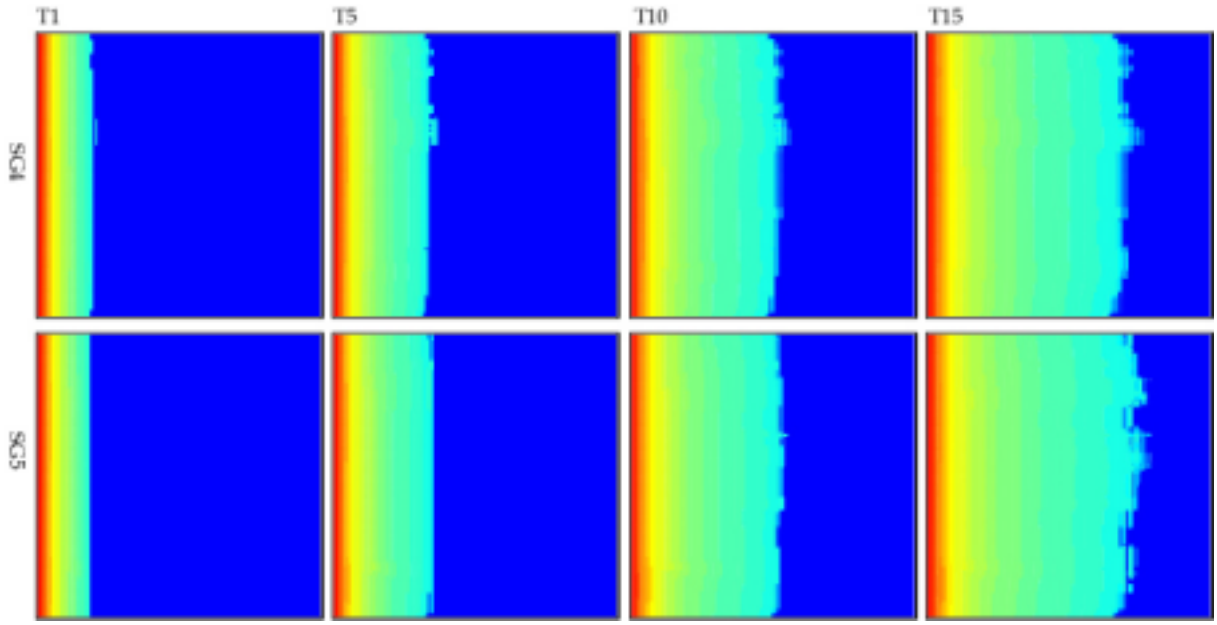

Figure 39: snapshot showing the saturation evolution of pattern SG4 and SG5 at four different time step. The flow is perpendicular to the fractures.

The front is linear in the first steps and irregularity of the front is developing with time. Nevertheless, we do not observe fingering or a strong heterogeneous front. This is essentially related to the presence of long fractures that have length close to the system size (see Figure 16).

We have also studied the influence of the orientation of the flow with respect to the fractures (Figure 40). The effect of fractures is much visible when flow is parallel to the structures. Fractures constitute channels inside which the invading fluid has difficulties to penetrate. Apart from it, the front is linear and no irregularity in the geometry is developing. Also, whatever the orientation of the inflow, the average front position remains the same.

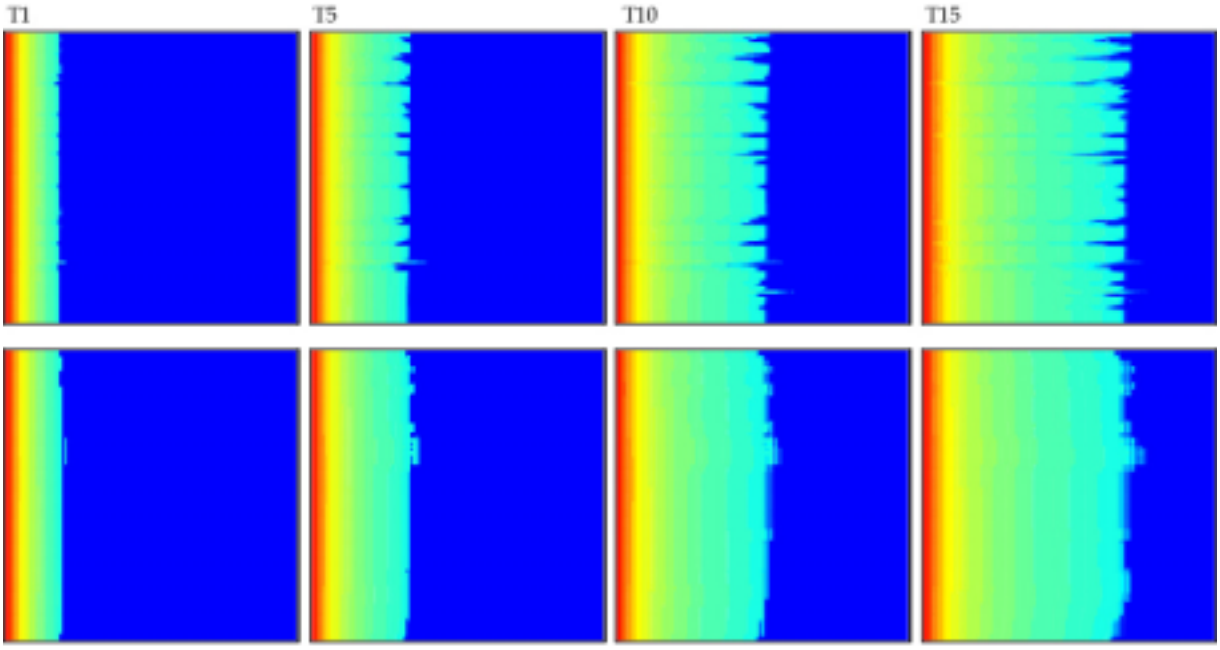

Figure 40: snapshots showing the saturation for the pattern SG4 when flow is parallel (top) and perpendicular to the fractures.

The time evolution of the saturation for patterns SG4 and SG5 is represented on Figure 41. In the case of parallel structures (left and middle), the front shows small fingering associated to the fractures and which indicates that saturation is delay at the outflow boundary. The saturation curves are similar for the two considered patterns SG4 and SG5. When fractures are perpendicular to the inflow, the front presents a planar geometry and the saturation curve shows a much more abrupt increase than in the case of parallel layers.

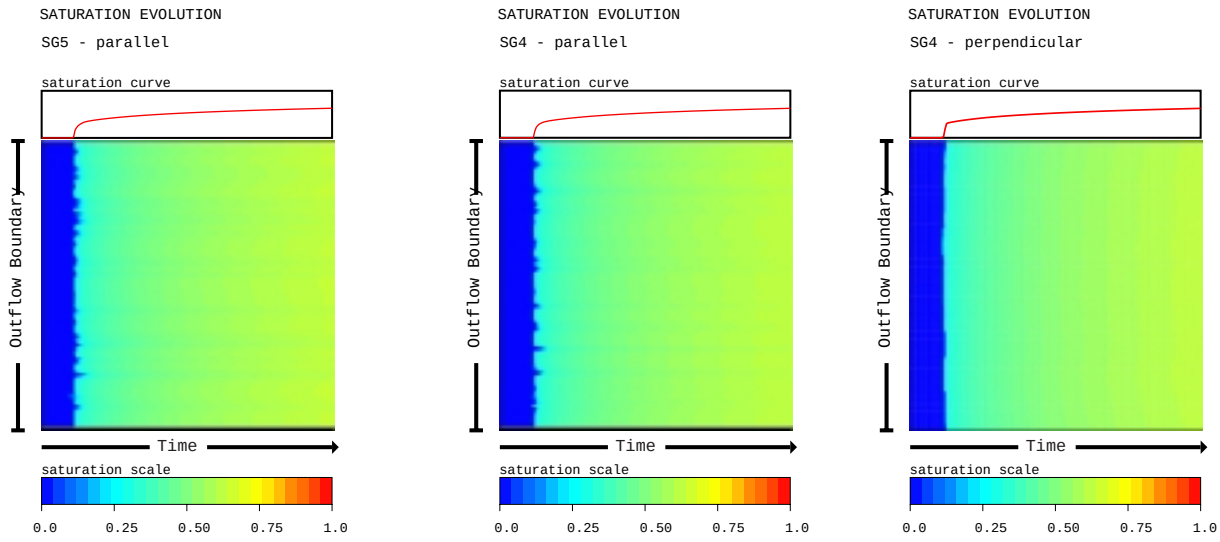

Figure 41: time plot showing the saturation at the outflow boundary for pattern SG4 and SG5 (respectively left and middle diagrams) when the flow is parallel to the structures. Also represent is the pattern SG4 when the flow is perpendicular to the fractures (right).

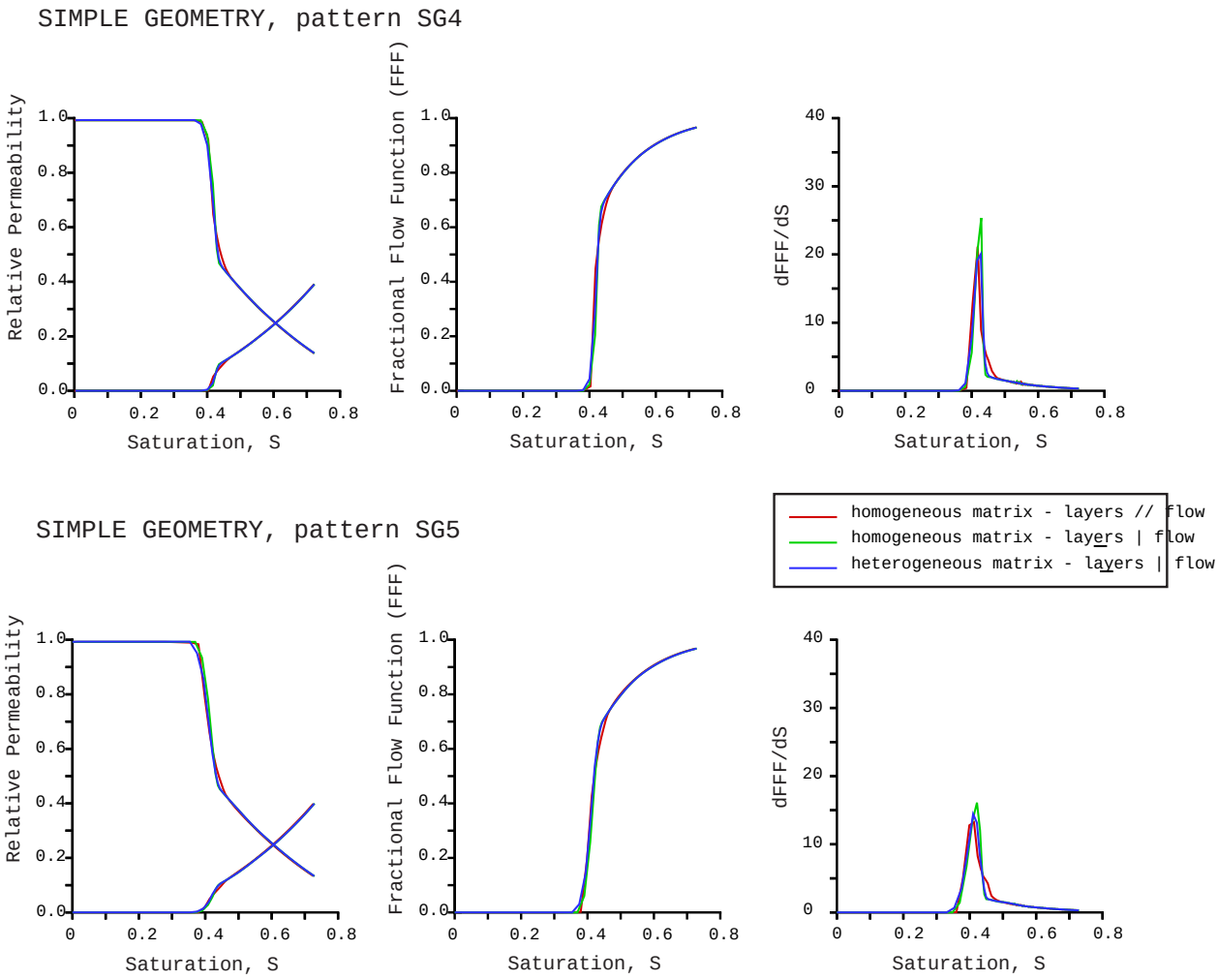

Figure 42: Pseudo relative (left), fractional flow function (middle) and its derivative (right) curves determined for patterns SG4 (top) and SG5 (bottom). In each case, three simulations are represented (see text).

The pseudo relative and fractional flow curves have been determined for the patterns SG4 and SG5. We have reported these curves, in the case of homogeneous matrix when fractures are parallel and perpendicular to the in flow and for a heterogeneous matrix with fractures perpendicular to the inflow (Figure 42). These three different cases do not show significant differences and pseudo relative, as fractional flow curves are similar. Furthermore, they appear to be close to the curves observed for the matrix alone (see Figure 28 for comparison), indicating that the heterogeneities do not affect the global behaviour of the system.

The derivative of the FFF curves reported shows amplitude less important than in the case of a single layer (see Figure 31 for comparison). The peak for the pattern SG5 is broader and presents lower amplitude than for SG4 (Figure 42-bottom right). This is related to the greater number of fractures in pattern SG5 and let us suggest that increasing the number of fractures (or similarly the density) decrease the shock velocity.

D-2. Complex turbidites geometry

1- Bulk rock permeability

A single phase flow model [*Odling and Webman*, 1991] was used to estimate the bulk permeability of the 7 cases above. The single phase flow model was run with Dirichlet boundary conditions (constant pressure) on two opposing boundaries and no flow conditions were imposed on the other boundaries. The global permeability of the entire area was calculated from Darcy's Law for single phase flow using the flow at the right hand model boundary. Ten estimates of global permeability in two perpendicular directions (parallel and perpendicular to layering) were made using 10 realizations of each case. These give accurate estimates of global permeability in the direction of the flow. In addition, for each realization the geometric mean (arithmetic mean of log permeability) of the all cell permeabilities was calculated. This is a method sometimes used to up-scale the permeability of a complex field, since it is computationally less intensive and therefore much quicker than direct flow modelling.

In Figure 43, the global permeabilities from the flow model are plotted against the geometric means of permeability. The true global permeabilities (estimated by the flow model) cover a range of 3 orders of magnitude, slightly less than the permeabilities range within each realization (up to 4 orders of magnitude). The geometric mean permeability is, of course, constant regardless of the orientation of flow. This results in differences between the geometric means and the flow model global permeabilities. For the cases of matrix only, cross-bedding and fluid escape structures there is little difference in global permeability parallel and perpendicular to the layering, and the geometric average gives a good estimate of global permeability. In all these cases, layering (bedding) does not present large contrasts in permeability. In the case of fluid escape structures, although thin layers of low permeability are present they are thin and discontinuous and thus produce only small effects on global permeability anisotropy.

However, where the layering displays frequent, large changes in permeability, there are large differences between global permeabilities parallel and perpendicular to bedding. This is shown by all the cases of turbidite sequences. For flow parallel to layering the high permeability layering dominates but for flow perpendicular to layering the low permeability layers dominate. Thus the geometric average, which is independent of orientation, underestimates global permeability parallel to layering and overestimated global permeability perpendicular to layering. These errors are 1-2 orders of magnitude and therefore significant and most pronounced for the direction perpendicular to layering. Global permeabilities parallel to layering for all turbidite models is similar regardless of layer continuity, but for the direction perpendicular to layering the difference between the flow model and geometric global permeabilities is greatest for continuous layering. In this case, flow is forced to go through the low permeability layers reducing global permeability.

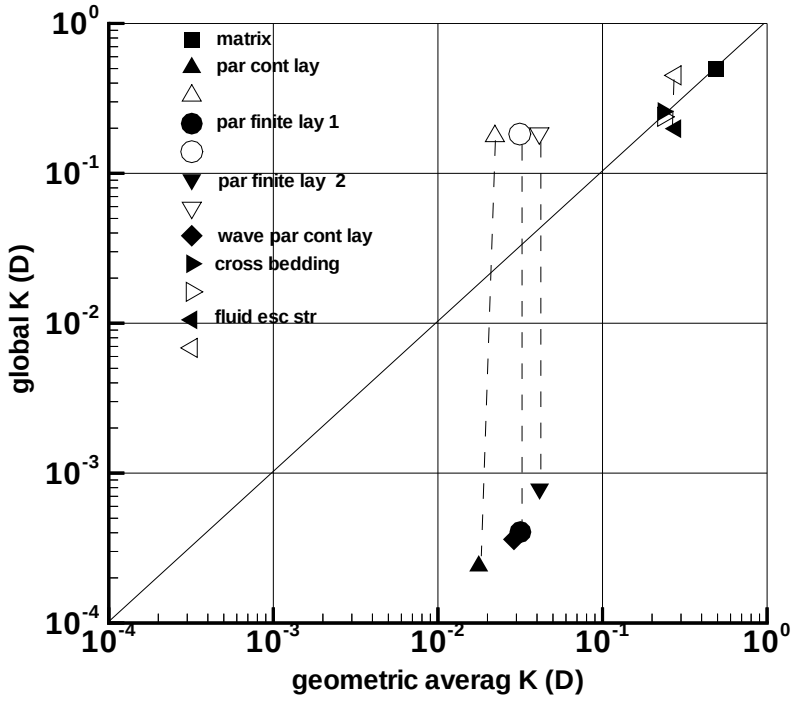

Figure 43: Global permeability determined using the flow model versus geometric mean permeability for the seven cases of sedimentary heterogeneity.

The results show that, for the cases where the layering does not represent large contrasts in permeability, the geometric mean of the permeability field gives a reasonable estimate of the global permeability. However, in the case where there is marked permeability layering, the geometric mean of the permeability field strongly overestimates global permeability perpendicular, and underestimates global permeability parallel, to layering.

2- Saturation field evolution

For each of the cases, a single realization was used to create a series of 6 snapshots to visualize the evolution of the flow field and CO_2 distribution. This was done using 'edge' injection (inflow along one side of the model).

The case of matrix only (Figure 44) shows a simple picture of the CO_2-water front moving as a line parallel to the injection edge across the modelled area. The random variations in permeability of one half order of magnitude cause small scale fingering that is most evident in the last snapshot. Due to the high viscosity ratio, the front is highly smeared out with most of the model in the last snapshot having saturation of less then 0.5.

The case of continuous parallel turbidite layers (Figure 44 (b)) shows a very similar picture to the matrix only case. This is because the layering is perfectly parallel, perpendicular to the pressure gradient. However, for the two cases of discontinuous layering (Figure 44 (c) and (d)) there are marked changes with highly complex saturation fields developing as the injected CO_2 flows round the low permeability shale layers. This produces large contrasts in saturation with areas of trapped water where flow rates are very slow and thin tongues of CO_2 reaching out into the water saturated region.

The two cases of perturbed layering (Figure 44 (e) and (f)) show that even small deviations from perfectly planar and parallel layering have significant effects on the flow patterns. The 'high' points or anticlines in the perturbations are places of preferential flow and the 'corners' where there are steps in the layering give rise to secondary tongues of increase CO_2 saturation. These effects increase as the CO_2 front moves through the model area being magnified at each low permeability layer crossed. The geometry of the perturbations is reflected in the frequency and the spacing of the CO_2 tongues as is seen by comparing the two examples.

The case of cross-bedding (Figure 44 (g)) is similar to the case of matrix only in that the CO_2 front advances as an approximately straight line perpendicular to the pressure gradient. However, the fingering effects are enhanced compared to the matrix only case. The effect of the different directions of cross-beds is seen in the thick bed near the base of the model but these effects appear to average out over the rest of the model to produce fingering parallel to the pressure gradient.

The case of fluid escape structures (Figure 44 (h)) show the most complex saturation field of all the models. The thin dish structures act as discontinuous flow barriers so this case resembles, in part, the discontinuous turbidite sequence case but with shorter low permeability layers. The fluid escape pipes form pathways of high flow which generated small CO_2 plumes at their low pressure ends. As CO_2 flows round the dish structures and along the fluid escape pipes, it leaves areas of high water saturation trapped behind the front creating highly complex and variable saturation fields.

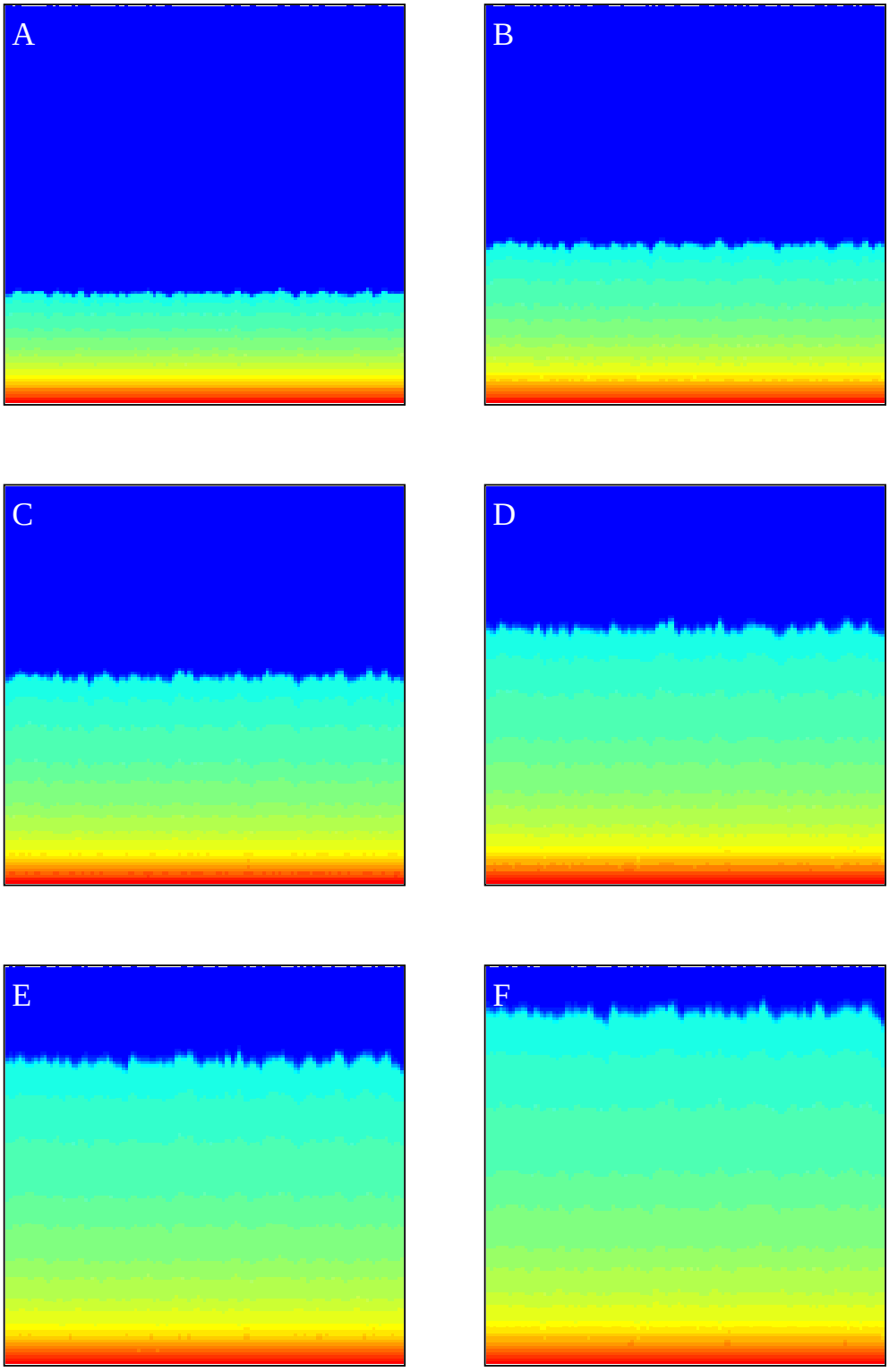

Figure 44(a): Snapshots of supercritical CO_2 and water flow in a region of homogeneous sands. The sand has a permeability of 0.1D and a standard deviation of log K of 0.1. CO_2 is injected along the bottom edge of the model which is initially water saturated. The modelled region is 38 by 38m. Boundary conditions are constant flow top and bottom and no flow conditions imposed right and left.

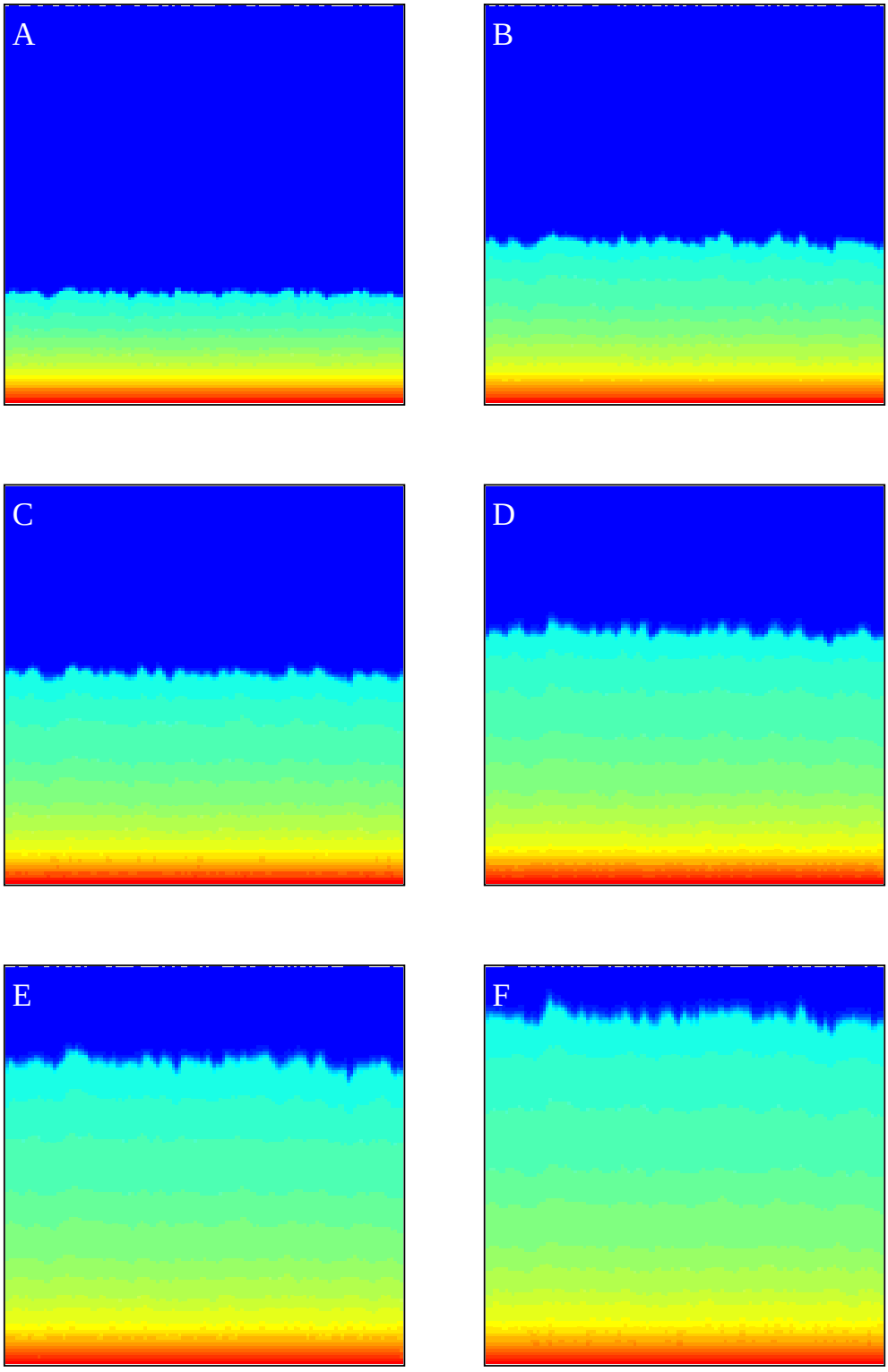

Figure 44 (b): Snapshots of supercritical CO_2 and water flow in a region of turbidite beds with parallel, continuous layering. CO2 is injected along the bottom edge of the model which initially water saturated. The modelled region is 38 by 38m. Constant flow boundary conditions with flow from bottom to top and no flow conditions imposed right and left. The saturation pattern resembles that of homogeneous sandstone.

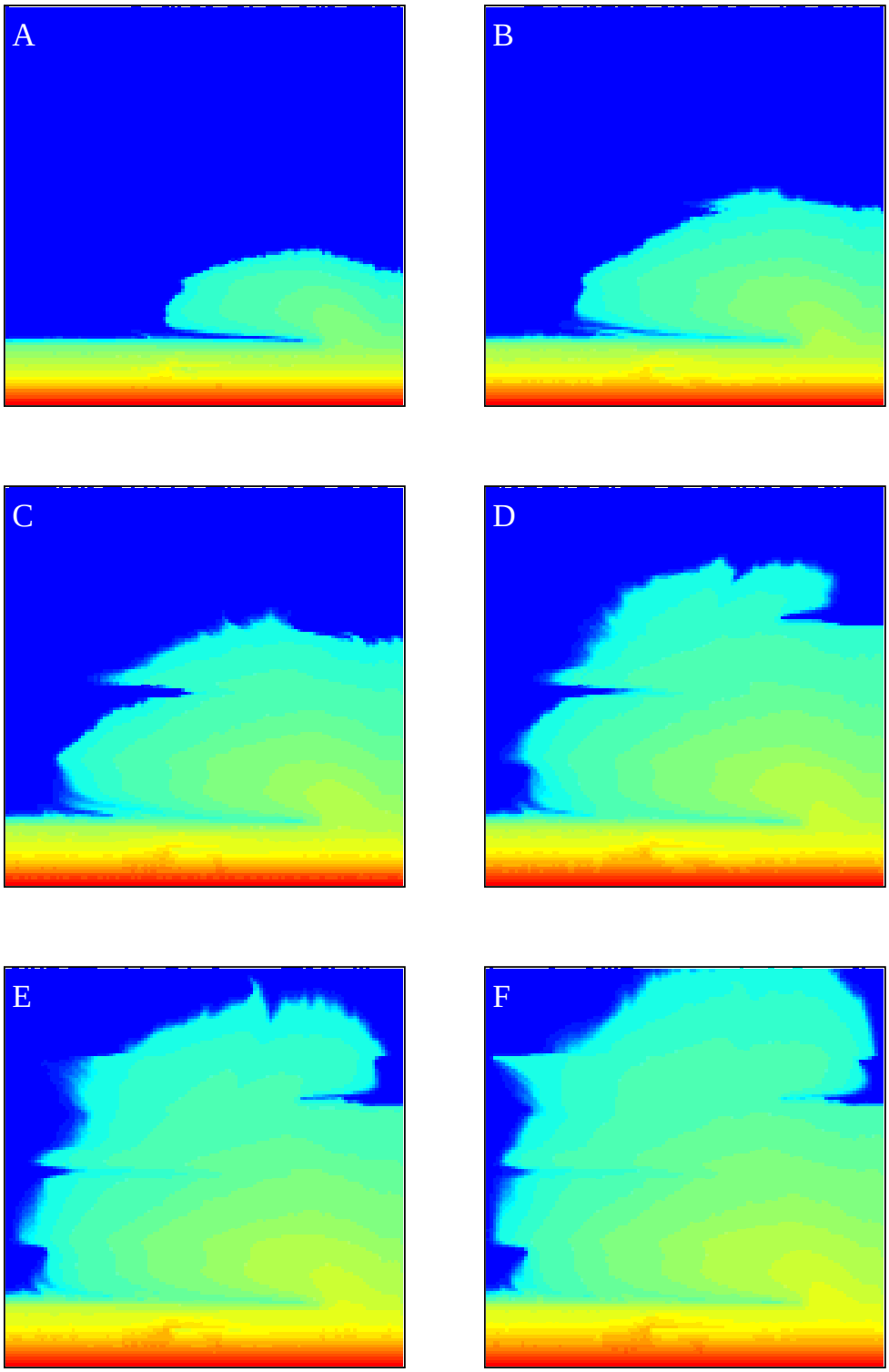

Figure 44 (c): Snapshots of supercritical CO_2 and water flow in a region of turbidite beds with parallel, discontinuous layering, with shale layers around 40m long. The modelled region is 38 by 38m. CO_2 is injected along the bottom edge of the model which is initially water saturated. Constant flow boundary conditions with flow from bottom to top and no flow conditions imposed right and left. The saturation field is heterogeneous.

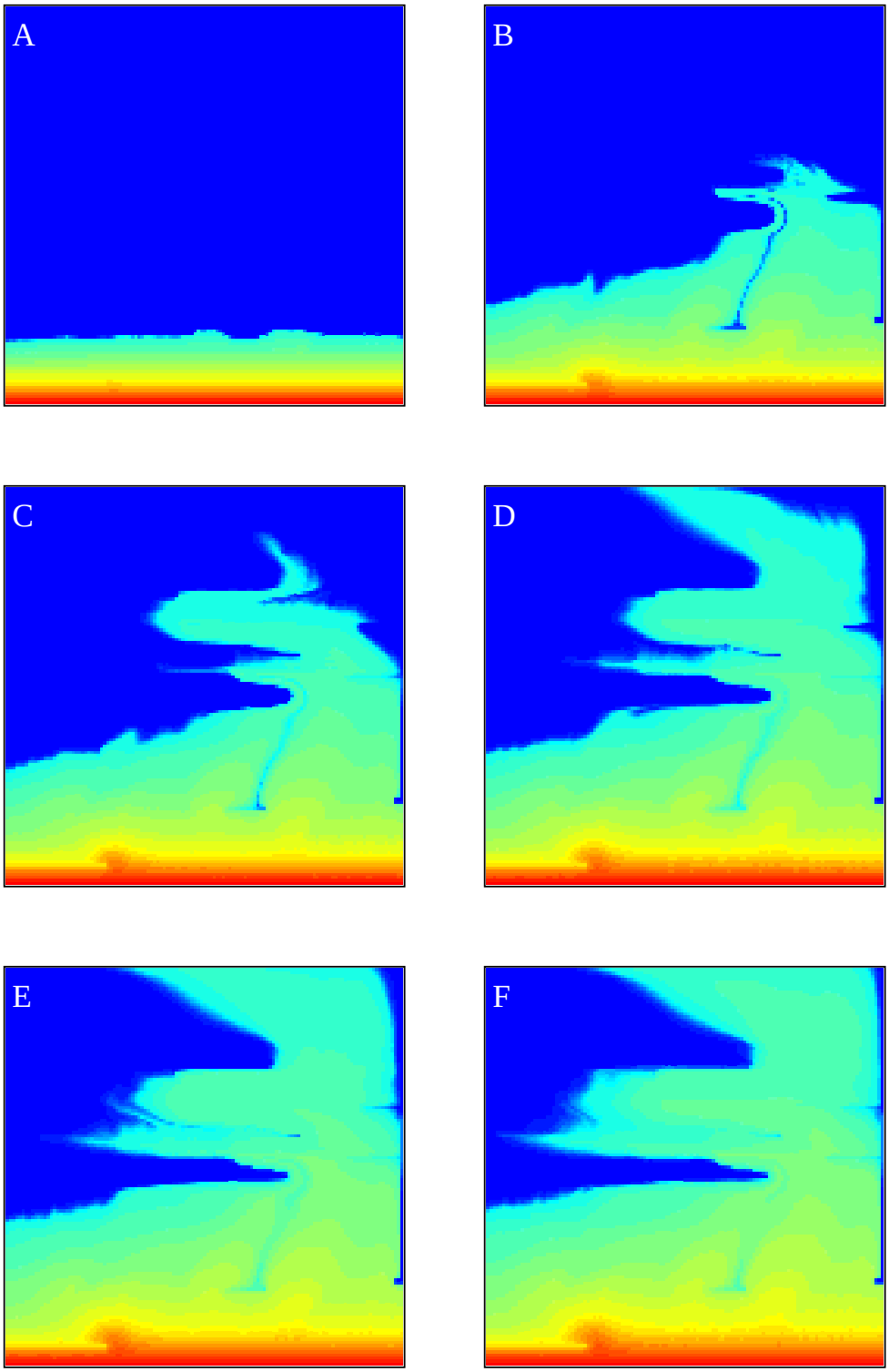

Figure 44 (d): Snapshots of supercritical CO_2 and water flow in a region of turbidite beds with parallel, discontinuous layering, with shale layers around 5m long. The modelled region is 38 by 38m. CO_2 is injected along the bottom edge of the model which is initially water saturated. Constant flow boundary conditions with flow from bottom to top and no flow conditions imposed right and left. The saturation field is highly heterogeneous

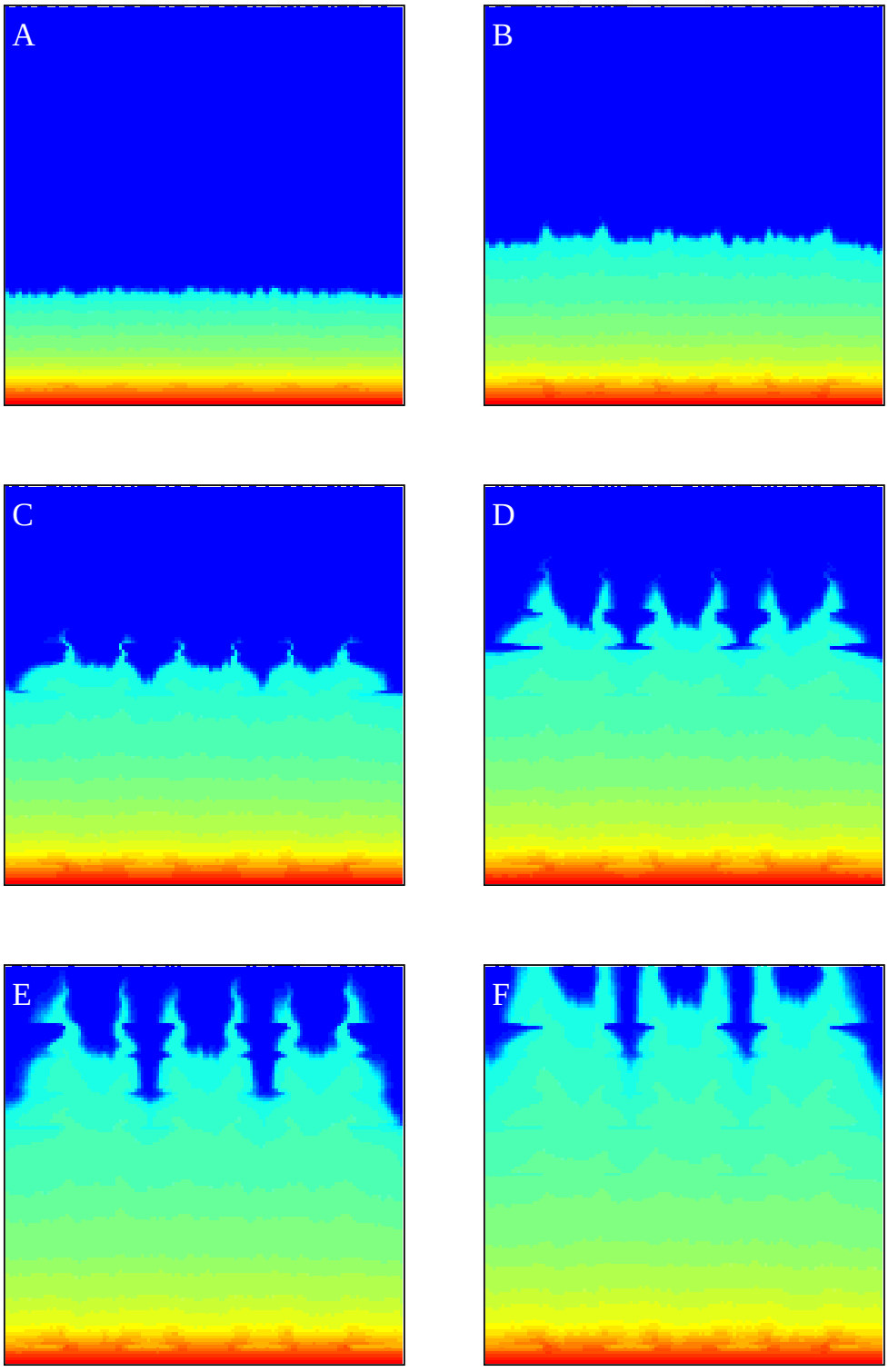

Figure 44 (e): Snapshots of supercritical CO_2 and water flow in a region of turbidite beds with parallel, discontinuous layering and wave-like perturbations 1. The modelled region is 38 by 38m. CO_2 is injected along the bottom edge of the model which is initially water saturated. Constant flow boundary conditions with flow from bottom to top and no flow conditions imposed right and left. Tongues of high CO_2 saturation develop corresponding to anticlines in the layering.

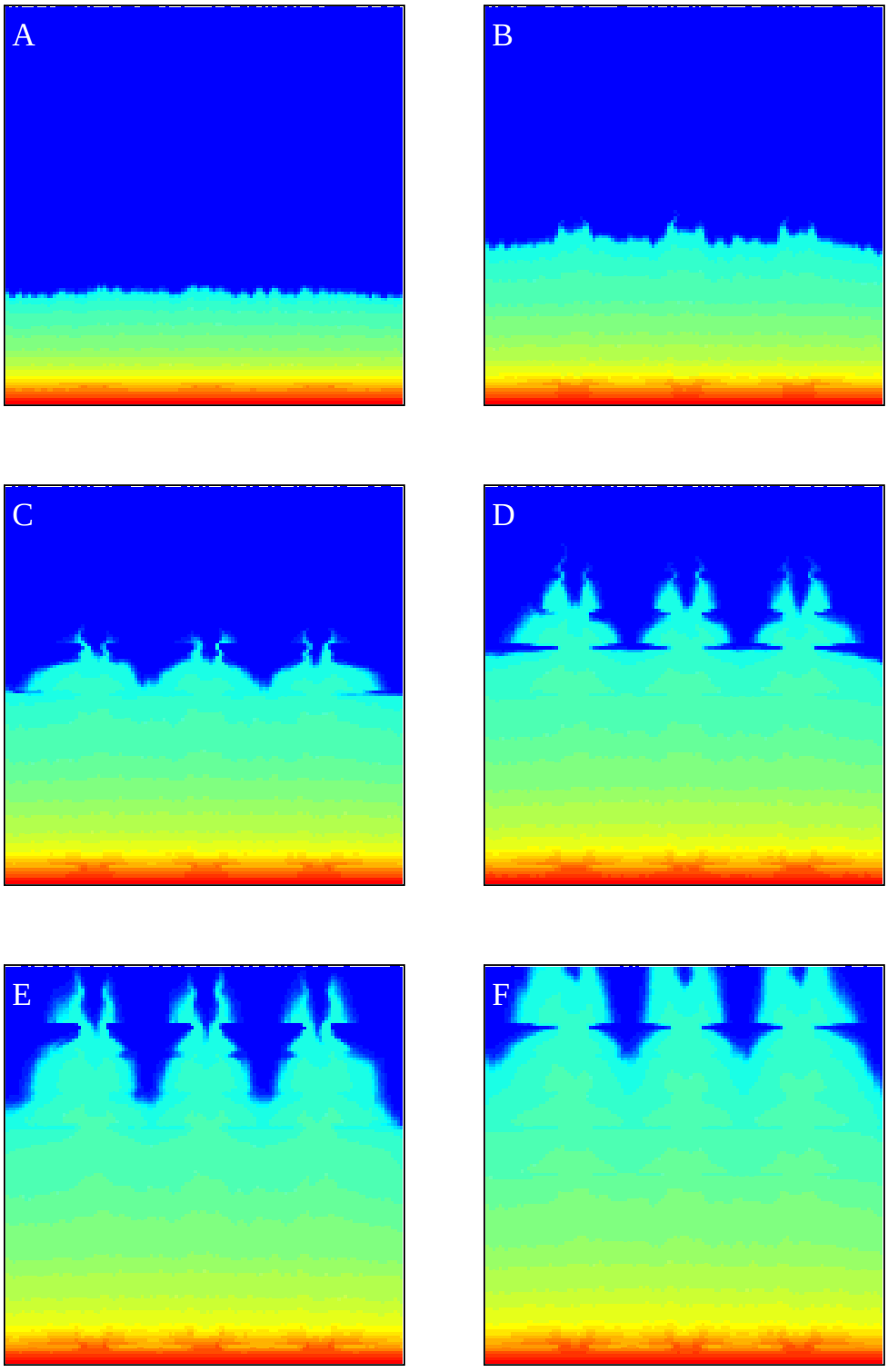

Figure 44 (f): Snapshots of supercritical CO_2 and water flow in a region of turbidite beds with parallel, discontinuous layering, with wave-like perturbations 2. The modelled region is 38 by 38m. CO_2 is injected along the bottom edge of the model which is initially water saturated. Constant flow boundary conditions with flow from bottom to top and no flow conditions imposed right and left. Tongues of high CO_2 saturation develop corresponding to anticlines in layering.

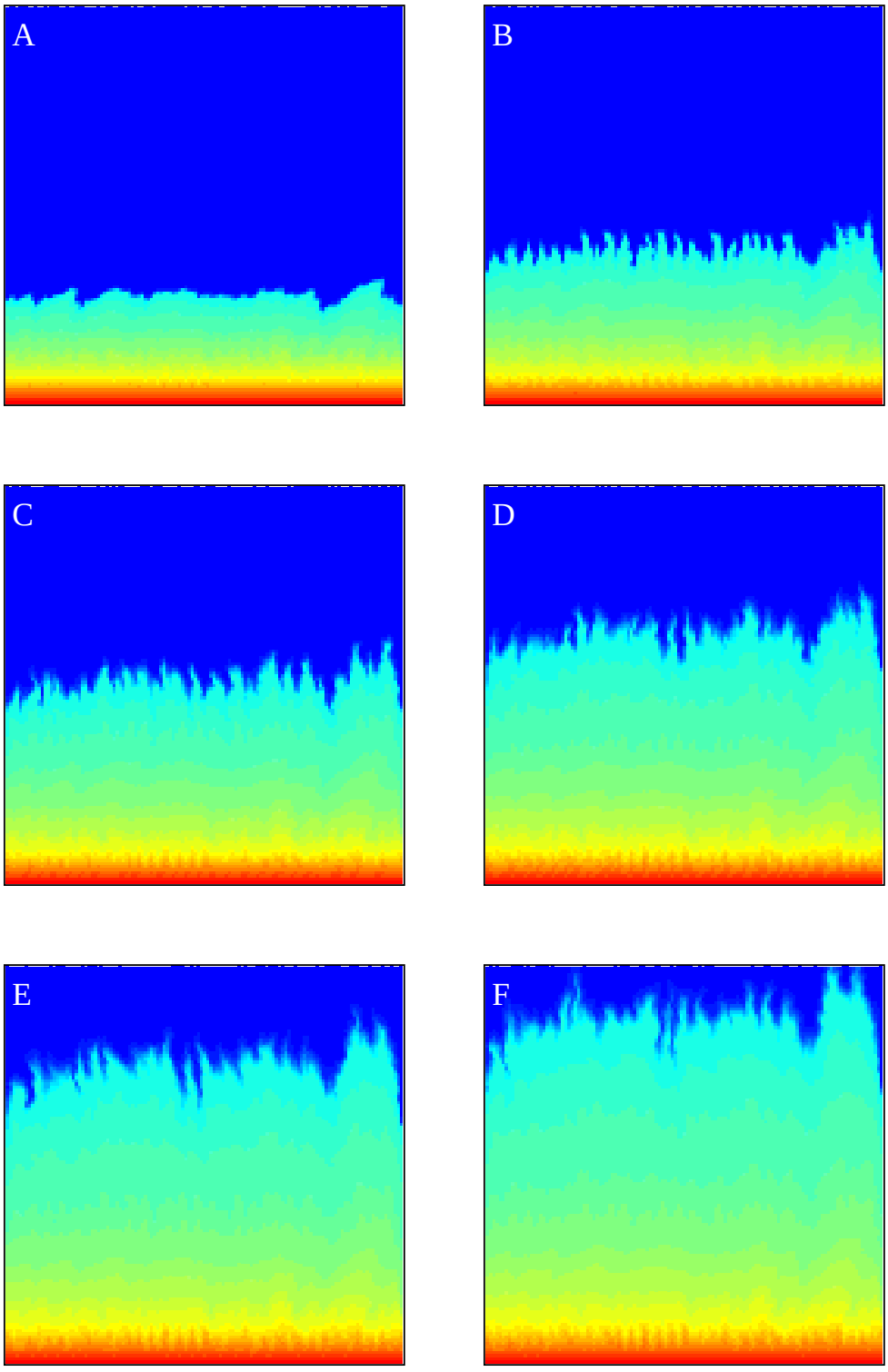

Figure 44 (g): Snapshots of supercritical CO_2 and water flow in a region of cross-bedded sandstone. The modelled region is 0.5 by 0.5m. CO_2 is injected along the bottom edge of the model which is initially water saturated. Constant flow boundary conditions with flow from bottom to top and no flow conditions imposed right and left. Some fingering is developed but otherwise the saturation field resembles that of homogeneous sands.

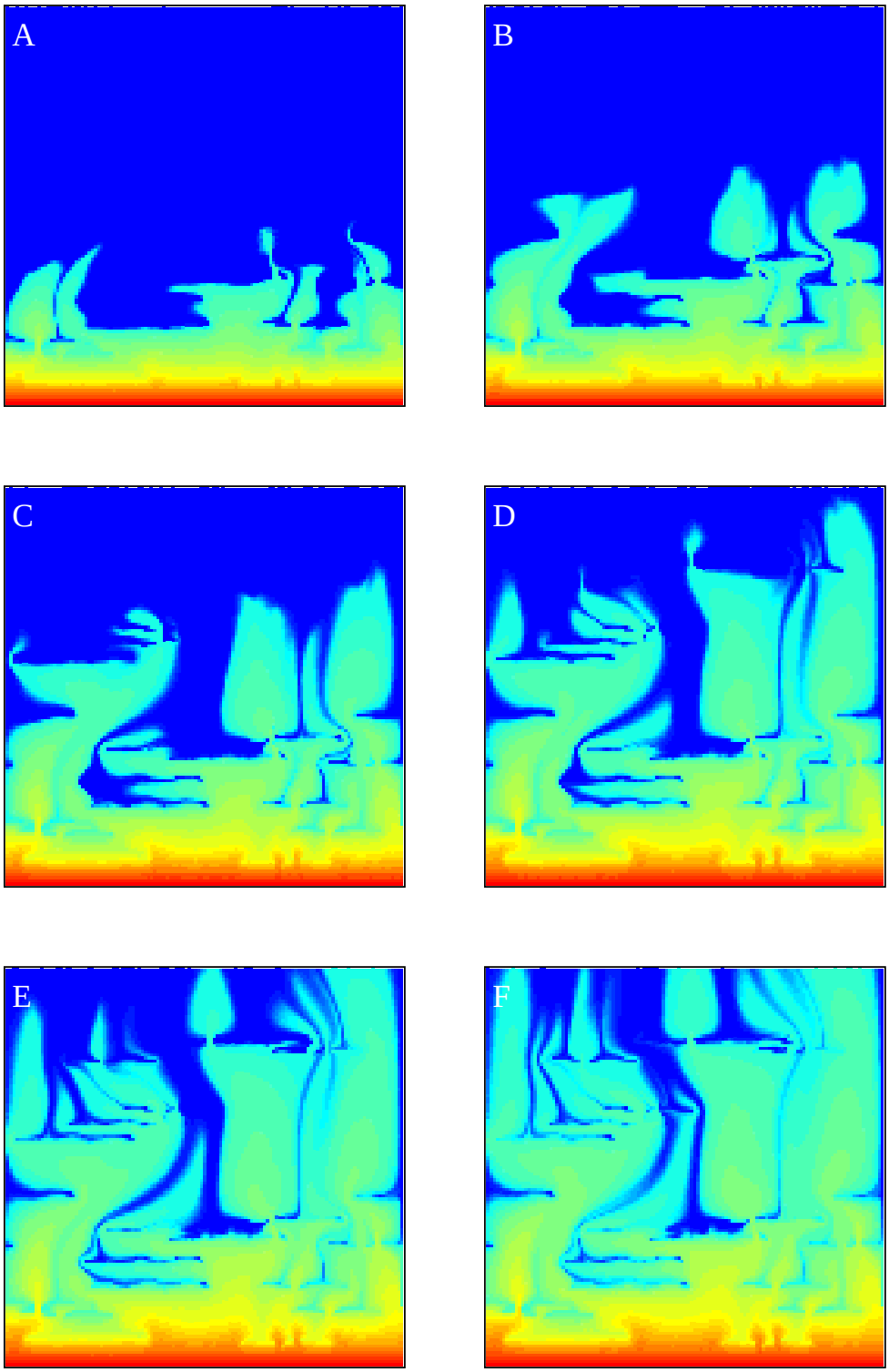

Figure 44 (h): Snapshots of supercritical CO_2 and water flow in a region of massive sands with fluid escape structures. The modelled region is 0.6 by 0.6m. CO_2 is injected along the bottom edge of the model which is initially water saturated. Constant flow boundary conditions with flow from bottom to top and no flow conditions imposed right and left. Highly heterogeneous saturation fields are developed.

3- Saturation evolution plots

One way of examining changes in the heterogeneity of the saturation field with time is to plot the saturation variation along the outflow boundary for each time step. In Figure 45, these 'saturation evolution' plots are shown together with the average saturation for the outflow boundary (equivalent to a 'breakthrough' curve for contaminant transport), for the seven cases with flow perpendicular and parallel to the layering.

For the case of parallel continuous layering in turbidite sequences (Figure 45 (a)), the plot for flow perpendicular to layering simply shows the arrival of a planar front and a gradual increase in saturation, very similar to the matrix only case. Saturations at a given time are slightly higher than in the matrix only case, indicating that the presence of low permeability layers tend to 'hold up' the front resulting in greater saturations when they arrive at the outflow boundary. When flow is parallel to the layering (Figure 45(a)), the high permeability layers are free to form rapid channel ways for injected CO_2 which arrives first at the outflow boundary. It can be seen that even in the lowest permeability layers flow occurs and CO_2 saturation increases, although more slowly, with time. These effects give a marked striped appearance to the plot.

In the case of parallel finite layering in turbidite sequences (Figure 45(a)), the arrival of CO_2 at the boundary is spread over a longer time period, and shows relative delay at the left hand edge of the model. Here irregularities in the front are on the scale of the whole model, following the lengths of the discontinuous layering. For flow parallel to layering (Figure 45(a)), the picture looks similar to that for parallel continuous layering with CO_2 reaching the boundary first along the high permeability layers. For the case of continuous layering with perturbations (Figure 45(b)), the break-though pattern records the arrival of the two sets of fingering seen in the snapshots giving a wave-like form to the break-through pattern.

In the case of cross-bedding (Figure 45(c)), the patterns for flow both perpendicular and parallel to layering show similar patterns. This is because the layering of permeability contrasts is 45^o to the bedding resulting in similar behaviour for these two directions. Both patterns are similar to the matrix only case except that fingering is slightly more pronounced. In the case of fluid escape structures (Figure 45(c)), flow parallel to layering shows a planar front with small sections that show delay, corresponding to the positions of the dish structures. When flow is perpendicular to the layering, arrival of CO_2 at the outflow boundary is spread over a larger time range and is more irregular. The plot has a stripped appearance showing the presence of narrow bands of reduced CO_2 saturation that are also visible in the snapshots.

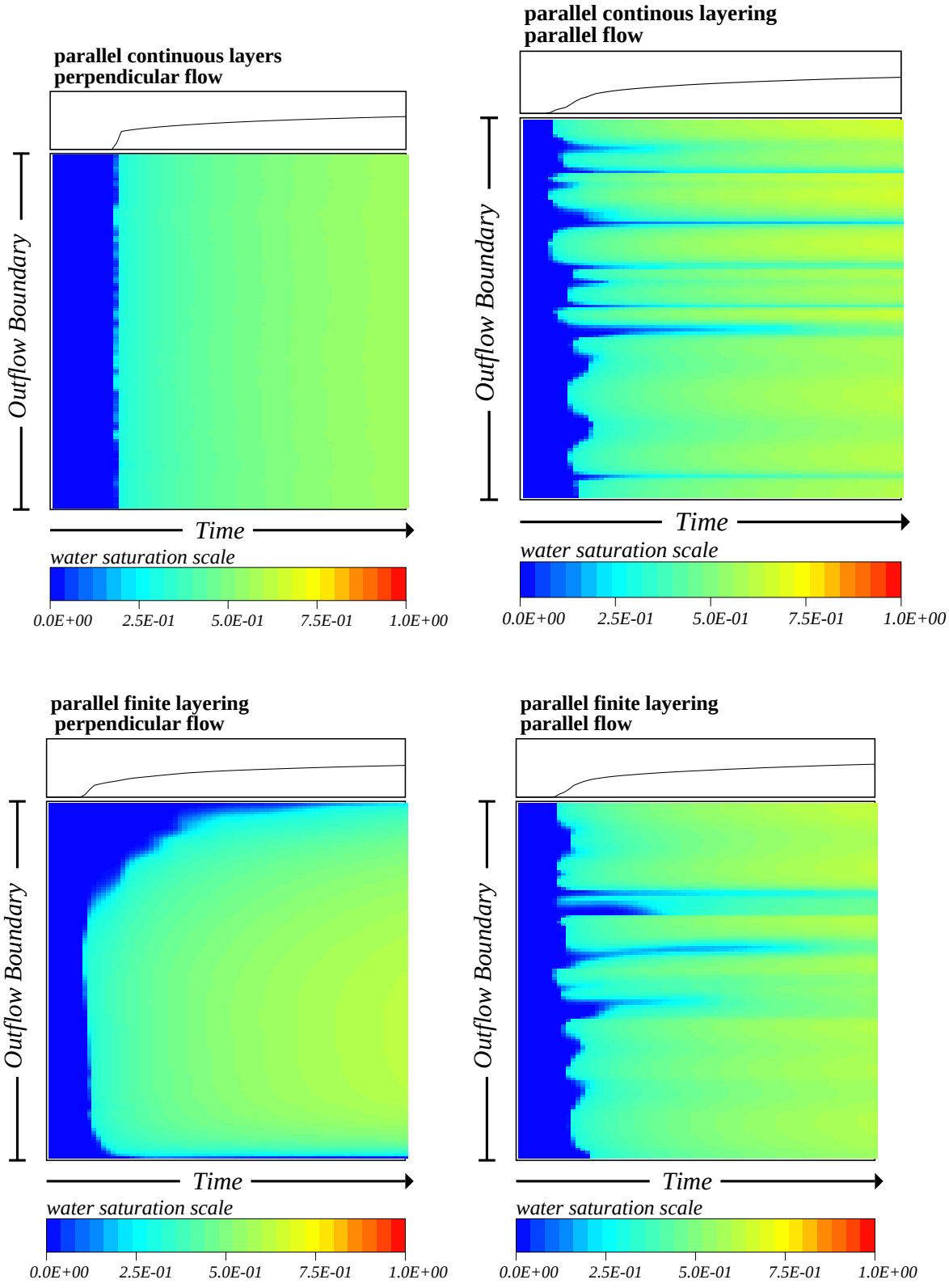

Figure 45 (a): Saturation evolution plots showing the changes in the saturation at the boundary with time through the simulations. Top – turbidite sequence with parallel continuous layering with flow perpendicular (left) and parallel (right) to layering. Bottom - turdidite sequence with parallel discontinuous layering (shale layers around 5m long) and flow perpendicular (left) and parallel (right) to layering.

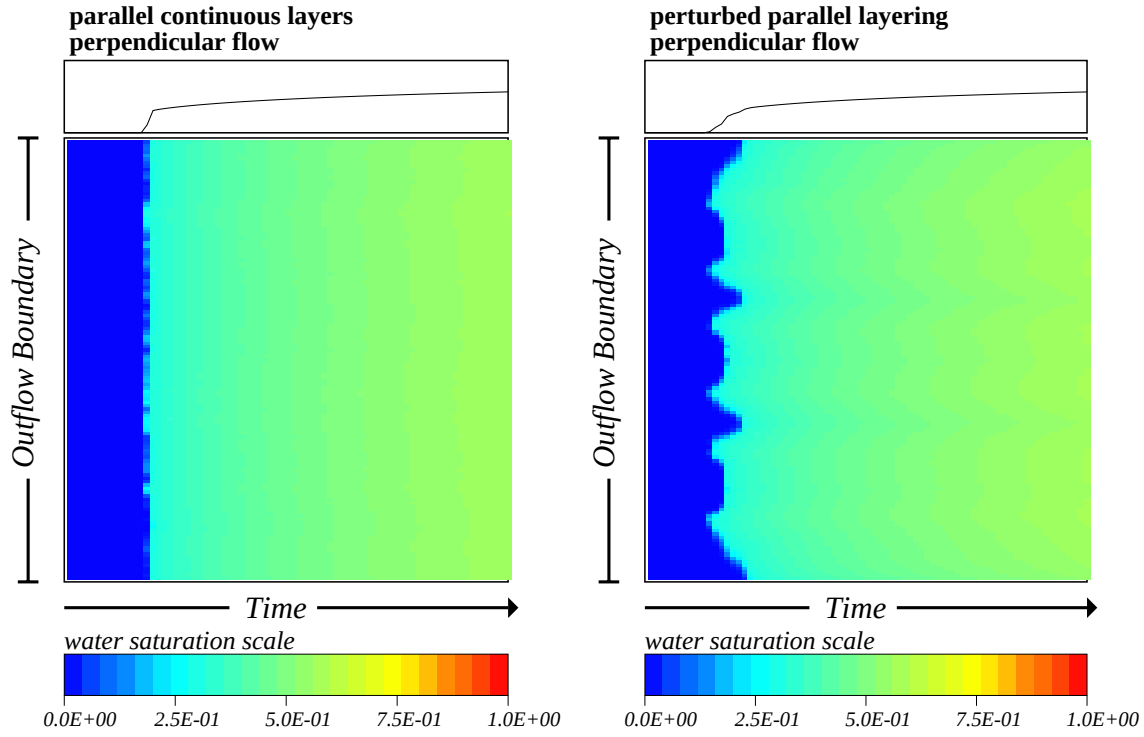

Figure 45 (b): Saturation evolution plots showing the changes in the saturation at the boundary with time through the simulations. Left – turbidite sequence with parallel continuous layering. Right - turbidite sequence with parallel continuous layering and wave-like perturbations.

4- Pseudo-curves and sensibility analysis

The output saturation fields at each time step are used to determine 'pseudo' relative permeability curves, representative of the whole modelled region, using the method of *Kyte and Berry* [1975] outline in the previous section. Here the flows of CO_2 and water at the outflow boundary at each time step are used to determine representative values of relative permeability to supercritical CO_2 and water. These are plotted against the saturation of the whole model to give 'pseudo' relative permeability curves representative of the whole modelled region. For each heterogeneity case, a series of ten realizations with inflow along one boundary was made to test the sensitivity of the resultant curves to heterogeneity geometry.

In Figure 46(a), the pseudo relative permeability curves and saturation versus pore volume injected for the cases of turbidite layering (continuous and discontinuous) where flow is perpendicular to the layering are shown. It can be seen that the case of parallel continuous layers gives curves very similar to those for matrix and that the curves for the ten realizations are very similar. The only difference from the matrix only case, is that saturation increases more rapidly for pore volumes injected. This is due to the 'compression' of the CO_2-water front caused by the presence of low permeability layers, as discussed above. By contrast, the case of parallel discontinuous layering shows a wide scatter of relative permeability curves that show shallower slopes and migration of the cross-over point to lower saturation values. The curves for saturation versus pore volumes injected also show a wide scatter. It is clear that in this case, a 'representative area' for which constant curves can be expected, has not been reached and must be larger than the model presented (38 by 38 m).

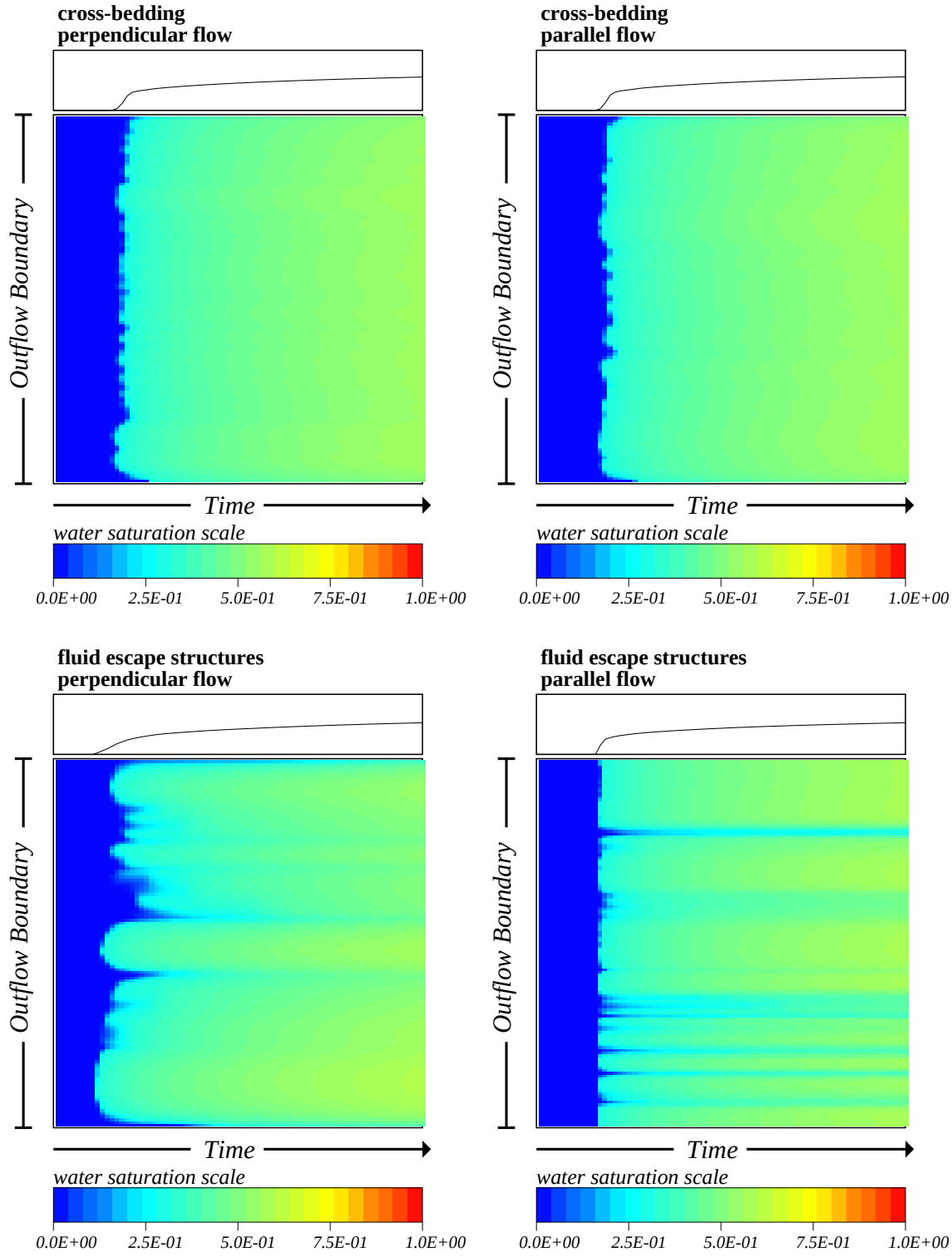

Figure 45 (c): Saturation evolution plots showing the changes in the saturation at the boundary with time through the simulations. Top – cross-bedding with flow perpendicular (left) and parallel (right) to layering. Bottom – massive sands with fluid escape structures with flow perpendicular (left) and parallel (right) to layering.

The plots for the case of flow parallel to the layering are shown in Figure 46(b). Here the cases of continuous and discontinuous layering give similar results for relative permeability curves. The curves for saturation versus pore volumes injected show that saturation increases more slowly for the

continuous than the discontinuous case. This is probably due to slightly lower proportion of shales in the discontinuous layer case simulations.

Figure 46(c), show the effect of introducing perturbations into parallel continuous layering which is to produce some scatter in the curves although not a pronounced as in the case of discontinuous layering. Such perturbations also tend to reduce the rate at which saturation increases with fluid injection.

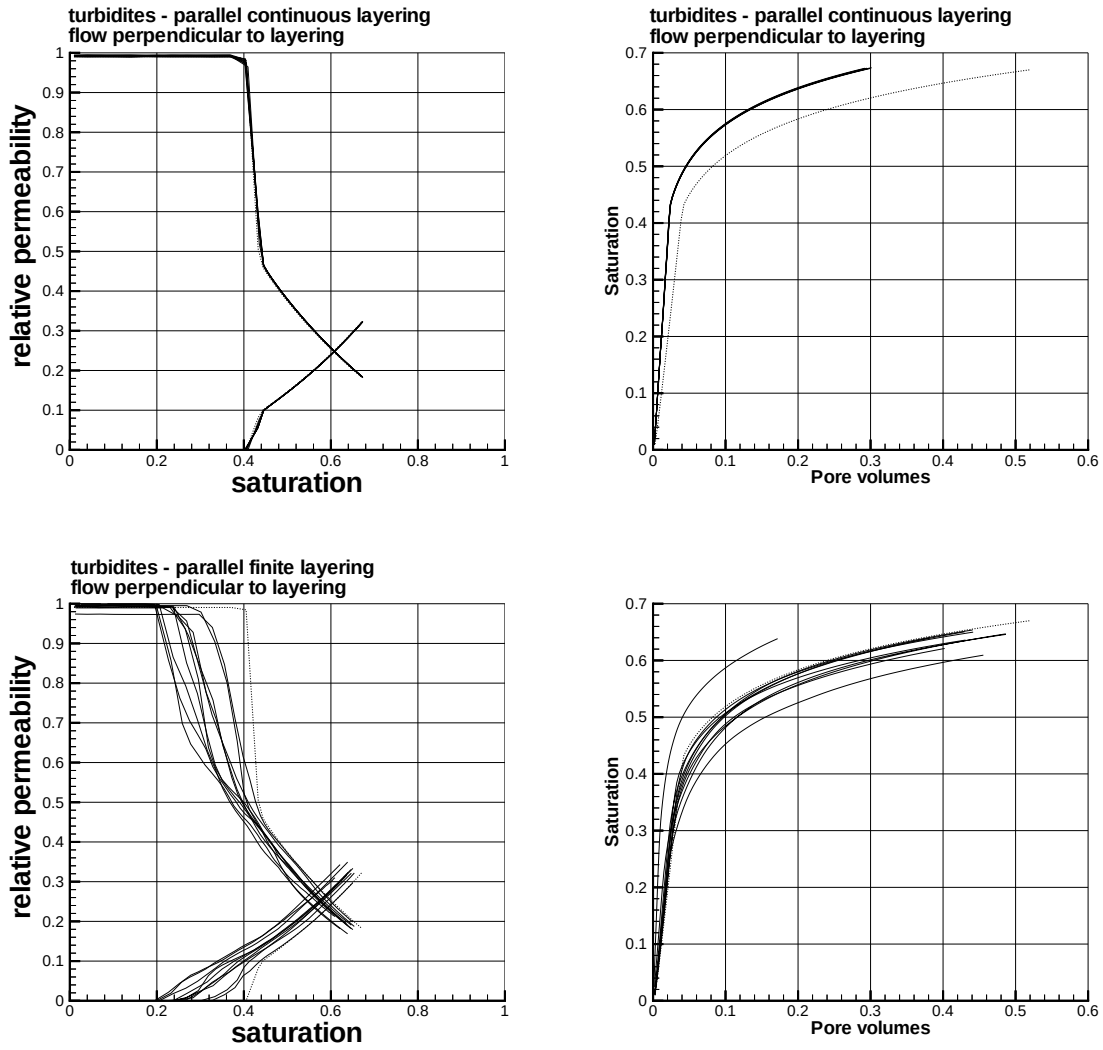

Figure 46(a): Pseudo relative permeability curves (left) and saturation versus injected pore volume of fluid (right). Top – turbidite sequence with parallel continuous layering. Bottom - turbidite sequence with parallel discontinuous layering (shales around 5m long). Dotted line – case for homogeneous sands.

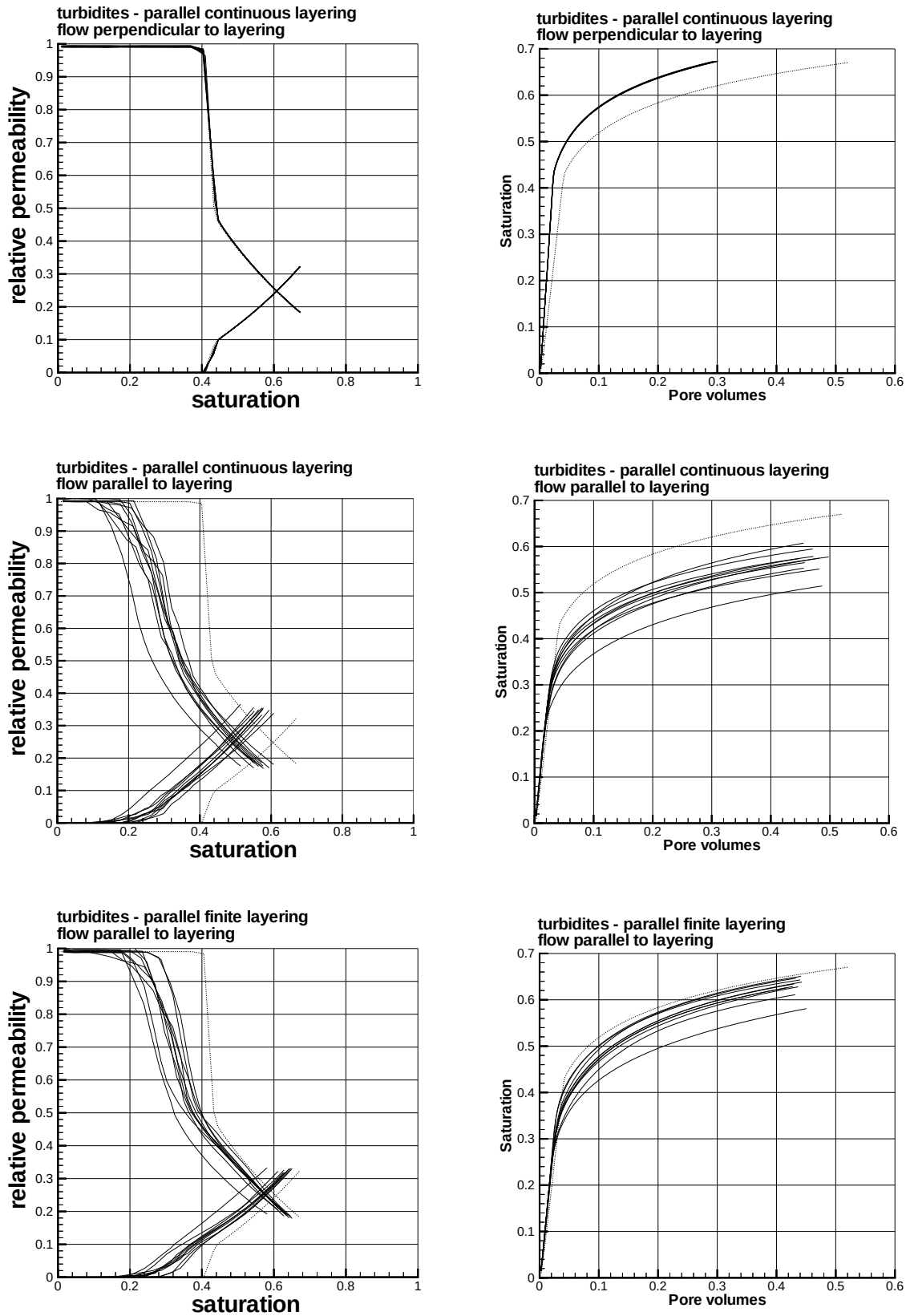

Figure 46(b): Pseudo relative permeability curves (left) and saturation versus injected pore volume of fluid (right). Top – turbidite sequence with parallel continuous layering, flow perpendicular to layering. Centre – turbidite sequence with parallel continuous layering, flow parallel to layering. Bottom - turbidite sequence with parallel discontinuous layering and flow parallel to layering. Dotted line – case for homogeneous sands.

The case of matrix only (Figure 44(a)) shows a simple picture of the CO_2-water front moving as a line parallel to the injection edge across the modelled area. The random variations in permeability of one half order of magnitude cause small scale fingering that is most evident in the last snapshot. Due to the high viscosity ratio, the front is highly smeared out with most of the model in the last snapshot having saturation of less then 0.5.

The case of continuous parallel turbidite layers (Figure 44(b)) shows a very similar picture to the matrix only case. This is because the layering is perfectly parallel, perpendicular to the pressure gradient. However, for the two cases of discontinuous layering (Figure 44(c) and (d)) there are marked changes with highly complex saturation fields developing as the injected CO_2 flows round the low permeability shale layers. This produces large contrasts in saturation with areas of trapped water where flow rates are very slow and thin tongues of CO_2 reaching out into the water saturated region.

The two cases of perturbed layering (Figure 44(e) and (f)) show that even small deviations from perfectly planar and parallel layering have significant effects on the flow patterns. The 'high' points or anticlines in the perturbations are places of preferential flow and the 'corners' where there are steps in the layering give rise to secondary tongues of increase CO_2 saturation. These effects increase as the CO_2 front moves through the model area being magnified at each low permeability layer crossed. The geometry of the perturbations is reflected in the frequency and the spacing of the CO_2 tongues as is seen by comparing the two examples.

The case of cross-bedding (Figure 44(g)) is similar to the case of matrix only in that the CO_2 front advances as an approximately straight line perpendicular to the pressure gradient. However, the fingering effects are enhanced compared to the matrix only case. The effect of the different directions of cross-beds is seen in the thick bed near the base of the model but these effects appear to average out over the rest of the model to produce fingering parallel to the pressure gradient.

The case of fluid escape structures (Figure 44(h)) shows the most complex saturation field of all the models. The thin dish structures act as discontinuous flow barriers so this case resembles, in part, the discontinuous turbidite sequence case but with shorter low permeability layers. The fluid escape pipes form pathways of high flow which generated small CO_2 plumes at their low pressure ends. As CO_2 flows round the dish structures and along the fluid escape pipes, it leaves areas of high water saturation trapped behind the front creating highly complex and variable saturation fields.

For the cases of small scale heterogeneities, the case of cross-bedding (Figure 46(d)) shows similar results to the matrix only case with minor scatter introduced. However, the rate of saturation increase is slightly enhanced over the matrix case. Fluid escape structures produce a scatter similar to that for discontinuous layering with a similar migration of the cross over to lower saturations. The rate at which saturation increases is slightly lower than the matrix only case. From the scatter, it is clear that the model area of 0.6 by 0.6 m is not large enough to be representative.

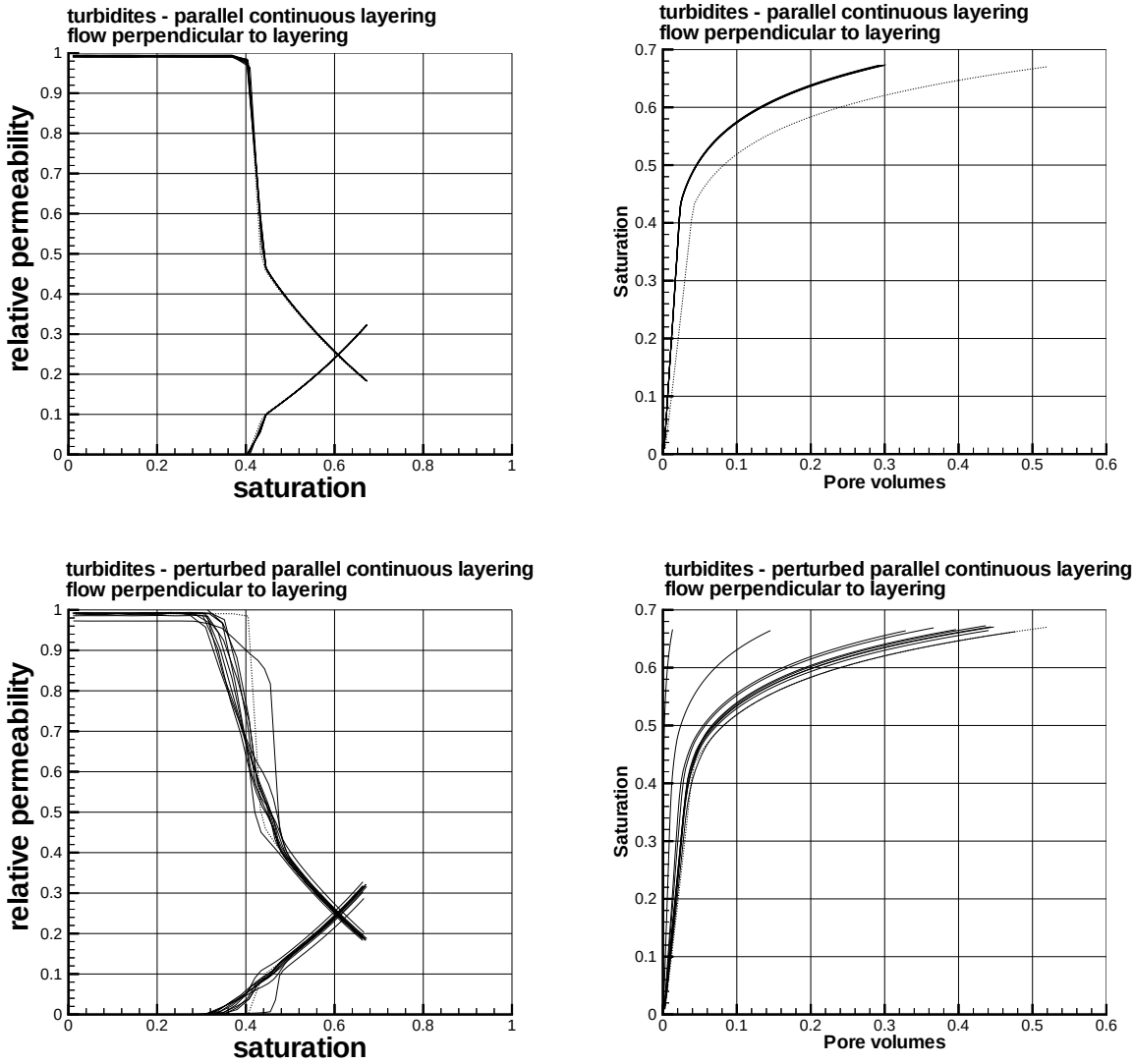

Figure 46(c): Pseudo relative permeability curves (left) and saturation versus injected pore volume of fluid (right). Flow perpendicular to layering. Top – turbidite sequence with parallel continuous layering. Bottom - turbidite sequence with parallel continuous layering and wave-like perturbations.

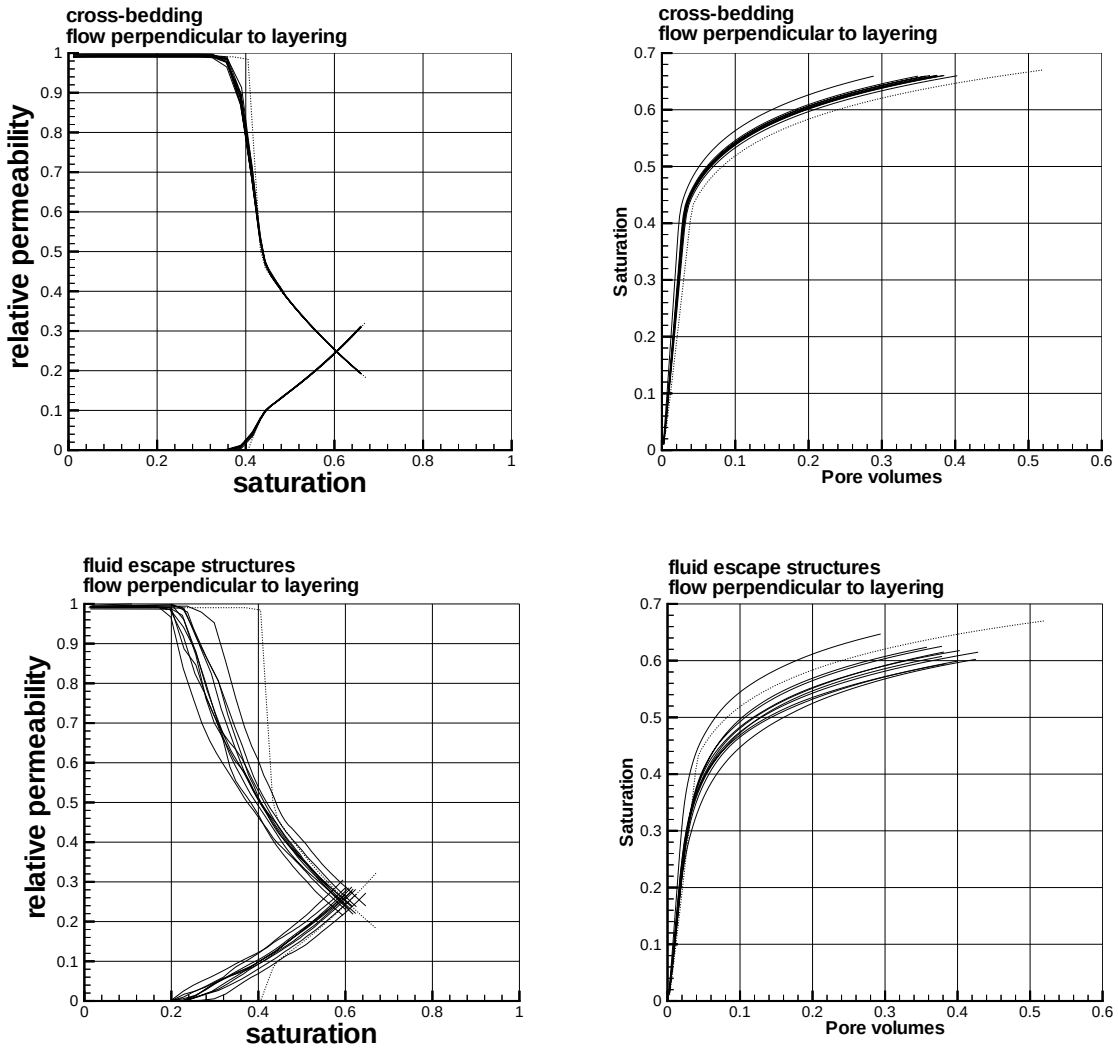

Figure 46(d): Pseudo relative permeability curves (left) and saturation versus injected pore volume of fluid (right). Top – cross-bedding with flow perpendicular (left) and parallel (right) to layering. Bottom - massive sandstones with fluid escape structures with flow perpendicular (left) and parallel (right) to layering.

D-3. Fractal Fracture Patterns: Flow Barriers and Conduits

1- Permeability contrast dependence

Here we will investigate the effect of the permeability contrast on the geometry of the front for a given fracture pattern[7]. The chosen pattern is characterised by a fractal dimension *D* of 2 and a length exponent *a* of 1.5. The geometrical characteristics of the pattern are described in Table 9 - section C-2. Fractures are oriented at 30° with respect to the inflow boundary. The matrix is heterogeneous and the varying parameter is the permeability contrast R_k existing between the fractures and the matrix. Simulations have been realised to better constrain the influence of the permeability ratio on the front geometry. Three different sizes and pattern density have been considered whose geometrical characteristics are summarised in Table 2.

Name	Area (m^2)	Mass (m)	Density (m/m^2) (d= Mass/Area)	N_{layers}	Density (m^{-2}) ($d=N_{layers}/Area$)	N_{int}	l_{max} (m)	P_{elt} (%)
Pattern R1	1	16.78	16.78	42	42	55	1.151	9.02
Pattern R2	900	503.61	0.5595	42	0.046	55	34.53	9.02
Pattern R3	10^6	20.8 10^4	0.208	2000	0.002	9552	1149	64.86

Table 13: geometrical parameters of the layer networks.

The patterns used are represented figure and the simulations performed are summarised in Table 16, Table 15, and Table 14.

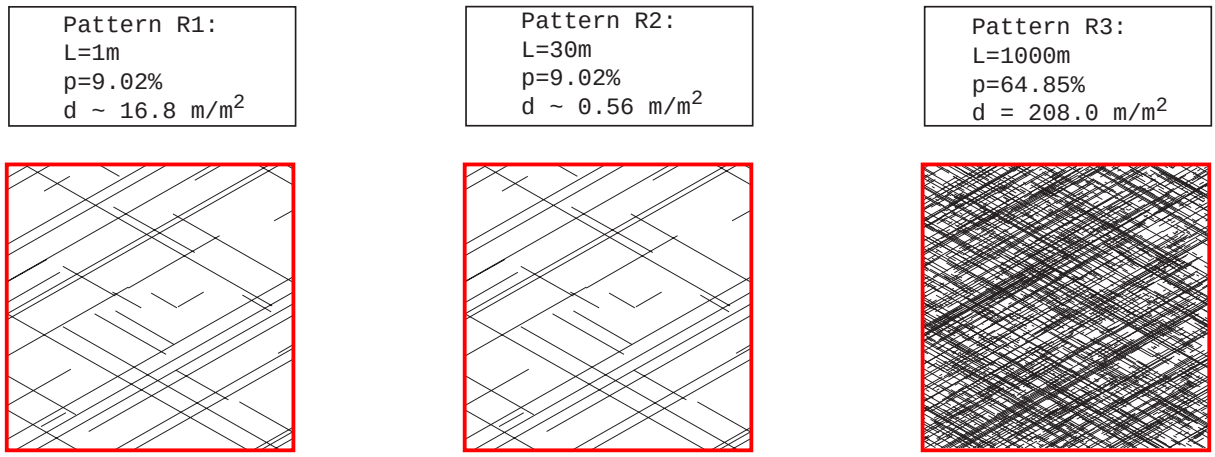

Figure 47: geometry of the various patterns used to study the influence of the layer/matrix permeability contrast on the front geometry and on the saturation evolution.

[7] Fracture patterns can also be assimilated to deformation bands.

Simulation	η_{water} (Pa.s)	η_{CO2} (Pa.s)	Flow rates ($m.s^{-1}$)	Φ_l	Φ_m	<Km> (darcy)	σ	Aperture (μm)	Ratio R_k
R1a	1	10	0.225	0.1	0.3	1	0.15	0.05	$2.11\ 10^{-4}$
R1b	1	10	0.225	0.1	0.3	1	0.15	0.1	$8.44\ 10^{-4}$
R1c	1	10	0.225	0.1	0.3	1	0.15	0.3	$7.60\ 10^{-3}$
R1d	1	10	0.225	0.1	0.3	1	0.15	0.5	$2.11\ 10^{-2}$
R1e	1	10	0.225	0.1	0.3	1	0.15	1	$8.44\ 10^{-2}$
R1f	1	10	0.225	0.1	0.3	1	0.15	3	0.76
R1g	1	10	0.225	0.1	0.3	1	0.15	5	2.11

Table 14: parameters assigned in the simulation using the pattern R1. Φ_l is the porosity of the fracture and Φ_m the porosity of the matrix

Simulation	η_{water} (Pa.s)	η_{CO2} (Pa.s)	Flow rates ($m.s^{-1}$)	Φ_l	Φ_m	<Km> (darcy)	σ	Aperture (μm)	Ratio R_k
R2a	1	10	0.225	0.1	0.3	10	0.15	0.2	$3.37\ 10^{-4}$
R2b	1	10	0.225	0.1	0.3	10	0.15	0.3	$7.60\ 10^{-4}$
R2c	1	10	0.225	0.1	0.3	10	0.15	0.5	$2.11\ 10^{-3}$
R2d	1	10	0.225	0.1	0.3	10	0.15	1	$8.43\ 10^{-3}$
R2e	1	10	0.225	0.1	0.3	10	0.15	2	$3.37\ 10^{-2}$
R2f	1	10	0.225	0.1	0.3	10	0.15	5	0.21
R2g	1	10	0.225	0.1	0.3	10	0.15	10	0.84

Table 15: parameters assigned in the simulation using the pattern R2.

Simulation	η_{water} (Pa.s)	η_{CO2} (Pa.s)	Flow rates ($m.s^{-1}$)	Φ_l	Φ_m	<Km> (darcy)	σ	Aperture (μm)	Ratio R_k
R3a	1	10	0.225	0.1	0.6	1	0.1	0.05	$2.11\ 10^{-4}$
R3b	1	10	0.225	0.1	0.6	1	0.1	0.10	$8.44\ 10^{-4}$
R3c	1	10	0.225	0.1	0.6	1	0.1	0.15	$1.90\ 10^{-3}$
R3d	1	10	0.225	0.1	0.6	1	0.1	0.20	$3.37\ 10^{-3}$
R3e	1	10	0.225	0.1	0.6	10	0.1	1.00	$8.44\ 10^{-3}$
R3f	1	10	0.225	0.1	0.6	1	0.1	0.50	$2.11\ 10^{-2}$
R3g	1	10	0.225	0.1	0.6	1	0.1	1.00	$8.44\ 10^{-2}$
R3h	1	10	0.225	0.1	0.6	1	0.1	2.00	$3.37\ 10^{-1}$
R3I	1	10	0.225	0.1	0.6	1	0.1	3.44	1

Table 16: parameters assigned in the simulation using the pattern R3

1-1 Saturation field

We first consider the simulation R1 and R2 for which the associated patterns presents the same geometry (same length exponent and same fractal dimension). Also the proportion of elements acting as a barrier is similar (P~9%). The difference lies in the size of the considered system. Simulation R1 is 1*m* long and R2 is 30*m*.

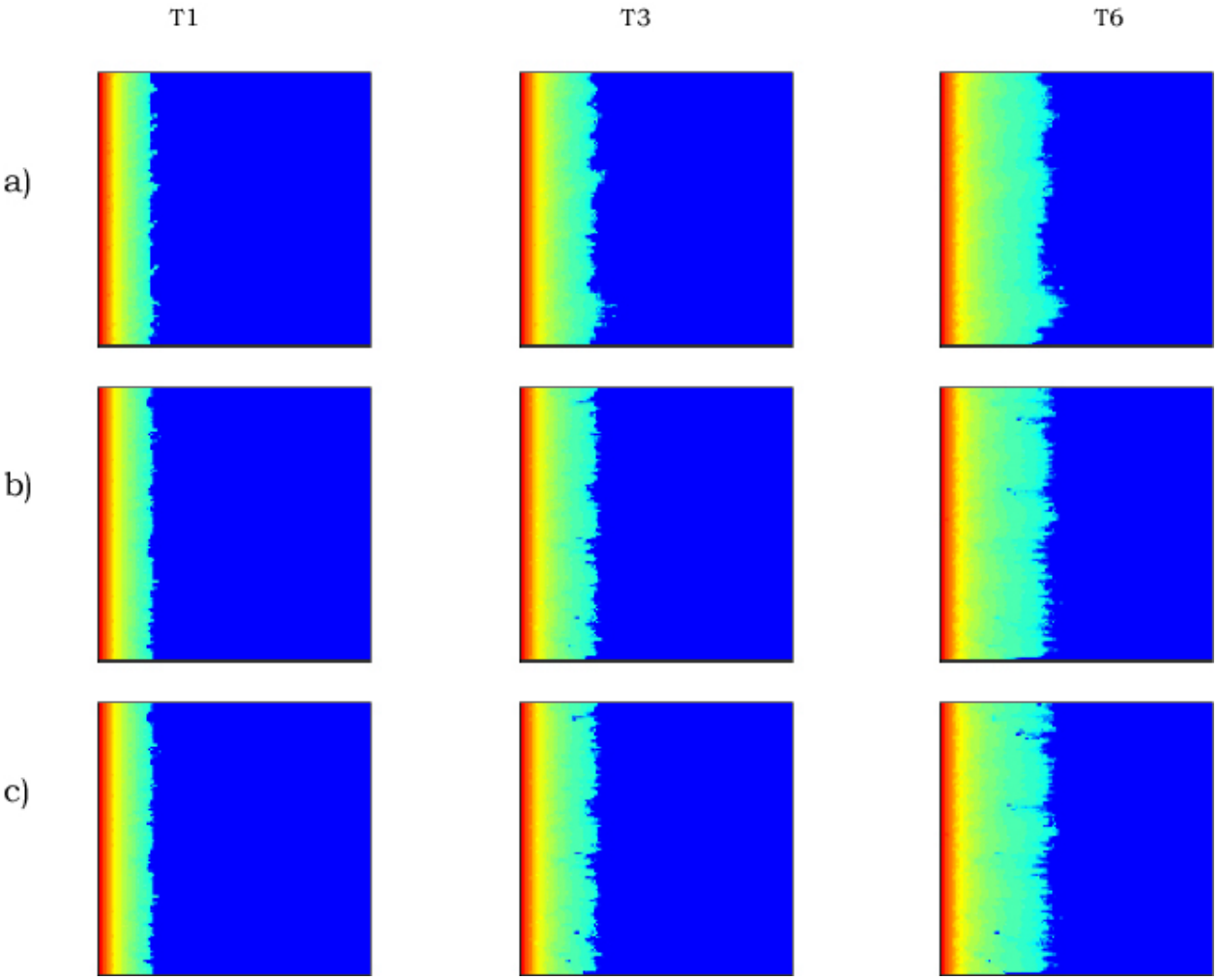

Figure 48: Snapshot of the saturation evolution for the pattern R1 when (a) R_k=8 10^{-1}, (b) R_k=8 10^{-3} and (c) R_k=8 10^{-4}. (d) Layer pattern R1 superposed on the saturation field T6-c. Circles indicate intersections where water is trapped.

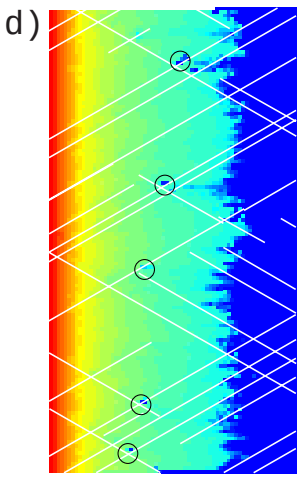

Figure 48 represents three snapshots of the saturation field, using pattern R1 for three different permeability ratio. In each case, the front is globally planar and presents locally small fingering. Also, its average position for different time step is the same. The irregularity of the front increases with the layers / matrix permeability contrast and a small amount of defending fluids can be trapped (snapshot T6-b, T3-c and T6-c), which is associated with layers intersections (Figure 48d). Also, although heterogeneities are oriented at 30°, and controlled the saturation (even for small contrast as illustrates in snapshot T1-a), the front remains planar.

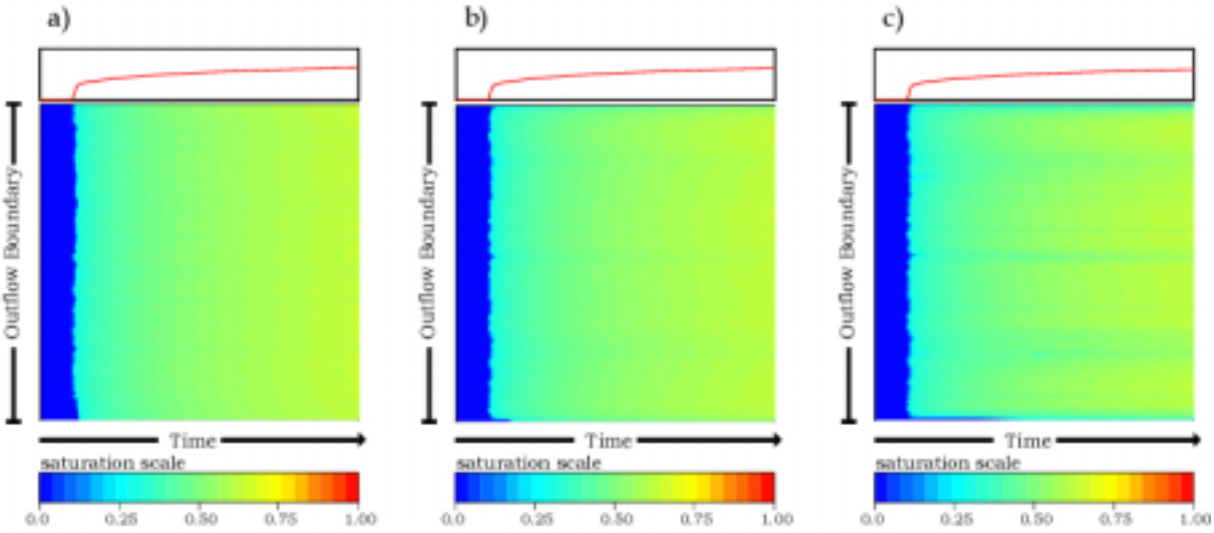

Figure 49: Time evolution of the saturation field for the pattern R1 when R_k is (a) 8 10^{-1}, (b) 8 10^{-3} and (c) 8 10^{-4}.

Time evolution saturation for the three different cases considered above are shown on Figure 49. The front geometry is the same as the saturation curves. This indicates that the permeability ratio has not a strong effect on the average saturation history and that the behaviour is close to the case of matrix alone.

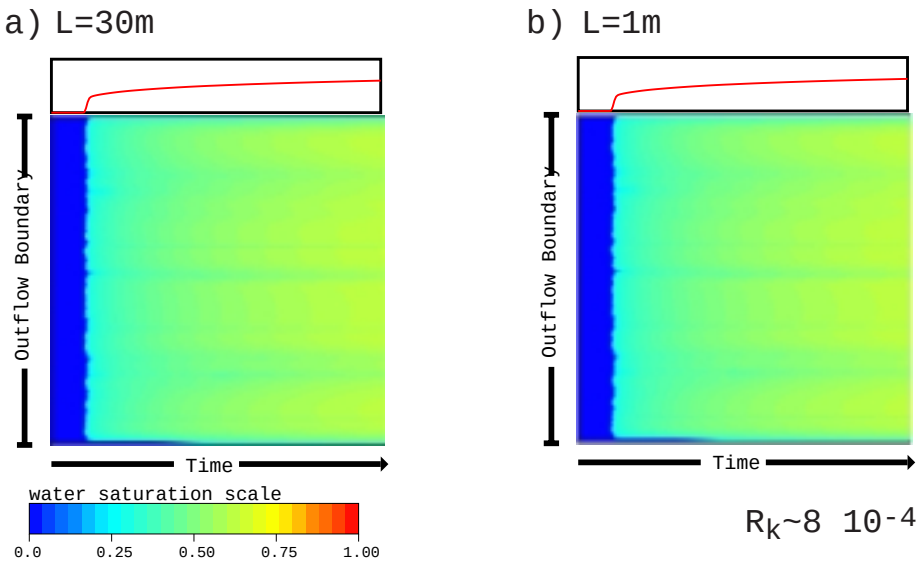

Figure 50: comparison of the time evolution of the saturation field for pattern R1 and R2.

Increasing the size gives the same time evolution (Figure 50), suggesting therefore that the pertinent density parameter required characterising our simulation is the percentage *P* of element acting as heterogeneity. Hence simulations R1 and R2 are similar and one can compare the different parameters derived from pseudo relative and fractional flow curves such as the cross over saturation - for which the relative CO_2 permeability is equal to the relative water permeability -, the irreducible CO2 saturation, and the saturation at the peak and its intensity observed on the derivative of the fractional flow curves.

1-2 Pseudo relative and fractional flow curves

We have determined the pseudo relative and fractional curves for all considered permeability ratios (Figure 51 and Figure 52). They all show the same evolution with the saturation, similar to the matrix case as illustrated previously.

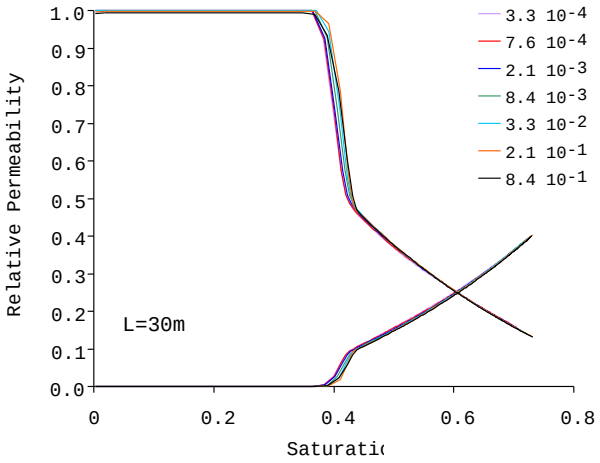

The irreducible CO_2 saturation and the cross over saturation S_c are independent of R_k (Figure 51). CO_2 starts to be mobile for saturation around 0.4 and becomes dominant when S~0.6 (corresponding to the cross over saturation). The derivative of the fractional flow curves shows a peak at saturation Sp~0.41 (Figure 52-right), identical to the matrix alone case (see Figure 28 in section D1). No variations in the slope of both pseudo relative and fractional flow curves are observed, suggesting that the sensitivity of the model to R_k is negligible.

Figure 51: pseudo relative curves for simulations performed on pattern R1.

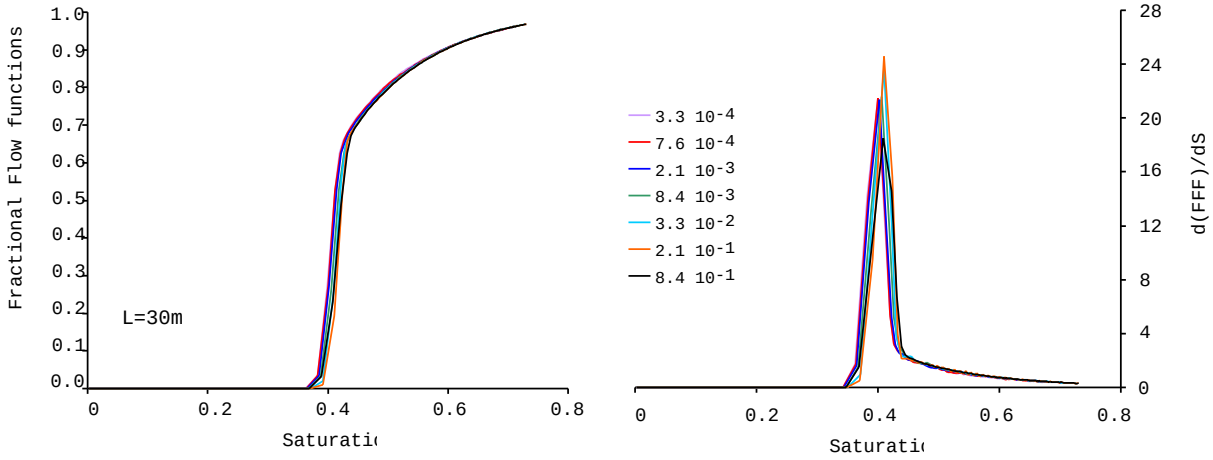

Figure 52: Fractional flow and its derivative for the simulations performed on patterns R1 and R2

Evolution of the cross over saturation, and irreducible CO2 saturation for pattern R1 and R2 with respect to the layer / matrix permeability ratio is shown on Figure 53. Results concerning a simulation where heterogeneities act as preferential paths has been add and R_k covers nearly five orders of magnitude. S_c is stable on all the considered range, and even when layers are more permeable than the matrix, S_c remains the same (Figure 53-left). The irreducible saturation is constant around 0.35 (Figure 53-right) and suggests to a first order that in the presence of barriers, the mobility of CO_2 is not affected by R_k. When R_k>1, *i.e.* when layers act as preferential paths, we observe a smaller IS_{CO2} value indicating that the CO_2 is mobile more rapidly. As observe in the case of simple geometry (see section D-1.1-), this decrease should be more important when layers are much more permeable than the matrix.

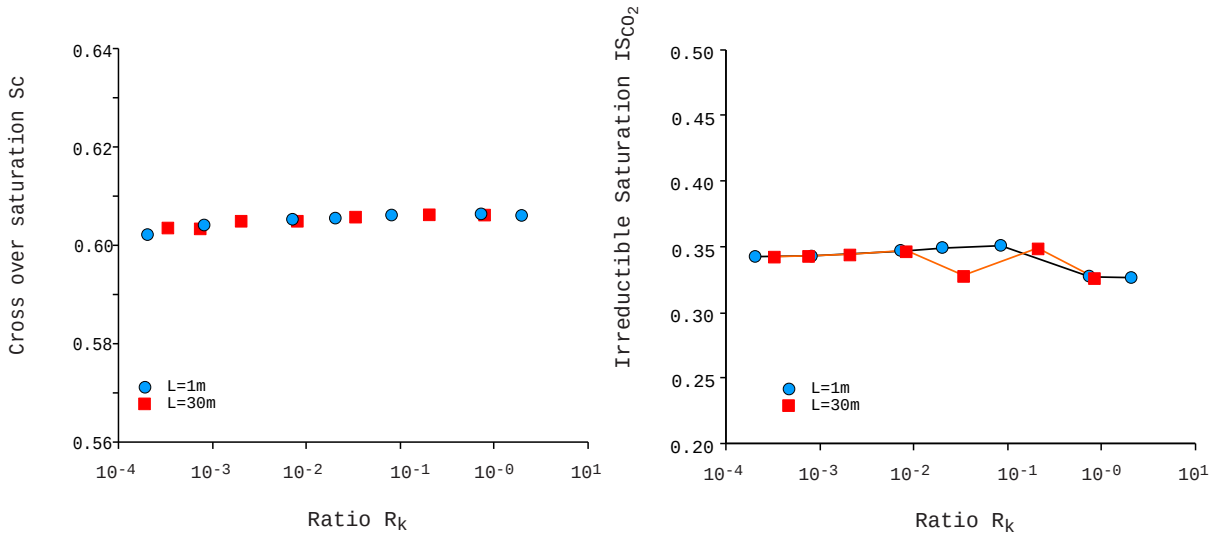

Figure 53: Evolution of the cross over saturation S_c and of the irreducible CO_2 saturation (IS_{CO2}) with respect to the permeability ratio for patterns R1 and R2.

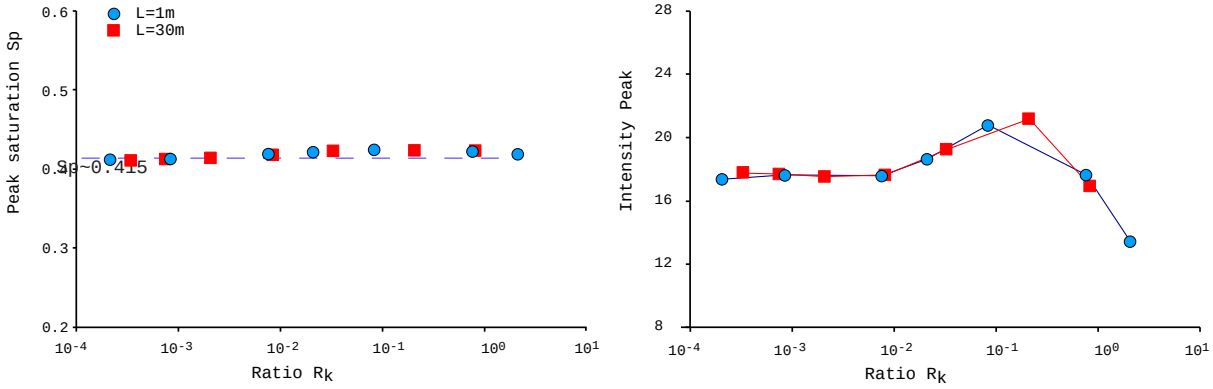

Figure 54: evolution of the peak saturation Sp (left) and of the peak intensity (right) with respect to the permeability ratio.

The saturation at which the derivative of the fractional flow curve shows an increase (corresponding to the maximum front velocity) is insensible to R_k on the considered range (Figure 54-left) while on contrary, the peak intensity (or peak amplitude) shows fluctuations (Figure 54-right). This latest shows an increase for $R_k>10^{-2}$ and an abrupt decrease for $R_k>0.5$. This indicates that increasing the layer / matrix permeability contrast makes the front move slower and that to a certain extent the layers inhibit the propagation of the front. The decrease observe when we approach the case where matrix and layer have similar permeability (R_k~1) is related to the influence of layers that enhance the mobility of fluid as soon as they have been injected (see the case of simple geometry section D-1.1-).

1-3 Presence of an escape structure

(a)- Snapshot of saturation field

In a first approach, we consider the simulation performed on the pattern R3 to study the influence of the permeability contrast. Figure 55 illustrates the saturation field calculated at five different time step for the pattern R3 and for a permeability ratio equal to 1 corresponding to simulation R3i (bottom) and a ratio equal to 2 10^{-4} corresponding to simulation R3a (top).

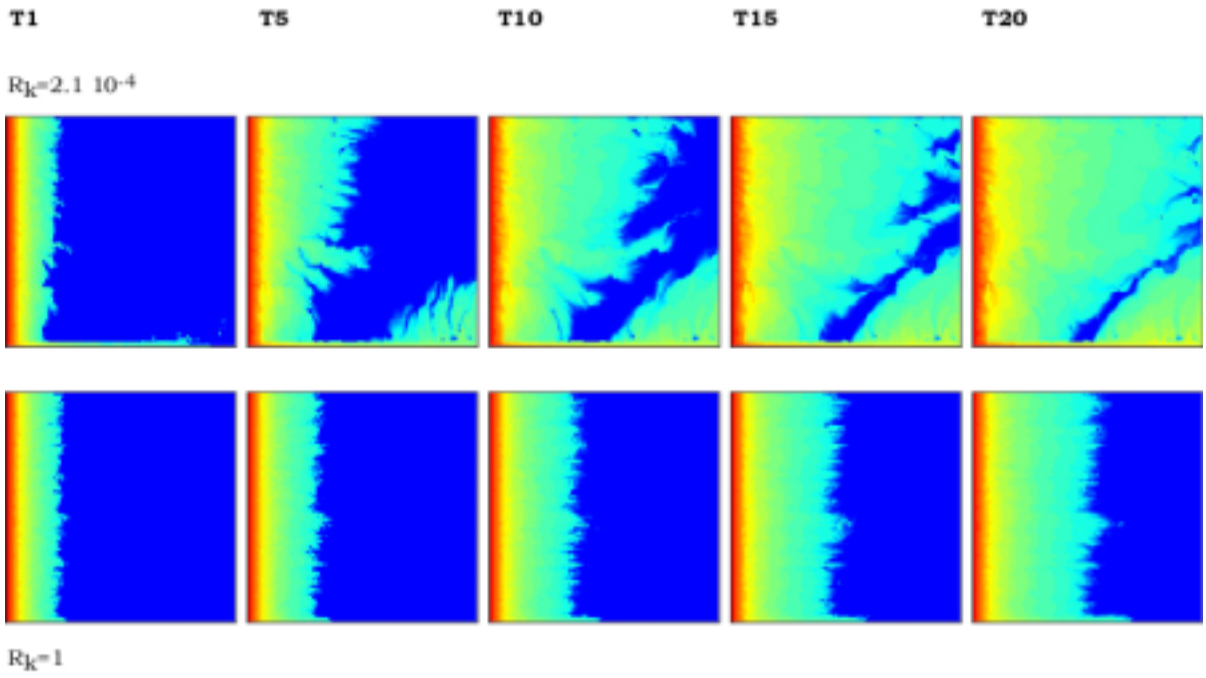

Figure 55: snapshots of the saturation evolution for a strong permeability contrast (top row) and for a null one (bottom row) for the pattern R3. Time step is similar in both simulations.

Pattern R3 is constituted of numerous fractures and the proportion of the grid elements acting as barriers is 64%. Therefore, for a strong layer / matrix permeability contrast, the system can be assimilated to a strongly non-permeable medium inside which exists preferential paths. This is illustrated in Figure 55 (bottom) where we observe that for a ratio of 2.1 10^{-4} the injected fluid uses a non-fractured channel situated at the bottom of the pattern. This permits a rapid dispersion of the invading fluid through the entire system. At a given time one observe zone for which the invading fluid saturation is maximal and others situated along the same vertical lines where it is null. Water is trapped in a fully CO_2 saturated medium. When R_k is equal to 1, the saturation evolution corresponds to the case of a heterogeneous matrix; layers are acting neither as barriers nor as preferential path. The front is not as heterogeneous as the one observed for a strong contrast but some small perturbations and fingering is developing, associated to the heterogeneity of the matrix.

The saturation evolution plot displays a different geometry according to R_k (Figure 56). For R_k=1 (Figure 56a) the front displays fingering as observed previously that is associated to the matrix heterogeneity. This indicates that regions are saturated more rapidly. When R_k increases, this behaviour is exacerbated and more particularly in the zone situated at the bottom where no heterogeneities are presents (Figure 56c and d). In this part, the saturation is rapidly complete and the bigger the contrast the greater the saturated zone.

This sensitivity to the permeability contrast is express through saturation curves (Figure 57). Each of these curves corresponds to one saturation field reported on Figure 56 and shows a shallower slope when R_k is decreasing. This indicates that the transport of the invading fluid, *i.e.* the saturation, is much more rapid in the high contrast case and that the shock velocity is smaller.

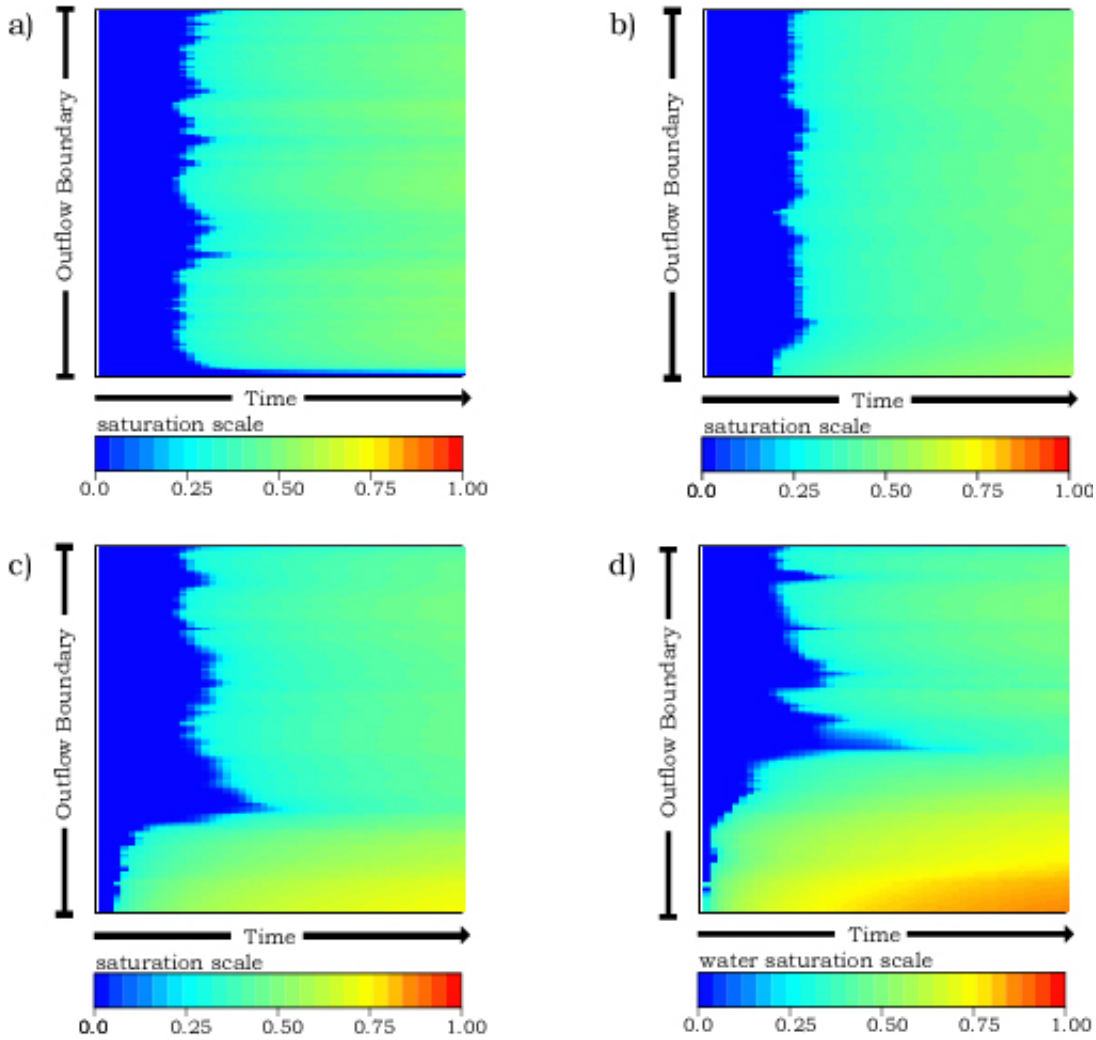

Figure 56: Time evolution plot determined for four different permeability ratio for the pattern R3 (a) R_k=1, (b) R_k=8.4 10^{-2}, (c) R_k=8.4 10^{-3}, and (d) R_k=8.4 10^{-4}.

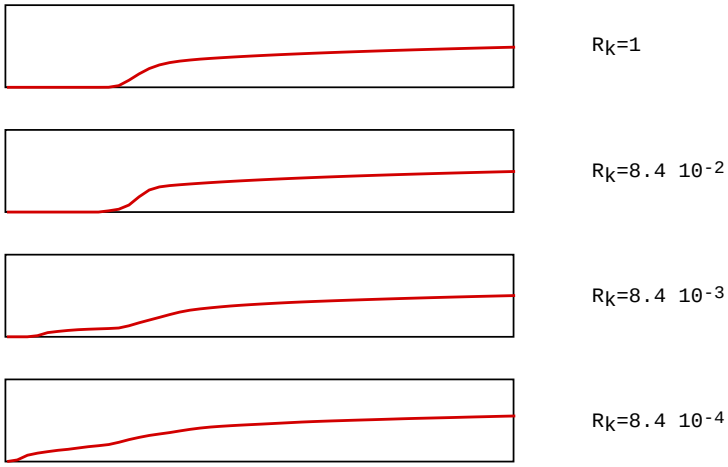

Figure 57: saturation curves corresponding to the saturation plots reported in Figure 56.

(b)- Pseudo relative and fractional flow curves

The output saturation field at each time step has been used to determine the fractional flow and pseudo relative curves for each of the simulations performed above. In Figure 58 the pseudo relative curves for varying permeability contrast are shown.

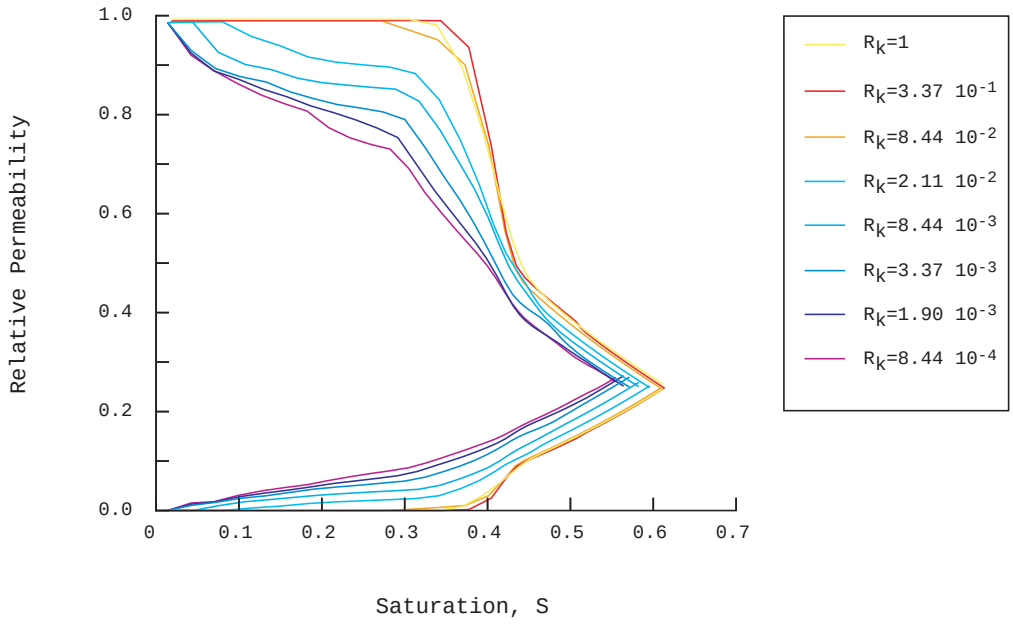

Figure 58: pseudo relative curves determined for a permeability ratio varying from 1to 10^{-4} for a pattern with *D*=2, *a*=1.5, and *P*=64.8%.

When increasing the contrast, we observe a general decrease of the slope and an earlier mobility of the CO_2. The modification in the slope is effective when R_k is lower than $8\ 10^{-2}$. For greater ratio the system behaves similarly to the matrix case (R_k=1). Modification in the slope is sharp and occurs for R_k lying between $8\ 10^{-2}$ and $2\ 10^{-2}$. The difference in the irreducible CO_2 saturation between the two extreme cases - matrix case for which R_k=1, and strong barriers case for which $R_k=10^{-4}$ - is important and we pass from a saturation of 0.4 to a saturation close to 0.

The fractional flow curves display similar trends and shows the same tendency of decrease in the irreducible CO_2 saturation (Figure 59). Also, the shape of the fractional curves shows different behaviour. For small permeability contrast, we observe a sharp sigmoidal curve with an inflexion point similar to that observes in the matrix only case. On contrary, for higher ratio, a more continuous curve is observed where the inflexion point typical of FFF curves is less pronounced. Therefore, since variations in the curve are less important this imply a decrease of the front velocity (corresponding to $\partial FFF / \partial S$) and in the limit $R_k \rightarrow 0$, we should observe a linear fractional flow curve, which imply a constant front velocity.

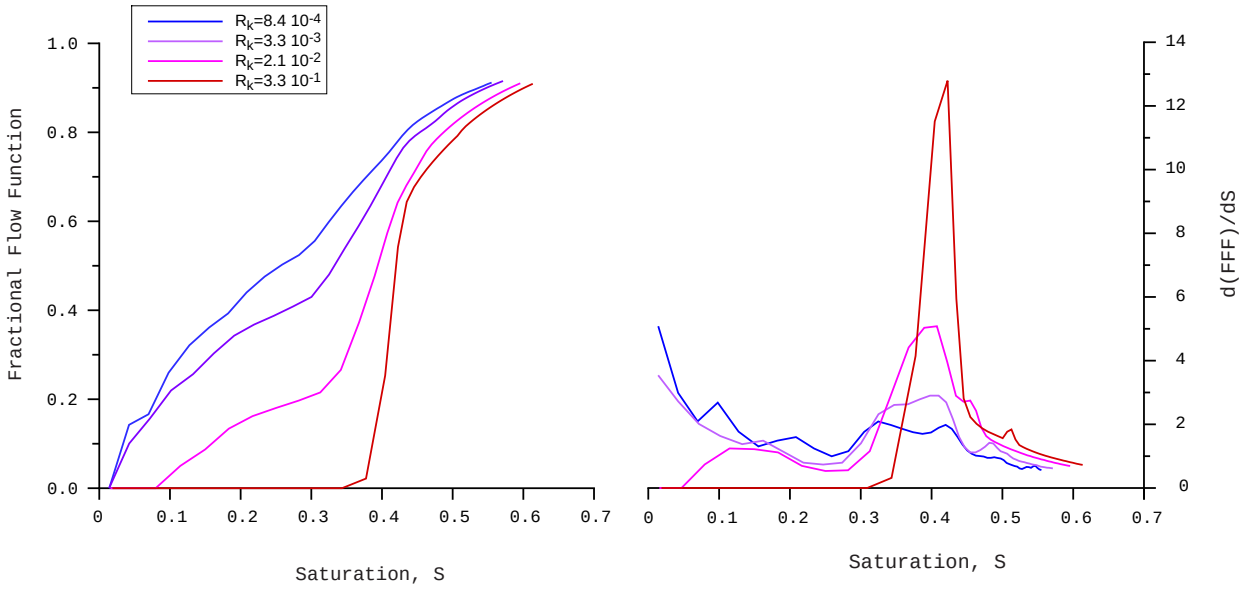

Figure 59: Fractional flow curves (left) and its derivative (right) determined for a permeability ratio varying from 1to 10^{-4} and for a pattern with *D*=2, *a*=1.5, and *P*=64.8%.

The derivative of FFF with respect to the saturation is presented in Figure 59. When decreasing R_k, we observe a decrease in the amplitude of the peak, which also broaden. Associated to it, an increase in $\partial FFF / \partial S$ is observed for saturation close to 0. Such an increase can be related to the passage of the invading fluid in the narrow channel in the very first time step (as observe in Figure 55).

For each of the performed simulation, using the pseudo relative curves, we have determined the irreducible CO_2 saturation (IS_{CO2}), corresponding to the saturation needs for the CO_2 to be mobile. We also estimate the cross over saturation S_c. Using the derivative of the fractional flow function with respect to the saturation S, we estimates the CO_2 saturation S_p when the velocity of the front reach its maximum (peak saturation) and the intensity of the peak. Each of these results are reported in Table 17.

Name	K_f/K_m	IS_{CO2}	S_c	Sp for max[∂(FFF)/ ∂Sat]	Peak Intensity
R1a	$2.11\ 10^{-4}$	$1.47\ 10^{-2}$	0.618310	0.420295	1.69363
R1b	$8.44\ 10^{-4}$	$1.41\ 10^{-2}$	0.550550	0.4199	1.98258
R1c	$1.90\ 10^{-3}$	$1.38\ 10^{-2}$	0.554054	0.421275	2.44254
R1d	$3.37\ 10^{-3}$	$1.39\ 10^{-2}$	0.561310	0.410023	2.90108
R1e	$8.44\ 10^{-3}$	$4.41\ 10^{-2}$	0.578274	0.414079	4.01591
R1f	$2.11\ 10^{-2}$	$7.97\ 10^{-2}$	0.594022	0.389611	5.03228
R1g	$8.44\ 10^{-2}$	0.27203	0.608848	0.420586	11.157
R1h	$3.37\ 10^{-1}$	0.309139	0.613275	0.422606	12.7936
R1i	1	0.271433	0.615937	~ 0.4045	~ 8.52

Table 17: Irreducible CO_2 saturation (IS_{CO2}), cross over saturation S_c, peak saturation Sp and peak intensity determined using the pseudo relative and fractional flow curves for the pattern R3 and for various permeability contrasts (from 1 to 10^{-4}).

Evolution of IS_{CO2} and S_c with respect to the permeability ratio is reported on Figure 60. Dependence of the peak saturation Sp and of the peak intensity is reported on Figure 61. From Figure 60 (left), we observe a sigmoidal shape for the evolution of IS_{CO2} and two thresholds can be individualised: the first one corresponds to a permeability ratio of 10^{-1} and the second to 10^{-2}. When $R_k>10^{-1}$, or $R_k<10^{-2}$, the saturation required for the CO_2 to be mobile is constant and independent on the permeability ratio. On contrary, for ratio between 10^{-1} and 10^{-2} a strong dependence is observed. Each of these three domains is related to the action either of the matrix or of the heterogeneities. When $R_k>10^{-1}$ the matrix dominates the saturation evolution and we observe IS_{CO2} value close to the matrix only case. For $R_k<10^{-2}$, the permeability contrast is important and since the proportion of barrier elements is important, the saturation is controlled by the presence of path as previously observed on Figure 55 (top). The invading fluid is mobile as soon as it is injected. Between these two R_k values, we are in a transitional zone where both matrix and heterogeneities are important. These results are qualitatively similar to what has been observe on Figure 22 (section C-3).

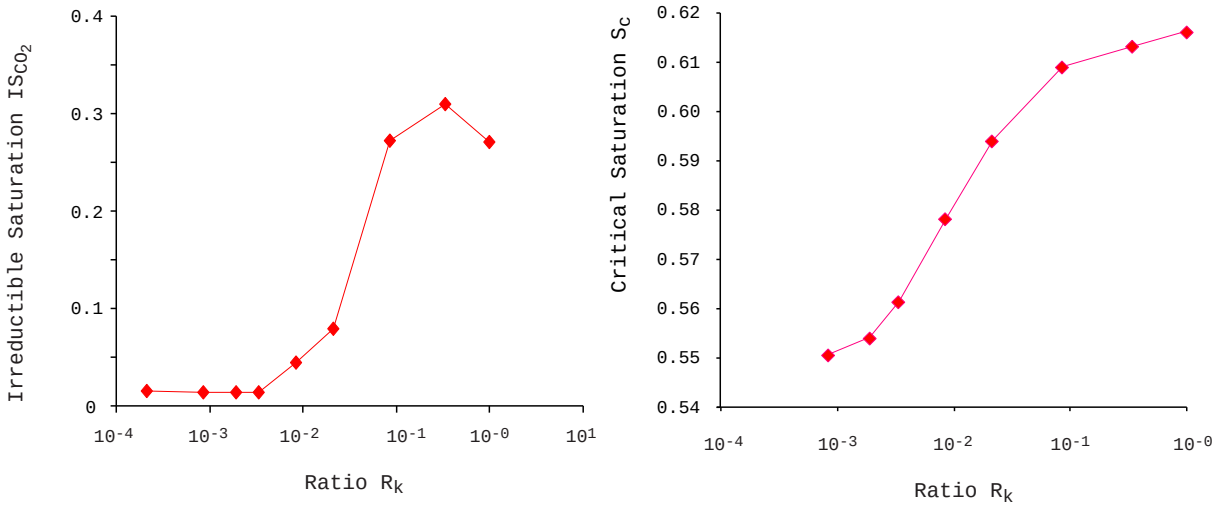

Figure 60: Evolution of the irreducible saturation IS_{CO2} (left) and of the cross over saturation S_c (right) with respect to the permeability ratio R_k.

The evolution of the cross over saturation with respect to the permeability ratio R_k displays the same type of evolution (Figure 60 - right). We observe a lower value of S_c for strong contrast. This indicates that the saturation at which the invading fluid becomes predominant is less.

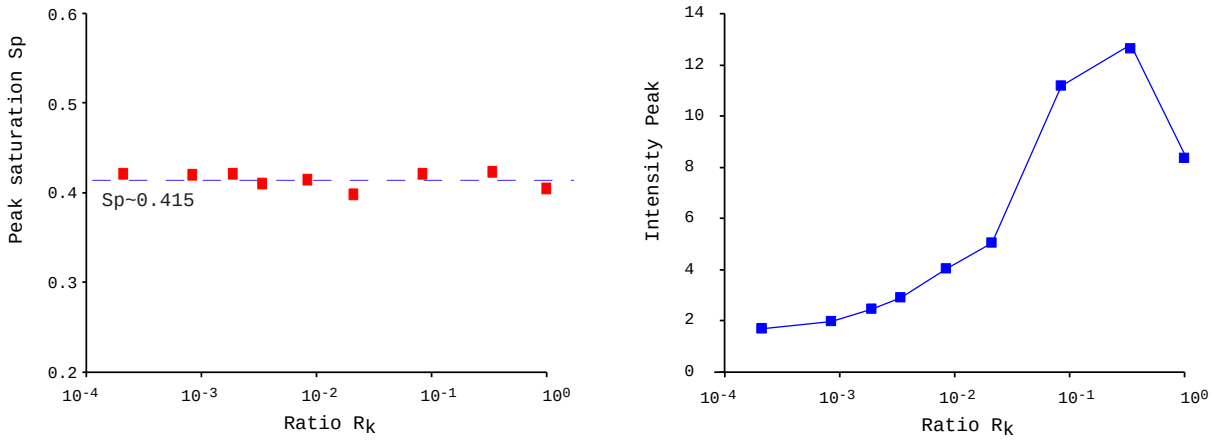

Figure 61: evolution of the peak saturation Sp (left) and of the peak intensity (right) with respect to the permeability ratio.

The saturation for which the front velocity reach its maximum (Sp) is insensible to the permeability ratio as illustrated in Figure 61 (left) and is equal to the value observed for the matrix only case. On contrary the intensity of the peak decreases and for small R_k tends toward a constant value around 2. Therefore, since Sp is constant and close to the value of the matrix only case, and since peak intensity decrease, this signifies that the role of the matrix becomes less important.

2- Density dependence

2-1 Presentation

We have studies in more details here the influence of the density (the proportion of grid element acting as barriers on the geometry of the front). As previously we have considered a homogeneous pattern (D=2) and a length exponent equal to 1.5. Fractures are oriented at 30° with respect to the inflow boundary. The matrix is heterogeneous and the varying parameter is the density p, corresponding to the percentage of elements that belongs to a layer.

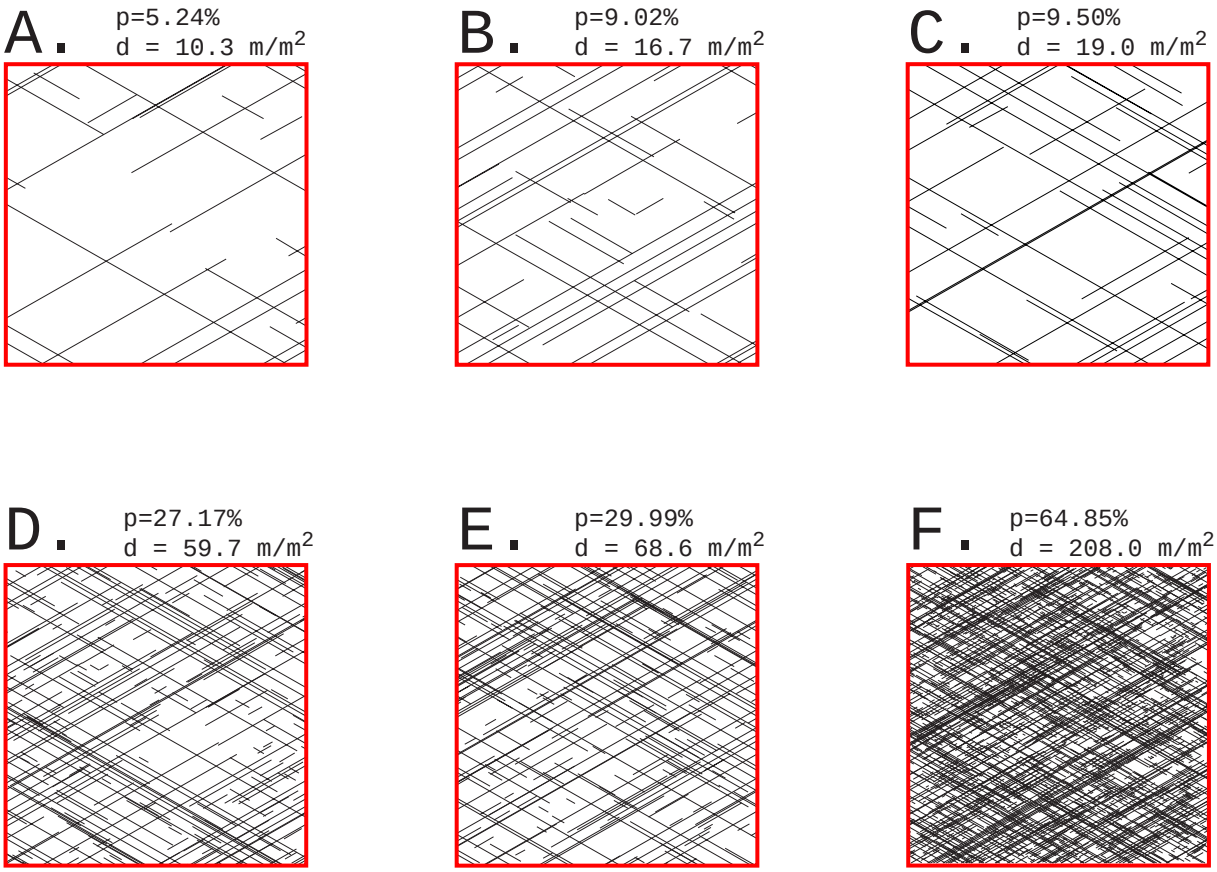

Figure 62: geometry of the two different patterns used to establish the dependence of the permeability ratio R_k on the geometry of the front.

Simulations have been performed for a permeability ratio equal to 16.8, 10^{-3} and 2 10^{-4}. Hence, the cases where fractures act as preferential path and as barriers have been considered. Patterns are represented on Figure 62 and Table 18 summaries the geometrical characteristics of each of these patterns. The simulations performed are summarised in Table 19 and Table 20.

Name	Area (m^2)	Mass (m)	Density (m/m^2) (d= Mass/Area)	N_{layers}	Density (m^{-2}) ($d=N_{layers}/Area$)	N_{int}	l_{max} (m)	P_{elt} (%)
Pattern A	1	10.36	10.36	30	30	26	1.073	5.24
Pattern B	1	16.78	16.78	42	42	55	1.151	9.02
Pattern C	1	19.01	19.01	37	37	85	1.153	9.50
Pattern D	1	59.74	59.74	255	255	735	1.151	27.17
Pattern E	1	68.60	68.60	255	255	1047	1.151	29.99
Pattern F	1	208.0	208.02	2000	2000	9552	1.149	64.85

Table 18: geometrical parameters of the networks used to study the density dependence.

Simulation	η_{water} (Pa.s)	η_{CO2} (Pa.s)	Flow rates ($m.s^{-1}$)	Φ_l	Φ_m	<Km> (darcy)	σ	Aperture (μm)	Ratio R_k
D1a	1	10	0.225	0.1	0.3	0.2	0.15	0.05	$1.05\ 10^{-3}$
D1b	1	10	0.225	0.1	0.3	0.2	0.15	0.05	$1.05\ 10^{-3}$
D1c	1	10	0.225	0.1	0.3	0.2	0.15	0.05	$1.05\ 10^{-3}$
D1d	1	10	0.225	0.1	0.3	0.2	0.15	0.05	$1.05\ 10^{-3}$
D1e	1	10	0.225	0.1	0.3	0.2	0.15	0.05	$1.05\ 10^{-3}$
D1f	1	10	0.225	0.1	0.3	0.2	0.15	0.05	$1.05\ 10^{-3}$
D1a2	1	10	0.225	0.1	0.3	1	0.15	0.05	$2.11\ 10^{-4}$
D1b2	1	10	0.225	0.1	0.3	1	0.15	0.05	$2.11\ 10^{-4}$
D1c2	1	10	0.225	0.1	0.3	1	0.15	0.05	$2.\ 11\ 10^{-4}$

Table 19: parameters assigned in the simulation using the different pattern shown on Figure 62 when layers act as barriers to the flow.

Simulation	η_{water} (Pa.s)	η_{CO2} (Pa.s)	Flow rates ($m.s^{-1}$)	Φ_l	Φ_m	<Km> (darcy)	σ	Aperture (μm)	Ratio R_k
D2a	1	10	0.225	0.05	0.5	0.005	0.10	1.0	16.88
D2b	1	10	0.225	0.05	0.5	0.005	0.10	1.0	16.88
D2c	1	10	0.225	0.05	0.5	0.005	0.10	1.0	16.88
D2d	1	10	0.225	0.05	0.5	0.005	0.10	1.0	16.88
D2e	1	10	0.225	0.05	0.5	0.005	0.10	1.0	16.88
D2f	1	10	0.225	0.05	0.5	0.005	0.10	1.0	16.88

Table 20: parameters assigned in the simulation using the different pattern shown on Figure 62 when layers act as preferential path to the flow.

2-2 Saturation evolution - barrier case

We first consider the results obtained with simulation D1 for which fractures act as barriers and $R_k=10^{-3}$ (simulations D1a to D1f). The percentage *p* of grid elements that inhibits the flow varies from 5 to 64%.

(a)- Snapshot of saturation evolution

T1 T2 T3 T4

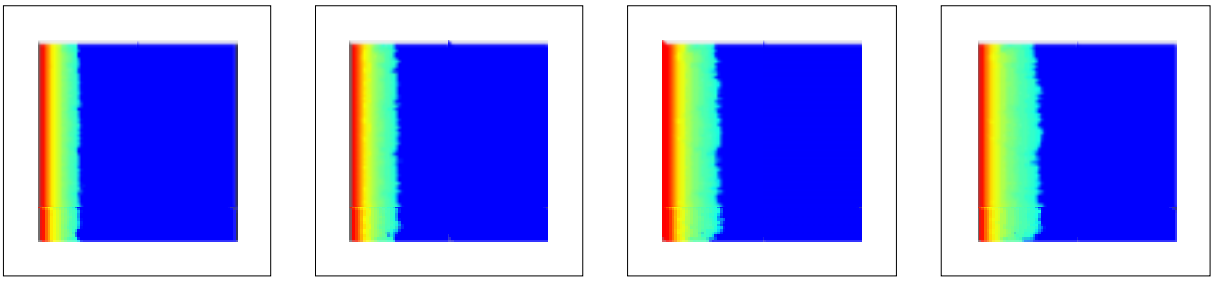

p=5.24%

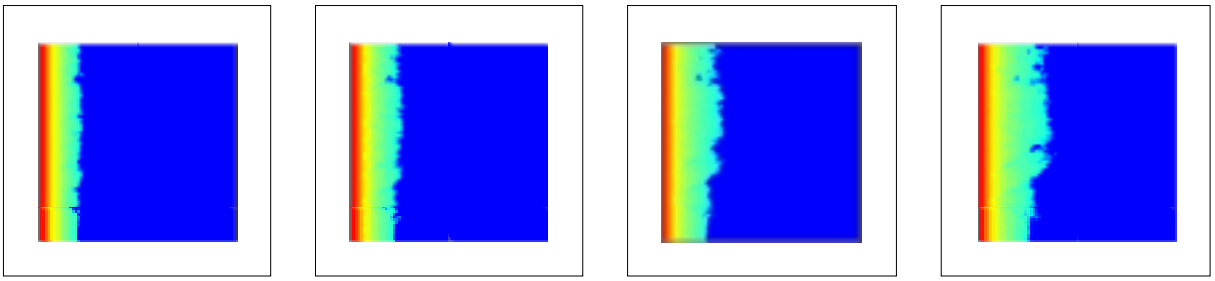

p=9.50%

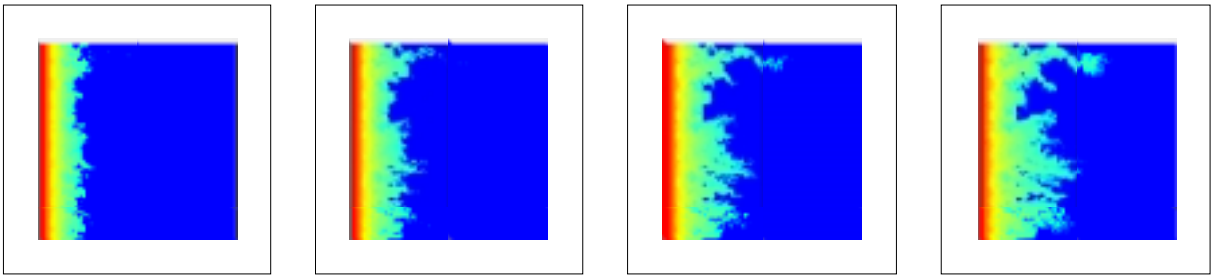

p=29.99%

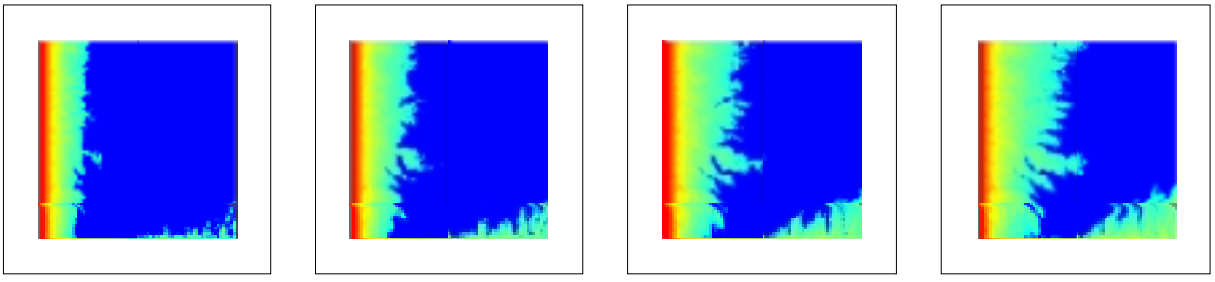

p=64.85%

Figure 63: snapshot showing the saturation field at four different time step for the same permeability ratio and four different densities.

The saturation field indicates clearly that density of barrier is a major factor affecting the dispersion of the invading fluids. We pass from a front geometry regime where fingering is limited in size (p<10%) to a regime where fingering dominates (p~30%). For greater p value, and as observed in § 1-3 (section D-3), the system behaves like an impermeable medium where exists a few preferential paths (p~65%).

The front heterogeneity has been quantified using the difference between the position of the maximum saturated element X_{max}, and the position of the minimum unsaturated element X_{min}. This distance has been normalised by the system size and gives a measure of the width of the saturation front. When fingering is important, the width will be large and when not the front has a planar shape. To avoid artefacts related to boundary effects, we do not take into account the elements close to the lower and upper borders. Also, we consider only the first time steps, when the saturation front does not connect the right and left boundaries of the system.

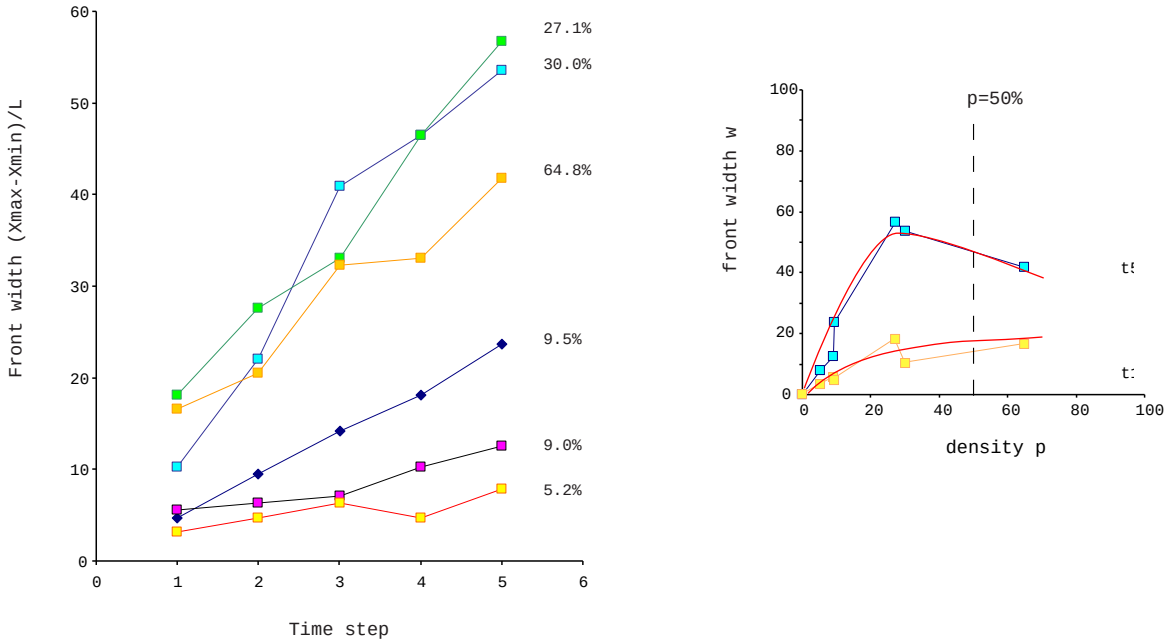

Figure 64: evolution for the five first time step of the front width *w* for various layer densities (left) and evolution of *w* with respect to density for time step t1 and t5 (right) - line are only guide for the eyes.

Figure 64 (left) shows the evolution of the front width with respect to the saturation (time steps) for the different patterns study. The width of the front is increasing regularly with time for all considered densities with a slope that depends on p. When p<9.0% the slope is small indicating that the saturation front does not present strong spatial variations: the front is planar. On contrary for p>10% the front width takes rapidly strong value. In that case, the front width is already bigger than the width observed at time step t5 when p=5 or 9%. These high values indicate the early development of fingering.

Since geometrical parameters (length exponent and fractal dimension) are the same, the modification of the front geometry and the development of fingering are associated to the density of elements acting as barriers. Figure 64 (right) shows the dependence of the front width with respect to the density for two different steps (t1 and t5). In the first saturation step (t1) the width increase with p indicating the development of fingering. For t5, the increase is continuous until p~30% and shows a small decrease afterward. This observed decrease when p~65% and the general evolution of the saturation field has to be associated to the proportion of preferential path q present in the system

(equal here to ~35%). Also as noted in § 1-3, this low value can be related to the presence of the homogeneous permeable zone located at the bottom of the model and to its strong influence on the general geometry of the front.

To better constrain the way the front is moving we have reported the normalised minimum and maximum front position X_{min} and X_{max} with time for each considered density (Figure 65). When the front is planar (p=5.2% and 9.0%), the lower and bigger position are evolving similarly. On contrary when fingering develops, only the maximum distance is increasing, the minimum one being constant with time.

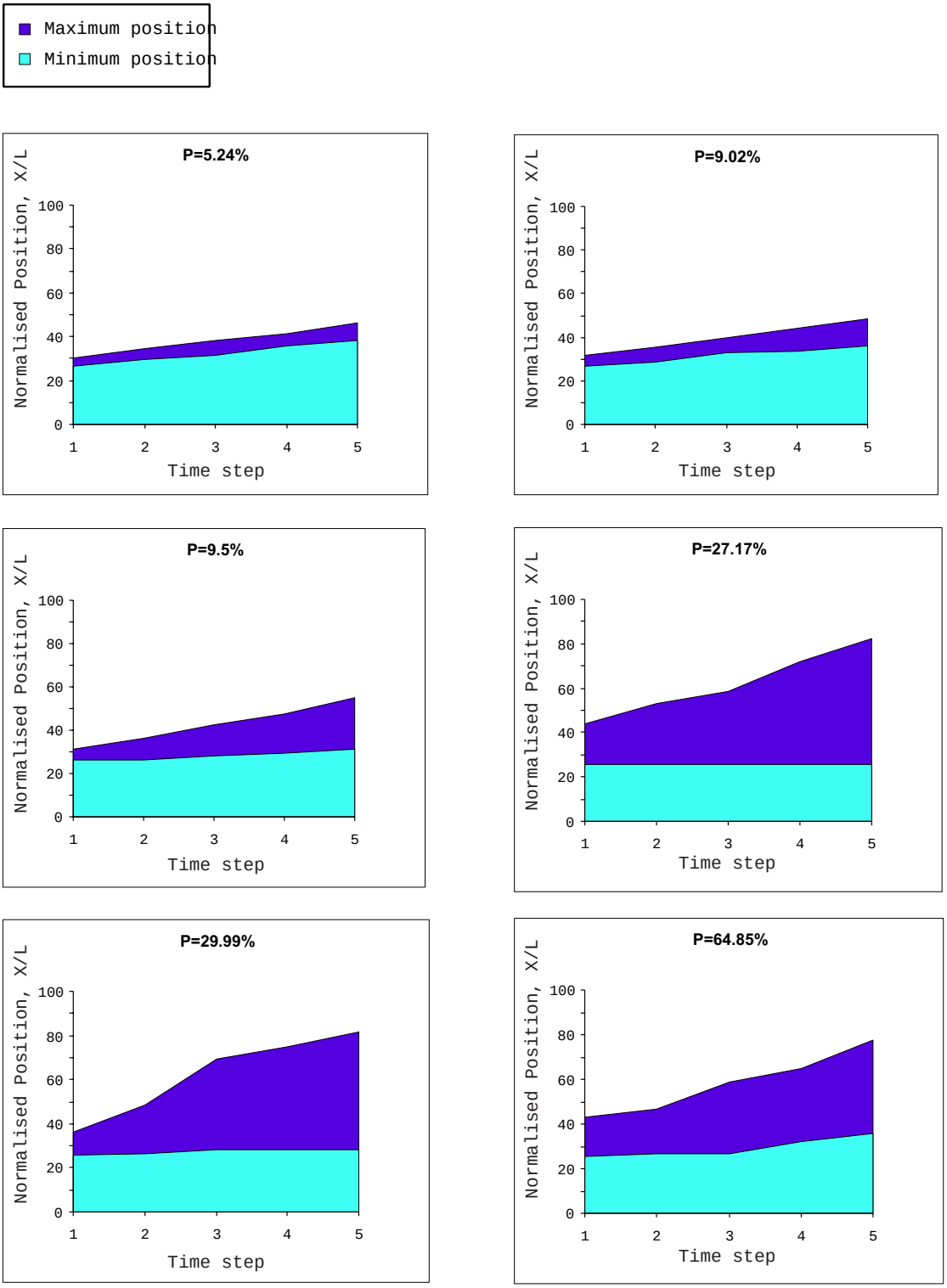

Figure 65: Maximum and minimum position of the front for the 5 first time steps and for various density.

(b)- Time evolution

Time evolution of the saturation is shown Figure 66. For low density (p=5%), the front appears planar, and a gradual increase, similar to the case of matrix alone. When p~10%, the arrival of the CO_2 at the outflow boundary is spread over a longer period and is more irregular as shown by the lines going through the simulation. These lines reflecting the irregularity arrival of CO_2 are more numerous when p~30%. Saturation curves indicate also this early arrival of CO_2 when density of layers increases. Finally, for p~65%, the saturation appears more heterogeneous as indicated by the red spot in the right-lower part. This is related to the existence of the escape structure situated at bottom side of the pattern. In that latest case, the contrast is so important that the matrix constitutes a preferential way through which CO_2 flow.

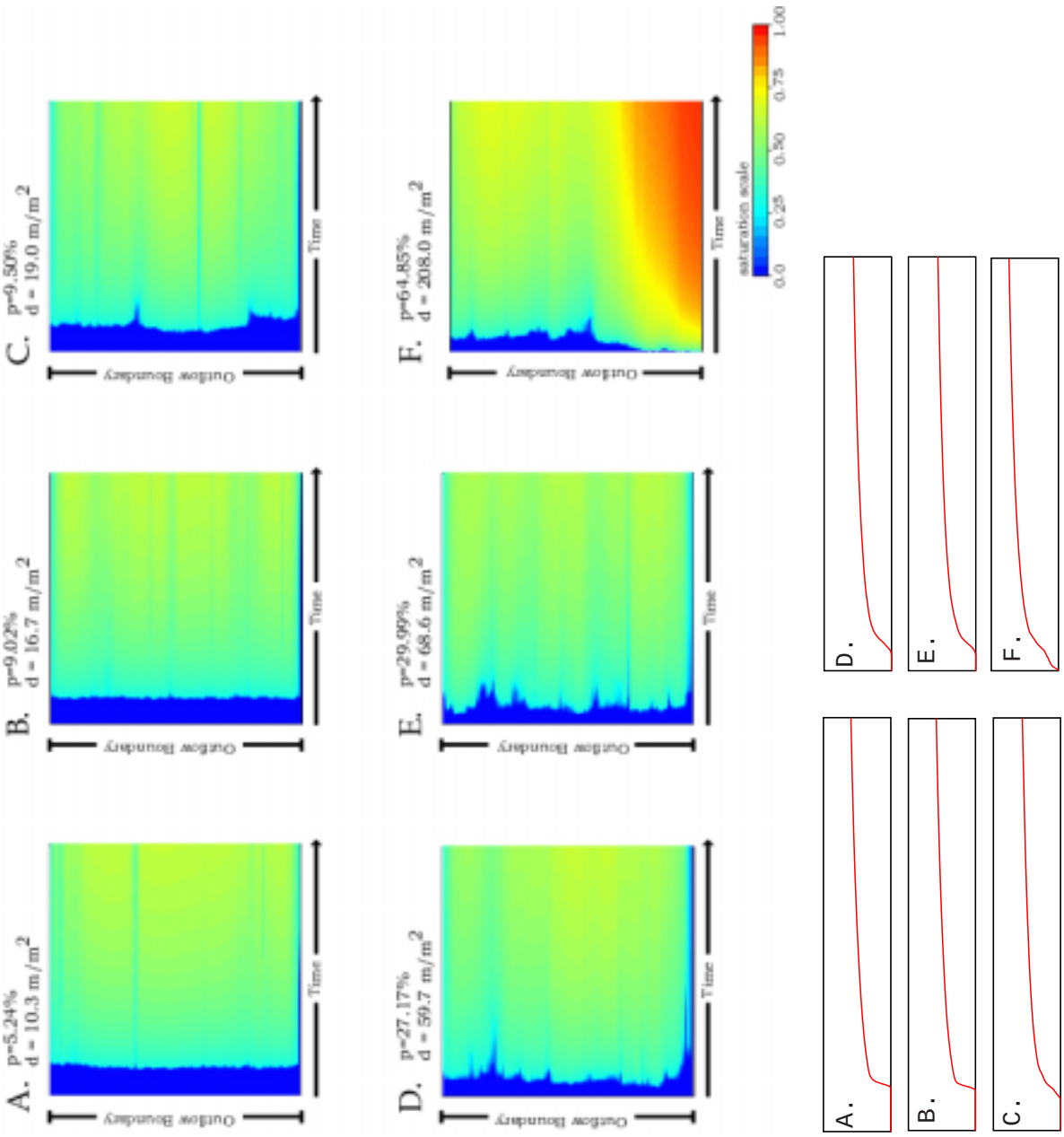

Figure 66: time evolution of the saturation field for the six different considered density and saturation curves associated to it.

2-3 Saturation evolution - preferential path case

The case where the fractures act as preferential path for the invading fluid has also been study. We have considered a permeability ratio of 16.8. Figure 67 shows the saturation field observed during the four first time steps when layers act as preferential path (R_k=16.8) and when layers act as barriers (R_k=10^{-3}). In all cases, fingering develops and the front width is much more important when layers act as paths. Also, the geometry of the front appears thinner and more detailed. For small proportion of heterogeneities, difference in front geometry for path and barrier cases is important and CO_2 reach the opposite system side more rapidly in the paths case than in the barrier case. When *p*~30% the difference between fronts geometry is smoother, related in that case to a similar proportion of barrier and path present in both simulations. Also the moment when the invading fluid reach the outflow boundary is comparable. Finally, when *p*=65%, the opposite is observed and it is when layers act as barrier that connection between inflow and outflow boundary is first achieved.

Figure 68 displays the time saturation for all patterns. Compare with the case of barriers, the front shows more irregular shape and saturation occurred faster. Arrival of CO_2 at the outflow boundary is enhanced by fractures as illustrated by the presence of horizontal strips. Also, the arrival of CO_2 depends on the density of heterogeneities and the more important *p*, the earlier the saturation.

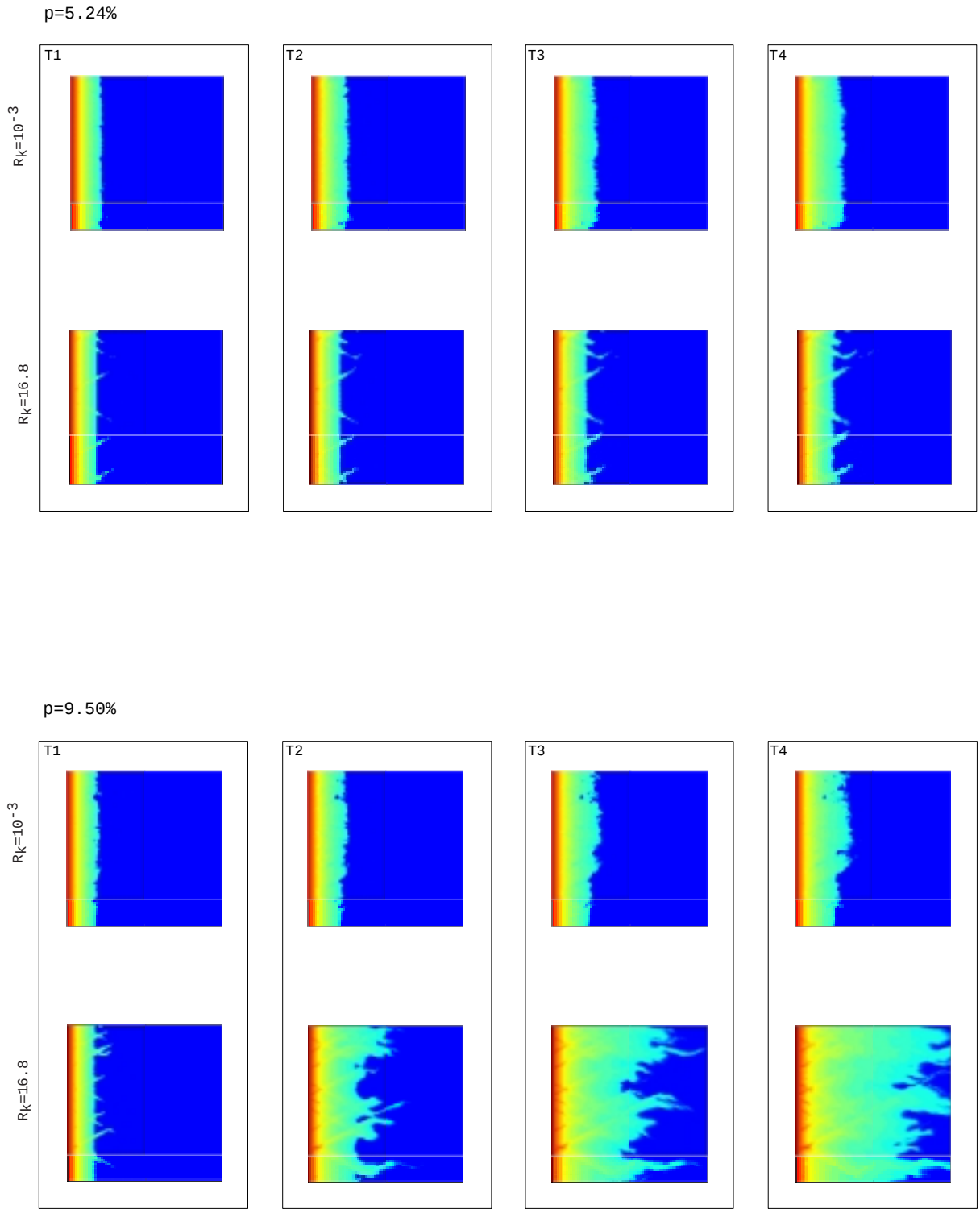

Figure 67: comparison of the saturation field for the four first time step when layers act as barrier ($R_k=10^{-3}$) and as preferential path ($R_k=16.8$), for pattern A (top) and C (bottom).

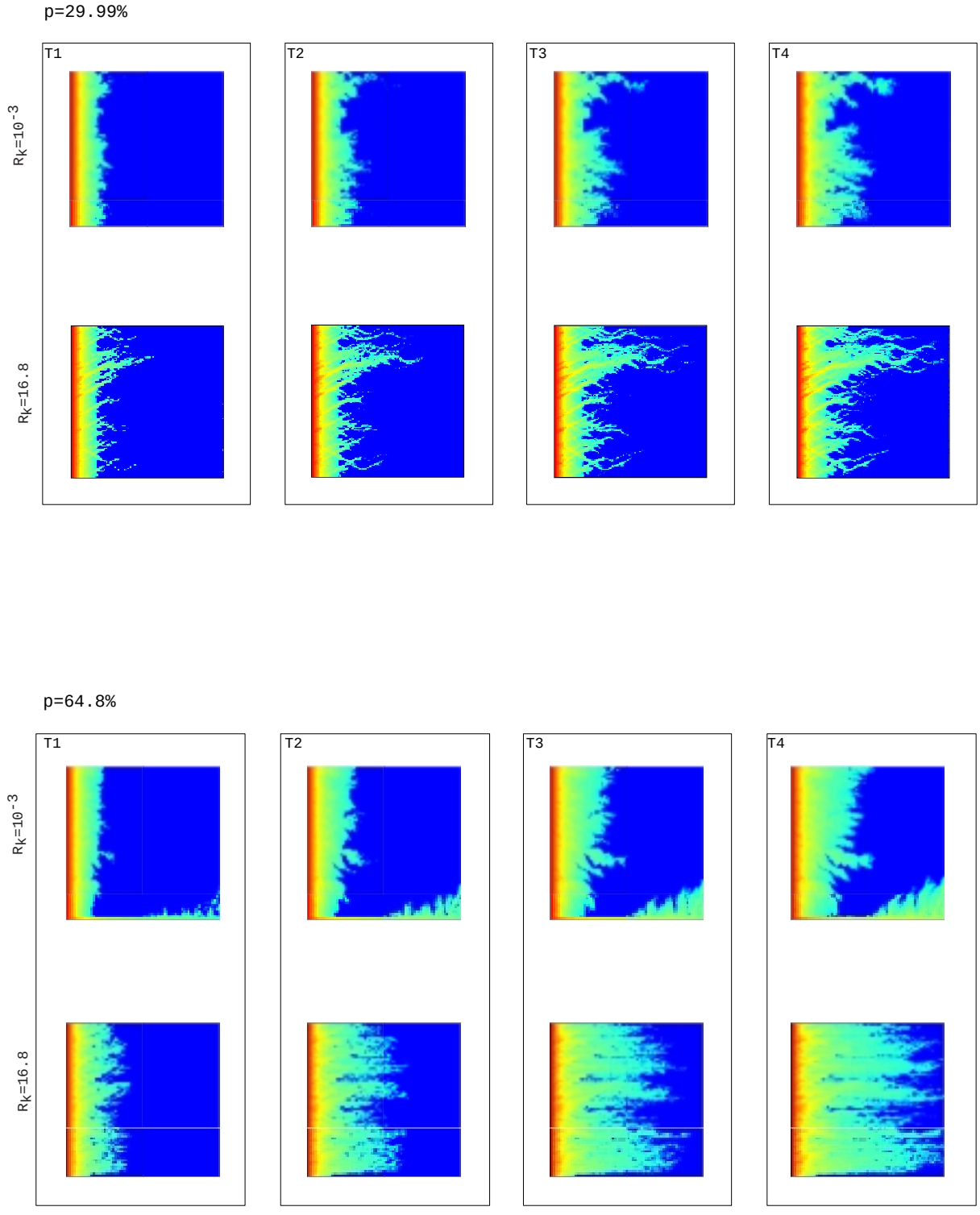

Figure 67 (continued): comparison of the saturation field for the four first time step when layers act as barrier ($R_k=10^{-3}$) and as preferential path ($R_k=16.8$), for pattern E (top) and F (bottom).

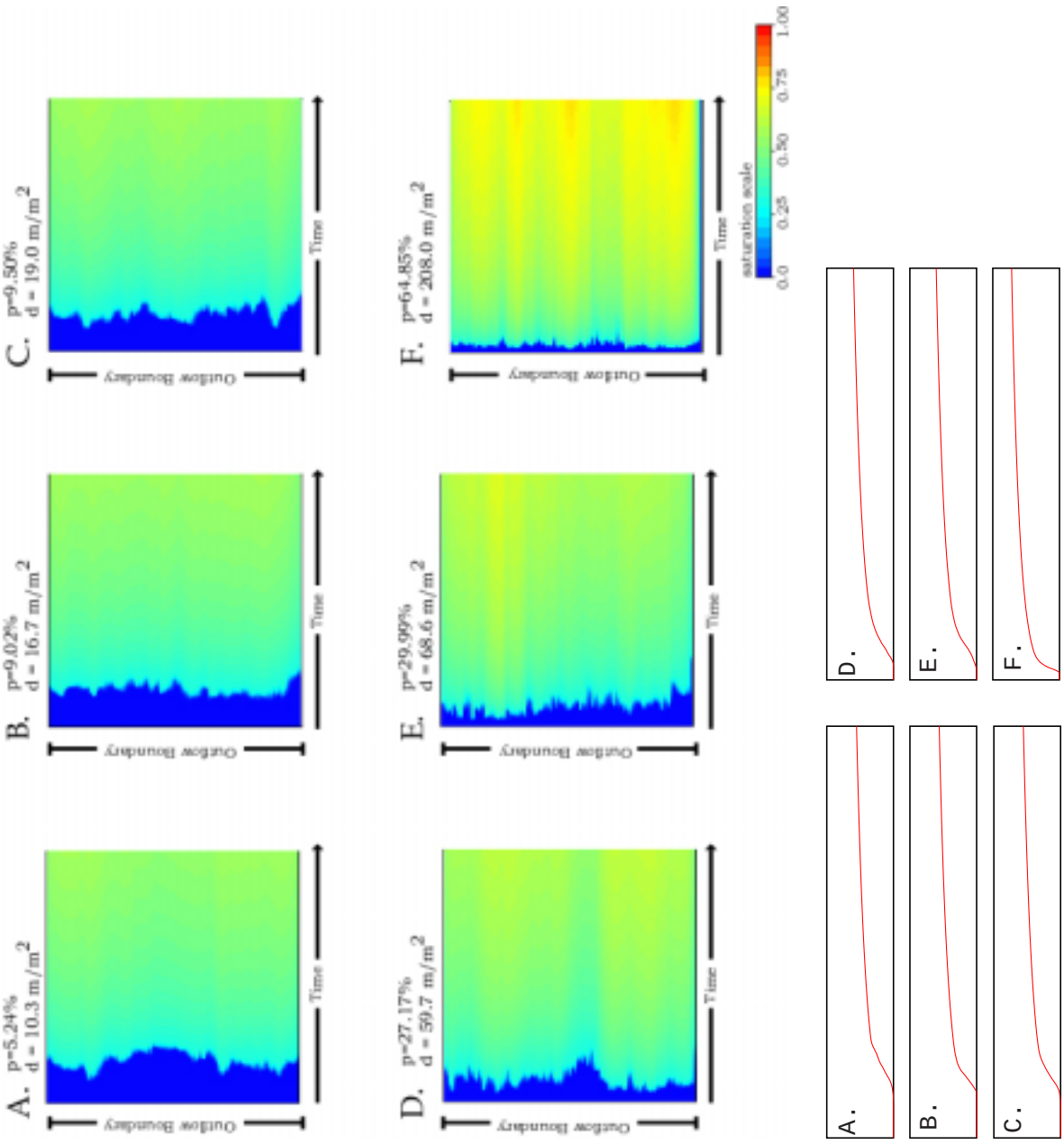

Figure 68: Time evolution of the saturation at the outflow boundary for all considered patterns (from A. to F). Corresponding saturation curves are shown on the right part.

A detailed comparison of the saturation curves has been made to better determine how heterogeneities influence the flux (Figure 69). For each density and at each time step, we have reported the difference between the saturation at the outflow boundary for barriers and paths cases. When the difference $S_{barr}(t)$-$S_{path}(t)$ is positive a time t, saturation at the outflow boundary in the barrier case is more important. On contrary when $S_{barr}(t)$-$S_{path}(t)$ is negative, saturation is greater when layers act as path.

All curves display two peaks: first a small negative peak and then a narrow positive one. This suggests that the connection between the two opposite sides of the system is faster in the case of path (negative peak). Also, the positive peak suggests that the quantity of injected CO_2 that arrives at the outflow boundary is much more important in the case of barrier. Finally, the behaviour of the tail for large time differs with p. When p>30% $S_{barr}(t)$-$S_{path}(t)$ remains negative which indicates that the saturation in the case of preferential path is more important. On contrary, when p<30%, $S_{barr}(t)$-$S_{path}(t)$ is positive which indicates that the saturation at the outflow boundary is much more important for barriers case.

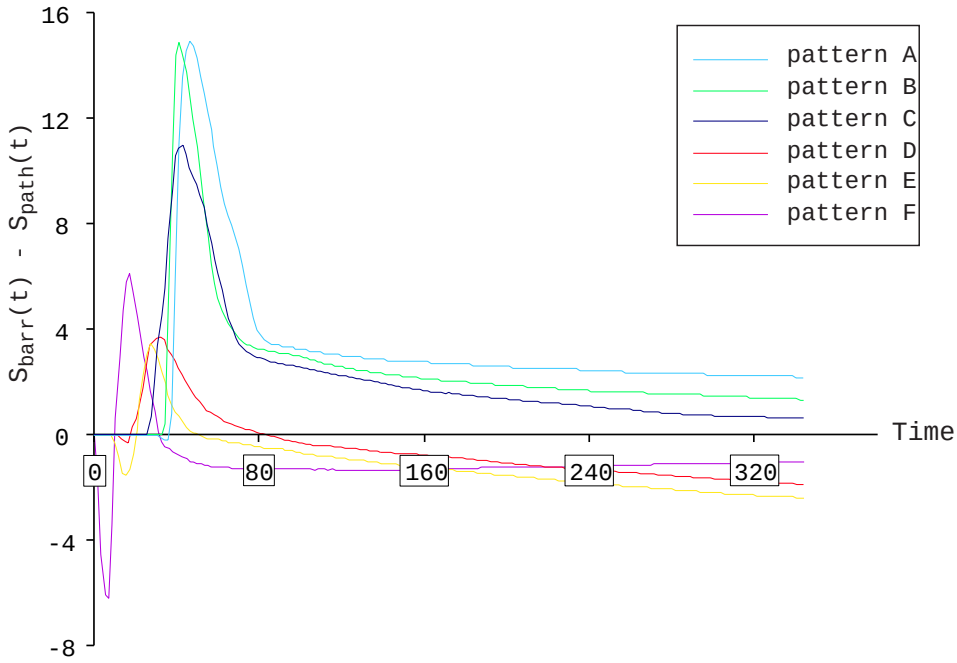

Figure 69: evolution of the saturation difference $S_{barr}(t)$-$S_{path}(t)$ for the same pattern when layers act as barrier and as path with respect to time.

The front width has also been investigated and its evolution with respect to density of heterogeneities *p* and time is shown in Figure 70. We observe an increase of W with *p*, which is more important than when layers act as barriers, nearly equal to the system size (W~ 80% for t5). As for the barrier case, we observe also a small decrease of the front width when *p*>30%. Modification and increase in the front width is also rapid when *p*<30%, and a small increase in the density can change dramatically the saturation field, leading to the development of highly heterogeneous saturation front.

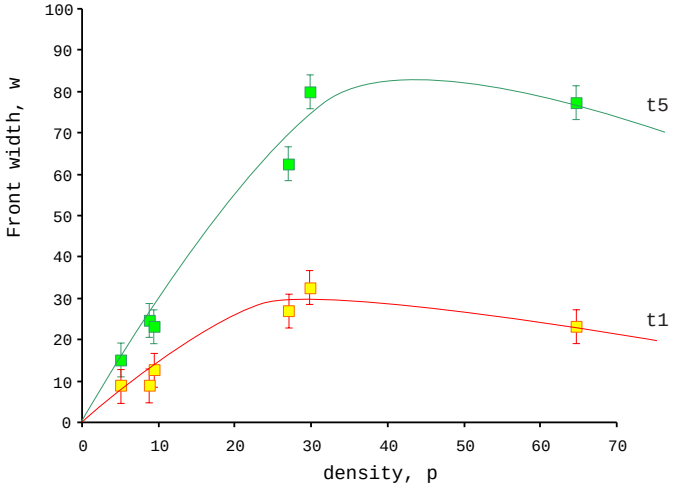

Figure 70: evolution of the front width *w* with respect to the density *p* of layers for time step t1 and t5. Layers act as preferential path and lines are guides for the eyes.

2-4 Pseudo relative and fractional flow curves

We have determined the pseudo relative and fractional flow curves for patterns A to F when R_k=16.8 and 10^{-3}. In both cases, the increase in the proportion of heterogeneities leads to an earlier mobility of the CO_2 as indicated by the diminution of slopes (Figure 71a).

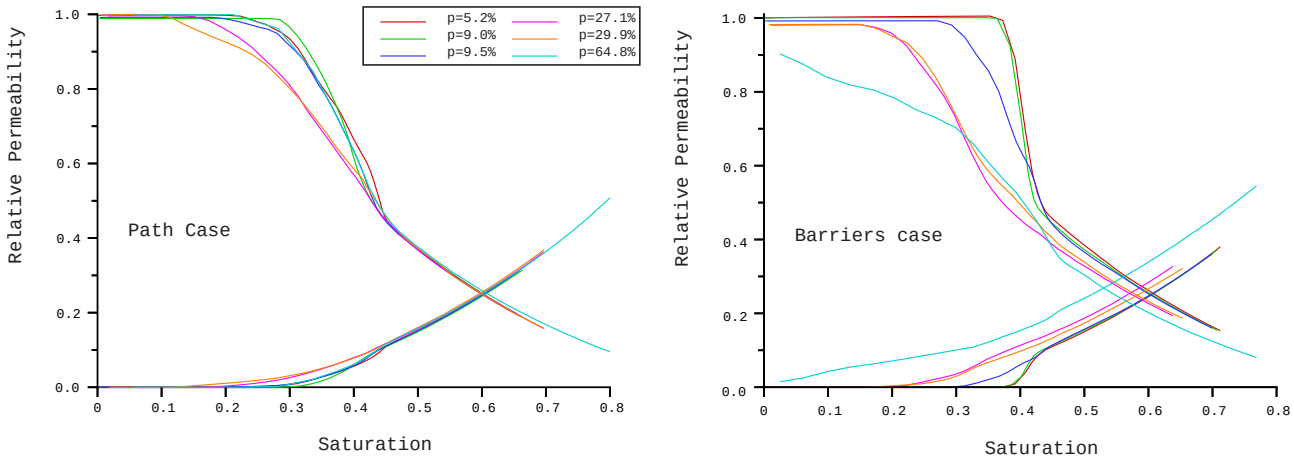

Figure 71a: pseudo relative curves determined for patterns A to F. Left: case where layers act as preferential path. Right: case where layers act as flow barriers.

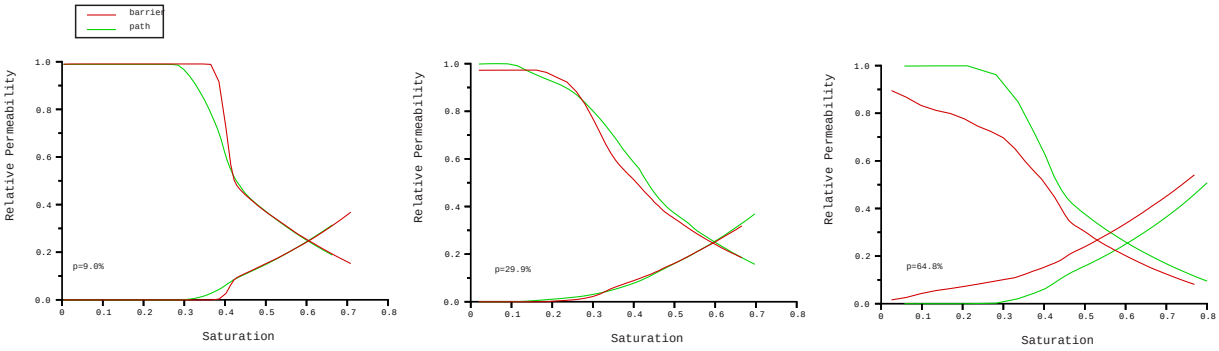

Figure 71(b): Comparison of pseudo relative curves in the case of path (green curve) and barrier (red curves) for density p=9.02% (left), 29.9% (middle) and 64.8% (right).

Comparison of pseudo relative curves for a same pattern but for different permeability ratio, indicates a different behaviour of the CO_2 mobility that depends on the proportion of heterogeneities *p*. When *p*~9%, CO_2 mobility is earlier for path while in the case of barrier, the average behaviour is close to that of the matrix alone case. When p~30% the evolution of pseudo curves is similar for barrier and path cases. Finally when p~65% mobility of CO_2 occurs much more early in the case of layers acting as barriers. In that case as discuss previously, it is the matrix (more permeable than the layers) that act as heterogeneities and that enhance the saturation.

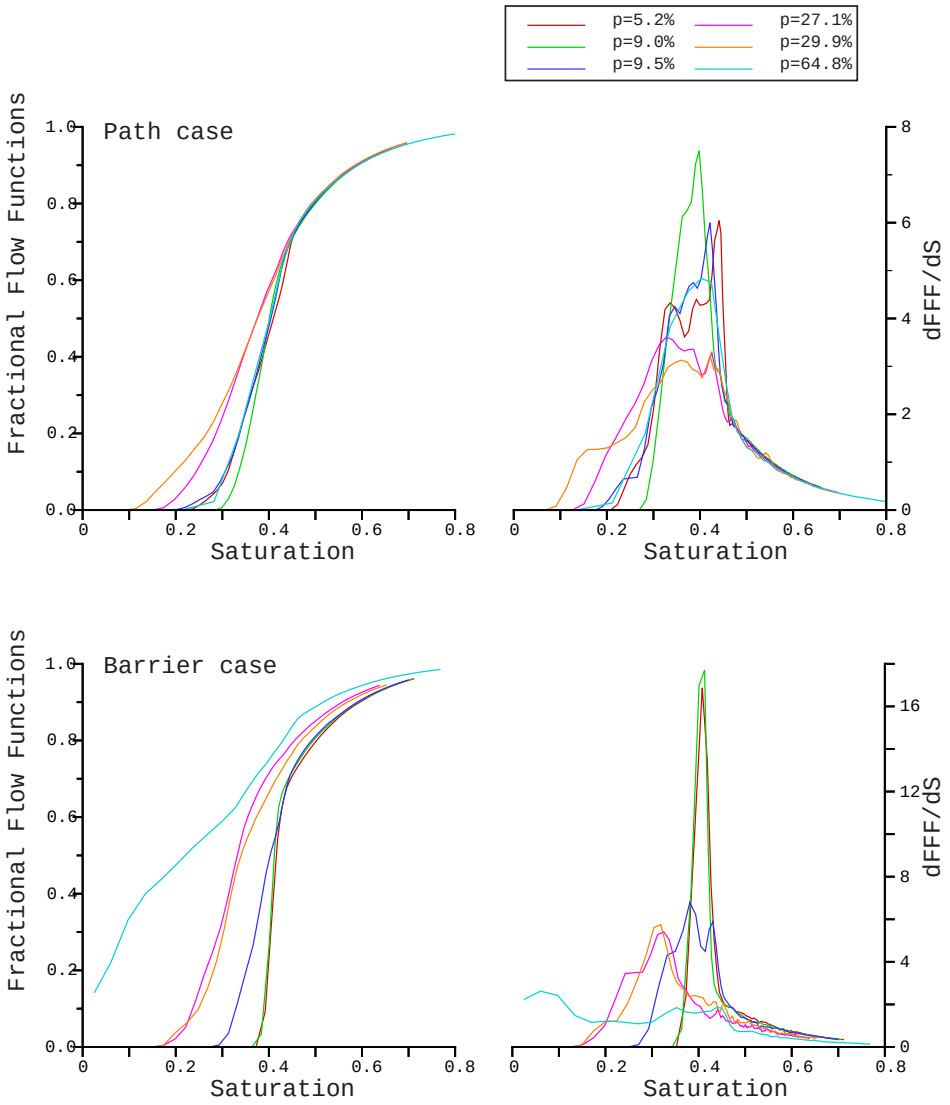

Figure 72a: Fractional flow curves determined for patterns A to F. Top: case where layers act as preferential path. Bottom: case where layers act as flow barriers.

Analysis of fractional flow curves displays the same type of information about the irreducible CO_2 saturation than the pseudo curves shown previously. These curves show also a decrease in the slope that emphasises a decrease in the front velocity, which is also shown with the derivative of the fractional flow with respect to the saturation. Indeed it presents a peak that broaden and whose intensity decrease when *p* increase. For a given density (Figure 72b, top and middle), peaks are also broader and more important in size in the case of barrier than for path. This indicates that a ratio R_k greater than 1 leads to a less important front velocity. When *p*~65%, the opposite is observe as already shown (peak in the path case is more important than in barrier case).

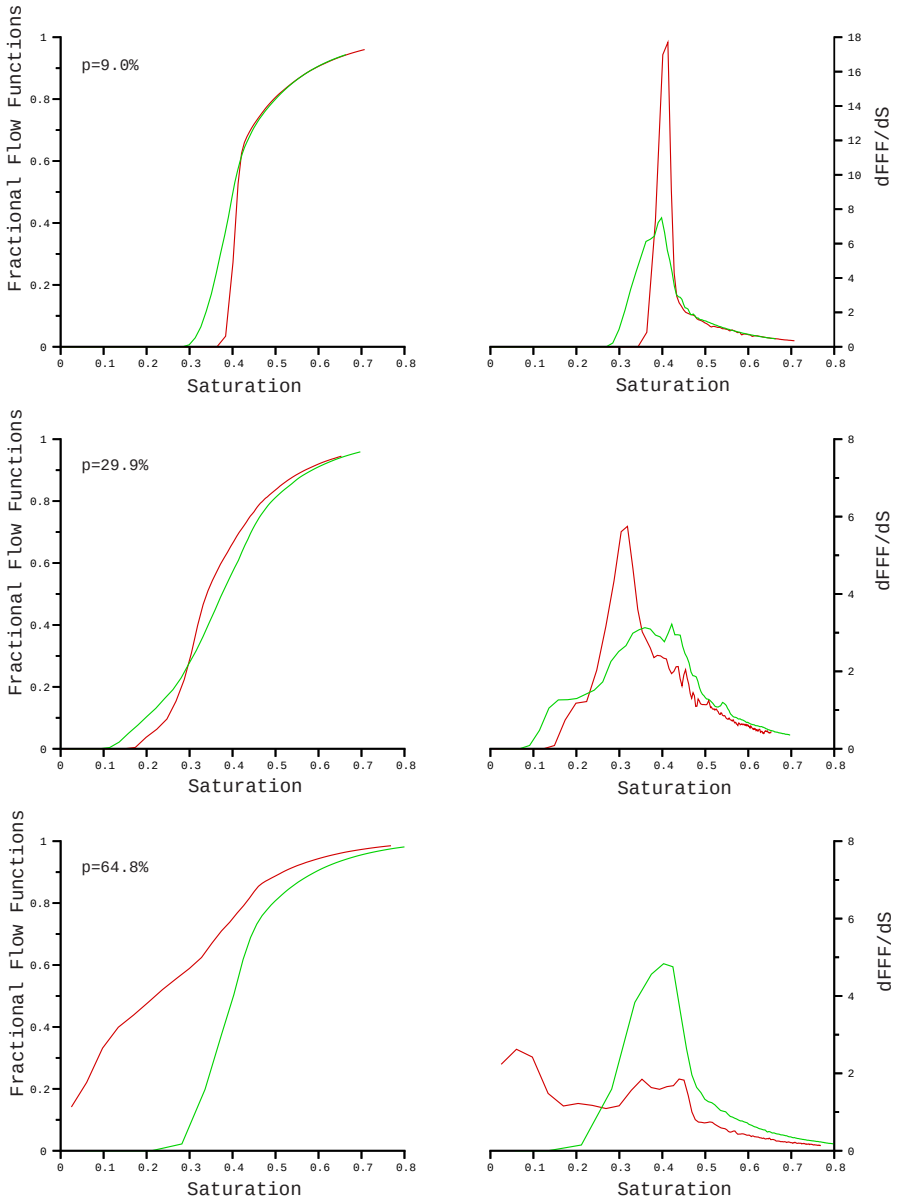

Figure 72b: Comparison of fractional flow curves when layers act as path (green curves) and as barrier (red curves) for a density of 9.02% (top), 29.9% (middle) and 64.8% (bottom).

We have reported the cross over saturation, the irreducible CO2 saturation, the peak saturation at the maximum front velocity, and its intensity with respect to the proportion of heterogeneities (Figure 73).

The cross over saturation S_c presents a different evolution with p, depending on the permeability ratio (Figure 73a-left). In the case of preferential path, S_c remains constant with p, suggesting that the density does not affect the moment when the invading fluid becomes preponderant. On contrary, when layers act as barrier, S_c decreases regularly. The peak saturation at the maximum front velocity displays also the same type of behaviour (Figure 73b-left).

The irreducible CO_2 saturation shows the same type of dependence with p in the case of barrier or path (Figure 73(a)-right). The peak intensity shows a more important decrease with p in the case of barriers (Figure 73(b)-right) which emphasises a decrease of the invading fluid velocity with increasing the proportion of heterogeneities.

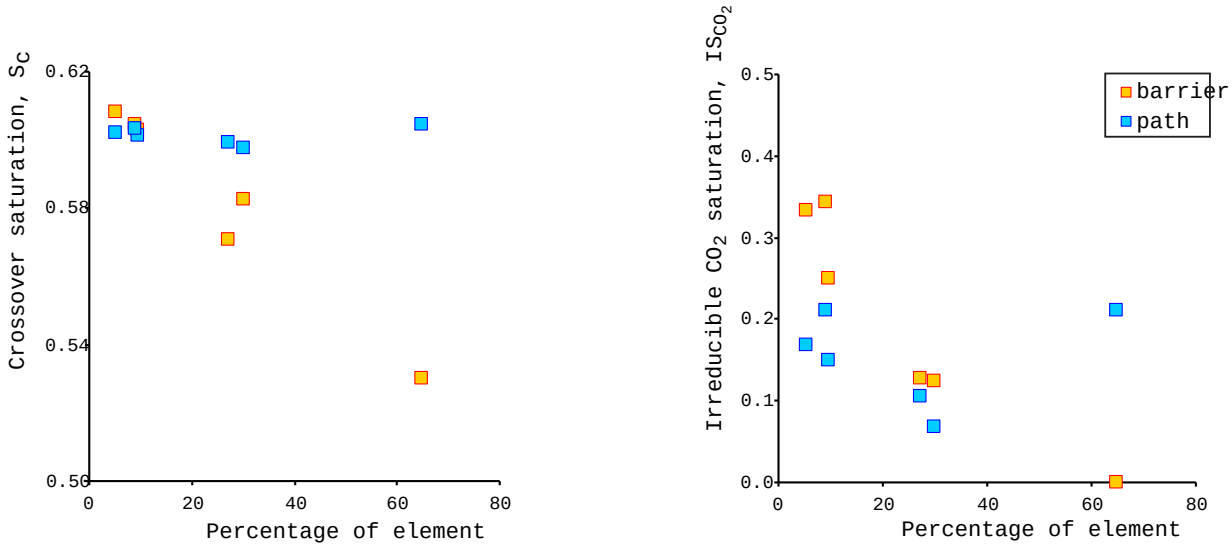

Figure 73(a): dependence of the cross over saturation S_c (left) and of the irreducible CO_2 saturation IS_{CO2} (right) with respect to the percentage of heterogeneities presents in the system when layers act as path (blue square) and as barrier (orange square).

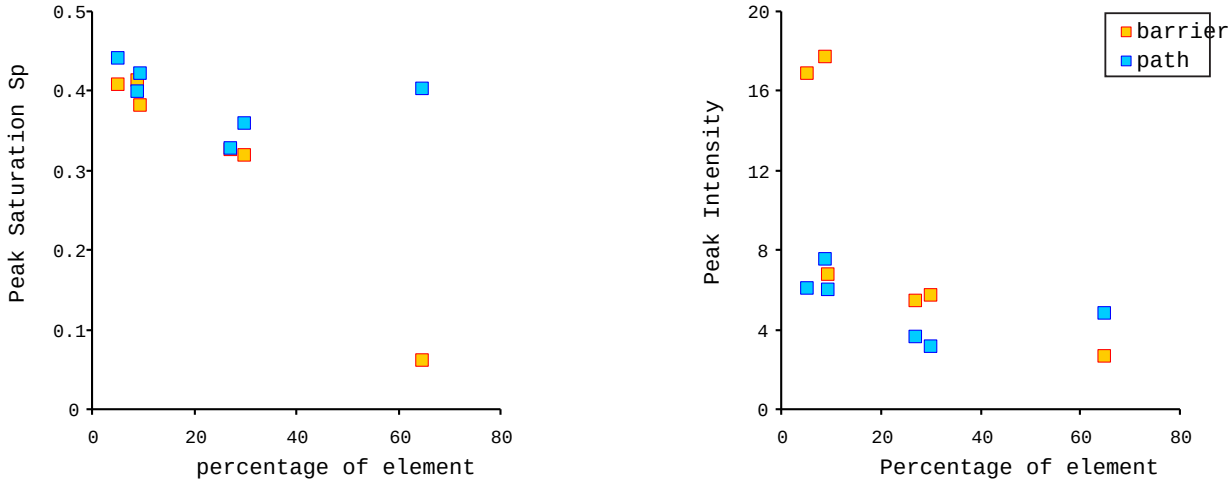

Figure 73 (b): dependence of the saturation at the peak *Sp* observed on FFF curves (left) and of the peak intensity (right) with respect to the percentage of heterogeneities presents in the system.

3- Variable fractal dimension

3-1 Introduction and geometrical characteristics

All previous results has been derived from patterns that was presenting

(1) a random spatial distribution (D=2) and

(2) a low length distribution exponent, meaning that layers have large lengths.

We have extended our analysis of the saturation to system presenting other spatial organisation. The following part shows results obtain with a varying fractal dimension and a constant length exponent (here equal to 2.7).

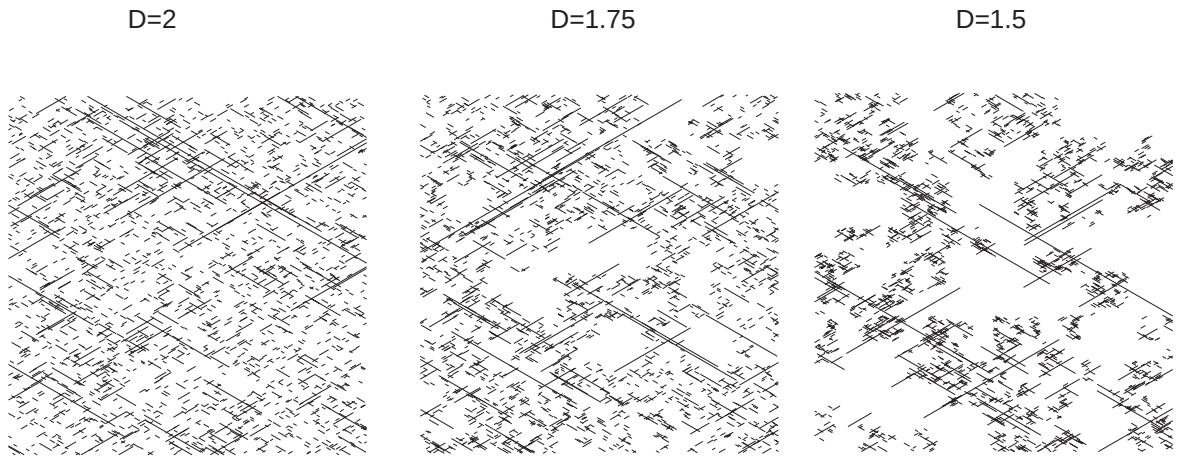

Figure 74: Fractal patterns used to study the influence of spatial organisation of heterogeneities on the saturation evolution. (Left) pattern L_3, D=2, (middle) pattern L_2, D=1.75, (right) pattern L_1, D=1.5.

The geometrical characteristics of the different patterns used for our simulations are synthesised in Table 21 and all performed simulations are summarised in Table 22. Patterns used are also represented in Figure 74. Decreasing the fractal dimension leads to the creation of fractures pattern with empty area where no heterogeneities are presents. Note also that all the patterns are connected to the system boundaries.

The observe geometry, with local clustering may influence the way the saturation front evolves with time. Also, since we have investigated the effect of the density of heterogeneities on a homogeneous pattern (D=2), so have we done for layers patterns described with a fractal dimension D=2 (*i.e.* D=1.5 and 1.75).

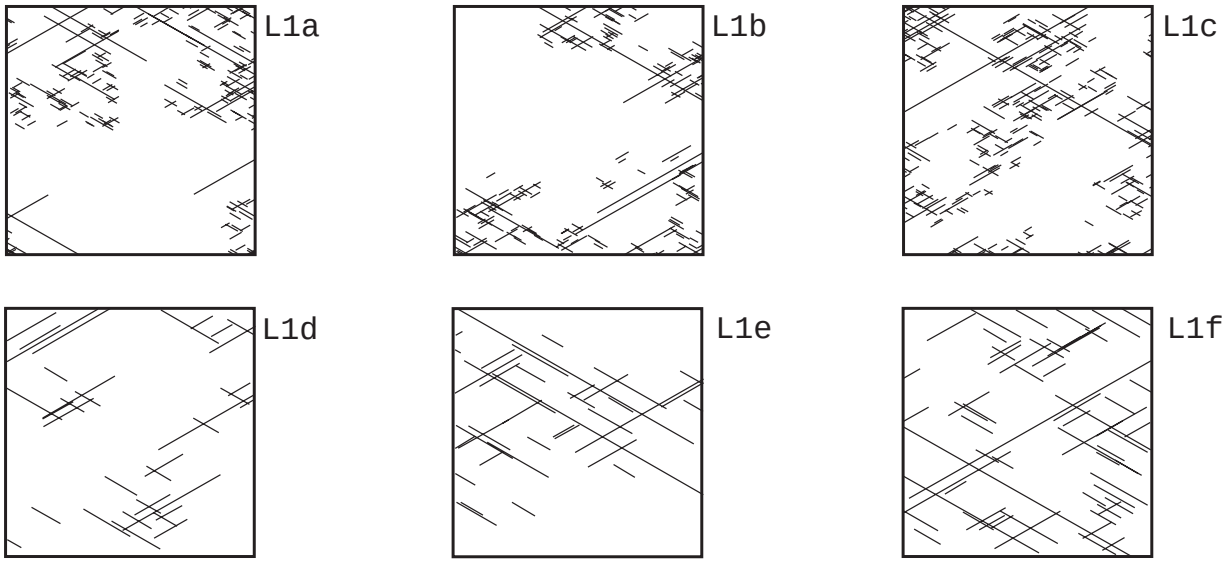

Figure 75: Pattern used to study the density dependency when *D*=1.5. All geometrical characteristics are summarised in Table 21.

Name	Area (m^2)	Mass (m)	Density (m/m^2) (d= Mass/Area)	N_{layers}	Density (m^{-2}) ($d=N_{layers}/Area$)	N_{int}	l_{max} (m)	P_{elt} (%)
Pattern L1	1	44.54	44.54	1939	1939	1177	0.620	14.83
Pattern L2	1	46.60	46.60	2000	2000	644	0.465	17.30
Pattern L3	1	46.22	46.22	1988	1988	508	0.791	18.38

Name	Area (m^2)	Mass (m)	Density (m/m^2) (d= Mass/Area)	N_{layers}	Density (m^{-2}) ($d=N_{layers}/Area$)	N_{int}	l_{max} (m)	P_{elt} (%)
Pattern L1a	1	13.68	13.68	210	210	123	0.547	6.14
Pattern L1b	1	12.92	12.92	174	174	128	0.763	5.81
Pattern L1c	1	19.23	19.23	287	287	170	1.131	8.65
Pattern L1d	1	6.519	6.519	35	35	22	0.453	3.38
Pattern L1e	1	8.293	8.293	37	37	22	1.099	4.20
Pattern L1f	1	13.20	13.20	64	64	47	1.119	6.60

Name	Area (m^2)	Mass (m)	Density (m/m^2) (d= Mass/Area)	N_{layers}	Density (m^{-2}) ($d=N_{layers}/Area$)	N_{int}	l_{max} (m)	P_{elt} (%)
Pattern L2a	1	13.747	13.747	195	195	56	0.980	6.66
Pattern L2b	1	17.994	17.994	225	225	84	1.077	8.69

Name	Area (m^2)	Mass (m)	Density (m/m^2) (d= Mass/Area)	N_{layers}	Density (m^{-2}) ($d=N_{layers}/Area$)	N_{int}	l_{max} (m)	P_{elt} (%)
Pattern L3a	1	16.1917	16.1917	211	211	59	1.144	7.69
Pattern L3b	1	15.085	15.085	208	208	57	0.4937	7.59

Table 21: geometrical parameters of the fractal layer networks used.

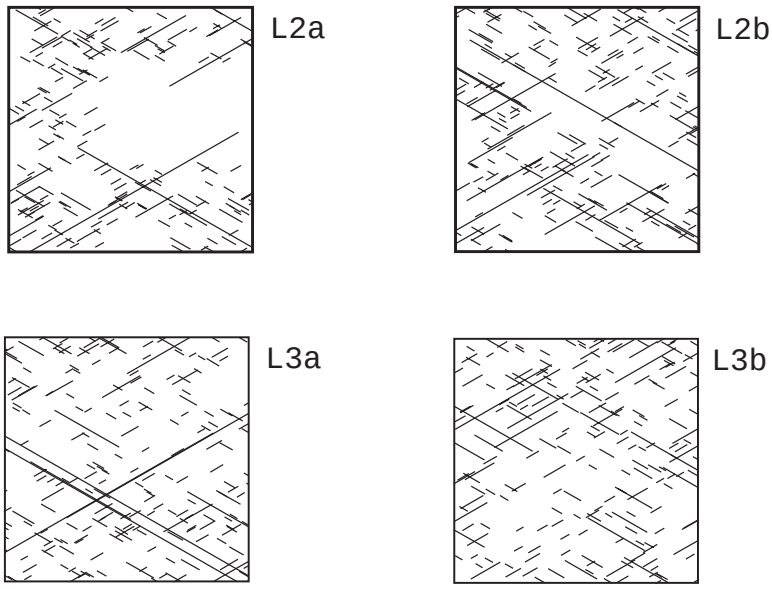

Figure 76: pattern L2 (D=1.75) and L3 (D=2) used to study the density dependence on fractal pattern.

Simulation	η_{water} (Pa.s)	η_{CO2} (Pa.s)	Flow rates ($m.s^{-1}$)	Φ_l	Φ_m	<Km> (darcy)	σ	Aperture (μm)	Ratio R_k
L1	1	10	0.225	0.1	0.3	0.2	0.15	0.05	$1.05\ 10^{-3}$
L2	1	10	0.225	0.1	0.3	0.2	0.15	0.05	$1.05\ 10^{-3}$
L3	1	10	0.225	0.1	0.3	0.2	0.15	0.05	$1.05\ 10^{-3}$

Table 22: parameters assigned in the simulation using the fractal patterns.

3-2 Saturation field

In the studied range, the geometry of the fracture pattern does not affect the shape of the front and fingering has the same importance in the three cases (Figure 77). The previous simulations suggest that the permeability contrast and the density of element acting as heterogeneity are the factors that affect the most significantly the front geometry.

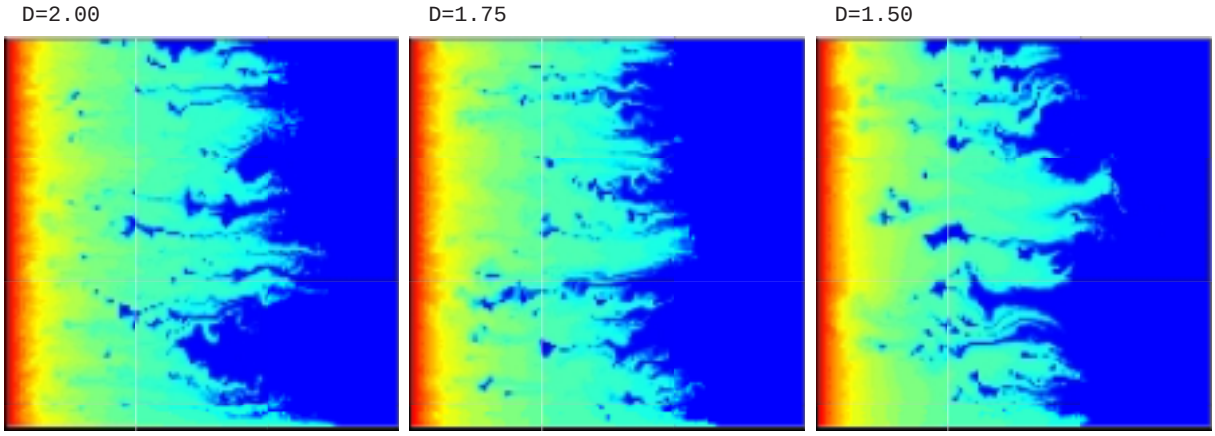

Figure 77: Saturation plot observed for a permeability contrast between fractures and matrix of 10^{-3}, for three patterns displaying a different fractal dimension. The amplitude of the viscous fingering is the same in the three cases.

From the temporal evolution of the fluid front, it appears that decreasing the fractal dimension (*i.e.* increasing empty space) makes the injected fluid move faster. Connection to boundaries is faster in the case where D=1.5 (Figure 78). This earlier arrival is illustrated by the presence of a more important number of peaks and "*stripes*" spanning the system.

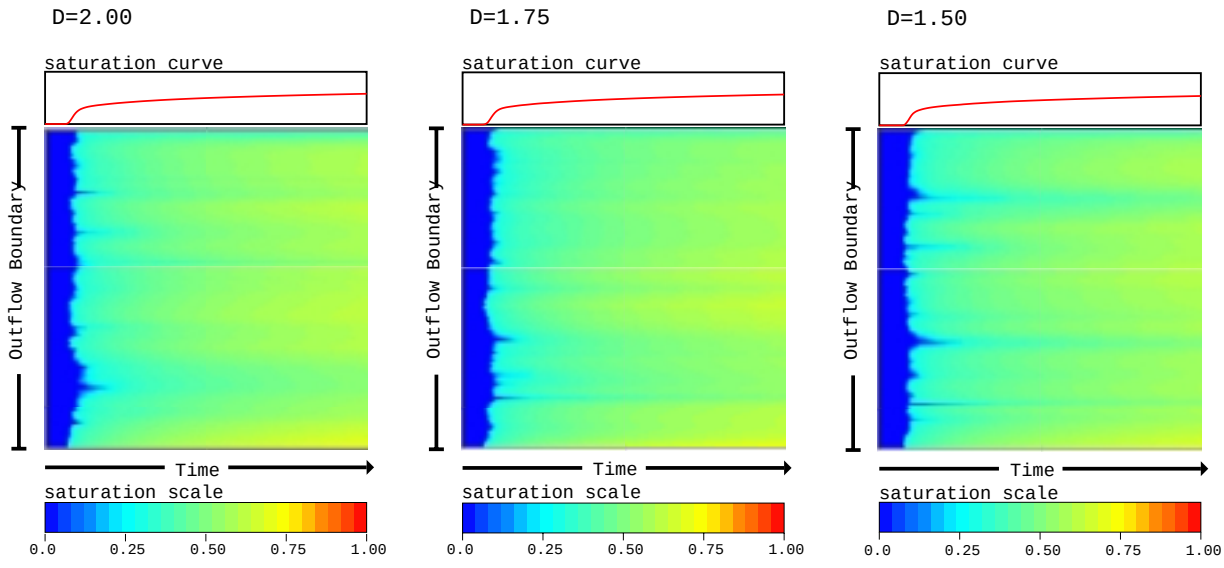

Figure 78: Time evolution of the saturation front for three different fractal dimension.

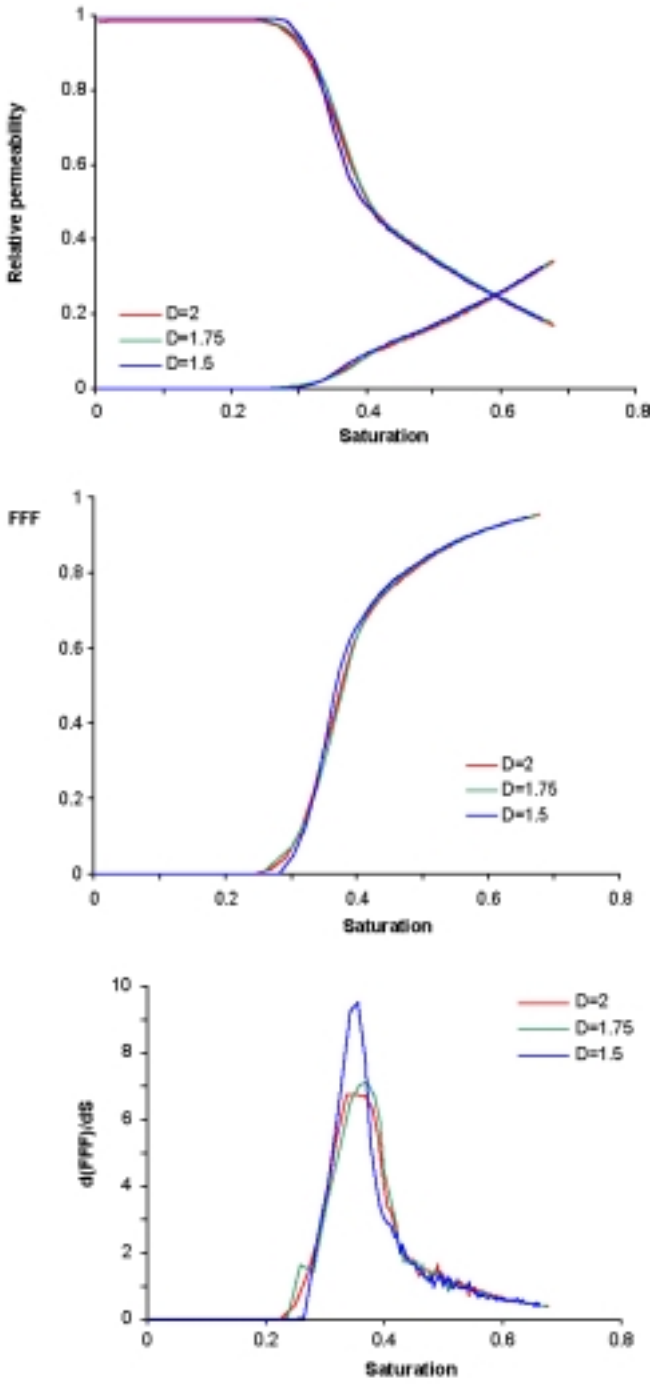

The evolution of the pseudo relative curves also does not show significant differences between the three geometry (Figure 79-top). The saturation for which the cross over takes place is identical in the three cases. The onset of mobility (IS_{CO2}) is also similar as indicated in Figure 79 (middle). The main difference comes from a modification of the front velocity (Figure 79-bottom). When the system presents large non-fractured area (D=1.5), the velocity is more important which agree with the observation of stripes on the time evolution observed previously (Figure 78).

Figure 79: evolution of the pseudo relative curves (top), the fractional flow function (middle) and its derivative (bottom) with respect to the saturation for the three considered geometry.

3-3 Density dependence

We have also investigated the effect of the density on the evolution of the fluid front for a fractal pattern[8] and given a small proportion of element acting as flow barrier, the influence of the fractal geometry on the saturation evolution.

[8]The previous study was for a homogeneous pattern *i.e.* D=2 (see section D-3.2-).

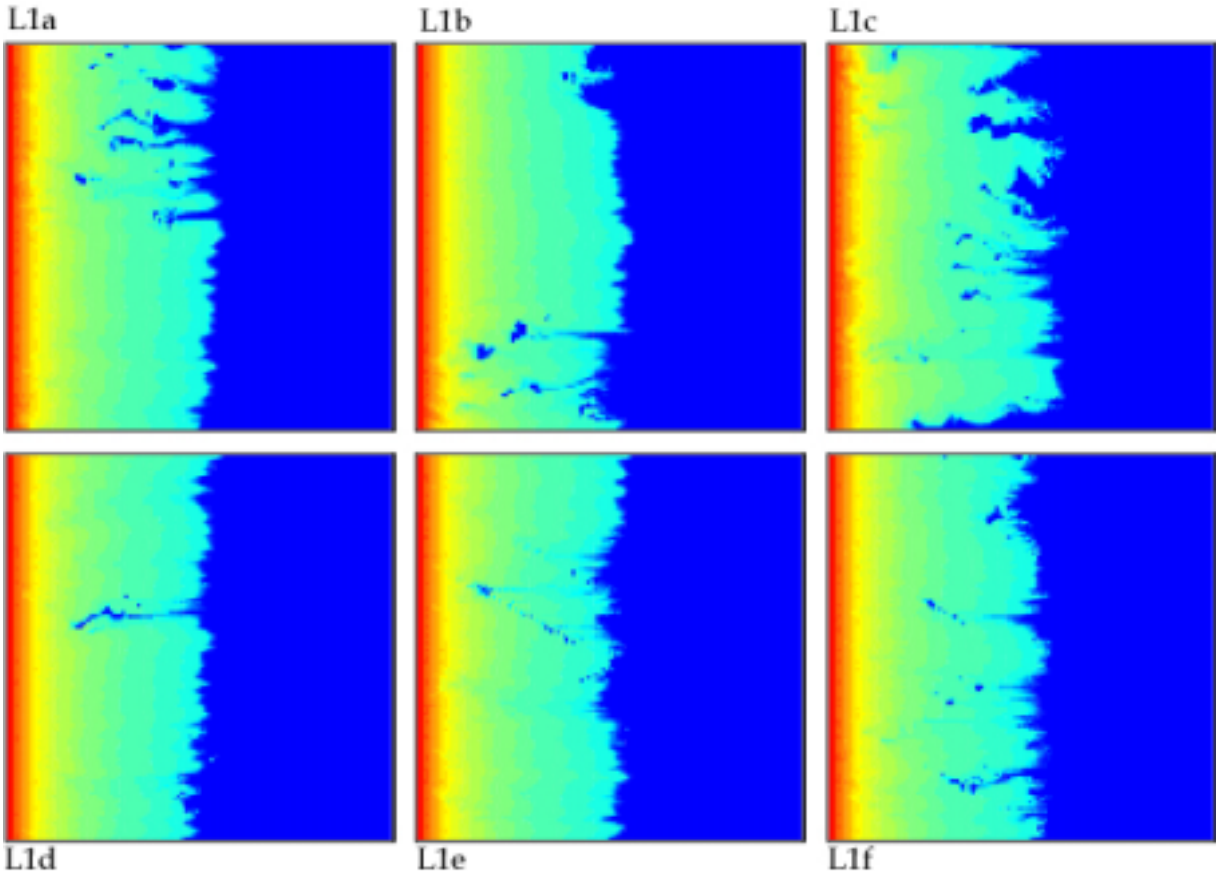

Figure 80: observed front geometry for six different densities (see Table 21).

The front geometry observed for pattern L1 (D=1.5) at increment T10 is illustrated in Figure 80. The six different patterns correspond to densities ranging from 3.4 to 8.6%. The fracture organisation or the density does not modify the average position of the front, which is similar in all cases, but has some influence on the local organisation. Some portions of fluid are trapped where fractures are presents. For example the front geometry observed for pattern L1a shows strong fingering in the upper side corresponding to the place where fractures are present (see also the patterns presented Figure 75, p118).

The geometry of the front is much more linear than what was observed previously (Figure 77). Also from these six examples, the fingering is increasing when the proportion of heterogeneity increases. Pattern L1d has a density p=3.8 and exhibit nearly a linear front while pattern L1c, that displays important fingering, contains a proportion of 8.6% of heterogeneities.

For each pattern and front evolution, we reported the pseudo relative curves (Figure 81-top left) and the derivative of the fractional flow function with respect to the saturation (Figure 81-bottom left). Pseudo relative curves indicate that the cross over saturation is similar in the three cases. This is illustrated on the right part of the figure where we reported Sc with respect to p. As element of comparison we add the value found for the matrix case (p=0) and for the entire pattern (p=15%). Between these two values, Sc is roughly equal. Hence, this suggests that the saturation over which the injected fluid dominates over the defending one start to decrease when the number of heterogeneity is larger than 10%.

The derivative of the fractional flow function indicates that an increase in the proportion of elements acting as barriers reduce significantly the front velocity given by the peak amplitude (or intensity) (Figure 81-bottom).

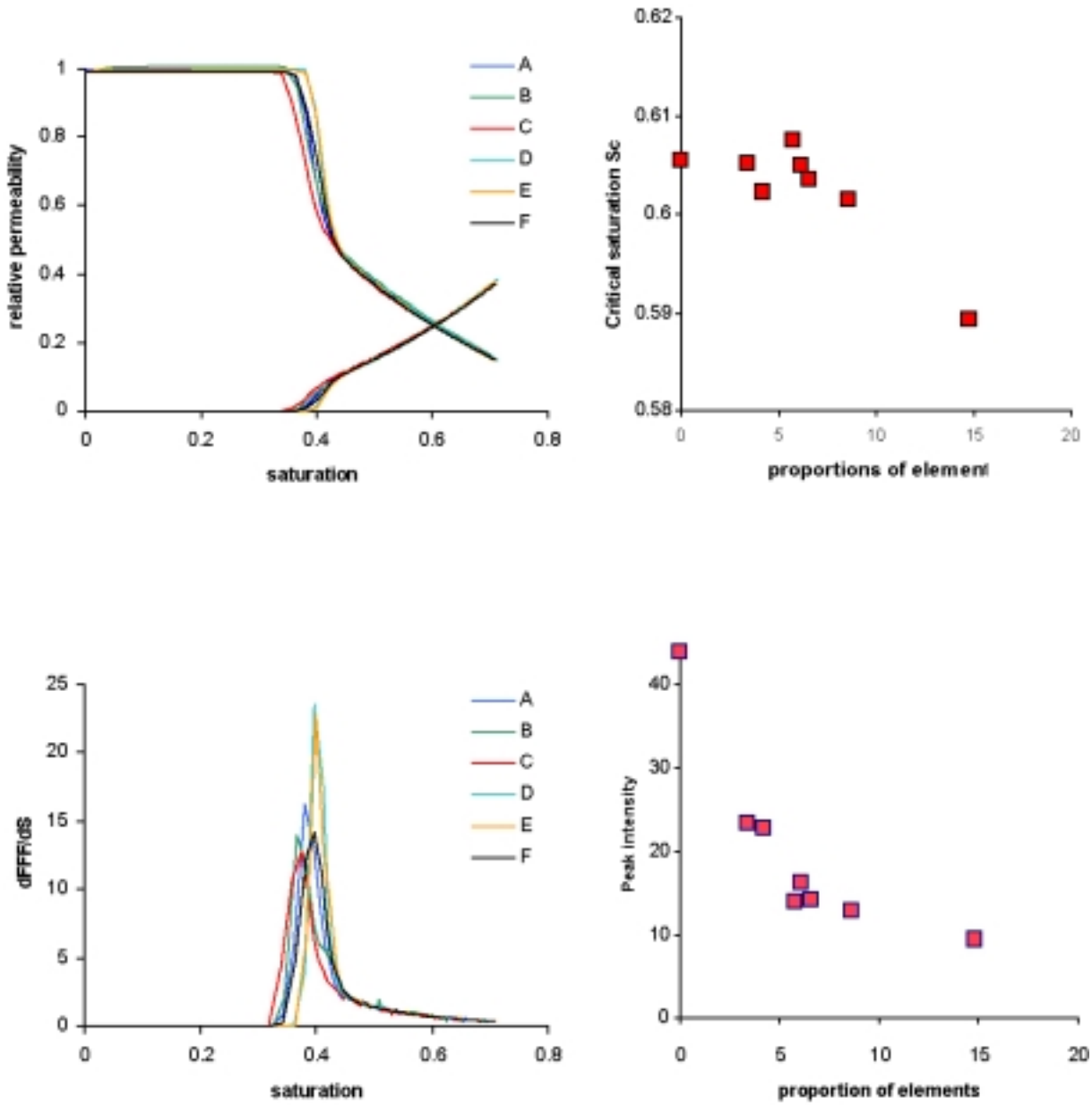

Figure 81: Left column: evolution of the pseudo relative curves (top) for the six different patterns presented above, and of the derivative of the fractional flow function (bottom), with respect to the saturation. Right column: evolution with respect to the proportion of heterogeneity of the cross over saturation Sc and of the peak intensity.

We report here the saturation evolution for a lower density for the three considered patterns (D=1.5, 1.75, 2.0). Figure 82 gives a snapshot of the front geometry for pattern L1f, L2a and L3a at T=10. The front becomes less linear when D increase. Also we observe in the three cases that fluids stay trapped.

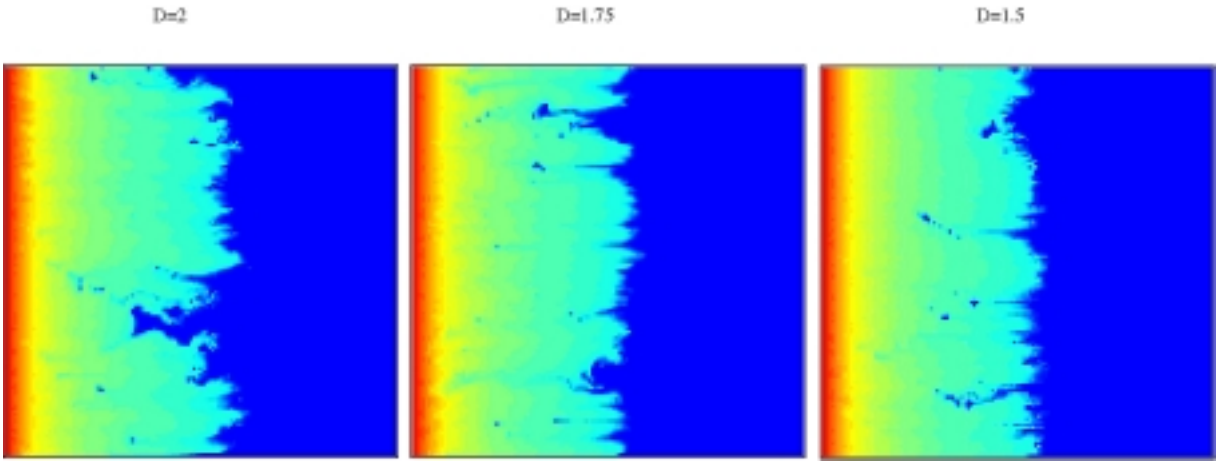

Figure 82: front geometry at T=10 for the three different considered geometry and for a proportion of element acting as barriers equal to 6%.

As observe in the previous section, decreasing the fractal dimension leads in an earlier arrival at the outflow boundary of the injected fluid.

PART E. DISCUSSION AND CONCLUSION

At present there is very little information available on the nature of the sediments of the Utsira Sand and the Utsira Formation. There have been varying interpretation of the depositional environment from shallow to deep water conditions but recent work on seismic sections [*Gregersen* 1997, *Lothe and Zweigel* 1999, *Torp* 1999] suggest that the Utsira Formation may represent a sub-marine fan complex. As such, the sediments can be expected to be heterogeneous and contain internal sedimentary structures on the scale of cm to km. The most common of these could include, on the scale of 10s to 100s m, turbidites with sand beds of varying grain size and sorting, and shales of differing lengths and continuity. On a smaller scale (10s cm to 1m), features such as cross-bedding and fluid escape structures can be expected. Although the Utsira Sand where CO_2 is currently being injected is thought to be dominated by sands, there is evidence that it contains a number of shale layers which may extend laterally by as much as 2 km. Due to the limited resolution of the available data, it is possible, and indeed probable, that this unit contains many additional shales thinner than 1 m of unknown lateral extent.

Different cases of sedimentary heterogeneity likely to occur in the sediments of a sub-marine fan complex have been investigated for their impact on supercritical CO_2 migration and dispersion using a two-phase flow model. Representative permeability and porosity fields have been generated using the coupled Markov chain method together with information from sediment analogues and the permeability of weakly to unconsolidated sands and shales/clays from the literature. This model can produce, using information from logs and maps, any number of stochastic realizations of a heterogeneous field that possess the same spatial characteristics. Also patterns presenting a fractal organisation have been used in the simulations.

The simulation of the saturation evolution during CO_2 injection shows how the nature of layering (bedding) affects CO_2 migration. For flow perpendicular to layering, where sand and shale layers are perfectly parallel, flow behaves similarly to that in a homogeneous sand. However, small deviations from this simple pattern has large consequences for the nature of the saturation field. In fact, the simple picture of perfectly parallel layers is very unrealistic as, in nature, shale and sand layers are discontinuous and due to erosion events, differential compaction rates and faulting, layers are not perfectly planar. The flow simulations show that discontinuous shale layers produce highly heterogeneous saturation fields and complex fluid fronts.

Wave-like perturbations give rise to fingering (tongues of CO_2) on the same wavelengths as that of the perturbations. On a smaller scale, the permeability contrasts expected in cross-bedded sands did not greatly affect the heterogeneity of the saturation field but the presence of fluid escape structures (dish structures and fluid escape pipes) can produce highly heterogeneous saturation fields. Thus the presence of thin discontinuous low permeability layers, which has little impact on the global permeability, can have large effects on the two phase flow properties.

The simulations suggest that heterogeneities on a wide range of scales can insignificantly impact on the migration and dispersion of injected CO_2. The flow model results have been quantified through the determination of pseudo relative permeability curves for blocks of heterogeneous sediment. These curves can be used as input parameters to large scale multi-phase flow models to up-scale heterogeneities on a scale below the resolution of the model. The pseudo curves show generally, that as the level of permeability heterogeneity increases, the slope of the pseudo curves decreases and the cross-over between curves for water and supercritical CO_2 migrates to the left (to lower saturations). Pseudo curves are different for flow perpendicular and parallel to layering, particularly when the layering reflects large contrasts in permeability. As heterogeneity increases, the rate at which the CO_2 saturation in the modelled region increases with pore volumes of injected CO_2 is reduced.

Model results for ten realisations for each heterogeneity case show that the level of heterogeneity also affects the reproducibility of the pseudo curves. In addition curves are different for flow perpendicular and parallel to layering. The variations in the resulting pseudo curves indicate that the size of the representative elementary volume (REV) for two-phase flow has not been reached in these cases. The REV is defined as the minimum volume for which small changes in size and location result in only small changes in two-phase flow properties. In the case of layering with strong permeability contrasts (like inter-bedded sands and shales/clays or dish structures) the REV will only be reached when the length of the shale layers is small compared to the volume considered.

While in the case of fluid escape structures, a volume of some 5 to 10 m across may be sufficient to satisfy this condition, shale layers have a probable wide range of possible lengths, possibly up to 2 km [*Lothe and Zweigel* 1999]. In this case, it is obvious that a meaningful REV does not exist. As an alternative, a stochastic approach may be adopted where pseudo curves are allowed to vary over the large scale flow model in an attempt to incorporate the effect of heterogeneities in a meaningful fashion.

It can be seen from the 'snapshot' saturation fields that there is noticeable, although much lower, flow in the shales compared to the sands. In running the two-phase flow program it was found that up to 4 orders of magnitude contrast in permeability could be managed. The program at present cannot handle zero permeability. The shales in the turbidite sequences were assigned a value of 0.05mD and the clay layers in dish structures, 0.2mD. These values lie at the top end of the possible range of shale/clay permeabilities at reservoir conditions (0.01 to 1.0e-06 mD) and thus the model maximises the possible role of the shales in conducting flow.

The two-phase flow program used here does not take capillary pressure into accounts. There may therefore be some effects, which are not captured by the presented model results. In addition, the two-phase flow model does not model the effects of take gravity. Close the injection point, flow of CO_2 is probably dominated by the pressure gradient between the injected fluid and reservoir conditions. However, far from the injection point the migration of CO_2 will be driven by the density difference between water and CO_2 which causes CO_2 to rise. In the laterally unconfined conditions of the aquifer this can be expected to lead to more pronounced flow parallel to layering than is shown by the snapshots of the saturation fields in Fig.11, as CO_2 spreads sideways under the low permeability shale layers.

The permeability of shales remains one of the greatest uncertainties in the modelling. It is now thought that shales always have non-zero permeability [*Neuzil* 1994] and thus cannot form a complete seal for infinite lengths of time. Shale permeability depends on clay mineralogy, internal structure, depth and fluid chemistry and can vary by several orders of magnitude at any depth. In the short term

(days, months) permeability contrasts between shales and sands mean that flow is dominated by the more permeable sands. However, in the long term (years), ponds of CO_2 will build up under the cap rock of the Nordland shales and under shale layers within the Utsira Sand generating pressure gradients. The permeability of the shales will then determine the length of time they can act as an efficient seals. With the information presently available on the hydraulic properties of the shales, this remains largely unknown.

Simulations made on fractal patterns indicate that the permeability contrast between fracture and the matrix control the shape of the front. Also it strongly affect the shape of the pseudo permeability curves. Increasing this ratio lead in the shallower slope and to a migration of the cross-over saturation to lower saturation. Modification in the saturation evolution occurs abruptly for a ratio of 10^{-2}.

The density as the spatial organisation may also modify the front geometry. When increasing the proportion of the heterogeneity in the system, we observe a passage from a nearly linear front to strong fingering. Also this leads to the capture of small pocket of fluids.

The main conclusion from the modelling is that heterogeneities which are very likely to be present in the Utsira Formation will have a significant effect on the migration of injected CO_2. This has been confirmed by the comparison of the recent seismic survey and a survey taken before injection began which indicates that already injected CO_2 is present in a wide region reaching the height of the Utsira Sand (200 m) and over twice as broad (500 m). This compares with early simulations by IKU (Torp 1999) of the CO_2 bubble using a homogeneous sediment which indicates a narrow column only some 50 m broad. Later models by IKU, however, where impermeable shale layers were included clearly show how shale layers can greatly increase the lateral migration of injected CO_2. The breadth of the CO_2 plume indicated by the seismic surveys can most likely be attributed to sediment heterogeneity. Such heterogeneity reduces the effective storage of the aquifer since saturation fields become heterogeneous with trapped pockets of water and increased the volume of low saturations. However, this increased dispersion of injected CO_2 could increase the rates at which CO_2 dissolves in the formation waters and reacts with the host sediments to become permanently stored. The modelling presented here has been used to generated pseudo relative permeability curves for flow perpendicular and parallel to layering (bedding) for blocks of heterogeneous sediment. These curves could be used as input to large-scale flow models in order to include the effects of heterogeneities on scales below the size of a large scale simulator grid block. This may allow more representative simulations of the long term effects of CO_2 injection to the Utsira Formation.

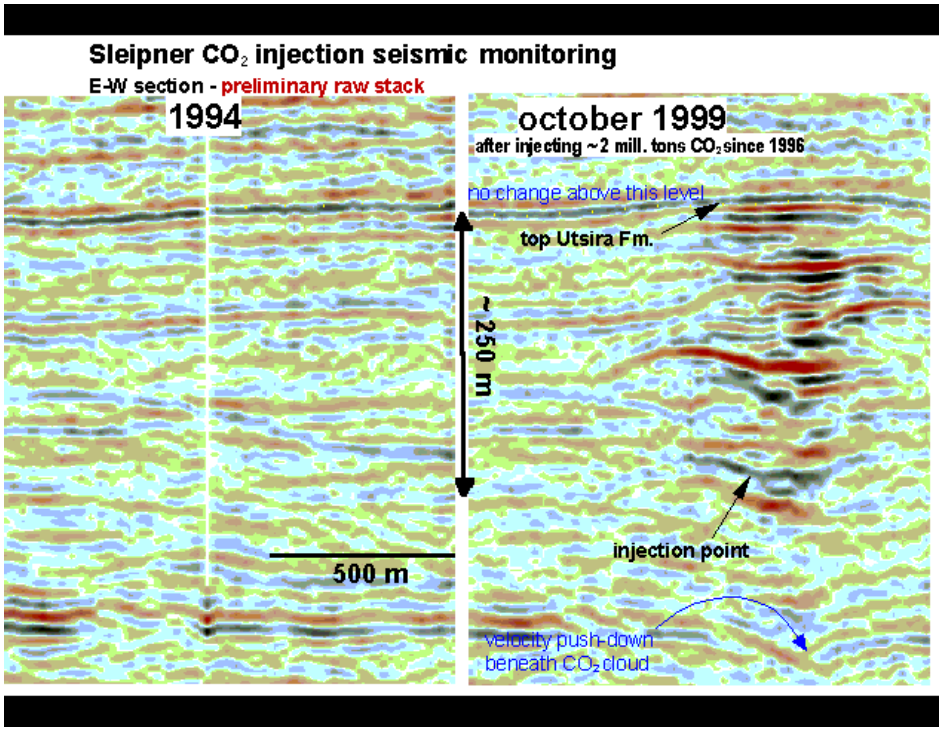

Figure 83: Comparison of seismic surveys before and 2 years after start of CO_2 injection. The CO_2 plume is about 200m high and 500m broad (recent results from SACS project).

1. If the Utsira Formation is a sub-marine fan system, commonly occurring heterogeneities could include turbidite sequences of inter-bedded sands and shales / clays (10's m scale) showing discontinuous shale / clay layers and wave-like perturbations of layering, and small scale features (1 m scale) such as cross-bedding and fluid escape structures.

2. The largest impact of CO_2 migration is shown by turbidite sequences with discontinuous shale / clay layers but significant effects occur due to wave-like perturbations of layering geometry. The permeability contrasts expected in cross-bedding have a small effect only, but fluid escape structures can generate highly heterogeneous permeability fields. That heterogeneities can significantly affect the migration of injected CO_2 is confirmed by the recent comparison of seismic surveys which shows that the CO_2 plume is much broader than predicted for a homogeneous aquifer.

3. The effects of sediment heterogeneity are reflected in the nature of the relative permeability 'pseudo' curves. As heterogeneity increases, the slopes of curves become less steep and the cross-over point migrates left towards lower CO_2 saturations. The variations in the curves for stochastically similar simulations also increases. This indicating that the size of the REV is increasing and a meaningful REV may not exist for the case of discontinuous shale layers.

4. The presence of heterogeneities also results in a reduced rate saturation increase with pore volumes of CO_2 injected. The lower saturations and complex fluid fronts that result will promote dissolution of CO_2 into the formation waters and reaction with the host sediments.

PART F. BIBLIOGRAPHY

Aker E., K.J.Måløy, and A. Hansen, Simulating temporal evolution of pressure in two-phase flow in porous media, *Phys. Rev. E*, Vol. 58, pp. 2217-2226, 1998.

Barker J.W. and Thibeau S. 1997: A critical review of the use of pseudo-relative permeabilities for upscaling. SPE Reservoir Engineering, May 1997.

Bonnet, E., O. Bour, N.E. Odling, P. Davy, I. Main, P. Cowie, and B. Berkowitz, Scaling of fracture systems in geological media, *Rev. Geophys.*, In press.

Bour O., and P. Davy, Connectivity of random fault network following a power law fault length distribution, *Wat. Res. Res.*, Vol. 33, pp. 1567-1583, 1997.

Buller A.T., Johnsen S.O., Rueslåtten H., Rundberg Y. The Tertiary section in Block 30/6 (wells 30/6-1, 2, 3, 4) confidential report to Statoil, Geologisk Inst., NTH, Trondheim, 1982.

Bouma A.H. Sedimentology of some flysch deposits. Elsevier, Amsterdam, 168pp., 1962

Clark J.D. Detailed section across the Ainsa II channel complex, south central Pyrenees, Spain. In: Pickering K.T., Hiscott R.N., Kenyon N.H., Ricci Licchi F. and Smith R.D.A.(Eds*) Atlas of deep water environments, architectural style in turbidite systems*. Chapman & Hall, London, 139-144, 1995.

Dake L.P., Fundamentals of reservoir engineering. Developments in Petroleum Science, 8, Elsevier, Amsterdam, 443pp., 1978.

Deegan C.E. and Scull B.J., A standard lithostratigraphic nomenclature for the Central and Northern North Sea, Report 77/25, Bull.1. Institute of Geological Sciences, London; Oljedirektoratet, Stavanger, 1977.

Dewhurst D.N. and Aplin A.C., Compaction-driven evolution of porosity and permeability in natural mudstones: an experimental study. *J.Geophys. Res.*, 103(B), 651-661, 1998.

Eidvin T. and Riis F., Neogen og øvre paleogen stratigrafi på norsk kontinentalsokkel (fra Ekofisk-feltet i sentral Nordsjøen til Bjørnøya-Vest i sydvestlige deler av Barentshavet), Oljedirektoratet, Stavanger, p. 144, 1995.

England W.A. MaKenzie A.S., Mann D.M., Quigley T.M., The movement and entrapment of petroeum fluids in the subsurface. J.Geol.Soc.Lond., 149, 327-347, 1987.

Elfeki A.M.M., Uffink G.J.M. and Barends F.B.J., Groundwater contaminant, 1997.

Feder J., *Fractals*. Plenum Press, New York, 283pp., 1988.

Fetter C.W. *Applied Hydrogeology*. Merrill Publ. Company, Columbus, Ohio, 592pp.

Gouyet J.F., Physique et structure fractale, *Masson*, Paris, 1992.

Gregersen U., Michelsen O. and Sorensen J.C., Stratigraphy and facies distribution of the Utsira Formation and the Pliocene sequences in the northern North Sea. Marine and Petroleum Geology, 14, 893-914, 1997.

Gregersen U., Upper Cenozoic channels and fans on 3D seismic data in the northern Norwegian North Sea. Petroleum Geoscience 4, 67-80.

Hansen, A., Hinrichsen, E.L., and Roux, S., Scale invariant disorder in fracture related breakdown phenomena, *Phys. Rev. B.*, p. 665-678, 1991.

Heggland R., Detection gas migration from a deep source by use of exploration 3D seismic data. Marine Geology 137, 41-47, 1997.

Hilscott, R.,N., A. Coletta, P. Pezard, M.A. Lovell, and A.Malinverno, Sedimentology of deep water volcaniclastics, Oligocene Izu-Bonin forearc basin, based on formation micro-scanner images, *In Proceeding of the Ocean Drilling Program, Scientific results*, Vol., 126, pp. 75-96, 1992.

Hurst A., Permeability variations in sandstones and their relationship to sedimentary structures. In: Lake L.W., Carrol H.B.Jr., Wesson T.C. (eds*) Reservoir Characterization II*, NPF, 167-196, 1991.

Hurst A., Sedimentary flow units in hydrocarbon reservoirs: some shortcomings and a case for high-resolution permeability data. Spec. Publ. Ass. Sediment 15, 191-204, 1993.

Isaksen D. and Tonstad K., A revised Cretaceuos and Tertiaty standard lithostratigraphic nomenclature for the Norwegian North Sea, NPD bull.5; Oljedirektoratet, Stavanger, 1989.

James A.M. and Lord M.P., *Macmillan's Chemical and Physical Data*. Macmillan, London, 1992.

Jordt H., Faleide J.I., Bjørlykke K., Ibrahim M.T., Cenozoic sequence stratigraphy of the central and northern North Sea Basin, tectonic development, sediment distribution and provenance areas. Mar.Petrol.Geol., 12, 845-879, 1995.

Gidman J., Schweller W.J., Reed A.A., Reservoir character of deep marine sandstones, Inglewood field, Los Angeles Basin. In: Rhodes E.G., Moslow T.F. (eds*) Marine Clastic Reservoirs, Examples and Analogues.*, 231-262, 1993.

Kyte J.R. and Berry D.W., New pseudo functions to control numerical dispersion. SPEJ, August 1975, 269-275.

Langlo P. 1992: *Macrodispersion for two-phase flow in heterogeneous media*. Ph.D. Thesis, University of Bergen, 101pp, 1975.

Malinverno, A., On the power law size distibution of turbidite beds, *Bas. Res.*, Vol. 9, pp. 263-274, 1997.

Morrow N.R., Huppler J.D., Simmons A.B. Porosity and permeability of unconsolidated, upper Miocene sands from grain size analysis. J. Sed. Geol., 39, 312-321, 1969.

Lothe A., Zweigel P., Saline Aquifer CO_2 Storage (SACS). Annual report 1999 of SINTEF Petroleum Research's results in work area 1 "Reservoir Geology", 1999.

Neuzil C.E., How permeable are clays and shales? Water Resour. Research 30, 145-150, 1994.

Odling N.E., Scaling and connectivity in a joint system in sandstones from western Norway. *J. Struct. Geol*. 19, 1257-1271, 1997.

Odling N.E. and Webman I., A conductance mesh approach to the permeability of natural and simulated fracture patterns. Water Resour. Res., 10, 2633-2643, 1991.

Pettersen Ø., Grunnkurs i Revervoarmekanikk (Basic course in reservoir mechanics) Publ. Univ. Bergen, Bergen, 103pp, 1990.

Pfannkuch, H.O., Contribution à l'étude des déplacements de fluides miscibles dans un milieu poreux, *Rev. IFP*, Vol. 18, pp.215-270, 1963.

Pickering K.T., Hiscott R.N., Kenyon N.H., Ricci Licchi F. and Smith R.D.A.(Eds), *Atlas of deep water environments, architectural style in turbidite systems.* Chapman & Hall, London, 333pp, 1995.

Pickup G.E., Ringrose P.S., Forrester M.M., Jensen J.L. and Sorbie K.S., The geopseudo atlas: geologically based upscaling of multi-phase flow.SPE 27565, 1994.

Pickup G.E., Carruthers D., Effective flow parameters for 3D reservoir simulation. SPE 35495, April 1996, 1996.

Pilkey, O,.H., S.D. Locker, and W.J. Cleary, Comparison of sand layer geometry on flat floor of 10 modern depositional basins, *Bull. Am. Ass. Petrol. Geol.*, Vol. 64, pp. 841-856, 1980.

Pirmez, C., R.N. Hiscott, and J.D. Kronen jr, Sandy turbidite successions at the base of channel-levee systems of the amazon fan revealed by FMS logs and cores: unraveling the facies architecture of large submarine fans, *In Proceeding of the Ocean Drilling Program, Scientific Results*, Vol. 155, pp. 7- 33, 1997.

Reuil A. and Cathles III L.M., Permeability of shaley sands. Water Resour.Research 35, 651-662, 1999.

Rothman, D.H., J.P. Grotzinger, and P. Fleming, Scaling in turbidite deposition, *J. Sedim. Res.*, Vol. A64, pp. 59-67, 1994.

Scheidegger A.E., *The Physics of Flow Through Porous Media*. Univ. Toronto Press, 1974.

Schuppers J.D., Quantification of turbidite facies in a reservoir analogue submarine fan channel sandbody, south-central Pyrenees, Spain. Spec.Publ.Int.Ass. Sediment, 15, 99-112, 1993.

Sclater J.G. and Christie P.A.F., Continental stretching: an explanation of the post Mid-Cretaceous subsidence of the central North Sea basin. J.Geophys. Res., 85(B), 3711-3739, 1980.

Stow D.A.V. (Editor) *Deep water turbidite systems*. Blackwell Scientific Publications. Int. Assoc. Sedimentologists Reprint Series 3, 473pp.

Stølum, H.H. Fractal heterogeneity of clastic reservoirs, *In Reservoir Characterization* II , Ed. by L.W.Lake, H.B. Caroll, and T.C. Wesson, Academic Press, San Diego, pp. 579-612, 1991.

Taylor W.L., D.D.Pollard, and A. Aydin, Fluid flow in discrete joint sets: field observations and numerical simulations, *J. Geophys. Res.*, Vol. 104 - N° B12, pp. 28983-29006, 1999.

Weber K.J., Eijpe R., Leijnse P., Moens C., Permeability distribution in a Holocene distributary channel-fill near Leerdam, The Netherlands. Geologie en Mijnbouw 51, 53-62, 1972.

Wadsley M.W., Thermodynamics of multi-phase equilibria in the CO_2-seawater system. Proceedings of the Second Int, Workshop on interaction between CO_2 and ocean, Tsukuba, Japan, June 1993, 88-110, 1993.

Walker R.G. Deep-water sandstone facies and ancient sub-marine fans: models for exploration for stratigraphic traps. AAGG 62, 932-966, 1978.

Torp T.(Editor) SACS - Saline Aquifer CO2 Storage - final technical report, 2000.

Wilkinson I.P. The biostratigraphical and palaeo-ecological application of calcareous microfaunas from the Utsira Formation in Norwegian well 15/9-A23. BGS report WH99/124R, 1999.

Index of Tables and Figures

Table 1: measured permeability k and porosity Φ achieved for different granular medium (<d> corresponds to the mean grain size). 24
Table 2: parameters of the three considered simple networks. 35
Table 3: parameters assigned in the simulation using patterns SG1, SG2 and SG3 . Note that Simulation 1 for the pattern SG1 corresponds to the case where the layer acts as a preferential path. All others simulations considers layers as a flow barrier. 36
Table 4: geometrical characteristics of the multiple parallel layers patterns, with variable length. 37
Table 5 : parameters used and simulations realised in the case of multiple parallel layers with variable length. 38
Table 6- lithology classes for the Ainsa turbidite sequence and associated permeability and porosity 39
Table 7: lithologies and parameters for cross-bedding simulations 42
Table 8: lithologies and parameters for massive sandstone with fluid escape structures. 42
Table 9: parameters of the three different patterns shown on Figure 19. 43
Table 10: parameters of the three different patterns shown on Figure 20. 44
Table 11: data on viscosity of water and liquid CO_2 [*James and Lord*, 1992]. 51
Table 12: permeability ratio corresponding to the various apertures used in the multiple parallel fracture patterns. 60
Table 13: geometrical parameters of the layer networks. 90
Table 14: parameters assigned in the simulation using the pattern R1. Φ_l is the porosity of the fracture and Φ_m the porosity of the matrix 91
Table 15: parameters assigned in the simulation using the pattern R2. 91
Table 16: parameters assigned in the simulation using the pattern R3 91
Table 17: Irreducible CO_2 saturation (IS_{CO2}), cross over saturation S_c, peak saturation Sp and peak intensity determined using the pseudo relative and fractional flow curves for the pattern R3 and for various permeability contrasts (from 1 to 10^{-4}). 99
Table 18: geometrical parameters of the networks used to study the density dependence. 103
Table 19: parameters assigned in the simulation using the different pattern shown on Figure 62 when layers act as barriers to the flow. 103
Table 20: parameters assigned in the simulation using the different pattern shown on Figure 62 when layers act as preferential path to the flow. 103
Table 21: geometrical parameters of the fractal layer networks used. 119
Table 22: parameters assigned in the simulation using the fractal patterns. 119

Figure 1: Cross-section showing the Sleipner field and Sleipner A platform. CO_2 removed from produced oil is re-injected into a salt water aquifer in the Utsira Formation. 12
Figure 2: for a given system, distribution of a local property *p*. Two different distributions having the same mean value are shown. The thick grey line displays a broader spectrum than the dashed dark one, which indicates a more heterogeneous system. 12
Figure 3: The extent of the Utsira Formation and the Utsira Sand in the Northern North Sea (modified from *Gregersen* [1997]. 16
Figure 4: Sketch of submarine fan morphology and sediment types (after *Walker* [1978]). 19
Figure 5: cumulative distribution of the measured thickness of turbidite beds from the Amazon fan. Distribution follows a power law characterised either by one or two exponents (After *Pirmez et al.*, [1997]). 21
Figure 6: bed length versus bed thickness from the Hatteras abyssal plain data (from *Pilkey et al.*, [1980]). The lines represents the slope for the relationship between *l* and T_{max} as in eq. (2). In that case, the exponent ξ lie in the range 0.7, 1.1 (Modified after *Malinverno* [1997]). 22
Figure 7: bed depocentres barycentre in map view and the corresponding correlation dimension D. 23
Figure 8: Porosity versus permeability for slightly to unconsolidated sands (modified from *Gidman et al.* [1993]). The bar and open circle are estimates of porosity and permeability for the Utsira Sand 25

Figure 9: Permeability versus porosity for shales (modified from *Neuzil* [1994]). The grey cross-hatched fields are those that have pressure conditions most closely resembling that of the Utsira Formation. 27

Figure 10: Trends for porosity versus depth for sands and shales (after Sclater and Christie *[1980]*). The open circles represent the depth of the Utsira Formation at the injection point. 27

Figure 11: Examples of fields generated using the coupled Markov chain model. Top – horizontal continuous layers, middle – horizontal discontinuous layers, bottom – cross-bedding. 30

Figure 12: *(Top)* example of three different pattern showing the same fractal dimension (D=2) and three different length exponent (a=1.5-left, a=2.5-medium, and a=3.5-rigth). *(Bottom)* the corresponding length distribution $n(l)$. 33

Figure 13: principle of a heterogeneous statistical fractal (from *Bour* [1997]). (a) A dark square indicates that fault centroids are present inside and a white square indicates its absence. Passage from one scale to another depends on the mass ratio that allows several configurations. (b) Example of three successive steps using this type of generator to create a fractal pattern. 33

Figure 14: example of three different pattern showing the same length exponent (a=2.7) and three different fractal dimension (D=2.0-left, D=1.75-medium, and D=1.50-rigth). 34

Figure 15: simulated simple geometry of layer used as input to the two-phase flow model in the case of a homogeneous matrix. Permeability is normalised so that in all cases the maximum permeability is 1. 35

Figure 16a : simulated multiple parallel layers of constant length used as input to the two-phase flow model. 36

Figure 17: Orthogonal (top) and diagonal (bottom) pattern generated and used as input in the two-phase flow model. 38

Figure 18: Permeability fields for examples of turbidite sequences representing an area of 38 by 38m. Top left – parallel continuous layers, top right – discontinuous layers (shales around 40m), bottom - discontinuous layers (shales around 5m). 40

Figure 19: permeability field generated for a fractal pattern with the same dimension (D=2) and for different length distribution exponent (a=1.5,2.5 and 3.5). The number of faults and the size is the same for the three different patterns. The density (mass / area) is respectively equal to *(a)* 208.0 m / m², *(b)* 50.1 m / m² and *(c)* 32.3 m / m² 43

Figure 20: permeability field generated for a fractal pattern with the same length distribution exponent (a=2.5) and for different fractal dimension (D=2, 1.75 and 1.5). The number of faults and the size is the same for the three different patterns. The density (mass / area) is respectively equal to *(a)* 46.2 m / m², *(b)* 46.6 m / m² and *(c)* 44.5 m / m². P is respectively equal to 18.4%, 17.3% and 14.8%. 44

Figure 21: different front geometry observed depending on the capillary number Ca and on the viscosity ratio V_R. Left: viscous fingering, medium: capillary fingering, and right stable displacement (from [*Aker et al.* 1998]). 45

Figure 22: evolution of the geometry of the flow index with respect to the permeability contrast. 46

Figure 23: distribution of local permeability for a simulation performed with a fractal dimension D=1.5 and a length distribution exponent a=2.7 (see Figure 20). The parameters used leads to a difference of three orders of magnitude between the matrix and the layers. 47

Figure 24: (a) Assumed simple rock relative permeability curves for water (k_w) and CO_2 (k_{CO2}). Here the CO_2 correspond to the invading or wetting phase and water is the non wetting phase. (b) Form of a fractional flow curve for a homogeneous permeable medium. From the fractional flow function, the shock saturation can be determined. 48

Figure 25: pseudo relative curves (left), fractional flow function (middle) and its derivative (right) with the definition of the quantities deducted from the different curves (see text). 52

Figure 26: snapshot of the CO_2 saturation for 4 different time step. (Top) layer act as a preferential path for injected CO_2 and (bottom) as a barrier. Permeability ratios are respectively equal to 16.8 and 2.1 10^{-4}. 55

Figure 27: Saturation evolution plot showing the change in the saturation at the outflow boundary with time for the pattern SG1 (see section C-2). (a) layer act as a preferential path for injected CO_2 and (b) as a barrier. 56

Figure 28: Comparison of the relative permeability curves, the fractional flow functions and its derivative, determined for the simulations shown above. 57

Figure 29: Four different saturation field observed at instant T1, T5, T10 and T15. (Top row) homogeneous matrix permeability field and flow parallel to layers. (Middle row) homogeneous matrix and flow perpendicular to the layers. (Bottom row) Heterogeneous matrix permeability field with flow perpendicular to the layers. 58

Figure 30: Time evolution of the saturation when the flow is parallel (left) and perpendicular (middle) to the layer with a homogeneous matrix (see Table 3- section C-2). On the right is the saturation evolution when the flow is perpendicular to the layers and the matrix heterogeneous. 59

Figure 31: Relative permeability curves (left), fractional function (middle) and its derivative (right) calculated in the three different cases shown on Figure 30. 59

Figure 32: Simulations of two-phase flow in permeable regions with variable densities of parallel fractures. Above - flow evolution plots of fractured regions at densities of 1m / m² (left) and 3m / m² (right). Fracture aperture is 50 µm and the matrix permeability is 2 mD. Below left - fractional flow curves from fracture densities of 0.5 to 3 m / m². Below right - pseudo relative permeability curves for the fracture densities of 0.5 to 3 m / m². 62

Figure 33: Simulations of two-phase flow in permeable regions with parallel fractures of variable aperture. Above - flow evolution plots of fractured regions at apertures of 10 µm (left) and 100 µm (right). Fracture density is 1m / m² and the matrix permeability is 2 mD. Below left - fractional flow curves from fracture apertures of 10 to 100 µm. Below right - pseudo relative permeability curves for fracture apertures of 10 to 100 µm. 62

Figure 34: Simulations of two-phase flow in permeable regions with variable densities of diagonal fractures. Above - flow evolution plots of fractured regions at densities of 1m / m² (left) and 5m / m² (right). Fracture aperture is 50 µm and the matrix permeability is 2 mD. Below left - fractional flow curves from fracture densities of 1 to 5 m / m². Below right - pseudo relative permeability curves for the fracture densities of 1 to 5 m / m². 64

Figure 35: Simulations of two-phase flow in permeable regions with diagonal fractures of variable aperture. Above - flow evolution plots of fractured regions at apertures of 10 µm (left) and 100 µm (right). Fracture density is 1m / m² and the matrix permeability is 2 mD. Below left - fractional flow curves from fracture apertures of 10 to 100 µm. Below right - pseudo relative permeability curves for fracture apertures of 10 to 100 µm. 64

Figure 36: fractional flow and pseudo relative curves for three different area sizes, 5, 10 and 50 m. 65

Figure 37: Simulations of two-phase flow in permeable regions with variable densities of orthogonal fractures. Above - flow evolution plots of fractured regions at densities of 1m / m² (left) and 5m / m² (right). Fracture aperture is 50 µm and the matrix permeability is 2 mD. Below left - fractional flow curves from fracture densities of 1 to 5 m / m². Below right - pseudo relative permeability curves for the fracture densities of 1 to 5 m / m². 66

Figure 38: Simulations of two-phase flow in permeable regions with orthogonal fractures of variable aperture. Above - flow evolution plots of fractured regions at apertures of 10 µm (left) and 100 µm (right). Fracture density is 1 m / m² and the matrix permeability is 2 mD. Below left - fractional flow curves from fracture apertures of 10 to 100 µm. Below right - pseudo relative permeability curves for the fracture apertures of 10 to 100 µm. 66

Figure 39: snapshot showing the saturation evolution of pattern SG4 and SG5 at four different time step. The flow is perpendicular to the fractures. 67

Figure 40: snapshots showing the saturation for the pattern SG4 when flow is parallel (top) and perpendicular to the fractures. 68

Figure 41: time plot showing the saturation at the outflow boundary for pattern SG4 and SG5 (respectively left and middle diagrams) when the flow is parallel to the structures. Also represent is the pattern SG4 when the flow is perpendicular to the fractures (right). 68

Figure 42: Pseudo relative (left), fractional flow function (middle) and its derivative (right) curves determined for patterns SG4 (top) and SG5 (bottom). In each case, three simulations are represented (see text). 69

Figure 43: Global permeability determined using the flow model versus geometric mean permeability for the seven cases of sedimentary heterogeneity. 71

Figure 44(a): Snapshots of supercritical CO_2 and water flow in a region of homogeneous sands. The sand has a permeability of 0.1D and a standard deviation of log K of 0.1. CO_2 is injected along the bottom edge of the model which is initially water saturated. The modelled region is 38 by 38m. Boundary conditions are constant flow top and bottom and no flow conditions imposed right and left. 73

Figure 45 (a): Saturation evolution plots showing the changes in the saturation at the boundary with time through the simulations. Top – turbidite sequence with parallel continuous layering with flow perpendicular (left) and parallel (right) to layering. Bottom - turdidite sequence with parallel discontinuous layering (shale layers around 5m long) and flow perpendicular (left) and parallel (right) to layering. 82

Figure 46(a): Pseudo relative permeability curves (left) and saturation versus injected pore volume of fluid (right). Top – turbidite sequence with parallel continuous layering. Bottom - turbidite sequence with parallel discontinuous layering (shales around 5m long). Dotted line – case for homogeneous sands. 85

Figure 47: geometry of the various patterns used to study the influence of the layer / matrix permeability contrast on the front geometry and on the saturation evolution. 90

Figure 48: Snapshot of the saturation evolution for the pattern R1 when (a) R_k=8 10^{-1}, (b) R_k=8 10^{-3} and (c) R_k=8 10^{-4}. (d) Layer pattern R1 superposed on the saturation field T6-c. Circles indicate intersections where water is trapped. 92

Figure 49: Time evolution of the saturation field for the pattern R1 when R_k is (a) 8 10^{-1}, (b) 8 10^{-3} and (c) 8 10^{-4}. 93

Figure 50: comparison of the time evolution of the saturation field for pattern R1 and R2. 93

Figure 51: pseudo relative curves for simulations performed on pattern R1. 94

Figure 52: Fractional flow and its derivative for the simulations performed on patterns R1 and R2. 94

Figure 53: Evolution of the cross over saturation S_c and of the irreducible CO_2 saturation (IS_{CO2}) with respect to the permeability ratio for patterns R1 and R2. 95

Figure 54: evolution of the peak saturation Sp (left) and of the peak intensity (right) with respect to the permeability ratio. 95

Figure 55: snapshots of the saturation evolution for a strong permeability contrast (top row) and for a null one (bottom row) for the pattern R3. Time step is similar in both simulations. 96

Figure 56: Time evolution plot determined for four different permeability ratio for the pattern R3 (a) R_k=1, (b) R_k=8.4 10^{-2}, (c) R_k=8.4 10^{-3}, and (d) R_k=8.4 10^{-4}. 97

Figure 57: saturation curves corresponding to the saturation plots reported in Figure 56. 97

Figure 58: pseudo relative curves determined for a permeability ratio varying from 1to 10^{-4} for a pattern with D=2, a=1.5, and P=64.8%. 98

Figure 59: Fractional flow curves (left) and its derivative (right) determined for a permeability ratio varying from 1to 10^{-4} and for a pattern with D=2, a=1.5, and P=64.8%. 99

Figure 60: Evolution of the irreducible saturation IS_{CO2} (left) and of the cross over saturation S_c (right) with respect to the permeability ratio R_k. 100

Figure 61: evolution of the peak saturation Sp (left) and of the peak intensity (right) with respect to the permeability ratio. 100

Figure 62: geometry of the two different patterns used to establish the dependence of the permeability ratio R_k on the geometry of the front. 102

Figure 63: snapshot showing the saturation field at four different time step for the same permeability ratio and four different densities. 105

Figure 64: evolution for the five first time step of the front width w for various layer densities (left) and evolution of w with respect to density for time step t1 and t5 (right) - line are only guide for the eyes. 105

Figure 65: Maximum and minimum position of the front for the 5 first time steps and for various density. 107

Figure 66: time evolution of the saturation field for the six different considered density and saturation curves associated to it. 107

Figure 67: comparison of the saturation field for the four first time step when layers act as barrier (R_k=10^{-3}) and as preferential path (R_k=16.8), for pattern A (top) and C (bottom). 109

Figure 68: Time evolution of the saturation at the outflow boundary for all considered patterns (from A. to F). Corresponding saturation curves are shown on the right part. 111

Figure 69: evolution of the saturation difference $S_{barr}(t)$-$S_{path}(t)$ for the same pattern when layers act as barrier and as path with respect to time. 112

Figure 70: evolution of the front width w with respect to the density p of layers for time step t1 and t5. Layers act as preferential path and lines are guides for the eyes. 112

Figure 71a: pseudo relative curves determined for patterns A to F. Left: case where layers act as preferential path. Right: case where layers act as flow barriers. 113

Figure 72a: Fractional flow curves determined for patterns A to F. Top: case where layers act as preferential path. Bottom: case where layers act as flow barriers. 114

Figure 73(a): dependence of the cross over saturation S_c (left) and of the irreducible CO_2 saturation IS_{CO2} (right) with respect to the percentage of heterogeneities presents in the system when layers act as path (blue square) and as barrier (orange square). 116

Figure 74: Fractal patterns used to study the influence of spatial organisation of heterogeneities on the saturation evolution. (Left) pattern L_3, D=2, (middle) pattern L_2, D=1.75, (right) pattern L_1, D=1.5. 117

Figure 75: Pattern used to study the density dependency when D=1.5. All geometrical characteristics are summarised in Table 21. 118

Figure 76: pattern L2 (D=1.75) and L3 (D=2) used to study the density dependence on fractal pattern. 119

Figure 77: Saturation plot observed for a permeability contrast between fractures and matrix of 10^{-3}, for three patterns displaying a different fractal dimension. The amplitude of the viscous fingering is the same in the three cases. 120

Figure 78: Time evolution of the saturation front for three different fractal dimension. 120

Figure 79: evolution of the pseudo relative curves (top), the fractional flow function (middle) and its derivative (bottom) with respect to the saturation for the three considered geometry 121

Figure 80: observed front geometry for six different densities (see Table 21). 122

Figure 81: Left column: evolution of the pseudo relative curves (top) for the six different patterns presented above, and of the derivative of the fractional flow function (bottom), with respect to the saturation. Right column: evolution with respect to the proportion of heterogeneity of the cross over saturation Sc and of the peak intensity. 123

Figure 82: front geometry at T=10 for the three different considered geometry and for a proportion of element acting as barriers equal to 6%. 124

Figure 83: Comparison of seismic surveys before and 2 years after start of CO_2 injection. The CO_2 plume is about 200m high and 500m broad (recent results from SACS project). 128